

**School of Civil and Mechanical Engineering
Department of Mechanical Engineering**

**Dynamic Modelling of Planetary Gear Systems for Gear Tooth Fault
Detection**

Zhongwei WANG

**This thesis is presented for the Degree of
Master of Philosophy
of
Curtin University of Technology**

September 2010

Statement of Originality

"To the best of my knowledge and belief this thesis contains no material previously published by any other person except where due acknowledgment has been made. This thesis contains no material which has been accepted for the award of any other degree or diploma in any university."

..... (Signed)

..... (Date)

Acknowledgement

I would like to express my gratitude to all those who gave me the possibility to complete this research.

I am deeply indebted to my supervisor A/Prof. I. Howard from Curtin University of Technology whose stimulating suggestions and encouragement helped me in the research for this project. I would also like to extend my gratitude to the rest of the Department of Mechanical Engineering for providing assistance and understanding.

Finally I would like to give my special thanks to my family whose patient love enabled me to complete this research.

Abstract

Geared systems have been widely used in mechanical applications for more than a hundred years. A large range of literature has been published especially for spur/helical gear systems and the investigations into technical areas of spur/helical gears have been very well developed, including understanding of condition monitoring systems, diagnostic and prognostic methods. However, there is a lack of understanding on the general dynamic behavior of planetary gear systems with tooth faults. Planetary gears are normally used as effective power transmission elements with high power to weight/volume ratios, large speed reductions in compact volume, and high reliability. They tend to have high efficiency and are used in many applications, such as automotive, heavy truck/tractor, helicopter, wind turbines and bucket wheel reclaimer gearboxes.

The purpose of this research is to develop a vibration analysis system that simulates dynamic behavior of large low speed, high torque planetary spur gear systems such as used in bucket wheel reclaimer and wind turbine gearboxes, with and without gear element faults. This thesis investigates lumped mass modelling methods for planetary gearbox dynamic behavior based on previous gearbox modelling research including the use of the coupled torsional-transverse behavior of the gear body. The dynamic model of the planetary spur gear system includes effects such as: variable tooth mesh stiffness, dynamic transmission error effects, and pitch and profile excitation for gear fault detection purposes. Different tooth faults are simulated using the concept of combined torsional mesh stiffness. The dynamics of spur planetary gear systems with and without tooth faults are compared and analyzed to improve the understanding of fault detection in the present gear systems.

Dynamic modelling of gear systems, such as outlined in this thesis can assist in understanding the consequence of large transient events, including the fluctuations in tooth loads which can reduce gear fatigue life and lead to further tooth damage. Early detection of faults on gear teeth can be used to initiate maintenance actions in order to reduce repair work and avoid catastrophic breakdown.

Table of Contents

STATEMENT OF ORIGINALITY	1
ACKNOWLEDGEMENT	2
ABSTRACT	3
TABLE OF CONTENTS	4
ABBREVIATIONS.....	7
NOMENCLATURE	8
LIST OF TABLES.....	15
LIST OF FIGURES.....	16
1. INTRODUCTION	21
1.1. THE RESEARCH TITLE	21
1.2. THE RESEARCH OVERVIEW	21
1.3. THE RESEARCH OBJECTIVE	21
1.4. SIGNIFICANCE	22
1.5. THE RESEARCH METHOD	23
1.6. SPECIAL FEATURES.....	24
1.7. OVERVIEW OF CHAPTERS.....	24
2. LITERATURE REVIEW.....	26
2.1. OVERVIEW	26
2.2. DYNAMIC MODELLING OF GEARS IN MESH WITH SINGLE TOOTH ONLY.....	27
2.3. DYNAMIC MODELLING OF GEARS IN MESH WITH TOOTH AND OTHER ELEMENTS.....	28
2.4. DYNAMIC MODELLING OF OVERALL GEARBOX.....	29
3. DYNAMIC MODELLING OF PLANETARY GEAR SYSTEMS.....	32
3.1. SUN GEAR – PLANET GEAR PAIR	33
3.2. RING GEAR – PLANET GEAR PAIR.....	43
3.3. CARRIER ARM – PLANET GEAR PAIR.....	53
3.4. OVERALL PLANETARY GEAR SYSTEM.....	58
3.5. SUMMARY OF CHAPTER	67
4. PITCH AND PROFILE EXCITATION	68
4.1. GEAR GEOMETRY ERRORS AND RANDOM EXCITATION FOR A SPUR GEAR PAIR	69
4.2. TOOTH MESHING VARIATION.....	75
4.3. SIMULATION OF PITCH AND PROFILE EXCITATION WITH RANDOM IMPULSE FOR PLANETARY GEAR SYSTEMS	84
4.4. SUMMARY OF CHAPTER	90
5. TOOTH MESH STIFFNESS ANALYSIS	91
5.1. COMBINED TORSIONAL MESH STIFFNESS OF MESHING GEARS.....	91
5.2. SIMULATION OF MESH STIFFNESS WITHOUT TOOTH FAULTS.....	94
5.3. MODELLING OF TOOTH CRACK.....	97
5.4. MODELLING OF TOOTH SPALLING	100
5.5. SUMMARY OF CHAPTER	102
6. LARGE LOW SPEED, HIGH TORQUE PLANETARY SPUR GEAR SYSTEMS- BUCKET WHEEL RECLAIMER DESIGN.....	105
6.1. BUCKET WHEEL RECLAIMER DESIGN	105
6.2. BUCKET WHEEL DRIVE.....	106
6.3. THE MOTOR.....	106

6.4.	FLUID COUPLING	107
6.5.	REDUCTION GEAR BOX	108
6.6.	PLANETARY GEAR BOX	109
6.7.	BUCKET WHEEL AND LOAD MATERIAL	111
6.8.	SUMMARY OF CHAPTER	112
7.	GENERALISED SOFTWARE MODEL	114
7.1.	FLOW CHART OF PROGRAMS	114
7.2.	INPUT	116
7.3.	AUTOMATIC ASSEMBLY OF EQUATIONS OF MOTION (PROGRAM USED FOR CHAPTER 3)	119
7.4.	GENERATION PROGRAM OF TRANSMISSION ERRORS (PROGRAM USED FOR CHAPTER 4)	122
7.4.1.	PLANET GEAR PITCH ERROR	122
7.4.2.	RING GEAR PITCH ERROR	122
7.4.3.	SUN GEAR PITCH ERROR	122
7.4.4.	SUN GEAR - PLANET GEAR PAIR PROFILE ERROR	122
7.4.5.	RING GEAR - PLANET GEAR PAIR PROFILE ERROR	122
7.4.6.	RANDOM EXCITATION	122
7.4.7.	TOOTH MESHING VARIATION	123
7.4.8.	COMBINED PITCH AND PROFILE EXCITATION	123
7.5.	TOOTH MESH STIFFNESS (PROGRAM USED FOR CHAPTER 5)	123
7.6.	PROGRAM USED FOR CHAPTER 6	124
7.6.1.	TORQUE-SPEED CURVE OF MOTOR	124
7.6.2.	INERTIA OF CARRIER ARM WITH BUCKET WHEEL AND LOAD MATERIAL	125
7.6.3.	MASS OF CARRIER ARM WITH BUCKET WHEEL AND LOAD MATERIAL	125
7.7.	PROGRAM USED FOR CHAPTER 8	125
7.7.1.	INPUT TORQUE	125
7.7.2.	OUTPUT TORQUE	126
7.7.3.	SOLVER	126
7.8.	PROGRAM USED FOR CHAPTER 9	126
7.8.1.	RING-PLANET PROFILE ERROR ASSOCIATED WITH SPALLING	126
7.8.2.	SUN-PLANET PROFILE ERROR ASSOCIATED WITH SPALLING	126
7.9.	SUMMARY OF CHAPTER	127
8.	VIBRATION MODELLING WITH UNDAMAGED GEARS	129
8.1.	ASSUMPTIONS AND INPUT	129
8.2.	SIMULATION RESULTS	132
8.3.	COMPARISON OF CASE-1, CASE-2 AND CASE-3	149
8.4.	SUMMARY OF CHAPTER	152
9.	VIBRATION MODELLING WITH GEAR FAULTS	154
9.1.	MODEL WITH A LOCALISED TOOTH CRACK IN MESH	156
9.1.1.	CRACK ON SUN GEAR TOOTH	156
9.1.2.	CRACK ON RING GEAR TOOTH	169
9.1.3.	CRACK ON PLANET GEAR TOOTH	181
9.2.	MODEL WITH A LOCALISED TOOTH SPALL IN MESH	193
9.2.1.	SPALL ON SUN GEAR TOOTH	194
9.2.2.	SPALL ON RING GEAR TOOTH	205
9.2.3.	SPALL ON PLANET GEAR TOOTH	214
9.3.	SUMMARY OF CHAPTER	224
10.	DISCUSSION	227
11.	CONCLUSION	230
12.	REFERENCES	233
13.	APPENDIX	239
13.1.	MATLAB PROGRAM	239
13.1.1.	ipdata.m	239

13.1.2.	<i>velocityvector.m</i>	240
13.1.3.	<i>displacementvector.m</i>	240
13.1.4.	<i>cunfangMCKF.m</i>	241
13.1.5.	<i>erppp.m</i> & <i>esppp.m</i>	256
13.1.6.	<i>erppr.m</i>	256
13.1.7.	<i>espps.m</i>	256
13.1.8.	<i>espp.m</i>	256
13.1.9.	<i>erpp.m</i>	256
13.1.10.	<i>esppran.m</i>	257
13.1.11.	<i>erppran.m</i>	257
13.1.12.	<i>Ymr1.m</i> / <i>Ymr2.m</i> / <i>Ymr3.m</i>	257
13.1.13.	<i>Yms1.m</i> / <i>Yms2.m</i> / <i>Yms3.m</i>	258
13.1.14.	<i>yrrr.m</i>	259
13.1.15.	<i>ymss.m</i>	259
13.1.16.	<i>erp1.m</i> / <i>erp2.m</i> / <i>erp3.m</i>	260
13.1.17.	<i>esp1.m</i> / <i>esp2.m</i> / <i>esp3.m</i>	261
13.1.18.	<i>Kmr1.m</i> / <i>Kmr2.m</i> / <i>Kmr3.m</i>	262
13.1.19.	<i>Kms1.m</i> / <i>Kms2.m</i> / <i>Kms3.m</i>	264
13.1.20.	<i>mstiffr.m</i>	265
13.1.21.	<i>mstiffs.m</i>	267
13.1.22.	<i>TorM.m</i>	268
13.1.23.	<i>inertiaC.m</i>	268
13.1.24.	<i>massC.m</i>	269
13.1.25.	<i>TorqueS.m</i>	269
13.1.26.	<i>torqueOUT.m</i>	269
13.1.27.	<i>Vdp1.m</i>	270
13.1.28.	<i>emr1.m</i> / <i>emr2.m</i> / <i>emr3.m</i>	271
13.1.29.	<i>emrrr.m</i>	272
13.1.30.	<i>ems1.m</i> / <i>ems2.m</i> / <i>ems3.m</i>	273
13.1.31.	<i>emsss.m</i>	275
13.2.	RESULTS OF UNDAMAGED GEARBOX, CASE-2	276

Abbreviations

Abbreviation	Meaning
FEA	Finite Element Analysis
FEM	Finite Element Method
ODE	Ordinary Differential Equations
AN.	Assumption Number
FSA	Frequency Spectrum Analysis
CWTA	Continuous Wavelet Analysis

Nomenclature

Symbol	Symbol in Mfile	Meaning
a_1	a1	constant coefficient for mesh stiffness
a_2	a2	constant coefficient for mesh stiffness
a_3	a3	constant coefficient for mesh stiffness
B	B	face width
B	--	point, shown in Figure 4-12
b	--	gear face width
b_1	b1	constant coefficient for mesh stiffness
b_2	b2	constant coefficient for mesh stiffness
b_3	b3	constant coefficient for mesh stiffness
$B_r Q_3$	calculated	length, shown in Figure 4-12
BsCs	calculated	length, shown in Figure 4-12
BsDs	calculated	length, shown in Figure 4-12
BsEs	calculated	length, shown in Figure 4-12
BsNs	calculated	length, shown in Figure 4-12
BsPs	calculated	length, shown in Figure 4-12
BrCr	calculated	length, shown in Figure 4-12
BrDr	calculated	length, shown in Figure 4-12
BrEr	calculated	length, shown in Figure 4-12
BrPr	calculated	length, shown in Figure 4-12
<i>carrier</i>	c (short as)	carrier arm
C	--	point, shown in Figure 4-12
c_c	ccx; ccy	shaft transverse damping (shaft-carrier)
$C_{coupling}$	calculated	damping of coupling
c_{ct}	cct	shaft torsional damping (shaft-carrier)
c_{px}	Cpx	damping between planet gear and carrier arm, representing bearing damping, x direction
c_{py}	Cpy	damping between planet gear and carrier arm, representing bearing damping, y direction

c_r	crx; cry	base transverse damping (base-ring)
c_{rp_i}	Crp	gear mesh damping between ring and planet i
c_{rt}	crt	base torsional damping (base-ring)
c_s	csx; csy	shaft transverse damping (shaft-sun)
c_p	--	tooth tip clearance of planet gear
c_r	--	tooth tip clearance of ring gear
c_s	--	tooth tip clearance of sun gear
c_{sp_i}	Csp	gear mesh damping between sun and planet i
c_{st}	cst	shaft torsional damping (shaft-sun)
D	--	point, shown in Figure 4-12
d_p	dp	pitch diameter of planet gear
d_r	dr	pitch diameter of ring gear
D_{rb}	calculated	relative displacement between ring gear and base
D_{rcp_i}	Drcp	radial direction change from planet gear design center to real center
d_s	ds	pitch diameter of sun gear
D_{ss}	--	relative displacement between sun gear and sun gear shaft
D_{tcp_i}	Dtcp	direction change (perpendicular to radial direction) from planet gear design center to real center
E	--	point, shown in Figure 4-12
E	ipdata(21)	Young's Modulus
E_{mesh}	calculated	coefficient of equal stiffness effect
$e_{pitch}(t)$	esppp; espps; erppp; erppr	pitch error
$e_{profile}(t)$	espp; erpp	profile error
$E_{r_i}(t)$	fEr	run out functions
$e_{rp_i}(t)$	ferp	gear combined gear error (pitch and profile), ring-planet pair i
$E_{rp_i}(t)$	fErp	run out functions
$E_{s_i}(t)$	fEs	run out functions
$e_{sp_i}(t)$	fesp	gear combined gear error (pitch and profile), sun-planet pair i
$E_{sp_i}(t)$	fEsp	run out functions
F	calculated	force
G1	--	1 st gear of reduction gearbox
G2	--	2 nd gear of reduction gearbox
G3	--	3 rd gear of reduction gearbox

G4	--	4 th gear of reduction gearbox
G5	--	5 th gear of reduction gearbox
G6	--	6 th gear of reduction gearbox
f	ipdata(32)	supply frequency
h_p	h	tooth addendum height of planet gear
h_{pa}	ha	tooth dedendum height of planet gear
h_{pf}	hf	tooth height of planet gear
h_r	h	tooth addendum height of ring gear
h_{ra}	ha	tooth dedendum height of ring gear
h_{rf}	hf	tooth height of ring gear
h_s	h	tooth addendum height of sun gear
h_{sa}	ha	tooth dedendum height of sun gear
h_{sf}	hf	tooth height of sun gear
i	i or j	the i^{th}
I	--	tooth inertia
$inertia_b$	calculated	inertia of a single bucket
$inertia_o$	calculated	inertia of a full bucket of ore
$inertia_w$	calculated	inertia of bucket wheel body
J_c	calculated	mass moment of inertia, carrier arm
J_p	calculated	mass moment of inertia, planet gear
J_r	calculated	mass moment of inertia, ring gear
J_s	calculated	mass moment of inertia, sun gear
K	calculated	stiffness
K_{bg}	calculated	body stiffness of gear
K_{bp}	calculated	body stiffness of pinion
k_c	kcx; key	shaft transverse stiffness (shaft-carrier)
k_{ct}	kct	shaft torsional stiffness (shaft-carrier)
K_g	calculated	stiffness of gear
K_p	calculated	stiffness of pinion
k_{px}	Kpx	stiffness between planet gear and carrier arm, representing bearing stiffness, x direction
k_{py}	Kpy	stiffness between planet gear and carrier arm, representing bearing stiffness, y direction
k_r	krx; kry	base transverse stiffness (base-ring)
$k_{rpi}(t)$	Krp	gear mesh stiffness between ring and planet i

k_{rt}	krt	base torsional stiffness (base-ring)
k_s	ksx; ksy	shaft transverse stiffness (shaft-sun)
$k_{sp_i}(t)$	Ksp	gear mesh stiffness between sun and planet i
k_{st}	kst	shaft torsional stiffness (shaft-sun)
K_{tg}	calculated	tooth stiffness of gear
K_{tp}	calculated	tooth stiffness of pinion
m	module	module
$mass_b$	calculated	mass of a single bucket
$mass_o$	calculated	mass of a full bucket of ore
$mass_w$	calculated	mass of bucket wheel body
$MD_{rp_i}(t)$	MDrpi	relative mesh displacement along the line of action (ring-planet)
$MD_{sp_i}(t)$	MDspi	relative mesh displacement along the line of action (sun-planet)
m_c	massC	mass of carrier arm
m_p	mass(10); mass(11)	mass of planet gear
m_r	mass(4); mass(5)	mass of ring gear
m_s	mass(1); mass(2)	mass of sun gear
MsBs	calculated	length, shown in Figure 4-12
MsEs	calculated	length, shown in Figure 4-12
MsNs	calculated	length, shown in Figure 4-12
MsPs	calculated	length, shown in Figure 4-12
MrBr	calculated	length, shown in Figure 4-12
MrNr	calculated	length, shown in Figure 4-12
MrPr	calculated	length, shown in Figure 4-12
n	n; nofp	number of planetary gears
n_o	--	number of buckets with the same loading condition
O_c	--	center of carrier arm coordinate system
$Olcc$	ipdata(92)	ore loading condition coefficient
Op	--	design position of planet gear center on carrier arm
Op'	--	real position of planet gear center on carrier arm
Or	--	center of ring gear coordinate system
Os	--	center of sun gear coordinate system
P	--	point, shown in Figure 4-12

p	calculated	circular pitch
P	p	number of poles
p_i	P (short as)	the i^{th} planet gear
p_n	ipdata(20i) (partial)	an integer that varies for each planet gear corresponding to planet phasing
p_o	--	percentage of ore in a single bucket
p_{rb}	calculated	circular pitch
$P_r Q_3$	calculated	length, shown in Figure 4-12
p_{sb}	calculated	circular pitch
$P_s P_r$	calculated	length, shown in Figure 4-12
q_{cc}	qcc	coupling damping coefficient
Q_1	--	image of P_s when the contact line $M_s N_s$ is wrapped on the planet base circle
Q_2	--	point, an arc-length tb away from Q_1
$Q_2 B_r$	calculated	length, shown in Figure 4-12
Q_3	--	point, the first point in the ring gear - planet gear contact region $B_r E_r$ that is an integer number of base pitches away from Q_2
R_{pa}	Rpa	addendum circle diameter of planet gear
R_{pb}	Rpb	base circle radius of planet gear
R_{pf}	dpf, ($2 * R_{pf}$)	root circle radius of planet gear
R_{ra}	Rra	addendum circle diameter of ring gear
R_{rb}	Rrb	base circle radius of ring gear
R_{rf}	drf, ($2 * R_{rf}$)	root circle radius of ring gear
R_{sa}	Rsa	addendum circle diameter of sun gear
R_{sb}	Rsb	base circle radius of sun gear
R_{sf}	dsf, ($2 * R_{sf}$)	root circle radius of sun gear
r_c	rc	design radial distance between the centers of planet gear and carrier arm
r_{cp_i}	rcp	real radial distance between the centers of the i^{th} planet gear and carrier arm
<i>ring</i>	r (short as)	ring gear
r_{p_i}	rp	base circle of the i^{th} planet gear
r_r	rr	base circle of ring gear
$rrn(i)$	rrn(i)	relative phase between the n^{th} ring gear - planet gear mesh and the arbitrarily chosen first ring gear - planet gear mesh

r_{rb}	rb	radius of relative displacement measure point to ring gear center
r_s	rs	base circle of sun gear
$rsn(i)$	rsn(i)	relative phase between the n th sun gear - planet gear mesh and the arbitrarily chosen first sun gear - planet gear mesh
r_{ss}	rss	radius of relative displacement measure point to sun gear shaft center
rrs	rss	phase difference between sun gear - planet gear mesh and ring gear - planet gear mesh
s	--	tooth thickness
SP_{rp_i}	SPrp	tooth separation phenomenon (ring-planet) description function
SP_{sp_i}	SPsp	tooth separation phenomenon (sun-planet) description function
sun	s (short as)	sun gear
t_b	tb	planet tooth thickness at the base circle
T_c	Tc	carrier arm output torque
T_{fl}	calculated	full load torque
T_g	calculated	torque applied on gear
$T_{maximum}$	calculated	maximum torque
T_p	calculated	torque applied on pinion
T_{rb}	Trb	torque between ring gear and ring gear base
T_{ss}	Tss	torque between sun gear and sun gear shaft
$T_{start-up}$	calculated	start-up torque
u_c	uc	design circle linear speed of carrier arm (planet mounted circle)
u_{pi}	up	base circle linear speed of the i^{th} planet gear
u_r	ur	base circle linear speed of ring gear
u_s	us	base circle linear speed of sun gear
\dot{u}_r^*	calculated	ring gear total torsional displacement (in terms of linear displacement on pitch circle)
\dot{u}_s^*	calculated	sun gear total torsional displacement (in terms of linear displacement on pitch circle)
x_c	xc	x axis of carrier arm
x_{pi}	xp	x axis of the i^{th} planet gear
x_r	xr	x axis of ring gear
x_s	xs	x axis of sun gear
x_{pi}^*	calculated	planet gear displacement in x direction from the original sun gear centre

y_c	yc	y axis of carrier arm
y_{pi}	yp	y axis of the i^{th} planet gear
y_r	yr	y axis of ring gear
y_s	ys	y axis of sun gear
y_{pi}^*	calculated	planet gear displacement in y direction from the original sun gear centre
Z_g	calculated	tooth number of gear
Z_p	calculated	tooth number of pinion
z_p	zp	teeth number of planet gear
z_r	zr	teeth number of ring gear
z_s	zs	teeth number of sun gear
$\Delta\psi_i$	Dfae	angular change of the i^{th} planet gear center position about carrier arm center
α	--	coefficient of pitch/profile error amplitude
α_p	ap	pressure angle, planet gear
α_r	ar	pressure angle, ring gear
α_s	as	pressure angle, sun gear
θ	calculated	angular displacement
θ_c	calculated	torsional angle displacement of carrier arm
θ_g	calculated	angular displacement of gear
θ_p	calculated	angular displacement of pinion
θ_{pi}	calculated	torsional angle displacement of the i^{th} planet gear
θ_r	calculated	torsional angle displacement of ring gear
θ_s	calculated	torsional angle displacement of sun gear
θ_t	calculated	number of teeth have meshed
ψ_i	fae	the i^{th} planet gear angle position about sun gear/ring gear coordinate system
ψ_n	ipdata(20i)	circumferential angle of planet gears measured positive counter-clockwise
\dot{symbol}	D; d	differential symbol

List of Tables

TABLE 3-1 THE TABULAR METHOD FOR THE PLANETARY GEAR RATIOS	65
TABLE 4-1 DEVELOPMENT OF EQUATIONS REPRESENTING MESH PHASING VARIATION.....	75
TABLE 4-2 SYMBOLS CONTAINED IN FIGURE 4-12 AND THE CORRESPONDING GEAR MESH PARAMETERS	79
TABLE 4-3 DETERMINING THE SIGN OF r_{rs} ⁵⁶	83
TABLE 6-1 PARAMETERS OF REDUCTION GEARS	108
TABLE 6-2 PARAMETERS OF PLANETARY GEARS	109
TABLE 6-3 THE TABULAR METHOD FOR THE PLANETARY GEAR RATIOS	110
TABLE 6-4 MAJOR PARAMETERS OF THE BUCKET WHEEL RECLAIMER COMPONENTS	112
TABLE 7-1 LIST OF INPUTS	116
TABLE 8-1 ASSUMPTIONS AND VALUES OF INPUTS ASSOCIATED WITH MODELLING WITH UNDAMAGED TOOTH (*AN SHORT FOR ASSUMPTION NUMBER; I , MORE REALISTIC; II, MORE DETAILED; III, MORE COMPUTATIONAL EFFICIENT)	129
TABLE 9-1 DETECTABILITY OF SUN GEAR TOOTH CRACK BASED ON AVERAGED SIGNALS	161
TABLE 9-2 DETECTABILITY OF SUN GEAR TOOTH CRACK BASED ON FSA.....	165
TABLE 9-3 DETECTABILITY OF SUN GEAR TOOTH CRACK BASED ON CWTA	165
TABLE 9-4 DETECTABILITY OF RING GEAR TOOTH CRACK BASED ON AVERAGED SIGNALS	174
TABLE 9-5 DETECTABILITY OF RING GEAR TOOTH CRACK BASED ON FSA	177
TABLE 9-6 DETECTABILITY OF RING GEAR TOOTH CRACK BASED ON CWTA	178
TABLE 9-7 DETECTABILITY OF PLANET GEAR-1 TOOTH CRACK BASED ON AVERAGED SIGNALS	186
TABLE 9-8 DETECTABILITY OF PLANET GEAR-1 TOOTH CRACK BASED ON FSA	190
TABLE 9-9 DETECTABILITY OF PLANET GEAR-1 TOOTH CRACK BASED ON CWTA	190
TABLE 9-10 DETECTABILITY OF SUN GEAR TOOTH SPALLING BASED ON FSA	201
TABLE 9-11 DETECTABILITY OF SUN GEAR TOOTH SPALLING BASED ON CWTA	202
TABLE 9-12 DETECTABILITY OF RING GEAR TOOTH SPALLING BASED ON FSA	212
TABLE 9-13 DETECTABILITY OF RING GEAR TOOTH SPALLING BASED ON CWTA	213
TABLE 9-14 DETECTABILITY OF PLANET GEAR-1 TOOTH SPALLING BASED ON FSA.....	221
TABLE 9-15 DETECTABILITY OF PLANET GEAR-1 TOOTH SPALLING BASED ON CWTA	222
TABLE 9-16 SUMMARY OF THE INDICATION AND DETECTABILITY OF GEAR TOOTH FAULTS (*INDICATIONS OF DAMAGE ARE LISTED IN TABLE 9-17 IN THE CASE OF SINGLE TOOTH DAMAGE).....	224
TABLE 9-17 TYPES OF INDICATIONS OF TOOTH DAMAGE	226

List of Figures

FIGURE 2-1 CLASSIFICATION OF GEAR/GEARBOX DYNAMIC MODELLING ³	26
FIGURE 3-1 A SINGLE-STAGE PLANETARY GEAR SYSTEM WITH THREE SINGLE PLANET GEARS (YELLOW COLORED GEARS), ONE SUN GEAR (RED COLORED GEAR), ONE RING GEAR (GREEN COLORED GEAR) AND ONE CARRIER ARM (PURPLE COLORED PART)	32
FIGURE 3-2 A SUN-PLANET PAIR (WITH THE CONTACT POINT IN II QUADRANT ABOUT THE SUN GEAR)	33
FIGURE 3-3 A SUN-PLANET PAIR (WITH THE CONTACT POINT IN FOUR QUADRANTS ABOUT THE SUN GEAR RESPECTIVELY)	35
FIGURE 3-4 THE SIGN-RELATIONSHIP BETWEEN AXIAL RELATIVE DISPLACEMENT AND $MD_{sp_i}(t)$ WITH THE PLANET GEAR POSITIONED IN THE FOUR QUADRANTS ABOUT THE SUN GEAR RESPECTIVELY AS SHOWN IN FIGURE 3-3	36
FIGURE 3-5 FREE BODY DIAGRAM OF PLANET GEAR (SUN-PLANET PAIR ONLY)	37
FIGURE 3-6 FREE BODY DIAGRAM OF SUN GEAR	40
FIGURE 3-7 A RING-PLANET PAIR (WITH THE CONTACT POINT IN II QUADRANT ABOUT THE RING GEAR)	43
FIGURE 3-8 A RING-PLANET PAIR (WITH THE CONTACT POINT IN THE OTHER THREE QUADRANTS ABOUT THE RING GEAR)	45
FIGURE 3-9 THE SIGN-RELATIONSHIP BETWEEN AXIAL RELATIVE DISPLACEMENT AND $MD_{rp_i}(t)$ WITH THE PLANET GEAR POSITIONED IN THE FOUR QUADRANTS ABOUT THE RING GEAR RESPECTIVELY AS SHOWN IN FIGURE 3-8	46
FIGURE 3-10 FREE BODY DIAGRAM OF PLANET GEAR (RING-PLANET PAIR ONLY)	47
FIGURE 3-11 FREE BODY DIAGRAM OF RING GEAR	49
FIGURE 3-12 A CARRIER ARM AND A PLANET GEAR PAIR (WITH THE PIN-BEARING POSITIONED IN II QUADRANT ABOUT THE CARRIER ARM)	53
FIGURE 3-13 THE EQUATIONS RELATING THE PLANET GEAR MOUNTED IN POSITION ON THE CARRIER ARM AND THE RESULTING TRANSVERSAL RELATIVE DISPLACEMENTS	54
FIGURE 3-14 FREE BODY DIAGRAM OF PLANET GEAR (CARRIER-PLANET PAIR ONLY)	55
FIGURE 3-15 FREE BODY DIAGRAM OF CARRIER ARM	56
FIGURE 3-16 MASS MATRIX OF OVERALL EQUATION	59
FIGURE 3-17 (A) ACCELERATION VECTOR (B) VELOCITY VECTOR (C) DISPLACEMENT VECTOR OF OVERALL EQUATION	59
FIGURE 3-18 FORCE VECTOR CONTAINING (A) DAMPING AND (B) STIFFNESS FEATURES RESPECTIVELY	60
FIGURE 3-19 (A) MESH DAMPING MATRIX (ABOVE) AND CONTINUED (MIDDLE) AND (B) SUPPORT STRUCTURE DAMPING MATRIX	62
FIGURE 3-20 MESH STIFFNESS MATRIX (ABOVE) AND CONTINUED (MIDDLE AND BELOW)	63
FIGURE 4-1 TORSIONAL MODEL OF A SPUR GEAR PAIR (SUN GEAR - PLANET GEAR, SHOWN IN THIS FIGURE/ OR RING GEAR - PLANET GEAR)	69
FIGURE 4-2 PLANET GEAR PITCH ERROR (DETAILED PROGRAM IN SEC 7.4.4.1)	70
FIGURE 4-3 RING GEAR PITCH ERROR (DETAILED PROGRAM IN SEC 7.4.4.2)	71
FIGURE 4-4 SUN GEAR PITCH ERROR (DETAILED PROGRAM IN SEC 7.4.4.3)	71
FIGURE 4-5 RELATION BETWEEN THE PROFILE ERROR CHART AND THE INVOLUTE TOOTH PROFILE ⁵⁴	72
FIGURE 4-6 PROFILE ERROR ALONG THE ACTION LINE BY REFERENCE ⁵⁵	72
FIGURE 4-7 SUN GEAR - PLANET GEAR PAIR PROFILE ERROR (ASSUMED CONTACT RATIO EQUAL TO 1)	73
FIGURE 4-8 RING GEAR - PLANET GEAR PAIR PROFILE ERROR (ASSUMED CONTACT RATIO EQUAL TO 1)	74
FIGURE 4-9 RANDOM IMPULSE EXCITATION (400 SAMPLES) (DETAILED PROGRAM IN SEC 7.4.4.6)	74
FIGURE 4-10 MESH PHASING VARIATION OF SUN GEAR - PLANET GEAR MESHES (TOP FIGURE, MESH 1; MIDDLE FIGURE, MESH 2; BOTTOM FIGURE, MESH 3)	77
FIGURE 4-11 MESH PHASING VARIATION OF RING GEAR - PLANET GEAR MESHES (TOP FIGURE, MESH 1; MIDDLE FIGURE, MESH 2; BOTTOM FIGURE, MESH 3)	78
FIGURE 4-12 DETAILED MESH REPRESENTATIVE OF THE PLANETARY GEAR SYSTEM	79

FIGURE 4-13 PHASE DIFFERENCE BETWEEN SUN GEAR - PLANET GEAR MESH AND RING GEAR - PLANET GEAR MESH	83
FIGURE 4-14 NUMBER OF TEETH IN MESH, THE 1 ST SUN GEAR - PLANET GEAR PAIR	85
FIGURE 4-15 PROFILE ERROR ALONG THE ACTION LINE, TWO PAIRS OF TEETH IN CONTACT	85
FIGURE 4-16 SUN GEAR - PLANET GEAR PAIR PROFILE ERROR WITH CONSIDERATION OF TOOTH MESHING VARIATION, FIRST PAIR.....	86
FIGURE 4-17 RING GEAR - PLANET GEAR PAIR PROFILE ERROR WITH CONSIDERATION OF TOOTH MESHING VARIATION, FIRST PAIR.....	87
FIGURE 4-18 COMBINED GEAR ERROR EXCITATION FOR SUN GEAR - PLANET GEAR PAIRS; (A) FOR FIRST PAIR; (B) FOR SECOND PAIR; (C) FOR THIRD PAIR;	88
FIGURE 4-19 COMBINED GEAR ERROR EXCITATION FOR RING GEAR - PLANET GEAR PAIRS; (1) FOR FIRST PAIR; (2) FOR SECOND PAIR; (3) FOR THIRD PAIR;	89
FIGURE 5-1 TORSIONAL MESH STIFFNESS OF RING-PLANET PAIR (A, B, C) AND SUN-PLANET PAIR (D, E, F).....	94
FIGURE 5-2 TORSIONAL MESH STIFFNESS OF RING-PLANET PAIRS WITH A CRACK ON THE 83 RD TOOTH OF THE RING GEAR.....	98
FIGURE 5-3 TORSIONAL MESH STIFFNESS OF RING-PLANET PAIRS WITH TWO SPALLS	101
FIGURE 6-1 COMPACT BUCKET WHEEL RECLAIMER ⁵⁹	105
FIGURE 6-2 TORQUE-SPEED CURVE FOR A 450KW INDUCTION MOTOR	107
FIGURE 6-3 A TYPICAL GEARBOX ARRANGEMENT OF THE BUCKET WHEEL DRIVE (REDUCTION GEAR BOX WITH GEARS G1 TO G6, AND A PLANETARY GEAR BOX) ⁶⁵	108
FIGURE 6-4 MAJOR COMPONENTS USED IN THIS THESIS	112
FIGURE 7-1 FLOW CHART OF PROGRAM DEVELOPED IN THIS RESEARCH	115
FIGURE 7-2 FLOW CHART OF PROGRAM FOR GENERATION OF ODE EQUATIONS	120
FIGURE 7-3 FLOW CHART OF ODE FUNCTION GENERATOR <i>CUNFANGMCKFM</i>	121
FIGURE 7-4 FLOW CHART OF PROGRAM USED FOR TOOTH MESH STIFFNESS	124
FIGURE 8-1 CASE-1 SUN GEAR TIME(S)-DISPLACEMENT(M)	133
FIGURE 8-2 CASE-1 SUN GEAR AVERAGED SHAFT POSITION(DEGREE)-VELOCITY(M/S) VIBRATION	134
FIGURE 8-3 CASE-1 SUN GEAR TIME(S)-TORSIONAL VELOCITY(RPM) AND AVERAGED SHAFT POSITION(DEG)-TORSIONAL VELOCITY(RPM) VIBRATION	134
FIGURE 8-4 CASE-1 ENLARGED FIGURE SHOWS STARTING UP OF SUN GEAR TIME(S)-TORSIONAL VELOCITY(RPM)	135
FIGURE 8-5 CASE-1 FREQUENCY SPECTRUM OF SUN GEAR X DIRECTION VELOCITY VIBRATION...	136
FIGURE 8-6 CASE-1 FREQUENCY SPECTRUM OF SUN GEAR Y DIRECTION VELOCITY VIBRATION ...	136
FIGURE 8-7 CASE-1 FREQUENCY SPECTRUM OF SUN GEAR TORSIONAL VELOCITY VIBRATION	137
FIGURE 8-8 CASE-1 RING GEAR TIME(S)-DISPLACEMENT(M)	137
FIGURE 8-9 CASE-1 RING GEAR AVERAGED SHAFT POSITION(DEGREE)-VELOCITY(M/S) VIBRATION	138
FIGURE 8-10 CASE-1 FREQUENCY SPECTRUM OF RING GEAR X DIRECTION VELOCITY VIBRATION	139
FIGURE 8-11 CASE-1 FREQUENCY SPECTRUM OF RING GEAR Y DIRECTION VELOCITY VIBRATION	139
FIGURE 8-12 CASE-1 FREQUENCY SPECTRUM OF RING GEAR TORSIONAL VELOCITY VIBRATION .	140
FIGURE 8-13 CASE-1 CARRIER ARM TIME(S)-DISPLACEMENT(M)	141
FIGURE 8-14 CASE-1 CARRIER ARM AVERAGED SHAFT POSITION(DEGREE)-VELOCITY(M/S) VIBRATION	141
FIGURE 8-15 CASE-1 CARRIER ARM TIME(S)-TORSIONAL VELOCITY(RPM) AND AVERAGED SHAFT POSITION(DEG)-TORSIONAL VELOCITY(RPM) VIBRATION	142
FIGURE 8-16 CASE-1 ENLARGED FIGURE SHOWS STARTING UP OF CARRIER ARM TIME(S)-TORSIONAL VELOCITY(RPM)	142
FIGURE 8-17 CASE-1 FREQUENCY SPECTRUM OF CARRIER ARM X DIRECTION VELOCITY VIBRATION	143
FIGURE 8-18 CASE-1 FREQUENCY SPECTRUM OF CARRIER ARM Y DIRECTION VELOCITY VIBRATION	144
FIGURE 8-19 CASE-1 FREQUENCY SPECTRUM OF CARRIER ARM TORSIONAL VELOCITY VIBRATION	144
FIGURE 8-20 CASE-1 PLANET GEAR-1 TIME(S)-DISPLACEMENT(M)	145
FIGURE 8-21 CASE-1 PLANET GEAR-2 TIME(S)-DISPLACEMENT(M)	145
FIGURE 8-22 CASE-1 PLANET GEAR-3 TIME(S)-DISPLACEMENT(M)	146
FIGURE 8-23 CASE-1 PLANET GEAR-1 AVERAGED SHAFT POSITION(DEGREE)-VELOCITY(M/S) VIBRATION	146
FIGURE 8-24 CASE-1 FREQUENCY SPECTRUM OF PLANET GEAR-1 X DIRECTION VELOCITY	

VIBRATION.....	147
FIGURE 8-25 CASE-1 FREQUENCY SPECTRUM OF PLANET GEAR-1 Y DIRECTION VELOCITY VIBRATION.....	148
FIGURE 8-26 CASE-1 FREQUENCY SPECTRUM OF PLANET GEAR-1 TORSIONAL VELOCITY VIBRATION	148
FIGURE 8-27 (A) (B) CASE-1 AVERAGED SUN GEAR SHAFT POSITION(DEGREE)-TORSIONAL VELOCITY(RPM) VIBRATION AND ENLARGED FIGURE.....	149
FIGURE 8-28 (A) (B) CASE-1 AVERAGED CARRIER ARM SHAFT POSITION(DEGREE)-TORSIONAL VELOCITY(RPM) VIBRATION AND ENLARGED FIGURE.....	150
FIGURE 8-29 COMPARISON OF SUN GEAR SIGNALS OF UNDAMAGED PLANETARY GEAR SET IN CASE-1 AND CASE-2 (LEFT GRAPH, CASE-1; RIGHT GRAPH, CASE-2).....	152
FIGURE 9-1 SIMULATION OUTPUTS AFTER SIGNAL AVERAGING WITH A SINGLE 80% CRACK ON THE SUN GEAR AT THE 19 TH TOOTH.....	157
FIGURE 9-2 COMPARISON OF RESULTS, UNDAMAGED, 5% CRACKED AND 80% CRACKED SUN GEAR 19 TH TOOTH.....	160
FIGURE 9-3 CASE-2, FSA, SUN GEAR DAMAGE, SUN GEAR X-DIRECTION.....	161
FIGURE 9-4 CASE-2, FSA, SUN GEAR DAMAGE, SUN GEAR Y-DIRECTION.....	162
FIGURE 9-5 CASE-2, FSA, SUN GEAR DAMAGE, SUN GEAR TORSIONAL.....	162
FIGURE 9-6 CASE-2, FSA, SUN GEAR DAMAGE, RING GEAR X-DIRECTION.....	162
FIGURE 9-7 CASE-2, FSA, SUN GEAR DAMAGE, RING GEAR Y-DIRECTION.....	162
FIGURE 9-8 CASE-2, FSA, SUN GEAR DAMAGE, RING GEAR TORSIONAL.....	163
FIGURE 9-9 CASE-2, FSA, SUN GEAR DAMAGE, CARRIER ARM X-DIRECTION.....	163
FIGURE 9-10 CASE-2, FSA, SUN GEAR DAMAGE, CARRIER ARM Y-DIRECTION.....	163
FIGURE 9-11 CASE-2, FSA, SUN GEAR DAMAGE, CARRIER ARM TORSIONAL.....	163
FIGURE 9-12 CASE-2, FSA, SUN GEAR DAMAGE, PLANET GEAR-1 X-DIRECTION.....	164
FIGURE 9-13 CASE-2, FSA, SUN GEAR DAMAGE, PLANET GEAR-1 Y-DIRECTION.....	164
FIGURE 9-14 CASE-2, FSA, SUN GEAR DAMAGE, PLANET GEAR-1 TORSIONAL.....	164
FIGURE 9-15 CASE-2, CWTA, SUN GEAR CRACK, AVERAGED CARRIER ARM TORSIONAL VIBRATION	166
FIGURE 9-16 CASE-2, CWTA, SUN GEAR CRACK, AVERAGED SUN GEAR TORSIONAL VIBRATION ..	167
FIGURE 9-17 SIMULATION OUTPUTS AFTER SIGNAL AVERAGING WITH A SINGLE 80% CRACK ON THE 83 RD TOOTH OF THE RING GEAR.....	170
FIGURE 9-18 COMPARISON OF RESULTS, UNDAMAGED, 5% CRACKED AND 80% CRACKED RING GEAR 83 RD TOOTH.....	173
FIGURE 9-19 CASE-2, FSA, RING GEAR DAMAGE, SUN GEAR X-DIRECTION.....	174
FIGURE 9-20 CASE-2, FSA, RING GEAR DAMAGE, SUN GEAR Y-DIRECTION.....	174
FIGURE 9-21 CASE-2, FSA, RING GEAR DAMAGE, SUN GEAR TORSIONAL.....	175
FIGURE 9-22 CASE-2, FSA, RING GEAR DAMAGE, RING GEAR X-DIRECTION.....	175
FIGURE 9-23 CASE-2, FSA, RING GEAR DAMAGE, RING GEAR Y-DIRECTION.....	175
FIGURE 9-24 CASE-2, FSA, RING GEAR DAMAGE, RING GEAR TORSIONAL.....	175
FIGURE 9-25 CASE-2, FSA, RING GEAR DAMAGE, CARRIER ARM X-DIRECTION.....	176
FIGURE 9-26 CASE-2, FSA, RING GEAR DAMAGE, CARRIER ARM Y-DIRECTION.....	176
FIGURE 9-27 CASE-2, FSA, RING GEAR DAMAGE, CARRIER ARM TORSIONAL.....	176
FIGURE 9-28 CASE-2, FSA, RING GEAR DAMAGE, PLANET GEAR-1 X-DIRECTION.....	176
FIGURE 9-29 CASE-2, FSA, RING GEAR DAMAGE, PLANET GEAR-1 Y-DIRECTION.....	177
FIGURE 9-30 CASE-2, FSA, RING GEAR DAMAGE, PLANET GEAR-1 TORSIONAL.....	177
FIGURE 9-31 CASE-2, CWTA, RING GEAR CRACK, AVERAGED CARRIER ARM TORSIONAL VIBRATION	179
FIGURE 9-32 CASE-2, CWTA, RING GEAR CRACK, AVERAGED SUN GEAR TORSIONAL VIBRATION	180
FIGURE 9-33 SIMULATION OUTPUTS AFTER SIGNAL AVERAGING WITH A SINGLE 80% CRACK ON THE PLANET GEAR-1 AT THE 32 ND TOOTH.....	182
FIGURE 9-34 COMPARISON OF RESULTS, UNDAMAGED, 5% CRACKED AND 80% CRACKED PLANET GEAR-1 32 ND TOOTH.....	185
FIGURE 9-35 CASE-2, FSA, PLANET GEAR-1 DAMAGE, SUN GEAR X-DIRECTION.....	186
FIGURE 9-36 CASE-2, FSA, PLANET GEAR-1 DAMAGE, SUN GEAR Y-DIRECTION.....	187
FIGURE 9-37 CASE-2, FSA, PLANET GEAR-1 DAMAGE, SUN GEAR TORSIONAL.....	187
FIGURE 9-38 CASE-2, FSA, PLANET GEAR-1 DAMAGE, RING GEAR X-DIRECTION.....	187
FIGURE 9-39 CASE-2, FSA, PLANET GEAR-1 DAMAGE, RING GEAR Y-DIRECTION.....	187
FIGURE 9-40 CASE-2, FSA, PLANET GEAR-1 DAMAGE, RING GEAR TORSIONAL.....	188
FIGURE 9-41 CASE-2, FSA, PLANET GEAR-1 DAMAGE, CARRIER ARM X-DIRECTION.....	188

FIGURE 9-42 CASE-2, FSA, PLANET GEAR-1 DAMAGE, CARRIER ARM Y-DIRECTION	188
FIGURE 9-43 CASE-2, FSA, PLANET GEAR-1 DAMAGE, CARRIER ARM TORSIONAL.....	188
FIGURE 9-44 CASE-2, FSA, PLANET GEAR-1 DAMAGE, PLANET GEAR-1 X-DIRECTION	189
FIGURE 9-45 CASE-2, FSA, PLANET GEAR-1 DAMAGE, PLANET GEAR-1 Y-DIRECTION	189
FIGURE 9-46 CASE-2, FSA, PLANET GEAR-1 DAMAGE, PLANET GEAR-1 TORSIONAL	189
FIGURE 9-47 CASE-2, CWTA, PLANET GEAR-1 CRACK, AVERAGED CARRIER ARM TORSIONAL VIBRATION	191
FIGURE 9-48 CASE-2, CWTA, PLANET GEAR-1 CRACK, AVERAGED SUN GEAR TORSIONAL VIBRATION	192
FIGURE 9-49 A DESCRIPTION OF TOOTH SPALLING	193
FIGURE 9-50 SIMULATION OUTPUTS AFTER SIGNAL AVERAGING WITH A SINGLE W20E-5 SPALL ON THE SUN GEAR AT THE 19 TH TOOTH	194
FIGURE 9-51 COMPARISON OF RESULTS, 5E-5 SPALL, 10E-5 SPALL AND W20E-5 SPALL ON THE SUN GEAR 19 TH TOOTH.....	197
FIGURE 9-52 CASE-4, FSA, SUN GEAR DAMAGE, SUN GEAR X-DIRECTION	198
FIGURE 9-53 CASE-4, FSA, SUN GEAR DAMAGE, SUN GEAR Y-DIRECTION	198
FIGURE 9-54 CASE-4, FSA, SUN GEAR DAMAGE, SUN GEAR TORSIONAL	199
FIGURE 9-55 CASE-4, FSA, SUN GEAR DAMAGE, RING GEAR X-DIRECTION	199
FIGURE 9-56 CASE-4, FSA, SUN GEAR DAMAGE, RING GEAR Y-DIRECTION	199
FIGURE 9-57 CASE-4, FSA, SUN GEAR DAMAGE, RING GEAR TORSIONAL	199
FIGURE 9-58 CASE-4, FSA, SUN GEAR DAMAGE, CARRIER ARM X-DIRECTION	200
FIGURE 9-59 CASE-4, FSA, SUN GEAR DAMAGE, CARRIER ARM Y-DIRECTION.....	200
FIGURE 9-60 CASE-4, FSA, SUN GEAR DAMAGE, CARRIER ARM TORSIONAL	200
FIGURE 9-61 CASE-4, FSA, SUN GEAR DAMAGE, PLANET GEAR-1 X-DIRECTION	200
FIGURE 9-62 CASE-4, FSA, SUN GEAR DAMAGE, PLANET GEAR-1 Y-DIRECTION.....	201
FIGURE 9-63 CASE-4, FSA, SUN GEAR DAMAGE, PLANET GEAR-1 TORSIONAL	201
FIGURE 9-64 CASE-2, CWTA, SUN GEAR SPALL, AVERAGED CARRIER ARM TORSIONAL VIBRATION	202
FIGURE 9-65 CASE-2, CWTA, SUN GEAR SPALL, AVERAGED SUN GEAR TORSIONAL VIBRATION	204
FIGURE 9-66 SIMULATION OUTPUTS AFTER SIGNAL AVERAGING WITH A SINGLE W20E-5 SPALL ON THE RING GEAR AT THE 83 RD TOOTH	205
FIGURE 9-67 COMPARISON OF RESULTS, 5E-5 SPALL, 10E-5 SPALL AND W20E-5 SPALL ON THE RING GEAR AT THE 83 RD TOOTH.....	208
FIGURE 9-68 CASE-4, FSA, RING GEAR DAMAGE, SUN GEAR X-DIRECTION	209
FIGURE 9-69 CASE-4, FSA, RING GEAR DAMAGE, SUN GEAR Y-DIRECTION	209
FIGURE 9-70 CASE-4, FSA, RING GEAR DAMAGE, SUN GEAR TORSIONAL	209
FIGURE 9-71 CASE-4, FSA, RING GEAR DAMAGE, RING GEAR X-DIRECTION	210
FIGURE 9-72 CASE-4, FSA, RING GEAR DAMAGE, RING GEAR Y-DIRECTION.....	210
FIGURE 9-73 CASE-4, FSA, RING GEAR DAMAGE, RING GEAR TORSIONAL	210
FIGURE 9-74 CASE-4, FSA, RING GEAR DAMAGE, CARRIER ARM X-DIRECTION	210
FIGURE 9-75 CASE-4, FSA, RING GEAR DAMAGE, CARRIER ARM Y-DIRECTION.....	211
FIGURE 9-76 CASE-4, FSA, RING GEAR DAMAGE, CARRIER ARM TORSIONAL	211
FIGURE 9-77 CASE-4, FSA, RING GEAR DAMAGE, PLANET GEAR-1 X-DIRECTION	211
FIGURE 9-78 CASE-4, FSA, RING GEAR DAMAGE, PLANET GEAR-1 Y-DIRECTION.....	211
FIGURE 9-79 CASE-4, FSA, RING GEAR DAMAGE, PLANET GEAR-1 TORSIONAL	212
FIGURE 9-80 CASE-2, CWTA, RING GEAR SPALL, AVERAGED CARRIER ARM TORSIONAL VIBRATION	213
FIGURE 9-81 SIMULATION OUTPUTS AFTER SIGNAL AVERAGING WITH A SINGLE W20E-5 SPALL ON THE PLANET GEAR-1 AT THE 32 ND TOOTH	215
FIGURE 9-82 COMPARISON OF RESULTS, 5E-5 SPALL, 10E-5 SPALL AND W20E-5 SPALL ON THE PLANET GEAR-1 AT THE 32 ND TOOTH.....	217
FIGURE 9-83 CASE-4, FSA, PLANET GEAR-1 DAMAGE, SUN GEAR X-DIRECTION	218
FIGURE 9-84 CASE-4, FSA, PLANET GEAR-1 DAMAGE, SUN GEAR Y-DIRECTION.....	218
FIGURE 9-85 CASE-4, FSA, PLANET GEAR-1 DAMAGE, SUN GEAR TORSIONAL	219
FIGURE 9-86 CASE-4, FSA, PLANET GEAR-1 DAMAGE, RING GEAR X-DIRECTION	219
FIGURE 9-87 CASE-4, FSA, PLANET GEAR-1 DAMAGE, RING GEAR Y-DIRECTION.....	219
FIGURE 9-88 CASE-4, FSA, PLANET GEAR-1 DAMAGE, RING GEAR TORSIONAL	219
FIGURE 9-89 CASE-4, FSA, PLANET GEAR-1 DAMAGE, CARRIER ARM X-DIRECTION	220
FIGURE 9-90 CASE-4, FSA, PLANET GEAR-1 DAMAGE, CARRIER ARM Y-DIRECTION.....	220
FIGURE 9-91 CASE-4, FSA, PLANET GEAR-1 DAMAGE, CARRIER ARM TORSIONAL.....	220

FIGURE 9-92 CASE-4, FSA, PLANET GEAR-1 DAMAGE, PLANET GEAR-1 X-DIRECTION 220
FIGURE 9-93 CASE-4, FSA, PLANET GEAR-1 DAMAGE, PLANET GEAR-1 Y-DIRECTION..... 221
FIGURE 9-94 CASE-4, FSA, S PLANET GEAR-1 DAMAGE, PLANET GEAR-1 TORSIONAL..... 221
FIGURE 9-95 CASE-2, CWTA, PLANET GEAR-1 SPALL, AVERAGED CARRIER ARM TORSIONAL
VIBRATION..... 222

1. Introduction

1.1. THE RESEARCH TITLE

Dynamic Modelling of Planetary Gear Systems for Gear Tooth Fault Detection is the title of this research.

1.2. THE RESEARCH OVERVIEW

This research project aims to develop a general torsional-transverse coupled dynamic model of planetary spur gear system vibration using the lumped mass approach to improve the understanding of the dynamic behavior with and without tooth faults under extreme conditions such as very low speed and high torque. The model includes effects such as variable tooth mesh stiffness, dynamic transmission error effects and tooth stiffness, pitch and profile excitation and gear tooth faults (cracking and spalling) for gear fault detection purposes. The model is also developed to be general enough to contain components external to the planetary gear stage such as a motor, a reduction gearbox, a coupling and load along with extra details. To do so, matrix techniques are used. In order to conduct the simulation and calculation automatically, the MATLAB simulation program with symbolic math was employed.

The dynamic vibration results of all degrees of freedom were analyzed using signal averaging, frequency spectrum analysis (FSA) and continuous wavelet analysis (CWTA). The effects of different sizes of tooth cracks and spalls on the system dynamic behavior were compared and examined. Discussion and conclusion are included based on the overall results and analysis and future works are proposed.

1.3. THE RESEARCH OBJECTIVE

The purpose of this research is to develop a vibration model that simulates dynamic behavior of large spur planetary gear systems such as used in bucket wheel

reclaimers, with and without gear element faults. A $9+3n$ (n representing the number of planetary gears) degree of freedom 2-dimensional dynamic model is built for comparison of fault-free and simulated tooth fault cases.

The difference and comparison between the vibration signals with undamaged teeth, cracked teeth, and teeth with spalling is discussed by investigating some of the common diagnostic functions and changes to the frequency spectra results.

Based on the understanding and outcomes of the vibration simulation, improved fault detection, diagnosis and prognostic techniques will be discussed as well as further investigation with more detailed models and growth of faults. Dynamic modelling developed in this research can assist in understanding of the consequence of large transient events, including the fluctuations in tooth loads which can reduce gear fatigue life and lead to further tooth damage. Early detection of faults on gear teeth can be used to initiate maintenance actions in order to reduce repair work and avoid catastrophic breakdown.

1.4. SIGNIFICANCE

This study has the potential to benefit industry by providing an understanding of dynamic behavior of planetary gear sets and vibration fault detection methods applied to tooth faults as well as diagnosis and prognostic techniques, such as for the large gearbox systems as found in the mining industry. The early detection of incipient gear failure can be used to initiate maintenance actions and changes in operational loading before catastrophic breakdown occurs. In instances where the early stages of gear failure remains undetected, extensive repairs with considerable downtime and loss of production can result.

Although comprehensive analysis has been conducted on the fault detection and dynamic analysis of spur/helical gear systems, early fault detection and analysis of planetary drive systems are still in their infancy, especially for large low speed systems. This study can improve the understanding of these areas and develop viable methods for low speed applications.

1.5. THE RESEARCH METHOD

Lumped mass techniques (Newton's 2nd Law) are employed in order to efficiently develop the model differential equations. The model includes the following components;

- (i) Bucket wheel mass, inertia and assumed torque loading (provides large transient torque)
- (ii) Carrier arm mass, inertia and torsional stiffness
- (iii) Shaft torsional, lateral stiffness
- (iv) Bearing stiffness (associated with (iii) is considered as supporting stiffness for gear-shaft elements)
- (v) Gear teeth numbers and gear ratios
- (vi) Gear geometric characteristics
- (vii) Time variable gear tooth-tooth stiffness (as part of the mesh stiffness)
- (viii) Combined mesh stiffness
- (ix) Sun gear shaft input characteristics
- (x) Gear casing and support resonance (considered as supporting stiffness on assumed fixed elements).

The assumptions in developing the dynamic model normally include simplifications that are made to reduce the model to a solvable form within a limited time frame. The following items are normally considered to have negligible effect in the early stages of gear dynamic modelling;

- (i) Tooth static transmission error
- (ii) Tooth mesh friction

Industry standard methods will be used for solving the simultaneous differential equations using MATLAB and/or SIMULINK tools.

In this research, step-by-step detailed planetary gear set models were developed.

Initially, the planetary gear set was modeled without consideration of shafts and bearings. The simplest first stage model can even neglect gear mesh stiffness, ignore shaft effects and include a rigid ring gear. More detailed models with gear mesh stiffness, time varying mesh stiffness, shaft torsional/lateral stiffness, bearing stiffness; non-rigid ring gear, large inertia and large transient torque introduced by the bucket wheel, and different tooth faults were developed and analyzed step by step.

1.6. SPECIAL FEATURES

- (i) Fluid coupling was modeled by using an extra degree of freedom (torsional damping was taken into account) to simulate start up.
- (ii) MATLAB m-files were formed using symbolic math in order to create the differential equations, adjustable for different amounts of inputs automatically.
- (iii) Models with different numbers of planet gears with and without torsional/transverse responses can be easily simulated due to the advantage of (ii).

1.7. OVERVIEW OF CHAPTERS

In Chapter 2, the research background is introduced and background literature is reviewed.

In Chapter 3, a generalized lumped mass dynamic model of a single stage planetary gear set is developed with an overall equation obtained using matrix techniques. Detailed development of equations are shown and the advantages of matrix formulation is discussed.

In Chapter 4, pitch and profile excitations of single spur gear pair with one tooth in mesh and multiple teeth in mesh are developed. Tooth mesh variation is analyzed in terms of time variation of number of teeth in mesh. Pitch and profile excitations of the multiple gear pairs in the planetary gear set are examined. The simulation of random excitation is also included.

In Chapter 5, a common formulation of combined torsional mesh stiffness is developed which can simulate high contact ratio gear mesh stiffness. The formulation is capable of introducing damaged teeth with both cracking and spalling with simulation results shown. The advantages and limitations of the method are also discussed.

In Chapter 6, the major modelling parameters of a typical bucket wheel reclaimer are introduced, including detailed arrangement, detailed parameters and relative calculations which are needed for this research.

In Chapter 7, the flow chart of the overall software model is illustrated and the overall inputs are listed. MATLAB m-files used for each chapter (Chapter 3 to Chapter 9) are introduced with corresponding flow charts where applicable.

In Chapter 8, 32 assumptions are listed and explained, and the corresponding purposes are indicated. The overall dynamic model is applied to an undamaged planetary gear set. The results of all degree of freedom are then analyzed using signal averaging and frequency analysis method. Comparison of simulations for different cases is also demonstrated.

In Chapter 9, signal averaging, FSA and CWTA are applied to the resulting signals of overall dynamic models with different sizes of tooth cracks and spalls. The detectabilities of all three methods are determined, compared and discussed.

In Chapter 10 and Chapter 11, discussion and conclusion are made and future works are proposed.

In the appendix, all MATLAB mfiles are listed with detailed codes along with results from signal averaging, FSA and CWTA except those already presented in the text.

2. LITERATURE REVIEW

2.1. OVERVIEW

Over the last half century, there has been a significant amount of literature on dynamic modelling of gear systems for multiple purposes including the estimation of dynamic load sharing, further understanding of vibration generation and propagation, noise control and recently for condition monitoring, diagnostic and prognostic behavior of gears and other element faults.

A numbers of researchers have classified gear/gearbox dynamic modelling models/projects with respect to different points of view such as Ozguven and Houser¹, Zakrajsek², and Shu Du³. In this research, a classification based on that found by Shu Du is presented in Figure 2-1.

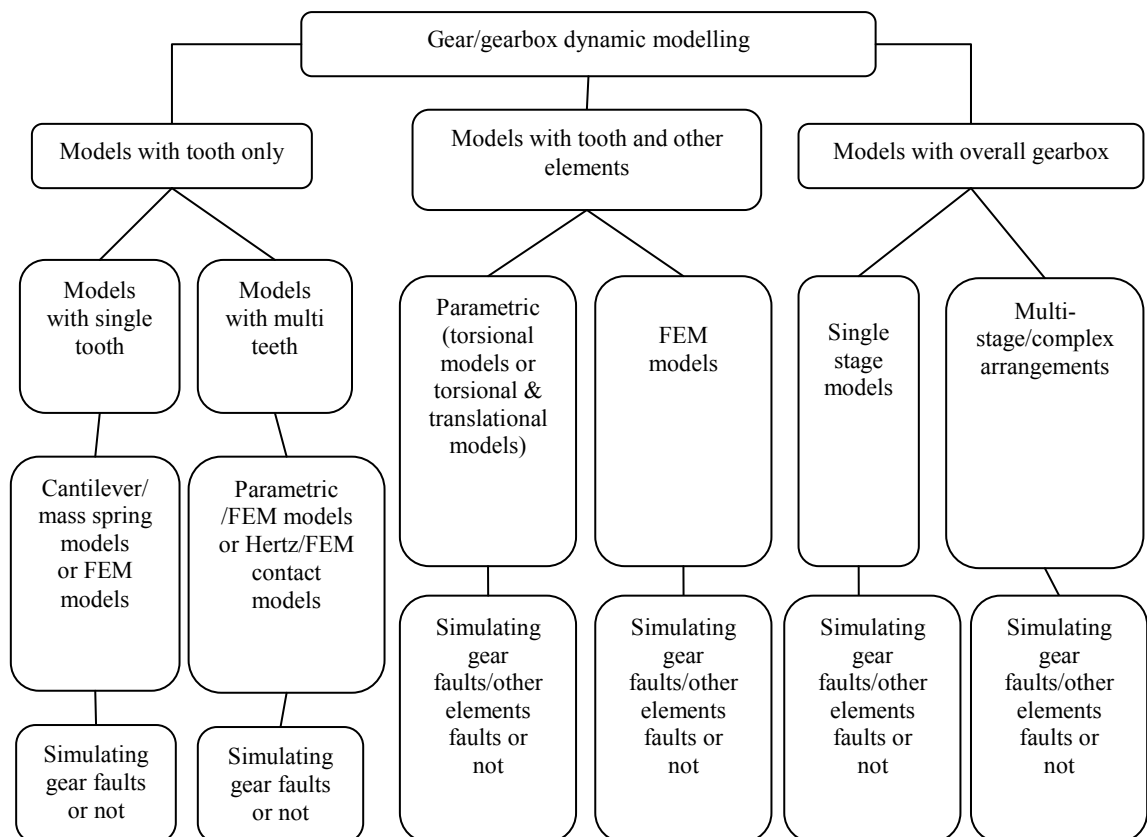


Figure 2-1 Classification of gear/gearbox dynamic modelling³

In the next sections, each group of the classification will be reviewed and major

publications will be highlighted.

2.2. DYNAMIC MODELLING OF GEARS IN MESH WITH SINGLE TOOTH ONLY

When only the compliance or stiffness of one meshing gear tooth is considered and all other elements are assumed to be perfectly rigid, the dynamic models can be called single tooth models. These models are mainly based on the cantilever beam theory. In 1973, Wallace and Seireg⁴ analyzed the stress, deformation and fracture patterns in a single tooth model when subjected to dynamic loading using the FEA method. In the late 1980s, Ramamurti and Rao⁵ developed a more advanced FEM approach (model with asymmetry of the load on the teeth and with a cyclic system of gear teeth allowing the stress distribution in the adjacent teeth to be calculated by analyzing one tooth only) to analysis the stress of spur gear teeth.

Single tooth models give the important initial understanding of gear dynamics. However, by the limitation of understanding and interests, faulted tooth features were not introduced into single tooth models as a major concern.

To consider the meshing and contact forces between meshing teeth, models with more than one tooth are needed. In 1958, Harris's work⁶ pointed out the importance of transmission error and parametric excitation of the gear mesh and introduced three vibration sources (manufacture errors, tooth stiffness vibration and loss of contact) into the dynamic model. In 1988, Vijayakar, Busby and Houser⁷ used a simplex type algorithm to impose frictional contact conditions on finite element models. In the same year, Ozguven and Houser⁸ developed a non-linear model with a single degree of freedom to calculate dynamic mesh and tooth forces using two methods. One was using dynamic factors based on stresses. Another used dynamic transmission error or loaded static transmission errors. In 1989, Kahraman and Singh⁹ focused on the backlash non-linearity as excited primarily by the transmission error between the spur gear pair both external and internal. In 1990, Sundarajan and Young¹⁰, as well as with Amin¹¹ had an important development using the three dimensional finite element substructure method associated with pre-processing software to gain high

accuracy and efficiency of computation. In 1993, Vijayakar and Houser¹² used a combined finite element (refined elements near contact zone and normalized elements out of contact zone) and surface integral method for contact analysis of meshing gears.

Recently, tooth faults have been introduced into gear dynamic models. For instance, Choy, et al., analyzed the effects of surface pitting and wear on the vibration of gear transmission systems¹³. Yesilyurt, Gu and Andrew¹⁴ studied the influence of gear wear faults by measurement of gear tooth stiffness reduction in their model analysis. Chaari, Bassar and Haddar analysed¹⁵ the effect of spalling and tooth breakage on gear mesh stiffness. Chaari, Fakhfakh and Haddar¹⁶ developed an analytical model with a spur gear tooth crack to study the influence on gear mesh stiffness.

2.3. DYNAMIC MODELLING OF GEARS IN MESH WITH TOOTH AND OTHER ELEMENTS

A model with other elements (shafts, bearing and host flexibility) other than with a single tooth only is considered necessary for a more general and more realistic model with fewer assumptions.

The models with torsional stiffness of gear-carrying shafts and/or supporting bearings, with both torsional and transverse stiffness of gear-carrying shafts and/or supporting bearings and the models using FEM which includes gear-carrying shafts and/or supporting bearings are classified in this group.

In the early 1960s, Johnson¹⁷ introduced a receptance coupling technique to calculate the natural frequencies from the receptance equation obtained by first separately finding the receptances at the meshing point of each of a pair of geared shafts. In 1969, Seager¹⁸ included flexible bearings in a three-degree-of-freedom model. In 1972, Wang and Morse¹⁹ developed a torsional model with shaft and constant mesh stiffness. In 1975, Rettig²⁰ modeled a single gear stage with four lateral and two torsional degrees. In 1980, Iida, et al., constructed a model with coupled torsional-flexural vibration of two shafts in a spur gear system, one output shaft assumed

flexible in bending and one input shaft rigid in bending²¹. In the later work, Iida and Tamura²² introduced a third shaft into the model. In 1984, Kucukay²³ developed an eight-degree-of-freedom model to include the rocking and axial motions of the rigid shafts. In 1985, Neriya, et al., also investigated the coupled torsional-flexural vibration of a geared system, but using FEM to solve the model²⁴. In 1987, Lin, et al., included motor and load inertias in a three-degree-of-freedom torsional model²⁵. In 1992, a finite element model of a geared rotor system on flexible bearings was constructed by Kahraman, et al.²⁶. By the same researcher, a linear dynamic model with helical gears was investigated in 1993.

In 2000, Bartelmus²⁷ constructed a torsional gear mesh model for gear fault diagnosis with a broken tooth simulated. High consistency was shown between the simulation and experimental work. In 2001, Lin and Kuang²⁸ investigated the effect of tooth wear on the vibration spectrum for condition monitoring based on their gear dynamic model.

2.4. DYNAMIC MODELLING OF OVERALL GEARBOX

Compared to the two former groups, dynamic modelling of the overall gearbox includes elements other than a gear pair or gear train and associated supporting shafts and bearings, such as a motor (input load), load (output load), casing and flexible or rigid mounts. The major advantage of this work has been the inclusion of non-rotating elements and input-output load features to accomplish more general models.

In 1991, T.C. Lim and R. Singh²⁹ developed linear time-invariant, discrete dynamic models of an overall gearbox by using lumped parameter and finite element methods and the effect of casing mass and mount stiffness has been studied. Also in 1991, Choy, et al., presented an analysis of a multi-stage gear transmission vibration focusing on the effect of casing motion and mass imbalance³⁰. In the same year, E.L. Saeidy and Fawzi³¹ constructed a vibration model for the simulation of a spur gearbox with major emphasis being the effect of tooth backlash and ball bearing dead band clearance. One year later, Choy³² continued their research with the multi-stage

gearbox coupled with gearbox casing by using the modal synthesis approach and the finite element method with a verification by experimental work in 1993³³. In 1996, Velez and Maatar³⁴ employed geometrical analysis to simulate shape deviation and mounting errors and developed a mathematical model for analysis of the relative influence. In 1997, Shu Du³⁵ developed a dynamic model of an overall gearbox including loaded static transmission error, time varying tooth mesh stiffness and effects of other connected elements and obtained good agreement with experimental results. In 2002, Lin and Parker³⁶ studied the instabilities in a two-stage gear system due to mesh stiffness variation by using assumed square wave mesh stiffness.

In 1994, Kahraman³⁷ developed a three dimensional dynamic simulation of a single-stage planetary gear train with six rigid body motions of the gears and carrier arm. Also in 1994, Kahraman³⁸ refined the previous model to include manufacturing errors, assembly errors, tooth separations and time-varying mesh stiffness.

Based on the dynamic model of Shu Du's work³⁵, in 2001, Howard, et al., developed a lumped parameter model including tooth friction and a local tooth crack to investigate the influence of the tooth crack on gearbox vibration signature³⁹. In 2004, Jia⁴⁰ developed a more detailed dynamic model to simulate gear faults such as a tooth crack and spalling. He also included geometry errors and friction forces to study the effects of these factors on the gearbox vibration signal.

In 2004, Yuksel and Kahraman⁴¹ employed a computational model of a planetary gear set to study the influence of surface wear on the dynamic behavior of a typical planetary gear set. In 2005, Vecchiato⁴² developed a planetary gear train model which is capable of self-regulation for compensation of various errors of alignment. In 2006, Jia and Howard presented a 26 degree of freedom gear dynamic model of three shafts and two pairs of spur gears in mesh for comparison of localized tooth spalling and damage⁴³.

In 2006, Abousleiman and Velez⁴⁴ developed a three-dimensional finite element model/ lumped parameter model to analyze the dynamic behavior of planetary spur and helical gears. In 2007, Ambarisha and Paker presented a work⁴⁵ examining the complex, nonlinear dynamic behavior of spur planetary gears using both analytical

and finite element models. The models included mesh stiffness variation excitation, corner contact, and gear tooth contact loss. In 2008, Inalpolat and Kahraman proposed a generalized dynamic model for multi-stage planetary gear trains⁴⁶.

This thesis presents a general torsional-transverse coupled dynamic model of planetary spur gear system vibration which is based on Kahraman's model³⁷, including more details and some major modifications such as detailed pitch and profile excitation, detailed time variable tooth mesh stiffness, capability of modelling tooth faults, inclusion of motor, reduction gearbox and flexible coupling drive.

3. DYNAMIC MODELLING OF PLANETARY GEAR SYSTEMS

A single-stage planetary gear system contains one sun gear, one ring gear, one carrier arm and a number of planet gears which can be mounted as shown in Figure 3-1. To achieve the full understanding of the reactions between each part of the gear system and generate the equations of motion easily, the overall system will be considered separately as three sub-systems, namely a sun gear - planet gear pair, a ring gear - planet gear pair and a carrier arm - planet gear pair. In this chapter, the first three sections examine each of the three pairs respectively and the equations of motion will be subsequently obtained including essential supporting shafts and bearings. Within the following section the equations of motion of the overall system will be assembled based on the equations from the first three sections. In order to form the overall equations with no difficulty and to introduce further detailed in-system and external supporting reactions into the system of equations, matrix techniques will be used.

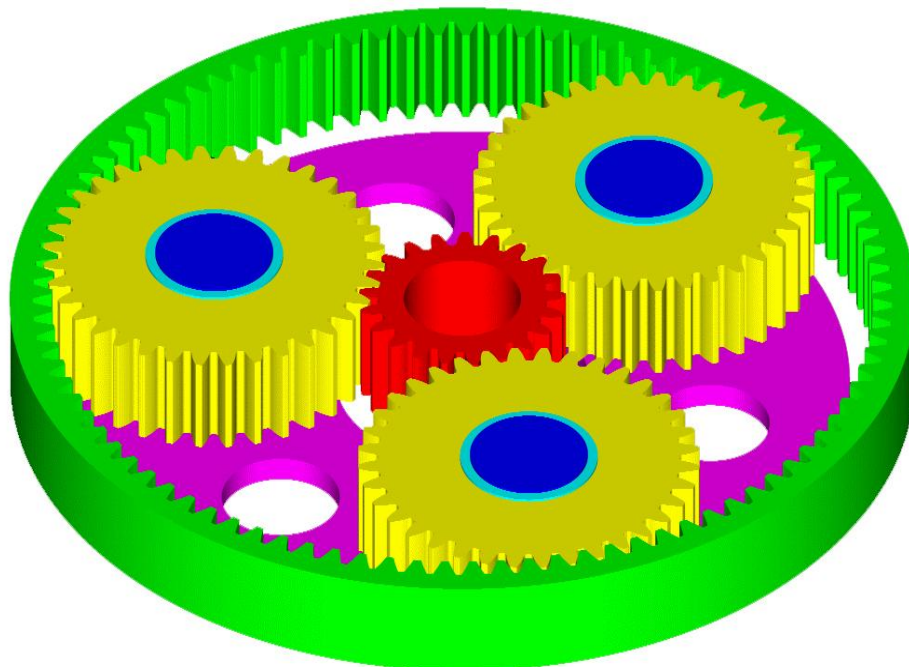


Figure 3-1 A single-stage planetary gear system with three single planet gears (yellow colored gears), one sun gear (red colored gear), one ring gear (green colored gear) and one carrier arm (purple colored part)

3.1. SUN GEAR – PLANET GEAR PAIR

A sun gear - planet gear pair is examined in this section with consideration of the interaction between sun-planet gears and sun gear shaft.

Figure 3-2 shows a sun gear and a planet gear in mesh with the i^{th} planet gear at an angle ψ_i about the sun gear using the Descartes coordinate system.

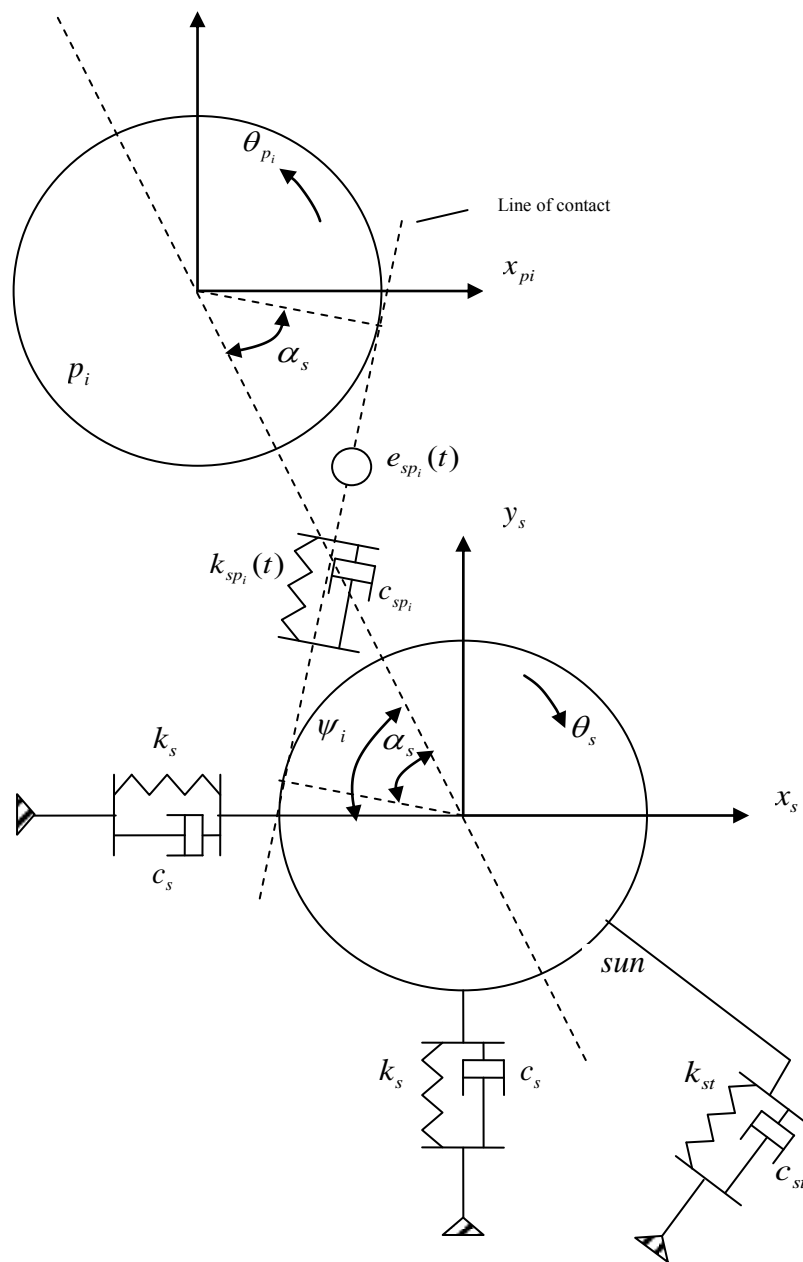


Figure 3-2 A sun-planet pair (with the contact point in II quadrant about the sun gear)

The sun gear is allowed to translate in both x and y directions, and rotate about its center of the plane of gears. The torsional angular displacement of the sun gear is shown as θ_s , and θ_{p_i} for the i^{th} planet gear respectively.

The rigid bodies of both sun gear and planet gear are connected through the gear mesh stiffness $k_{sp_i}(t)$ and gear mesh damping c_{sp_i} along the line of action, also with a combined gear error $e_{sp_i}(t)$.

The relative mesh displacement defined along the line of action is $MD_{sp_i}(t)$, so the displacement defined with respect to y_s is,

$$MD_{sp_i}(t) \cdot \cos(\psi_i - \alpha_s)$$

and the displacement with respect to x_s is,

$$MD_{sp_i}(t) \cdot \sin(\psi_i - \alpha_s)$$

where α_s is the pressure angle of the sun gear - planet gear pair. The positive sign of $MD_{sp_i}(t)$ occurs when the action line is under compression, and the different conditions when the planet gear rotates about the sun gear are shown and examined in Figure 3-3 and 3-4.

According to Figure 3-2, 3-3, and 3-4, $MD_{sp_i}(t)$ can be described as,

$$MD_{sp_i}(t) = (y_s - y_{p_i})\cos(\psi_i - \alpha_s) + (x_s - x_{p_i})\sin(\psi_i - \alpha_s) + (u_s + u_{p_i}) + e_{sp_i}(t) + E_{s_i}(t) - E_{sp_i}(t) \quad (3.1)$$

where, $u_s = r_s\theta_s$, r_s is the base circle of the sun gear, θ_s represents torsional angular displacement of the sun gear; $u_{p_i} = r_{p_i}\theta_{p_i}$, r_{p_i} is the base circle of the i^{th} planet gear, θ_{p_i} is the torsional angular displacement of the i^{th} planet gear; $e_{sp_i}(t)$ is the combined gear error; $E_{s_i}(t)$ and $E_{sp_i}(t)$ represent run out functions of the sun and planet teeth behavior respectively.

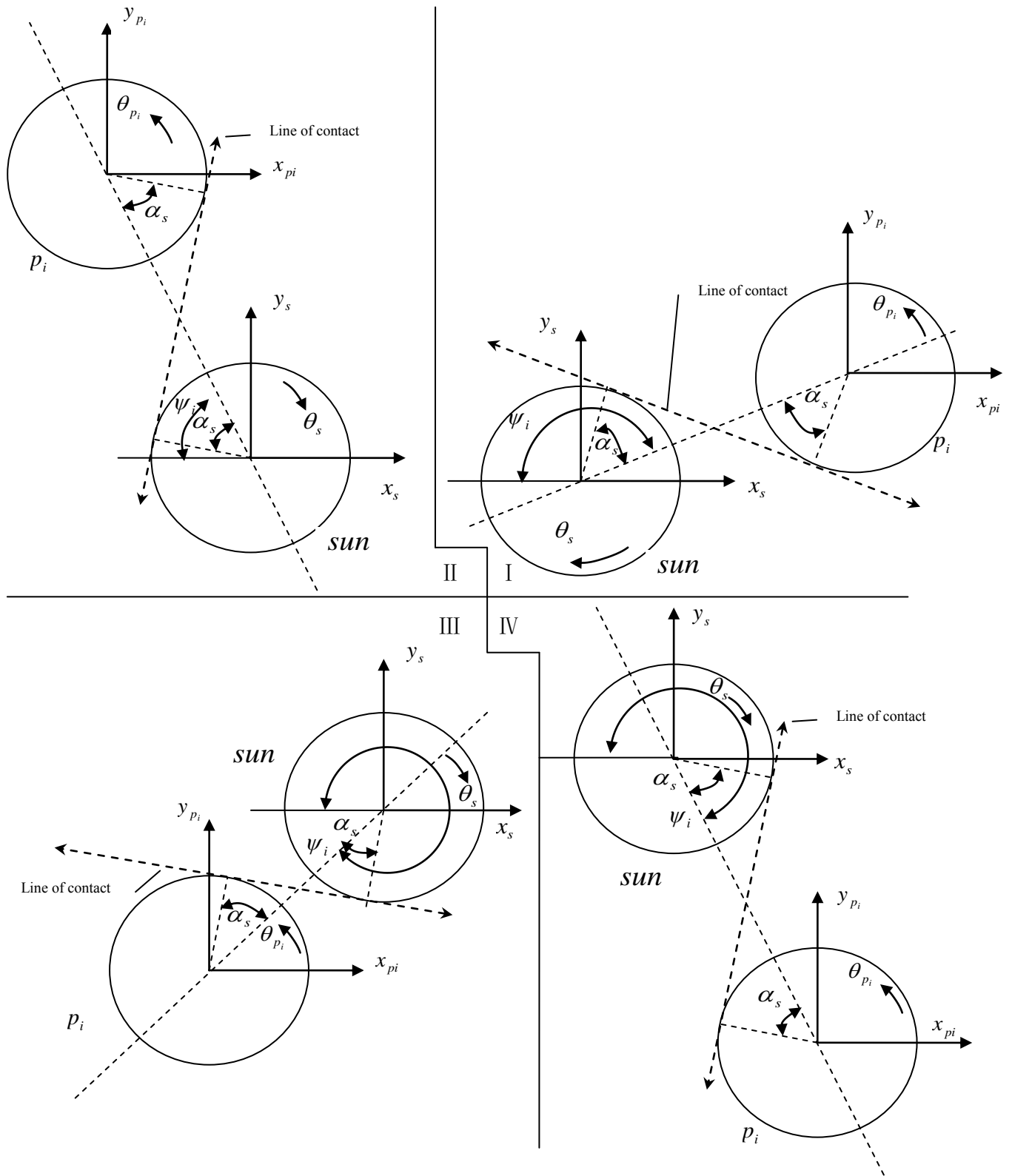


Figure 3-3 A sun-planet pair (with the contact point in four quadrants about the sun gear respectively)

II	$\cos(\psi_i - \alpha_s) \in (0 \ 1) > 0$ $\sin(\psi_i - \alpha_s) \in (0 \ 1) > 0$ $(y_s - y_{p_i}) \propto$ compression of action line $(x_s - x_{p_i}) \propto$ compression of action line $(y_s - y_{p_i})\cos(\psi_i - \alpha_s) \propto$ compression of action line $(x_s - x_{p_i})\sin(\psi_i - \alpha_s) \propto$ compression of action line	I	$\cos(\psi_i - \alpha_s) \in (-1 \ 0) < 0$ $\sin(\psi_i - \alpha_s) \in (0 \ 1) > 0$ $-(y_s - y_{p_i}) \propto$ compression of action line $(x_s - x_{p_i}) \propto$ compression of action line $(y_s - y_{p_i})\cos(\psi_i - \alpha_s) \propto$ compression of action line $(x_s - x_{p_i})\sin(\psi_i - \alpha_s) \propto$ compression of action line
III	$\cos(\psi_i - \alpha_s) \in (0 \ 1) > 0$ $\sin(\psi_i - \alpha_s) \in (-1 \ 0) < 0$ $(y_s - y_{p_i}) \propto$ compression of action line $-(x_s - x_{p_i}) \propto$ compression of action line $(y_s - y_{p_i})\cos(\psi_i - \alpha_s) \propto$ compression of action line $(x_s - x_{p_i})\sin(\psi_i - \alpha_s) \propto$ compression of action line	IV	$\cos(\psi_i - \alpha_s) \in (-1 \ 0) < 0$ $\sin(\psi_i - \alpha_s) \in (-1 \ 0) < 0$ $-(y_s - y_{p_i}) \propto$ compression of action line $-(x_s - x_{p_i}) \propto$ compression of action line $(y_s - y_{p_i})\cos(\psi_i - \alpha_s) \propto$ compression of action line $(x_s - x_{p_i})\sin(\psi_i - \alpha_s) \propto$ compression of action line

Figure 3-4 The sign-relationship between axial relative displacement and $MD_{sp_i}(t)$ with the planet gear positioned in the four quadrants about the sun gear respectively as shown in Figure 3-3

Tooth separation phenomenon is simulated by using the following unit step function,

$$SP_{sp_i} = \begin{cases} 1 & MD_{sp_i}(t) \geq 0 \\ 0 & MD_{sp_i}(t) < 0 \end{cases} \quad (3.2)$$

As the equation shows, when $MD_{sp_i}(t) < 0$, the teeth will lose contact and the resulting reaction force between the gear pair will be equal to zero.

A free body diagram of the planet gear is shown in Figure 3-5 (sun-planet pair only).

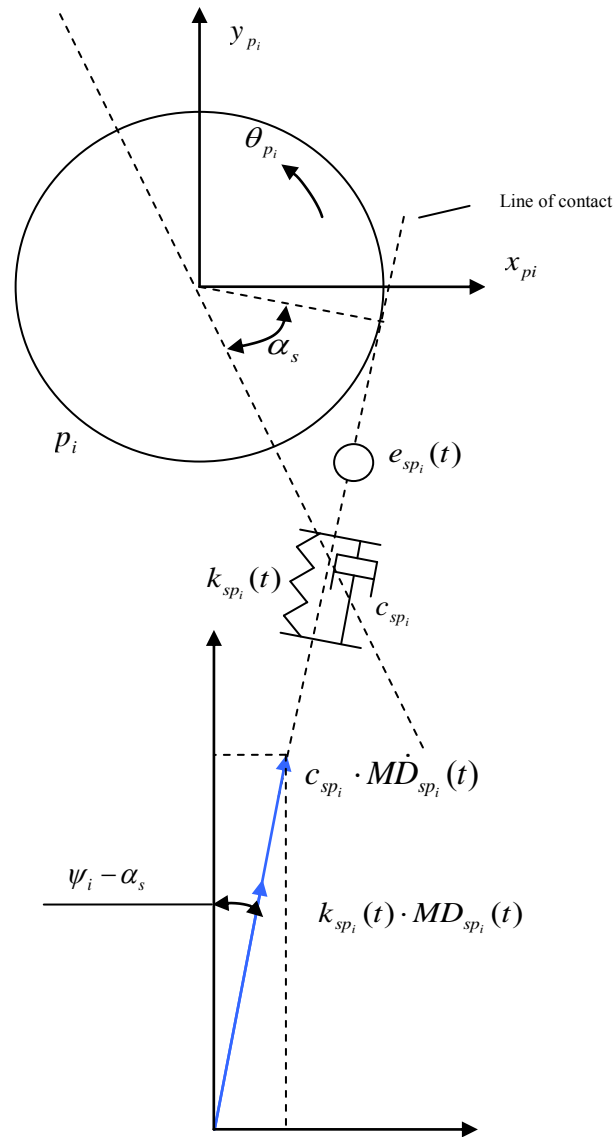


Figure 3-5 Free body diagram of planet gear (sun-planet pair only)

In the direction of x_{pi}^* , the resulting differential equation becomes,

$$m_p \cdot \ddot{x}_{pi}^* - c_{spi} \cdot \dot{MD}_{spi}(t) \cdot \sin(\psi_i - \alpha_s) - SP_{spi} \cdot k_{spi}(t) \cdot MD_{spi}(t) \cdot \sin(\psi_i - \alpha_s) = 0 \quad (3.3)$$

In the direction of y_{pi}^* , the resulting differential equation becomes,

$$m_p \cdot \ddot{y}_{pi}^* - c_{spi} \cdot \dot{MD}_{spi}(t) \cdot \cos(\psi_i - \alpha_s) - SP_{spi} \cdot k_{spi}(t) \cdot MD_{spi}(t) \cdot \cos(\psi_i - \alpha_s) = 0 \quad (3.4)$$

For the torsional degree of freedom, the resulting differential equation becomes,

$$(J_p / r_p^2) \cdot \ddot{u}_{p_i} + c_{sp_i} \cdot \dot{M}D_{sp_i}(t) + SP_{sp_i} \cdot k_{sp_i}(t) \cdot MD_{sp_i}(t) = 0 \quad (3.5)$$

$$\text{where } u_{p_i} = r_{p_i} \theta_{p_i}, \quad (3.6)$$

and where $\dot{M}D_{sp_i}(t)$ is the time differential of $MD_{sp_i}(t)$ which is expressed from Eqs 3.1, as follow,

$$\begin{aligned} \dot{M}D_{sp_i}(t) = & \cos(\psi_i - \alpha_s) \dot{y}_s - \sin(\psi_i - \alpha_s) \dot{\psi}_i y_s - \cos(\psi_i - \alpha_s) \dot{y}_{p_i} + \sin(\psi_i - \alpha_s) \dot{\psi}_i \\ & y_{p_i} + \sin(\psi_i - \alpha_s) \dot{x}_s + \cos(\psi_i - \alpha_s) \dot{\psi}_i x_s - \sin(\psi_i - \alpha_s) \dot{x}_{p_i} - \cos(\psi_i - \alpha_s) \\ & \dot{\psi}_i x_{p_i} + \dot{u}_s + \dot{u}_{p_i} + \dot{e}_{sp_i}(t) + \dot{E}_{s_i}(t) - \dot{E}_{sp_i}(t) \end{aligned} \quad (3.7)$$

Substituting Eqs 3.7 into Eqs 3.3, Eqs 3.4 and Eqs 3.5 gives,

In the direction of x_{p_i} , the resulting differential equation becomes,

$$\begin{aligned} m_p \cdot \ddot{x}_{p_i}^* - c_{sp_i} \sin(\psi_i - \alpha_s) \cos(\psi_i - \alpha_s) \dot{y}_s + c_{sp_i} \sin(\psi_i - \alpha_s) \sin(\psi_i - \alpha_s) \dot{\psi}_i y_s \\ + c_{sp_i} \sin(\psi_i - \alpha_s) \cos(\psi_i - \alpha_s) \dot{y}_{p_i} - c_{sp_i} \sin(\psi_i - \alpha_s) \sin(\psi_i - \alpha_s) \dot{\psi}_i y_{p_i} \\ - c_{sp_i} \sin(\psi_i - \alpha_s) \sin(\psi_i - \alpha_s) \dot{x}_s - c_{sp_i} \sin(\psi_i - \alpha_s) \cos(\psi_i - \alpha_s) \dot{\psi}_i x_s \\ + c_{sp_i} \sin(\psi_i - \alpha_s) \sin(\psi_i - \alpha_s) \dot{x}_{p_i} + c_{sp_i} \sin(\psi_i - \alpha_s) \cos(\psi_i - \alpha_s) \dot{\psi}_i x_{p_i} \\ - c_{sp_i} \sin(\psi_i - \alpha_s) \dot{u}_s - c_{sp_i} \sin(\psi_i - \alpha_s) \dot{u}_{p_i} - c_{sp_i} \sin(\psi_i - \alpha_s) \dot{e}_{sp_i}(t) \\ - c_{sp_i} \sin(\psi_i - \alpha_s) \dot{E}_{s_i}(t) + c_{sp_i} \sin(\psi_i - \alpha_s) \dot{E}_{sp_i}(t) \\ - SP_{sp_i} k_{sp_i}(t) \sin(\psi_i - \alpha_s) \cos(\psi_i - \alpha_s) y_s \\ + SP_{sp_i} k_{sp_i}(t) \sin(\psi_i - \alpha_s) \cos(\psi_i - \alpha_s) y_{p_i} \\ - SP_{sp_i} k_{sp_i}(t) \sin(\psi_i - \alpha_s) \sin(\psi_i - \alpha_s) x_s \\ + SP_{sp_i} k_{sp_i}(t) \sin(\psi_i - \alpha_s) \sin(\psi_i - \alpha_s) x_{p_i} \\ - SP_{sp_i} k_{sp_i}(t) \sin(\psi_i - \alpha_s) u_s - SP_{sp_i} k_{sp_i}(t) \sin(\psi_i - \alpha_s) u_{p_i} \\ - SP_{sp_i} k_{sp_i}(t) \sin(\psi_i - \alpha_s) e_{sp_i}(t) - SP_{sp_i} k_{sp_i}(t) \sin(\psi_i - \alpha_s) E_{s_i}(t) \\ + SP_{sp_i} k_{sp_i}(t) \sin(\psi_i - \alpha_s) E_{sp_i}(t) = 0 \end{aligned} \quad (3.8)$$

In the direction of y_{p_i} , the resulting differential equation becomes,

$$\begin{aligned} m_p \cdot \ddot{y}_{p_i}^* - c_{sp_i} \cos(\psi_i - \alpha_s) \cos(\psi_i - \alpha_s) \dot{y}_s + c_{sp_i} \cos(\psi_i - \alpha_s) \sin(\psi_i - \alpha_s) \dot{\psi}_i y_s \\ + c_{sp_i} \cos(\psi_i - \alpha_s) \cos(\psi_i - \alpha_s) \dot{y}_{p_i} - c_{sp_i} \cos(\psi_i - \alpha_s) \sin(\psi_i - \alpha_s) \dot{\psi}_i y_{p_i} \\ - c_{sp_i} \cos(\psi_i - \alpha_s) \sin(\psi_i - \alpha_s) \dot{x}_s - c_{sp_i} \cos(\psi_i - \alpha_s) \cos(\psi_i - \alpha_s) \dot{\psi}_i x_s \end{aligned}$$

$$\begin{aligned}
& + c_{sp_i} \cos(\psi_i - \alpha_s) \sin(\psi_i - \alpha_s) \dot{x}_{p_i} + c_{sp_i} \cos(\psi_i - \alpha_s) \cos(\psi_i - \alpha_s) \dot{\psi}_i x_{p_i} \\
& - c_{sp_i} \cos(\psi_i - \alpha_s) \dot{u}_s - c_{sp_i} \cos(\psi_i - \alpha_s) \dot{u}_{p_i} - c_{sp_i} \cos(\psi_i - \alpha_s) \dot{e}_{sp_i}(t) \\
& - c_{sp_i} \cos(\psi_i - \alpha_s) \dot{E}_{s_i}(t) + c_{sp_i} \cos(\psi_i - \alpha_s) \dot{E}_{sp_i}(t) \\
& - SP_{sp_i} k_{sp_i}(t) \cos(\psi_i - \alpha_s) \cos(\psi_i - \alpha_s) y_s \\
& + SP_{sp_i} k_{sp_i}(t) \cos(\psi_i - \alpha_s) \cos(\psi_i - \alpha_s) y_{p_i} \\
& - SP_{sp_i} k_{sp_i}(t) \cos(\psi_i - \alpha_s) \sin(\psi_i - \alpha_s) x_s \\
& + SP_{sp_i} k_{sp_i}(t) \cos(\psi_i - \alpha_s) \sin(\psi_i - \alpha_s) x_{p_i} \\
& - SP_{sp_i} k_{sp_i}(t) \cos(\psi_i - \alpha_s) u_s - SP_{sp_i} k_{sp_i}(t) \cos(\psi_i - \alpha_s) u_{p_i} \\
& - SP_{sp_i} k_{sp_i}(t) \cos(\psi_i - \alpha_s) e_{sp_i}(t) - SP_{sp_i} k_{sp_i}(t) \cos(\psi_i - \alpha_s) E_{s_i}(t) \\
& + SP_{sp_i} k_{sp_i}(t) \cos(\psi_i - \alpha_s) E_{sp_i}(t) = 0
\end{aligned} \tag{3.9}$$

For the torsional degree of freedom, the resulting differential equation becomes,

$$\begin{aligned}
(J_p / r_p^2) \cdot \ddot{u}_{p_i} + c_{sp_i} \cos(\psi_i - \alpha_s) \dot{y}_s - c_{sp_i} \sin(\psi_i - \alpha_s) \dot{\psi}_i y_s - c_{sp_i} \cos(\psi_i - \alpha_s) \dot{y}_{p_i} \\
+ c_{sp_i} \sin(\psi_i - \alpha_s) \dot{\psi}_i y_{p_i} + c_{sp_i} \sin(\psi_i - \alpha_s) \dot{x}_s + c_{sp_i} \cos(\psi_i - \alpha_s) \dot{\psi}_i x_s \\
- c_{sp_i} \sin(\psi_i - \alpha_s) \dot{x}_{p_i} - c_{sp_i} \cos(\psi_i - \alpha_s) \dot{\psi}_i x_{p_i} + c_{sp_i} \dot{u}_s + c_{sp_i} \dot{u}_{p_i} \\
+ c_{sp_i} \dot{e}_{sp_i}(t) + c_{sp_i} \dot{E}_{s_i}(t) + c_{sp_i} \dot{E}_{sp_i}(t) + SP_{sp_i} k_{sp_i}(t) \cos(\psi_i - \alpha_s) y_s \\
- SP_{sp_i} k_{sp_i}(t) \cos(\psi_i - \alpha_s) y_{p_i} + SP_{sp_i} k_{sp_i}(t) \sin(\psi_i - \alpha_s) x_s \\
- SP_{sp_i} k_{sp_i}(t) \sin(\psi_i - \alpha_s) x_{p_i} + SP_{sp_i} k_{sp_i}(t) u_s + SP_{sp_i} k_{sp_i}(t) u_{p_i} \\
+ SP_{sp_i} k_{sp_i}(t) e_{sp_i}(t) + SP_{sp_i} k_{sp_i}(t) E_{s_i}(t) - SP_{sp_i} k_{sp_i}(t) E_{sp_i}(t) = 0
\end{aligned} \tag{3.10}$$

A free body diagram of the sun gear is shown in Figure 3-6 (sun-planet pair only).

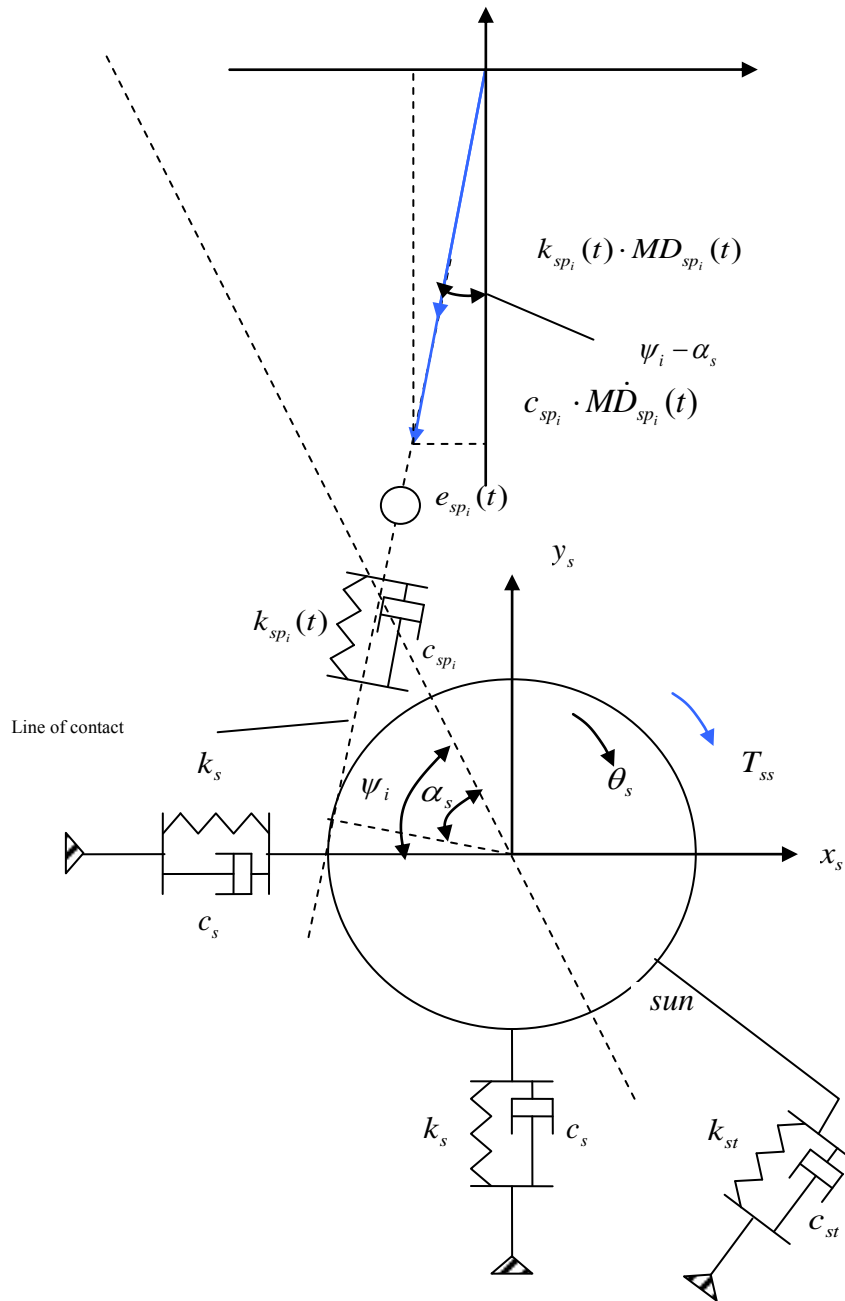


Figure 3-6 Free body diagram of sun gear

In the direction of x_s , the resulting differential equation becomes,

$$\begin{aligned}
 & m_s \cdot \ddot{x}_s + c_{sp_i} \cdot \dot{M}D_{sp_i}(t) \cdot \sin(\psi_i - \alpha_s) + SP_{sp_i} \cdot k_{sp_i}(t) \cdot MD_{sp_i}(t) \cdot \sin(\psi_i - \alpha_s) \\
 & + c_s \cdot \dot{x}_s + k_s \cdot x_s = 0
 \end{aligned} \tag{3.11}$$

In the direction of y_s , the resulting differential equation becomes,

$$\begin{aligned}
 & m_s \cdot \ddot{y}_s + c_{sp_i} \cdot \dot{M}D_{sp_i}(t) \cdot \cos(\psi_i - \alpha_s) + SP_{sp_i} \cdot k_{sp_i}(t) \cdot MD_{sp_i}(t) \cdot \cos(\psi_i - \alpha_s) \\
 & + c_s \cdot \dot{y}_s + k_s \cdot y_s = 0
 \end{aligned} \tag{3.12}$$

For the torsional degree of freedom, the resulting differential equation becomes,

$$(J_s / r_s^2) \cdot \ddot{u}_s^* + c_{sp_i} \cdot \dot{MD}_{sp_i}(t) + SP_{sp_i} \cdot k_{sp_i}(t) \cdot MD_{sp_i}(t) + c_{st} \cdot \dot{D}_{ss} \cdot r_{ss} / r_s + k_{st} \cdot D_{ss} \cdot r_{ss} / r_s - T_{ss} / r_s = 0 \quad (3.13)$$

$$\text{where } u_s^* = r_s \cdot \theta_s^*, \quad (3.14)$$

and where T_{ss} is the input torque applied to sun gear.

Substituting Eqs 3.7 into Eqs 3.11, Eqs 3.12 and Eqs 3.13 gives (excluding supporting damping and stiffness),

In the direction of x_s , the resulting differential equation becomes,

$$\begin{aligned} m_s \cdot \ddot{x}_s + c_{sp_i} \sin(\psi_i - \alpha_s) \cos(\psi_i - \alpha_s) \dot{y}_s - c_{sp_i} \sin(\psi_i - \alpha_s) \sin(\psi_i - \alpha_s) \dot{\psi}_i y_s \\ - c_{sp_i} \sin(\psi_i - \alpha_s) \cos(\psi_i - \alpha_s) \dot{y}_{p_i} + c_{sp_i} \sin(\psi_i - \alpha_s) \sin(\psi_i - \alpha_s) \dot{\psi}_i y_{p_i} \\ + c_{sp_i} \sin(\psi_i - \alpha_s) \sin(\psi_i - \alpha_s) \dot{x}_s + c_{sp_i} \sin(\psi_i - \alpha_s) \cos(\psi_i - \alpha_s) \dot{\psi}_i x_s \\ - c_{sp_i} \sin(\psi_i - \alpha_s) \sin(\psi_i - \alpha_s) \dot{x}_{p_i} - c_{sp_i} \sin(\psi_i - \alpha_s) \cos(\psi_i - \alpha_s) \dot{\psi}_i x_{p_i} \\ + c_{sp_i} \sin(\psi_i - \alpha_s) \dot{u}_s + c_{sp_i} \sin(\psi_i - \alpha_s) \dot{u}_{p_i} + c_{sp_i} \sin(\psi_i - \alpha_s) \dot{e}_{sp_i}(t) \\ + c_{sp_i} \sin(\psi_i - \alpha_s) \dot{E}_{s_i}(t) - c_{sp_i} \sin(\psi_i - \alpha_s) \dot{E}_{sp_i}(t) \\ + SP_{sp_i} k_{sp_i}(t) \sin(\psi_i - \alpha_s) \cos(\psi_i - \alpha_s) y_s \\ - SP_{sp_i} k_{sp_i}(t) \sin(\psi_i - \alpha_s) \cos(\psi_i - \alpha_s) y_{p_i} \\ + SP_{sp_i} k_{sp_i}(t) \sin(\psi_i - \alpha_s) \sin(\psi_i - \alpha_s) x_s \\ - SP_{sp_i} k_{sp_i}(t) \sin(\psi_i - \alpha_s) \sin(\psi_i - \alpha_s) x_{p_i} \\ + SP_{sp_i} k_{sp_i}(t) \sin(\psi_i - \alpha_s) u_s + SP_{sp_i} k_{sp_i}(t) \sin(\psi_i - \alpha_s) u_{p_i} \\ + SP_{sp_i} k_{sp_i}(t) \sin(\psi_i - \alpha_s) e_{sp_i}(t) + SP_{sp_i} k_{sp_i}(t) \sin(\psi_i - \alpha_s) E_{s_i}(t) \\ - SP_{sp_i} k_{sp_i}(t) \sin(\psi_i - \alpha_s) E_{sp_i}(t) = 0 \end{aligned} \quad (3.15)$$

In the direction of y_s , the resulting differential equation becomes,

$$\begin{aligned} m_s \cdot \ddot{y}_s + c_{sp_i} \cos(\psi_i - \alpha_s) \cos(\psi_i - \alpha_s) \dot{y}_s - c_{sp_i} \cos(\psi_i - \alpha_s) \sin(\psi_i - \alpha_s) \dot{\psi}_i y_s \\ - c_{sp_i} \cos(\psi_i - \alpha_s) \cos(\psi_i - \alpha_s) \dot{y}_{p_i} + c_{sp_i} \cos(\psi_i - \alpha_s) \sin(\psi_i - \alpha_s) \dot{\psi}_i y_{p_i} \\ + c_{sp_i} \cos(\psi_i - \alpha_s) \sin(\psi_i - \alpha_s) \dot{x}_s + c_{sp_i} \cos(\psi_i - \alpha_s) \cos(\psi_i - \alpha_s) \dot{\psi}_i x_s \\ - c_{sp_i} \cos(\psi_i - \alpha_s) \sin(\psi_i - \alpha_s) \dot{x}_{p_i} - c_{sp_i} \cos(\psi_i - \alpha_s) \cos(\psi_i - \alpha_s) \dot{\psi}_i x_{p_i} \end{aligned}$$

$$\begin{aligned}
& + c_{sp_i} \cos(\psi_i - \alpha_s) \dot{u}_s + c_{sp_i} \cos(\psi_i - \alpha_s) \dot{u}_{p_i} + c_{sp_i} \cos(\psi_i - \alpha_s) \dot{e}_{sp_i}(t) \\
& + c_{sp_i} \cos(\psi_i - \alpha_s) \dot{E}_{s_i}(t) - c_{sp_i} \cos(\psi_i - \alpha_s) \dot{E}_{sp_i}(t) \\
& + SP_{sp_i} k_{sp_i}(t) \cos(\psi_i - \alpha_s) \cos(\psi_i - \alpha_s) y_s \\
& - SP_{sp_i} k_{sp_i}(t) \cos(\psi_i - \alpha_s) \cos(\psi_i - \alpha_s) y_{p_i} \\
& + SP_{sp_i} k_{sp_i}(t) \cos(\psi_i - \alpha_s) \sin(\psi_i - \alpha_s) x_s \\
& - SP_{sp_i} k_{sp_i}(t) \cos(\psi_i - \alpha_s) \sin(\psi_i - \alpha_s) x_{p_i} \\
& + SP_{sp_i} k_{sp_i}(t) \cos(\psi_i - \alpha_s) u_s + SP_{sp_i} k_{sp_i}(t) \cos(\psi_i - \alpha_s) u_{p_i} \\
& + SP_{sp_i} k_{sp_i}(t) \cos(\psi_i - \alpha_s) e_{sp_i}(t) + SP_{sp_i} k_{sp_i}(t) \cos(\psi_i - \alpha_s) E_{s_i}(t) \\
& - SP_{sp_i} k_{sp_i}(t) \cos(\psi_i - \alpha_s) E_{sp_i}(t) = 0
\end{aligned} \tag{3.16}$$

For the torsional degree of freedom, the resulting differential equation becomes,

$$\begin{aligned}
& (J_s / r_s^2) \cdot \ddot{u}_s^* + c_{sp_i} \cos(\psi_i - \alpha_s) \dot{y}_s - c_{sp_i} \sin(\psi_i - \alpha_s) \dot{\psi}_i y_s - c_{sp_i} \cos(\psi_i - \alpha_s) \dot{y}_{p_i} \\
& + c_{sp_i} \sin(\psi_i - \alpha_s) \dot{\psi}_i y_{p_i} + c_{sp_i} \sin(\psi_i - \alpha_s) \dot{x}_s + c_{sp_i} \cos(\psi_i - \alpha_s) \dot{\psi}_i x_s \\
& - c_{sp_i} \sin(\psi_i - \alpha_s) \dot{x}_{p_i} - c_{sp_i} \cos(\psi_i - \alpha_s) \dot{\psi}_i x_{p_i} + c_{sp_i} \dot{u}_s + c_{sp_i} \dot{u}_{p_i} \\
& + c_{sp_i} \dot{e}_{sp_i}(t) + c_{sp_i} \dot{E}_{s_i}(t) - c_{sp_i} \dot{E}_{sp_i}(t) + SP_{sp_i} k_{sp_i}(t) \cos(\psi_i - \alpha_s) y_s \\
& - SP_{sp_i} k_{sp_i}(t) \cos(\psi_i - \alpha_s) y_{p_i} + SP_{sp_i} k_{sp_i}(t) \sin(\psi_i - \alpha_s) x_s \\
& - SP_{sp_i} k_{sp_i}(t) \sin(\psi_i - \alpha_s) x_{p_i} + SP_{sp_i} k_{sp_i}(t) u_s + SP_{sp_i} k_{sp_i}(t) u_{p_i} \\
& + SP_{sp_i} k_{sp_i}(t) e_{sp_i}(t) + SP_{sp_i} k_{sp_i}(t) E_{s_i}(t) - SP_{sp_i} k_{sp_i}(t) E_{sp_i}(t) = T_{ss} / r_s
\end{aligned} \tag{3.17}$$

It should be noticed that $x_{p_i}^*$ denotes the planet gear displacement in the x direction with reference to the origin of the sun gear centre, $y_{p_i}^*$ denotes the planet gear displacement in the y direction with reference to the origin of the sun gear centre, and \ddot{u}_s^* denotes the sun gear total torsional displacement (in terms of linear displacement on pitch circle). $x_{p_i}^*$, $y_{p_i}^*$, and \ddot{u}_s^* are defined in detail in Sec 3.4.

3.2. RING GEAR – PLANET GEAR PAIR

A ring gear - planet gear pair is examined in this section with consideration of the interaction between ring gear and ring gear supporting structure.

Figure 3-7 shows a ring gear and a planet gear in mesh, with the i^{th} planet gear at an angle ψ_i about the ring gear using the Descartes coordinate system. Positive direction for the ring gear have been defined as anticlockwise as shown in Figure 3-7.

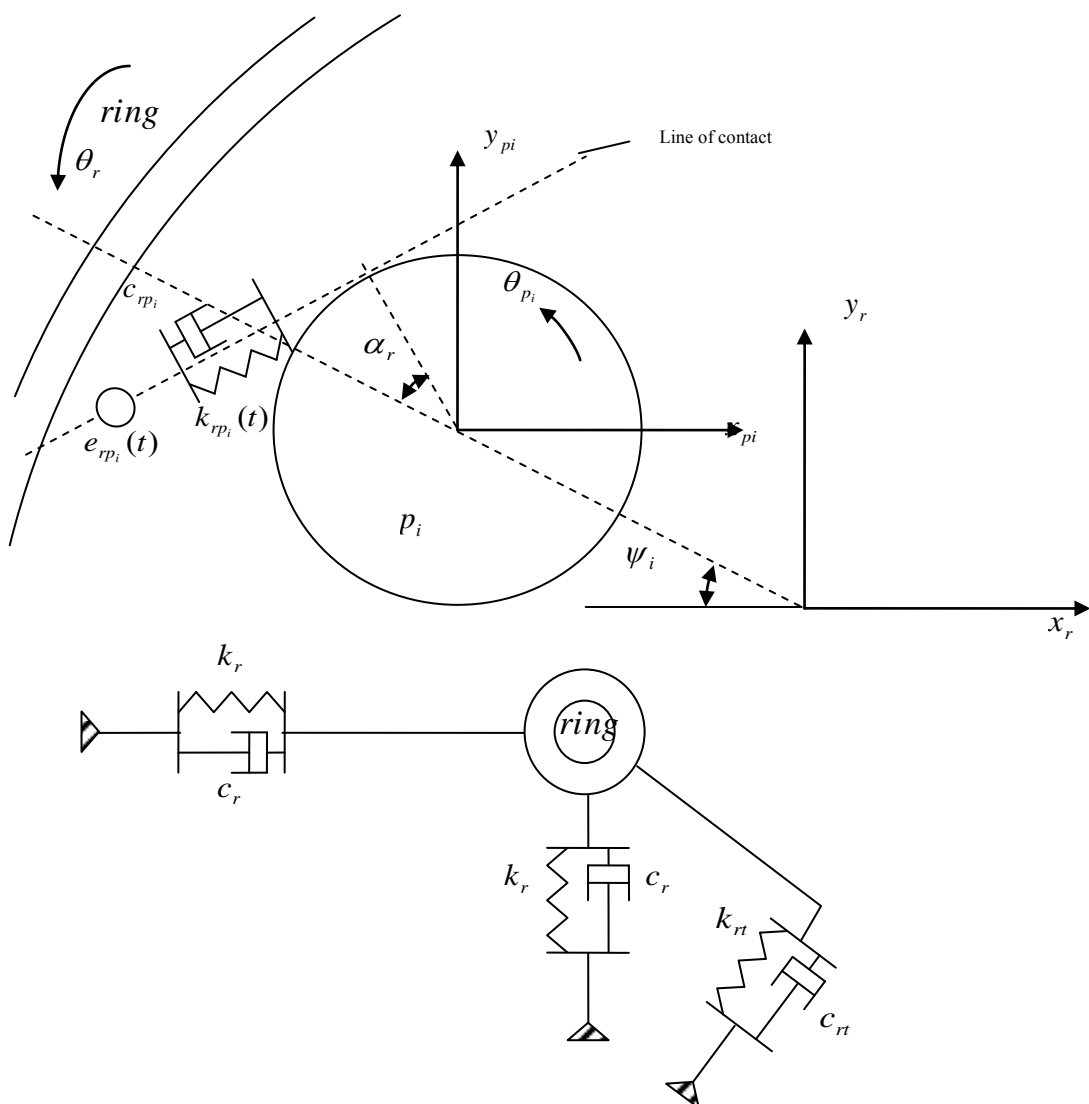


Figure 3-7 A ring-planet pair (with the contact point in II quadrant about the ring gear)

The ring gear is allowed to translate in both x and y directions, and rotate about its

center on the plane of gears. The torsional angular displacement of the ring gear is shown as θ_r , and θ_{p_i} for the i^{th} planet gear respectively.

The rigid bodies of the ring gear and planet gear are connected through the gear mesh stiffness $k_{rp_i}(t)$ and gear mesh damping c_{rp_i} along the line of action, also with a combined gear error $e_{rp_i}(t)$.

Defining the relative mesh displacement along the line of action as $MD_{rp_i}(t)$, the displacement with respect to y_r is,

$$MD_{rp_i}(t) \cdot \cos(\psi_i + \alpha_r)$$

and the displacement with respect to x_r is,

$$MD_{rp_i}(t) \cdot \sin(\psi_i + \alpha_r)$$

where α_r is the pressure angle of the ring gear - planet gear pair. The positive sign of $MD_{rp_i}(t)$ occurs when the action line is under compression, and the different conditions when the planet gear rotates about the ring gear are shown and analyzed in Figure 3-8 and 3-9.

According to Figure 3-7, 3-8, and 3-9, $MD_{rp_i}(t)$ can be described as,

$$MD_{rp_i}(t) = (y_r - y_{p_i})\cos(\psi_i + \alpha_r) + (x_r - x_{p_i})\sin(\psi_i + \alpha_r) + (u_r - u_{p_i}) + e_{rp_i}(t) + E_{r_i}(t) - E_{rp_i}(t) \quad (3.18)$$

where, $u_r = r_r\theta_r$, r_r is the base circle of the ring gear, θ_r is the torsional angular displacement of the ring gear; $u_{p_i} = r_{p_i}\theta_{p_i}$, r_{p_i} is the base circle of the i^{th} planet gear, θ_{p_i} is the torsional angular displacement of the i^{th} planet gear; $e_{rp_i}(t)$ is the combined gear error; $E_{r_i}(t)$ and $E_{rp_i}(t)$ are run out functions.

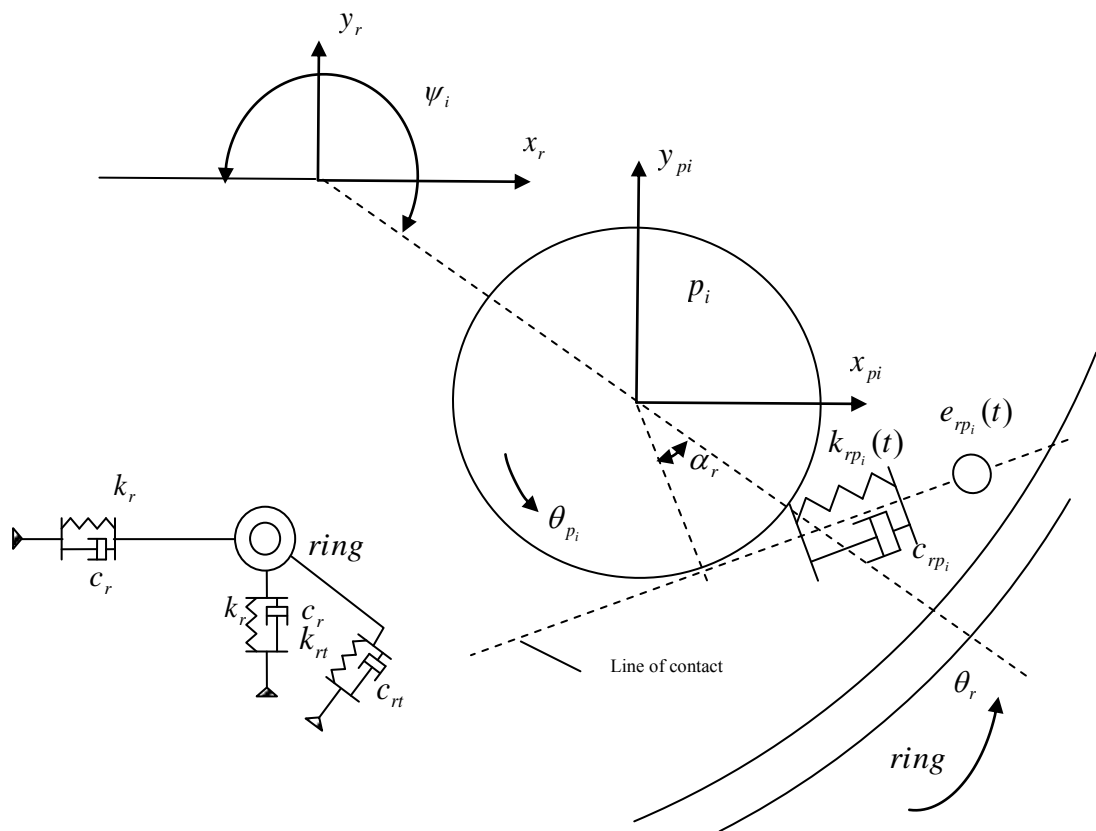
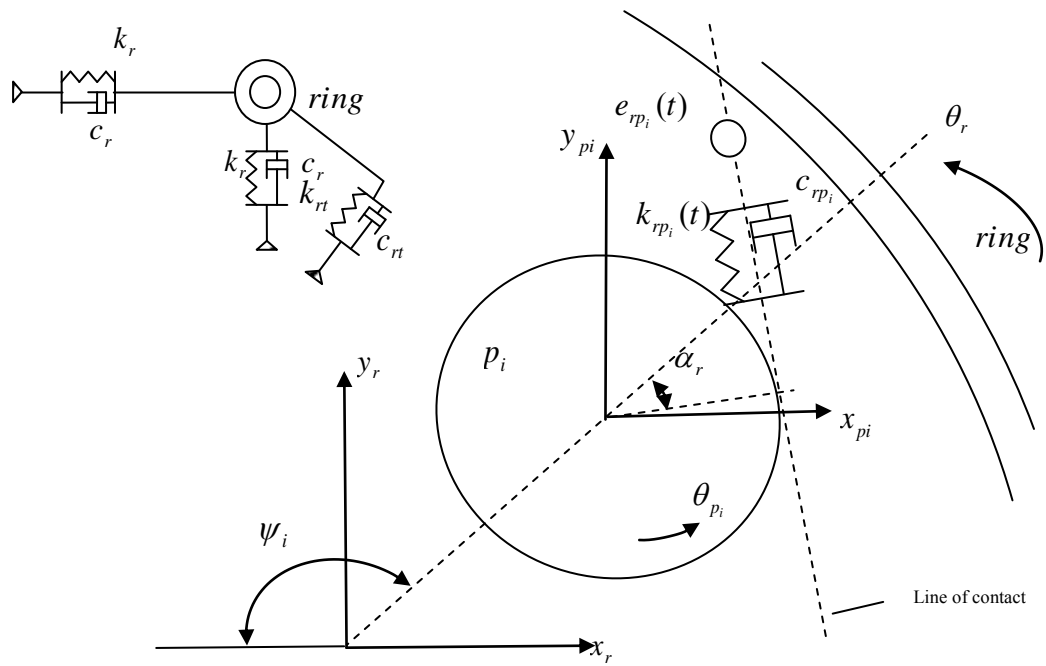


Figure 3-8 A ring-planet pair (with the contact point in the other three quadrants about the ring gear)

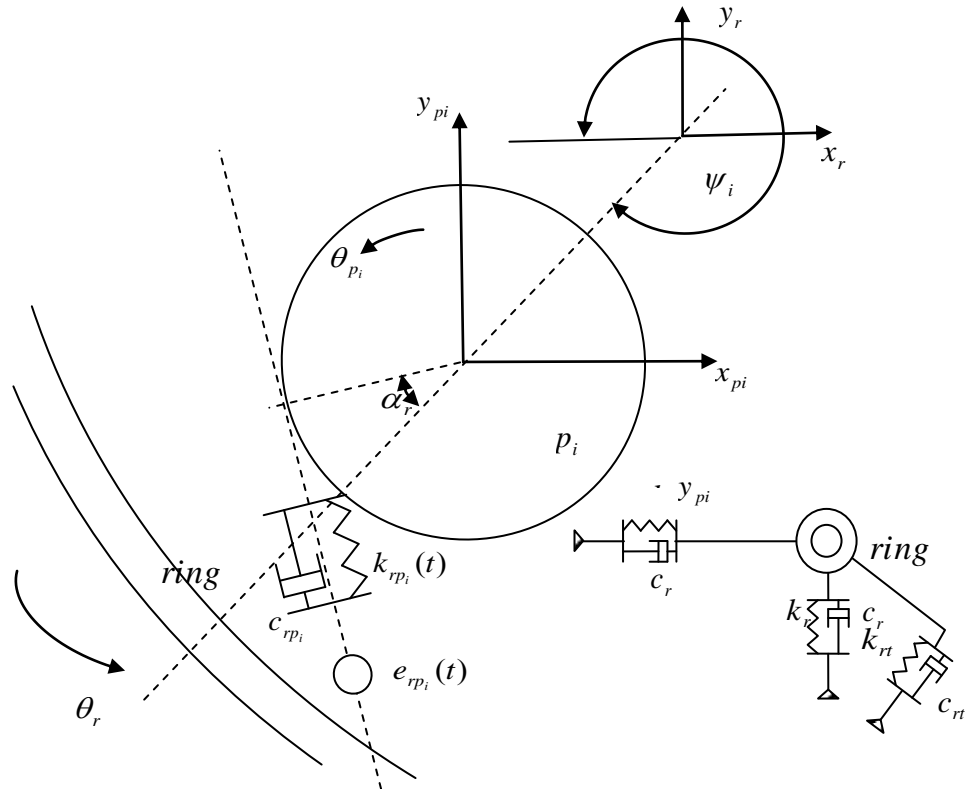


Figure 3-8 (continued) A ring-planet pair (with the contact point in the other three quadrants about the ring gear)

$\cos(\psi_i + \alpha_r) \in (0, 1) > 0$ $\sin(\psi_i + \alpha_r) \in (0, 1) > 0$ $(y_r - y_{p_i}) \propto$ compression of action line $(x_r - x_{p_i}) \propto$ compression of action line $(y_r - y_{p_i}) \cos(\psi_i + \alpha_r) \propto$ compression of action line $(x_r - x_{p_i}) \sin(\psi_i + \alpha_r) \propto$ compression of action line	II	$\cos(\psi_i + \alpha_r) \in (0, 1) < 0$ $\sin(\psi_i + \alpha_r) \in (0, 1) > 0$ $-(y_r - y_{p_i}) \propto$ compression of action line $(x_r - x_{p_i}) \propto$ compression of action line $(y_r - y_{p_i}) \cos(\psi_i + \alpha_r) \propto$ compression of action line $(x_r - x_{p_i}) \sin(\psi_i + \alpha_r) \propto$ compression of action line	I
$\cos(\psi_i + \alpha_r) \in (0, 1) > 0$ $\sin(\psi_i + \alpha_r) \in (0, 1) < 0$ $(y_r - y_{p_i}) \propto$ compression of action line $-(x_r - x_{p_i}) \propto$ compression of action line $(y_r - y_{p_i}) \cos(\psi_i + \alpha_r) \propto$ compression of action line $(x_r - x_{p_i}) \sin(\psi_i + \alpha_r) \propto$ compression of action line	III	$\cos(\psi_i + \alpha_r) \in (0, 1) < 0$ $\sin(\psi_i + \alpha_r) \in (0, 1) < 0$ $-(y_r - y_{p_i}) \propto$ compression of action line $-(x_r - x_{p_i}) \propto$ compression of action line $(y_r - y_{p_i}) \cos(\psi_i + \alpha_r) \propto$ compression of action line $(x_r - x_{p_i}) \sin(\psi_i + \alpha_r) \propto$ compression of action line	IV

Figure 3-9 The sign-relationship between axial relative displacement and $MD_{r_{p_i}}(t)$ with the planet gear positioned in the four quadrants about the ring gear respectively as shown in Figure 3-8

Tooth separation phenomenon is simulated by using the following unit step function,

$$SP_{rp_i} = \begin{cases} 1 & MD_{rp_i}(t) \geq 0 \\ 0 & MD_{rp_i}(t) < 0 \end{cases} \quad (3.19)$$

As the equation shows, when $MD_{rp_i}(t) < 0$, the teeth will lose contact and the resulting reaction force between the gear pair will be equal to zero.

A free body diagram of the planet gear is shown in Figure 3-10 (ring-planet pair only).

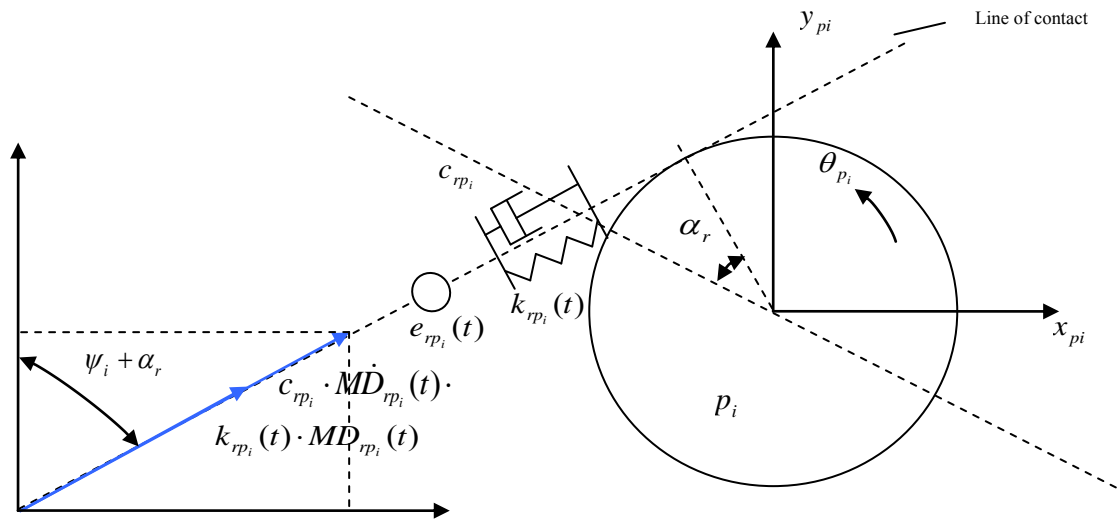


Figure 3-10 Free body diagram of planet gear (ring-planet pair only)

In the direction of x_{pi}^* , the resulting differential equation becomes,

$$m_p \cdot \ddot{x}_{pi}^* - c_{rp_i} \cdot \dot{MD}_{rp_i}(t) \cdot \sin(\psi_i + \alpha_r) - SP_{rp_i} \cdot k_{rp_i}(t) \cdot MD_{rp_i}(t) \cdot \sin(\psi_i + \alpha_r) = 0 \quad (3.20)$$

In the direction of y_{pi}^* , the resulting differential equation becomes,

$$m_p \cdot \ddot{y}_{pi}^* - c_{rp_i} \cdot \dot{MD}_{rp_i}(t) \cdot \cos(\psi_i + \alpha_r) - SP_{rp_i} \cdot k_{rp_i}(t) \cdot MD_{rp_i}(t) \cdot \cos(\psi_i + \alpha_r) = 0 \quad (3.21)$$

For the torsional degree of freedom, the resulting differential equation becomes,

$$(J_p / r_p^2) \cdot \ddot{u}_{pi} - c_{rp_i} \cdot \dot{MD}_{rp_i}(t) - SP_{rp_i} \cdot k_{rp_i}(t) \cdot MD_{rp_i}(t) = 0 \quad (3.22)$$

$$\text{where } u_{pi} = r_{pi} \theta_{pi}, \quad (3.23)$$

and where $\dot{MD}_{rp_i}(t)$ is the time differential of $MD_{rp_i}(t)$ which is expressed from Eqs 3.18, as follow,

$$\begin{aligned}
M\dot{D}_{rp_i}(t) = & \cos(\psi_i + \alpha_r) \dot{y}_r - \sin(\psi_i + \alpha_r) \dot{\psi}_i y_r - \cos(\psi_i + \alpha_r) \dot{y}_{p_i} + \sin(\psi_i + \alpha_r) \dot{\psi}_i y_{p_i} \\
& + \sin(\psi_i + \alpha_r) \dot{x}_r + \cos(\psi_i + \alpha_r) \dot{\psi}_i x_r - \sin(\psi_i + \alpha_r) \dot{x}_{p_i} - \cos(\psi_i + \alpha_r) \dot{\psi}_i x_{p_i} \\
& + \dot{u}_r - \dot{u}_{p_i} + \dot{e}_{rp_i}(t) + \dot{E}_{r_i}(t) - \dot{E}_{rp_i}(t)
\end{aligned} \tag{3.24}$$

Substituting Eqs 3.24 into Eqs 3.20, Eqs 3.21 and Eqs 3.22 gives,

In the direction of x_{p_i} , the resulting differential equation becomes,

$$\begin{aligned}
m_p \cdot \ddot{x}_{p_i}^* - c_{rp_i} \sin(\psi_i + \alpha_r) \cos(\psi_i + \alpha_r) \dot{y}_r + c_{rp_i} \sin(\psi_i + \alpha_r) \sin(\psi_i + \alpha_r) \dot{\psi}_i y_r \\
+ c_{rp_i} \sin(\psi_i + \alpha_r) \cos(\psi_i + \alpha_r) \dot{y}_{p_i} - c_{rp_i} \sin(\psi_i + \alpha_r) \sin(\psi_i + \alpha_r) \dot{\psi}_i y_{p_i} \\
- c_{rp_i} \sin(\psi_i + \alpha_r) \sin(\psi_i + \alpha_r) \dot{x}_r - c_{rp_i} \sin(\psi_i + \alpha_r) \cos(\psi_i + \alpha_r) \dot{\psi}_i x_r \\
+ c_{rp_i} \sin(\psi_i + \alpha_r) \sin(\psi_i + \alpha_r) \dot{x}_{p_i} + c_{rp_i} \sin(\psi_i + \alpha_r) \cos(\psi_i + \alpha_r) \dot{\psi}_i \\
- c_{rp_i} \sin(\psi_i + \alpha_r) \dot{u}_r + c_{rp_i} \sin(\psi_i + \alpha_r) \dot{u}_{p_i} - c_{rp_i} \sin(\psi_i + \alpha_r) \dot{e}_{rp_i}(t) \\
- c_{rp_i} \sin(\psi_i + \alpha_r) \dot{E}_{r_i}(t) + c_{rp_i} \sin(\psi_i + \alpha_r) \dot{E}_{rp_i}(t) \\
- SP_{rp_i} k_{rp_i}(t) \sin(\psi_i + \alpha_r) \cos(\psi_i + \alpha_r) y_r \\
+ SP_{rp_i} k_{rp_i}(t) \sin(\psi_i + \alpha_r) \cos(\psi_i + \alpha_r) y_{p_i} \\
- SP_{rp_i} k_{rp_i}(t) \sin(\psi_i + \alpha_r) \sin(\psi_i + \alpha_r) x_r \\
+ SP_{rp_i} k_{rp_i}(t) \sin(\psi_i + \alpha_r) \sin(\psi_i + \alpha_r) x_{p_i} \\
- SP_{rp_i} k_{rp_i}(t) \sin(\psi_i + \alpha_r) u_r + SP_{rp_i} k_{rp_i}(t) \sin(\psi_i + \alpha_r) u_{p_i} \\
- SP_{rp_i} k_{rp_i}(t) \sin(\psi_i + \alpha_r) e_{rp_i}(t) - SP_{rp_i} k_{rp_i}(t) \sin(\psi_i + \alpha_r) E_{r_i}(t) \\
+ SP_{rp_i} k_{rp_i}(t) \sin(\psi_i + \alpha_r) E_{rp_i}(t) = 0
\end{aligned} \tag{3.25}$$

In the direction of y_{p_i} , the resulting differential equation becomes,

$$\begin{aligned}
m_p \cdot \ddot{y}_{p_i}^* - c_{rp_i} \cos(\psi_i + \alpha_r) \cos(\psi_i + \alpha_r) \dot{y}_r + c_{rp_i} \cos(\psi_i + \alpha_r) \sin(\psi_i + \alpha_r) \dot{\psi}_i y_r \\
+ c_{rp_i} \cos(\psi_i + \alpha_r) \cos(\psi_i + \alpha_r) \dot{y}_{p_i} - c_{rp_i} \cos(\psi_i + \alpha_r) \sin(\psi_i + \alpha_r) \dot{\psi}_i y_{p_i} \\
- c_{rp_i} \cos(\psi_i + \alpha_r) \sin(\psi_i + \alpha_r) \dot{x}_r - c_{rp_i} \cos(\psi_i + \alpha_r) \cos(\psi_i + \alpha_r) \dot{\psi}_i x_r \\
+ c_{rp_i} \cos(\psi_i + \alpha_r) \sin(\psi_i + \alpha_r) \dot{x}_{p_i} + c_{rp_i} \cos(\psi_i + \alpha_r) \cos(\psi_i + \alpha_r) \dot{\psi}_i x_{p_i} \\
- c_{rp_i} \cos(\psi_i + \alpha_r) \dot{u}_r + c_{rp_i} \cos(\psi_i + \alpha_r) \dot{u}_{p_i} - c_{rp_i} \cos(\psi_i + \alpha_r) \dot{e}_{rp_i}(t) \\
- c_{rp_i} \cos(\psi_i + \alpha_r) \dot{E}_{r_i}(t) + c_{rp_i} \cos(\psi_i + \alpha_r) \dot{E}_{rp_i}(t) \\
- SP_{rp_i} k_{rp_i}(t) \cos(\psi_i + \alpha_r) \cos(\psi_i + \alpha_r) y_r
\end{aligned}$$

$$\begin{aligned}
& + SP_{rp_i} k_{rp_i}(t) \cos(\psi_i + \alpha_r) \cos(\psi_i + \alpha_r) y_{p_i} \\
& - SP_{rp_i} k_{rp_i}(t) \cos(\psi_i + \alpha_r) \sin(\psi_i + \alpha_r) x_r \\
& + SP_{rp_i} k_{rp_i}(t) \cos(\psi_i + \alpha_r) \sin(\psi_i + \alpha_r) x_{p_i} \\
& - SP_{rp_i} k_{rp_i}(t) \cos(\psi_i + \alpha_r) u_r + SP_{rp_i} k_{rp_i}(t) \cos(\psi_i + \alpha_r) u_{p_i} \\
& - SP_{rp_i} k_{rp_i}(t) \cos(\psi_i + \alpha_r) e_{rp_i}(t) - SP_{rp_i} k_{rp_i}(t) \cos(\psi_i + \alpha_r) E_{r_i}(t) \\
& + SP_{rp_i} k_{rp_i}(t) \cos(\psi_i + \alpha_r) E_{rp_i}(t) = 0
\end{aligned} \tag{3.26}$$

For the torsional degree of freedom, the resulting differential equation becomes,

$$\begin{aligned}
& (J_p / r_p^2) \cdot \ddot{u}_{p_i} - c_{rp_i} \cos(\psi_i + \alpha_r) \dot{y}_r + c_{rp_i} \sin(\psi_i + \alpha_r) \dot{\psi}_i y_r + c_{rp_i} \cos(\psi_i + \alpha_r) \dot{y}_{p_i} \\
& - c_{rp_i} \sin(\psi_i + \alpha_r) \dot{\psi}_i y_{p_i} - c_{rp_i} \sin(\psi_i + \alpha_r) \dot{x}_r - c_{rp_i} \cos(\psi_i + \alpha_r) \dot{\psi}_i x_r \\
& + c_{rp_i} \sin(\psi_i + \alpha_r) \dot{x}_{p_i} + c_{rp_i} \cos(\psi_i + \alpha_r) \dot{\psi}_i x_{p_i} - c_{rp_i} \dot{u}_r + c_{rp_i} \dot{u}_{p_i} - c_{rp_i} \dot{e}_{rp_i}(t) \\
& - c_{rp_i} \dot{E}_{r_i}(t) + c_{rp_i} \dot{E}_{rp_i}(t) - SP_{rp_i} k_{rp_i}(t) \cos(\psi_i + \alpha_r) y_r \\
& + SP_{rp_i} k_{rp_i}(t) \cos(\psi_i + \alpha_r) y_{p_i} - SP_{rp_i} k_{rp_i}(t) \sin(\psi_i + \alpha_r) x_r \\
& + SP_{rp_i} k_{rp_i}(t) \sin(\psi_i + \alpha_r) x_{p_i} - SP_{rp_i} k_{rp_i}(t) u_r + SP_{rp_i} k_{rp_i}(t) u_{p_i} \\
& - SP_{rp_i} k_{rp_i}(t) e_{rp_i}(t) - SP_{rp_i} k_{rp_i}(t) E_{r_i}(t) + SP_{rp_i} k_{rp_i}(t) E_{rp_i}(t) = 0
\end{aligned} \tag{3.27}$$

A free body diagram of the ring gear is shown in Figure 3-11 (ring-planet pair only).

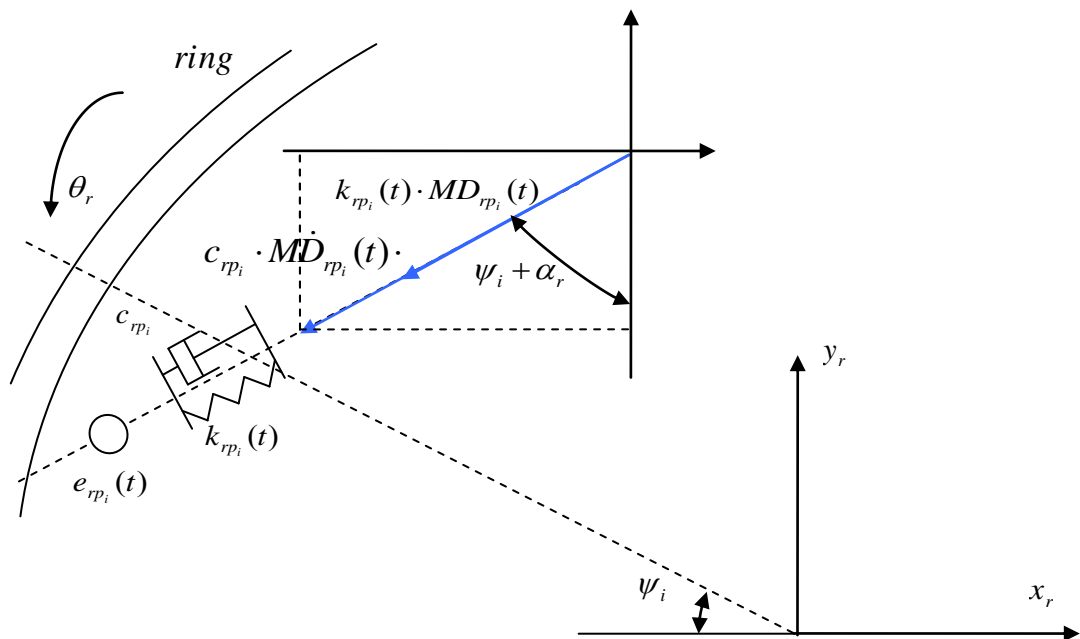


Figure 3-11 Free body diagram of ring gear

In the direction of x_r , the resulting differential equation becomes,

$$m_r \cdot \ddot{x}_r + c_{rp_i} \cdot \dot{MD}_{rp_i}(t) \cdot \sin(\psi_i + \alpha_r) + SP_{rp_i} \cdot k_{rp_i}(t) \cdot MD_{rp_i}(t) \cdot \sin(\psi_i + \alpha_r) + c_r \cdot \dot{x}_r + k_r \cdot x_r = 0 \quad (3.28)$$

In the direction of y_r , the resulting differential equation becomes,

$$m_r \cdot \ddot{y}_r + c_{rp_i} \cdot \dot{MD}_{rp_i}(t) \cdot \cos(\psi_i + \alpha_r) + SP_{rp_i} \cdot k_{rp_i}(t) \cdot MD_{rp_i}(t) \cdot \cos(\psi_i + \alpha_r) + c_r \cdot \dot{y}_r + k_r \cdot y_r = 0 \quad (3.29)$$

For the torsional degree of freedom, the resulting differential equation becomes,

$$(J_r / r_r^2) \cdot \ddot{u}_r^* + c_{rp_i} \cdot \dot{MD}_{rp_i}(t) + SP_{rp_i} \cdot k_{rp_i}(t) \cdot MD_{rp_i}(t) + c_{rt} \cdot \dot{D}_{rb} \cdot r_{rb} / r_r + k_{rt} \cdot D_{rb} \cdot r_{rb} / r_r = T_{rb} / r_r \quad (3.30)$$

$$\text{where } u_r^* = r_r \cdot \theta_r^*, \quad (3.31)$$

and where T_{rb} is the reaction torque applied to the outer circle of the ring gear by the ring gear supporting structure.

Substituting Eqs 3.24 into Eqs 3.28, Eqs 3.29 and Eqs 3.30 gives (excluding supporting damping and stiffness),

In the direction of x_r , the resulting differential equation becomes,

$$\begin{aligned} m_r \cdot \ddot{x}_r + c_{rp_i} \sin(\psi_i + \alpha_r) \cos(\psi_i + \alpha_r) \dot{y}_r - c_{rp_i} \sin(\psi_i + \alpha_r) \sin(\psi_i + \alpha_r) \dot{\psi}_i y_r \\ - c_{rp_i} \sin(\psi_i + \alpha_r) \cos(\psi_i + \alpha_r) \dot{y}_{p_i} + c_{rp_i} \sin(\psi_i + \alpha_r) \sin(\psi_i + \alpha_r) \dot{\psi}_i y_{p_i} \\ + c_{rp_i} \sin(\psi_i + \alpha_r) \sin(\psi_i + \alpha_r) \dot{x}_r + c_{rp_i} \sin(\psi_i + \alpha_r) \cos(\psi_i + \alpha_r) \dot{\psi}_i x_r \\ - c_{rp_i} \sin(\psi_i + \alpha_r) \sin(\psi_i + \alpha_r) \dot{x}_{p_i} - c_{rp_i} \sin(\psi_i + \alpha_r) \cos(\psi_i + \alpha_r) \dot{\psi}_i x_{p_i} \\ + c_{rp_i} \sin(\psi_i + \alpha_r) \dot{u}_r - c_{rp_i} \sin(\psi_i + \alpha_r) \dot{u}_{p_i} + c_{rp_i} \sin(\psi_i + \alpha_r) \dot{e}_{rp_i}(t) \\ + c_{rp_i} \sin(\psi_i + \alpha_r) \dot{E}_{r_i}(t) - c_{rp_i} \sin(\psi_i + \alpha_r) \dot{E}_{rp_i}(t) \\ + SP_{rp_i} k_{rp_i}(t) \sin(\psi_i + \alpha_r) \cos(\psi_i + \alpha_r) y_r \\ - SP_{rp_i} k_{rp_i}(t) \sin(\psi_i + \alpha_r) \cos(\psi_i + \alpha_r) y_{p_i} \\ + SP_{rp_i} k_{rp_i}(t) \sin(\psi_i + \alpha_r) \sin(\psi_i + \alpha_r) x_r \\ - SP_{rp_i} k_{rp_i}(t) \sin(\psi_i + \alpha_r) \sin(\psi_i + \alpha_r) x_{p_i} \\ + SP_{rp_i} k_{rp_i}(t) \sin(\psi_i + \alpha_r) u_r - SP_{rp_i} k_{rp_i}(t) \sin(\psi_i + \alpha_r) u_{p_i} \\ + SP_{rp_i} k_{rp_i}(t) \sin(\psi_i + \alpha_r) e_{rp_i}(t) + SP_{rp_i} k_{rp_i}(t) \sin(\psi_i + \alpha_r) E_{r_i}(t) \end{aligned}$$

$$- SP_{rp_i} k_{rp_i}(t) \sin(\psi_i + \alpha_r) E_{rp_i}(t) = 0 \quad (3.32)$$

In the direction of y_r , the resulting differential equation becomes,

$$\begin{aligned} m_r \cdot \ddot{y}_r + c_{rp_i} \cos(\psi_i + \alpha_r) \cos(\psi_i + \alpha_r) \dot{y}_r - c_{rp_i} \cos(\psi_i + \alpha_r) \sin(\psi_i + \alpha_r) \dot{\psi}_i y_r \\ - c_{rp_i} \cos(\psi_i + \alpha_r) \cos(\psi_i + \alpha_r) \dot{y}_{p_i} + c_{rp_i} \cos(\psi_i + \alpha_r) \sin(\psi_i + \alpha_r) \dot{\psi}_i y_{p_i} \\ + c_{rp_i} \cos(\psi_i + \alpha_r) \sin(\psi_i + \alpha_r) \dot{x}_r + c_{rp_i} \cos(\psi_i + \alpha_r) \cos(\psi_i + \alpha_r) \dot{\psi}_i x_r \\ - c_{rp_i} \cos(\psi_i + \alpha_r) \sin(\psi_i + \alpha_r) \dot{x}_{p_i} - c_{rp_i} \cos(\psi_i + \alpha_r) \cos(\psi_i + \alpha_r) \dot{\psi}_i x_{p_i} \\ + c_{rp_i} \cos(\psi_i + \alpha_r) \dot{u}_r - c_{rp_i} \cos(\psi_i + \alpha_r) \dot{u}_{p_i} + c_{rp_i} \cos(\psi_i + \alpha_r) \dot{e}_{rp_i}(t) \\ + c_{rp_i} \cos(\psi_i + \alpha_r) \dot{E}_{r_i}(t) - c_{rp_i} \cos(\psi_i + \alpha_r) \dot{E}_{rp_i}(t) \\ + SP_{rp_i} k_{rp_i}(t) \cos(\psi_i + \alpha_r) \cos(\psi_i + \alpha_r) y_r \\ - SP_{rp_i} k_{rp_i}(t) \cos(\psi_i + \alpha_r) \cos(\psi_i + \alpha_r) y_{p_i} \\ + SP_{rp_i} k_{rp_i}(t) \cos(\psi_i + \alpha_r) \sin(\psi_i + \alpha_r) x_r \\ - SP_{rp_i} k_{rp_i}(t) \cos(\psi_i + \alpha_r) \sin(\psi_i + \alpha_r) x_{p_i} \\ + SP_{rp_i} k_{rp_i}(t) \cos(\psi_i + \alpha_r) u_r - SP_{rp_i} k_{rp_i}(t) \cos(\psi_i + \alpha_r) u_{p_i} \\ + SP_{rp_i} k_{rp_i}(t) \cos(\psi_i + \alpha_r) e_{rp_i}(t) + SP_{rp_i} k_{rp_i}(t) \cos(\psi_i + \alpha_r) E_{r_i}(t) \\ - SP_{rp_i} k_{rp_i}(t) \cos(\psi_i + \alpha_r) E_{rp_i}(t) = 0 \end{aligned} \quad (3.33)$$

For the torsional degree of freedom, the resulting differential equation becomes,

$$\begin{aligned} (J_r / r_r^2) \cdot \ddot{u}_r^* + c_{rp_i} \cos(\psi_i + \alpha_r) \dot{y}_r - c_{rp_i} \sin(\psi_i + \alpha_r) \dot{\psi}_i y_r - c_{rp_i} \cos(\psi_i + \alpha_r) \dot{y}_{p_i} \\ + c_{rp_i} \sin(\psi_i + \alpha_r) \dot{\psi}_i y_{p_i} + c_{rp_i} \sin(\psi_i + \alpha_r) \dot{x}_r + c_{rp_i} \cos(\psi_i + \alpha_r) \dot{\psi}_i x_r \\ - c_{rp_i} \sin(\psi_i + \alpha_r) \dot{x}_{p_i} - c_{rp_i} \cos(\psi_i + \alpha_r) \dot{\psi}_i x_{p_i} + c_{rp_i} \dot{u}_r - c_{rp_i} \dot{u}_{p_i} \\ + c_{rp_i} \dot{e}_{rp_i}(t) + c_{rp_i} \dot{E}_{r_i}(t) - c_{rp_i} \dot{E}_{rp_i}(t) \\ + SP_{rp_i} k_{rp_i}(t) \cos(\psi_i + \alpha_r) y_r - SP_{rp_i} k_{rp_i}(t) \cos(\psi_i + \alpha_r) y_{p_i} \\ + SP_{rp_i} k_{rp_i}(t) \sin(\psi_i + \alpha_r) x_r - SP_{rp_i} k_{rp_i}(t) \sin(\psi_i + \alpha_r) x_{p_i} \\ + SP_{rp_i} k_{rp_i}(t) u_r - SP_{rp_i} k_{rp_i}(t) u_{p_i} + SP_{rp_i} k_{rp_i}(t) e_{rp_i}(t) \\ + SP_{rp_i} k_{rp_i}(t) E_{r_i}(t) - SP_{rp_i} k_{rp_i}(t) E_{rp_i}(t) = T_{rb} / r_r \end{aligned} \quad (3.34)$$

It should be noticed that $x_{p_i}^*$ denotes the planet gear displacement in the x direction

with reference to the origin of the sun gear centre, y_{pi}^* denotes the planet gear displacement in the y direction with reference to the origin of the sun gear centre, and \ddot{u}_r^* denotes the ring gear total torsional displacement (in terms of linear displacement on pitch circle). x_{pi}^* , y_{pi}^* , and \ddot{u}_r^* are defined in detail in Sec 3.4.

3.3. CARRIER ARM – PLANET GEAR PAIR

A carrier arm - planet gear pair is examined in this section with the consideration of planet pin-bearing assembly.

Figure 3-12 shows a carrier arm and a planet gear pair, with the i^{th} planet gear having a theoretical angle ψ_i about the carrier arm's coordinates. The carrier arm is allowed to translate in both x and y directions, and rotate about its center on the plane of gears.

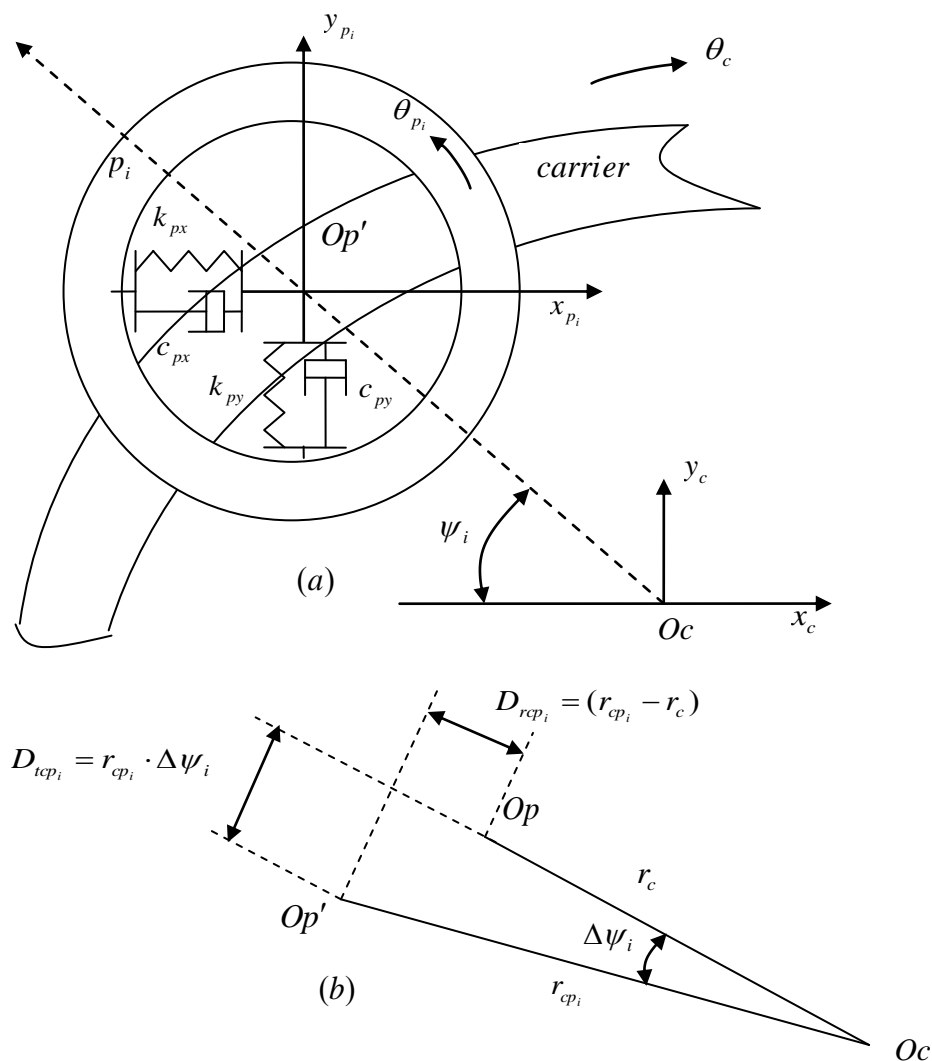


Figure 3-12 A carrier arm and a planet gear pair (with the pin-bearing positioned in II quadrant about the carrier arm)

The i^{th} planet gear is mounted on the carrier arm through the planet pin-bearing

assembly which is simulated with introduced stiffness and damping features to simplify the equations of motion shown in Figure 3-12. The rotational motion of the planet is completely uncoupled from the carrier arm's motion, as zero rotational friction force is assumed to simplify the system.

In Figure 3-13 the equations relating the planet gear mounted in position with the carrier arm and the resulting transversal interaction forces are analyzed.

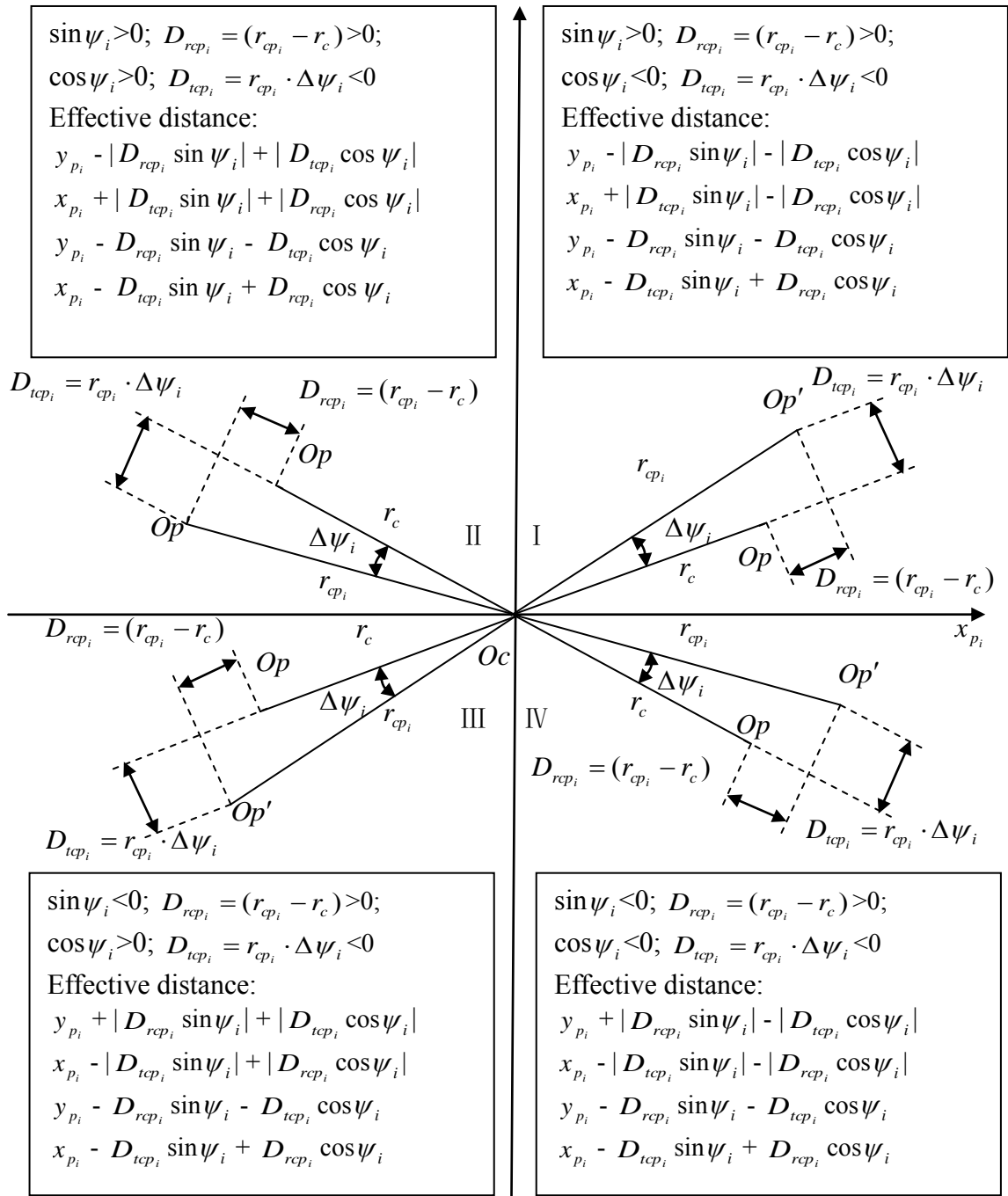


Figure 3-13 The equations relating the planet gear mounted in position on the carrier arm and the resulting transversal relative displacements

A free body diagram of the planet gear is shown in Figure 3-14 (carrier-planet pair only).

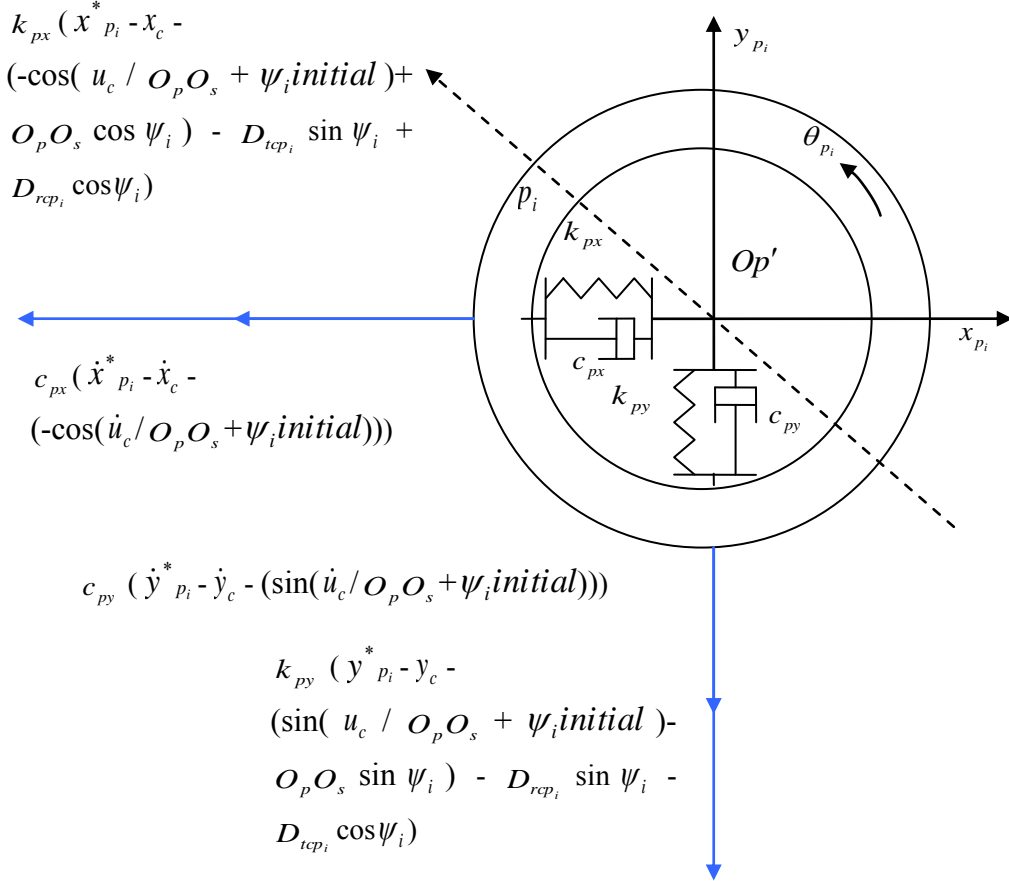


Figure 3-14 Free body diagram of planet gear (carrier-planet pair only)

In the direction of x_{pi}^* , the resulting differential equation becomes,

$$m_p \cdot \ddot{x}_{pi}^* + c_{px} (\dot{x}_{pi}^* - \dot{x}_c - (-\cos(\dot{u}_c / O_p O_s + \psi_i^{initial}))) + k_{px} (x_{pi}^* - x_c - (-\cos(u_c / O_p O_s + \psi_i^{initial}) + O_p O_s \cos \psi_i) - D_{tcp_i} \sin \psi_i + D_{rcp_i} \cos \psi_i) = 0, \quad (3.35)$$

$$u_c = r_c \theta_c \quad (3.36)$$

In the direction of y_{pi}^* , the resulting differential equation becomes,

$$m_p \cdot \ddot{y}_{pi}^* + c_{py} (\dot{y}_{pi}^* - \dot{y}_c - (\sin(\dot{u}_c / O_p O_s + \psi_i^{initial}))) + k_{py} (y_{pi}^* - y_c - (\sin(u_c / O_p O_s + \psi_i^{initial}) - O_p O_s \sin \psi_i) - D_{rcp_i} \sin \psi_i - D_{tcp_i} \cos \psi_i) = 0 \quad (3.37)$$

A free body diagram of the carrier arm is shown in Figure 3-15.

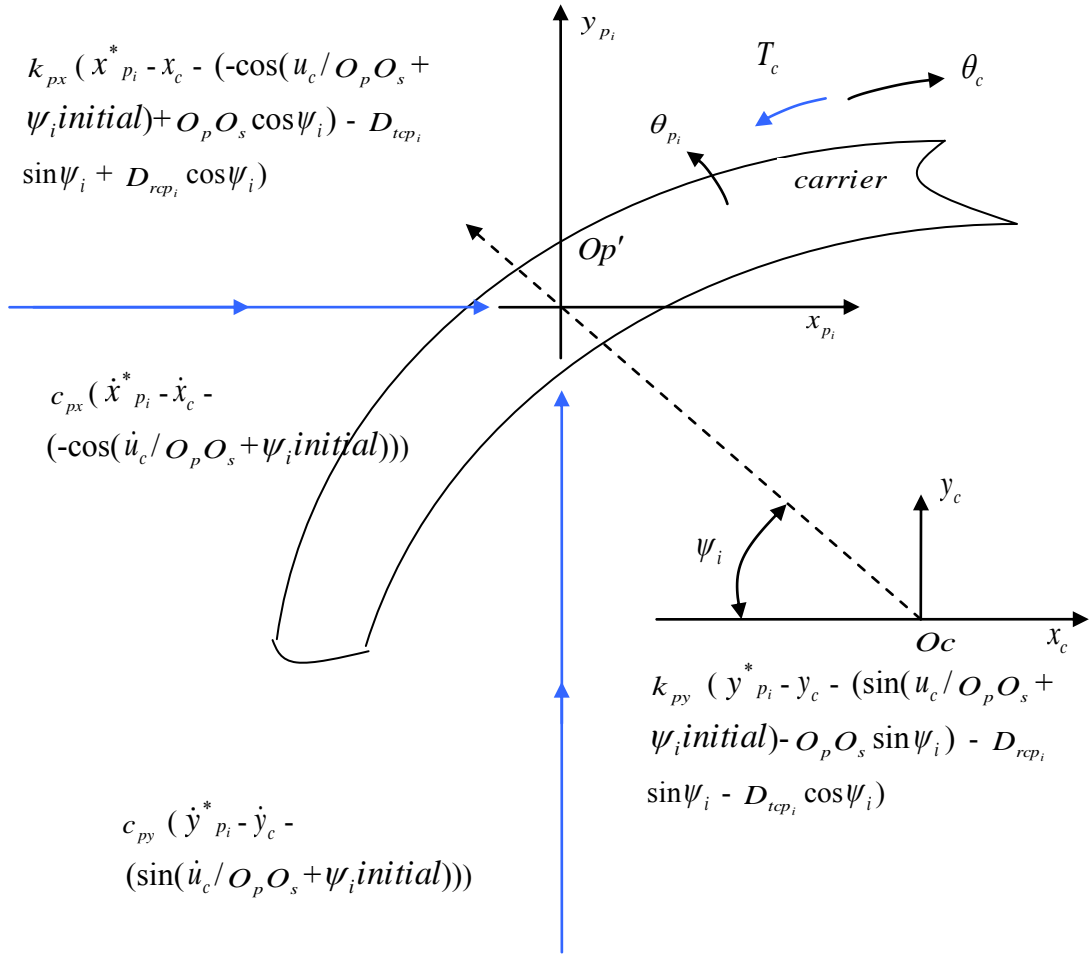


Figure 3-15 Free body diagram of carrier arm

In the direction of x_c , the resulting differential equation becomes,

$$m_c \ddot{x}_c - c_{px} (\dot{x}_{p_i}^* - \dot{x}_c - (-\cos(\dot{u}_c / O_p O_s + \psi_i \text{initial}))) - k_{px} (\dot{x}_{p_i}^* - \dot{x}_c - (-\cos(u_c / O_p O_s + \psi_i \text{initial}) + O_p O_s \cos \psi_i) - D_{tcp_i} \sin \psi_i + D_{rcp_i} \cos \psi_i) = 0 \quad (3.38)$$

In the direction of y_c , the resulting differential equation becomes,

$$m_c \ddot{y}_c - c_{py} (\dot{y}_{p_i}^* - \dot{y}_c - (\sin(\dot{u}_c / O_p O_s + \psi_i \text{initial}))) - k_{py} (y_{p_i}^* - y_c - (\sin(u_c / O_p O_s + \psi_i \text{initial}) - O_p O_s \sin \psi_i) - D_{rcp_i} \sin \psi_i - D_{tcp_i} \cos \psi_i) = 0 \quad (3.39)$$

For the torsional degree of freedom, the resulting differential equation becomes,

$$(J_c / r_c^2) \cdot \ddot{u}_c - c_{px} (\dot{x}_{p_i}^* - \dot{x}_c - (-\cos(\dot{u}_c / O_p O_s + \psi_i \text{initial}))) \sin \psi_i - k_{px} (\dot{x}_{p_i}^* - \dot{x}_c - (-\cos(u_c / O_p O_s + \psi_i \text{initial}) + O_p O_s \cos \psi_i) - D_{tcp_i} \sin \psi_i + D_{rcp_i} \cos \psi_i) = 0$$

$$\begin{aligned}
& / O_p O_s + \psi_i^{initial}) + O_p O_s \cos \psi_i) - D_{tcp_i} \sin \psi_i + D_{tcp_i} \cos \psi_i) \sin \psi_i - c_{py} (\dot{y}_{pi}^* - \dot{y}_c - \\
& (\sin(\dot{u}_c / O_p O_s + \psi_i^{initial}))) \cos \psi_i - k_{py} (y_{pi}^* - y_c - (\sin(u_c / O_p O_s + \psi_i^{initial}) - O_p O_s \sin \\
& \psi_i) - D_{tcp_i} \sin \psi_i - D_{tcp_i} \cos \psi_i) \cos \psi_i = -T_c / r_c \tag{3.40}
\end{aligned}$$

where T_c is the load applied to the outer circle of the carrier arm.

It should be noticed that x_{pi}^* denotes the planet gear displacement in the x direction with reference to the origin of the sun gear centre and y_{pi}^* denotes the planet gear displacement in the y direction with reference to the origin of the sun gear centre. x_{pi}^* and y_{pi}^* are defined in detail in Sec 3.4.

3.4. OVERALL PLANETARY GEAR SYSTEM

Based on the equations developed in the previous three sections, an overall equation can be formed using matrix techniques.

Keeping the matrix equation general, gives the ability to handle any arbitrary arrangement of planet gears using the same overall equation. In this research, three degrees of freedom have been considered for each component (gear and carrier arm) so that the overall model has a total of $3*(3 + n)$ degree of freedom (one sun gear, one ring gear, one carrier arm, n planet gears) . In this specific case, 3 planet gears are simulated so overall $3*(3+3) = 18$ degrees of freedom are contained in the overall equation. The equation of motion representing the entire planetary gear model is given as,

$$M\ddot{D} + [C + C_s]\dot{D} + [K + K_s]D = F_c(t) + F_k(t) \quad (3.41)$$

where matrix M represents the mass matrix, which has the form of $3*(3+n)$ by $3*(3+n)$, (in this specific case, 18 by 18), shown in Figure 3-16; \ddot{D} represents the acceleration vector, which has a form of $3*(3+n)$ by 1, (in this specific case, 18 by 1), shown in Figure 3-17(a); \dot{D} represents the velocity vector, which has a form of $3*(3+n)$ by 1, (in this specific case, 18 by 1), shown in Figure 3-17(b); D represents the displacement vector, which has a form of $3*(3+n)$ by 1, (in this specific case, 18 by 1), shown in Figure 3-17(c); $F_c(t)$ and $F_k(t)$ denotes the force vector containing damping and stiffness features respectively, and both of them have a form of $3*(3+n)$ by 1, (in this specific case, 18 by 1), shown in Figure 3-18; $[C]$ and $[C_s]$ are the mesh damping matrix and support structure damping matrix respectively, and both of them are of form $3*(3+n)$ by $3*(3+n)$, (in this specific case, 18 by 18), shown in Figure 3-19; $[k]$ and $[k_s]$ are the mesh stiffness matrix and the support structure stiffness matrix respectively, and both of them are of form $3*(3+n)$ by $3*(3+n)$, (in this specific case, 18 by 18), shown in Figure 3-20.

m_s	0	0	0	0	0	0	0	0	0	0	0	0	0	0	0	0
0	m_s	0	0	0	0	0	0	0	0	0	0	0	0	0	0	0
0	0	J_s/r^2_s	0	0	0	0	0	0	0	0	0	0	0	0	0	0
0	0	0	m_r	0	0	0	0	0	0	0	0	0	0	0	0	0
0	0	0	0	m_r	0	0	0	0	0	0	0	0	0	0	0	0
0	0	0	0	0	J_r/r^2_r	0	0	0	0	0	0	0	0	0	0	0
0	0	0	0	0	0	m_c	0	0	0	0	0	0	0	0	0	0
0	0	0	0	0	0	0	m_c	0	0	0	0	0	0	0	0	0
0	0	0	0	0	0	0	0	J_c/r^2_c	0	0	0	0	0	0	0	0
0	0	0	0	0	0	0	0	0	m_{p1}	0	0	0	0	0	0	0
0	0	0	0	0	0	0	0	0	0	m_{p1}	0	0	0	0	0	0
0	0	0	0	0	0	0	0	0	0	0	J_{p1}/r^2_{p1}	0	0	0	0	0
0	0	0	0	0	0	0	0	0	0	0	0	\	0	0	0	0
0	0	0	0	0	0	0	0	0	0	0	0	0	\	0	0	0
0	0	0	0	0	0	0	0	0	0	0	0	0	0	\	0	0
0	0	0	0	0	0	0	0	0	0	0	0	0	0	0	m_{pn}	0
0	0	0	0	0	0	0	0	0	0	0	0	0	0	0	0	m_{pn}
0	0	0	0	0	0	0	0	0	0	0	0	0	0	0	0	J_{pn}/r^2_{pn}

Figure 3-16 Mass matrix of overall equation

x''_s	x'_s	x_s
y''_s	y'_s	y_s
u''^*_s	u'_s	u_s
x''_r	x'_r	x_r
y''_r	y'_r	y_r
u''^*_r	u'_r	u_r
x''_c	x'_c	x_c
y''_c	y'_c	y_c
u''_c	u'_c	u_c
x''_{p1}	x'_{p1}	x^*_{p1}
y''_{p1}	y'_{p1}	y^*_{p1}
u''_{p1}	u'_{p1}	u_{p1}
x''_{pn}	x'_{pn}	x^*_{pn}
y''_{pn}	y'_{pn}	y^*_{pn}
u''_{pn}	u'_{pn}	u_{pn}

(a)

(b)

(c)

Figure 3-17 (a) acceleration vector (b) velocity vector (c) displacement vector of overall equation

$SP_{spi} \sum -cspisin(\psi_i - a_s)e'spi(t) - \sum cspisin(\psi_i - a_s)E'si(t) + \sum cspisin(\psi_i - a_s)E'spi(t)$
$SP_{spi} \sum -cspicos(\psi_i - a_s)e'spi(t) - \sum cspicos(\psi_i - a_s)E'si(t) + \sum cspicos(\psi_i - a_s)E'spi(t)$
$SP_{spi} \sum -cspie'spi(t) - \sum cspiE'si(t) + \sum cspiE'spi(t)$
$SP_{rpi} \sum -crpisin(\psi_i + a_r)e'rpi(t) - \sum crpisin(\psi_i + a_r)E'ri(t) + \sum crpisin(\psi_i + a_r)E'rpi(t)$
$SP_{rpi} \sum -crpicos(\psi_i + a_r)e'rpi(t) - \sum crpicos(\psi_i + a_r)E'ri(t) + \sum crpicos(\psi_i + a_r)E'rpi(t)$
$SP_{rpi} \sum crpie'rpi(t) + \sum crpiE'ri(t) - \sum crpiE'rpi(t)$
$-\sum cpx(-\cos(u'c/OpOs + \psi_{iinitial})) - \sum kpx(-\cos(uc/OpOs + \psi_{iinitial}) + OpOscos(\psi_i))$
$-\sum cpy(\sin(u'c/OpOs + \psi_{iinitial})) - \sum kpy(\sin(uc/OpOs + \psi_{iinitial}) - OpOssin(\psi_i))$
$\sum -kpxDtcpisin\psi_i/\sin\psi_i + \sum kpxDrepicos\psi_i/\sin\psi_i - \sum cpxsin(\psi_i)(-\cos(u'c/OpOs + \psi_{iinitial})) - \sum kpxsin(\psi_i)(-\cos(uc/OpOs + \psi_{iinitial}) + OpOscos(\psi_i)) - \sum cpycos(\psi_i)(\sin(u'c/OpOs + \psi_{iinitial})) - \sum kpycos(\psi_i)(\sin(uc/OpOs + \psi_{iinitial}) - OpOssin(\psi_i))$
$SP_{sp1} \sum csp1sin(\psi_1 - a_s)e'sp1(t) + \sum csp1sin(\psi_1 - a_s)E's1(t) - \sum csp1sin(\psi_1 - a_s)E'sp1(t) + SP_{rp1} \sum crp1sin(\psi_1 + a_r)e'r1(t) + \sum crp1sin(\psi_1 + a_r)E'r1(t) - \sum crp1sin(\psi_1 + a_r)E'r1(t) + cpx(-\cos(u'c/OpOs + \psi_1/\ln1(lal))) + kpx(-\cos(uc/OpOs + \psi_1/\ln1(lal)) + OpOscos(\psi_1))$
$SP_{sp1} \sum csp1cos(\psi_1 - a_s)e'sp1(t) + \sum csp1cos(\psi_1 - a_s)E's1(t) - \sum csp1cos(\psi_1 - a_s)E'sp1(t) + SP_{rp1} \sum crp1cos(\psi_1 + a_r)e'r1(t) + \sum crp1cos(\psi_1 + a_r)E'r1(t) - \sum crp1cos(\psi_1 + a_r)E'r1(t) + cpy(\sin(u'c/OpOs + \psi_1/\ln1(lal))) + kpy(\sin(uc/OpOs + \psi_1/\ln1(lal)) - OpOssin(\psi_1))$
$SP_{sp1} \sum csp1e'sp1(t) + \sum csp1E's1(t) - \sum csp1E'sp1(t) - SP_{rp1} \sum crp1e'r1(t) - \sum crp1E'r1(t) + \sum crp1E'r1(t)$
$\sum cspnsin(\psi_n - a_s)e'spn(t) + \sum cspnsin(\psi_n - a_s)E'sn(t) - \sum cspnsin(\psi_n - a_s)E'spn(t) + \sum crpnsin(\psi_n + a_r)e'rpn(t) + \sum crpnsin(\psi_n + a_r)E'rn(t) - \sum crpnsin(\psi_n + a_r)E'rpn(t) + cpx(-\cos(u'c/OpOs + \psi_{ninitial})) + kpx(-\cos(uc/OpOs + \psi_{ninitial}) + OpOscos(\psi_n))$
$\sum cspncos(\psi_n - a_s)e'spn(t) + \sum cspncos(\psi_n - a_s)E'sn(t) - \sum cspncos(\psi_n - a_s)E'spn(t) + \sum crpncos(\psi_n + a_r)e'rpn(t) + \sum crpncos(\psi_n + a_r)E'rn(t) - \sum crpncos(\psi_n + a_r)E'rpn(t) + cpy(\sin(u'c/OpOs + \psi_{ninitial})) + kpy(\sin(uc/OpOs + \psi_{ninitial}) - OpOssin(\psi_n))$
$\sum cspne'spn(t) + \sum cspnE'sn(t) - \sum cspnE'spn(t) - \sum crpne'rpn(t) - \sum crpnE'rn(t) + \sum crpnE'rpn(t)$

(a)

Figure 3-18 Force vector containing (a)damping and (b) stiffness features respectively

$\sum -SPspikspi(t)\sin(\psi i-\alpha s)espi(t)-\sum SPspikspi(t)\sin(\psi i-\alpha s)Esi(t)+\sum SPspikspi(t)\sin(\psi i-\alpha s)Esp i(t)$
$\sum -SPspikspi(t)\cos(\psi i-\alpha s)espi(t)-\sum SPspikspi(t)\cos(\psi i-\alpha s)Esi(t)+\sum SPspikspi(t)\cos(\psi i-\alpha s)Esp i(t)$
$\sum -SPspikspi(t)espi(t)-\sum SPspikspi(t)Esi(t)+\sum SPspikspi(t)Esp i(t)+T_{ss}/r_s$
$\sum -SPrpikrpi(t)\sin(\psi i+\alpha r)erpi(t)-\sum SPrpikrpi(t)\sin(\psi i+\alpha r)Eri(t)+\sum SPrpikrpi(t)\sin(\psi i+\alpha r)Erp i(t)$
$\sum -SPrpikrpi(t)\cos(\psi i+\alpha r)erpi(t)-\sum SPrpikrpi(t)\cos(\psi i+\alpha r)Eri(t)+\sum SPrpikrpi(t)\cos(\psi i+\alpha r)Erp i(t)$
$\sum SPrpikrpi(t)erpi(t)+\sum SPrpikrpi(t)Eri(t)-\sum SPrpikrpi(t)Erp i(t)+T_{rb}/r_r$
$\sum -k_{px}Dtepcis\psi i+\sum k_{px}Drepcicos\psi i$
$\sum -k_{py}Drepcis\psi i-\sum k_{py}Dtepcicos\psi i$
$\sum -k_{py}Drepcis\psi i\cos\psi i-\sum k_{py}Dtepcicos\psi i\cos\psi i-T_c/r_c$
$\sum SPsp1ksp1(t)\sin(\psi 1-\alpha s)esp1(t)+\sum SPsp1ksp1(t)\sin(\psi 1-\alpha s)E s1(t)-\sum SPsp1ksp1(t)\sin(\psi 1-\alpha s)Esp1(t)+\sum SPrp1krp1(t)\sin(\psi 1+\alpha r)erp1(t)+\sum SPrp1krp1(t)\sin(\psi 1+\alpha r)Er1(t)-\sum SPrp1krp1(t)\sin(\psi 1+\alpha r)Erp1(t)+\sum k_{px}Dtepc1sin\psi 1-\sum k_{px}Drepc1cos\psi 1$
$\sum SPsp1ksp1(t)\cos(\psi 1-\alpha s)esp1(t)+\sum SPsp1ksp1(t)\cos(\psi 1-\alpha s)E s1(t)-\sum SPsp1ksp1(t)\cos(\psi 1-\alpha s)Esp1(t)+\sum SPrp1krp1(t)\cos(\psi 1+\alpha r)erp1(t)+\sum SPrp1krp1(t)\cos(\psi 1+\alpha r)Er1(t)-\sum SPrp1krp1(t)\cos(\psi 1+\alpha r)Erp1(t)+\sum k_{py}Drepc1sin\psi 1+\sum k_{py}Dtepc1cos\psi 1$
$\sum SPsp1ksp1(t)esp1(t)+\sum SPsp1ksp1(t)Es1(t)-\sum SPsp1ksp1(t)Esp1(t)-\sum SPrp1krp1(t)erp1(t)-\sum SPrp1krp1(t)Er1(t)+\sum SPrp1krp1(t)Erp1(t)$
$\sum SPspnkspn(t)\sin(\psi n-\alpha s)esp n(t)+\sum SPspnkspn(t)\sin(\psi n-\alpha s)Esn(t)-\sum SPspnkspn(t)\sin(\psi n-\alpha s)Espn(t)+\sum SPrp nkrpn(t)\sin(\psi n+\alpha r)erp n(t)+\sum SPrp nkrpn(t)\sin(\psi n+\alpha r)Ern(t)-\sum SPrp nkrpn(t)\sin(\psi n+\alpha r)Erpn(t)+\sum k_{px}Dtepcns\psi n-\sum k_{px}Drepcncos\psi n$
$\sum SPspnkspn(t)\cos(\psi n-\alpha s)esp n(t)+\sum SPspnkspn(t)\cos(\psi n-\alpha s)Esn(t)-\sum SPspnkspn(t)\cos(\psi n-\alpha s)Espn(t)+\sum SPrp nkrpn(t)\cos(\psi n+\alpha r)erp n(t)+\sum SPrp nkrpn(t)\cos(\psi n+\alpha r)Ern(t)-\sum SPrp nkrpn(t)\cos(\psi n+\alpha r)Erpn(t)+\sum k_{py}Drepcns\psi n+\sum k_{py}Dtepcncos\psi n$
$\sum SPspnkspn(t)esp n(t)+\sum SPspnkspn(t)Esn(t)-\sum SPspnkspn(t)Espn(t)-\sum SPrp nkrpn(t)erp n(t)-\sum SPrp nkrpn(t)Ern(t)+\sum SPrp nkrpn(t)Erpn(t)$

(b)

Figure 3-18(continued) Force vector containing (a)damping and (b) stiffness features respectively

	Sun gear Subscript s	Planet gears Subscript p	Ring gear Subscript r	Carrier arm Subscript c
Step 1 Lock all gears and carrier arm; Rotate all parts as one through a in CW	+a	+a	+a	+a
Step 2 Lock carrier arm; Rotate ring gear through b in CCW	$-b\left(\frac{Z_r}{Z_s}\right)$	$b\left(\frac{Z_r}{Z_p}\right)$	b	0
Step 3 Sum step 1 and step 2	$a+b\left(\frac{Z_r}{Z_s}\right)$ (CW)	$b\left(\frac{Z_r}{Z_p}\right)-a$ (CCW)	b-a (CCW)	a (CW)

Table 3-1 The Tabular Method for the planetary gear ratios

For the ring-planet pair,

$$\theta_p = \frac{u_p}{r_p} = b\left(\frac{Z_r}{Z_p}\right) \quad (3.41)$$

$$\theta_r^* = \frac{u_r^*}{r_r} = b - a \quad (3.42)$$

$$\theta_r = \frac{u_r}{r_r} = b \quad (3.43)$$

Solving Eqs 3.41 and 3.42, gives,

$$a = b - \frac{u_r^*}{r_r} = \frac{u_p}{r_p} \left(\frac{Z_p}{Z_r}\right) - \frac{u_r^*}{r_r} = \frac{u_p}{r_r} - \frac{u_r^*}{r_r} \quad (3.44)$$

$$\frac{u_c}{r_c} = \theta_c = a = \frac{u_p}{r_r} - \frac{u_r^*}{r_r} \quad (3.45)$$

For the sun and ring,

$$\theta_r^* = \frac{u_r^*}{r_r} = b - a \quad (3.46)$$

$$\theta_s^* = \frac{u_s^*}{r_s} = b\left(\frac{Z_r}{Z_s}\right) + a \quad (3.47)$$

$$\theta_r = \frac{u_r}{r_r} = b \quad (3.48)$$

$$\theta_s = \frac{u_s}{r_s} = b \left(\frac{Z_r}{Z_s} \right) \quad (3.49)$$

Solving Eqs 3.46 and 3.47, gives,

$$\frac{u_s^*}{r_s} = \left(\frac{u_r^*}{r_r} + a \right) \left(\frac{Z_r}{Z_s} \right) + a = \frac{u_r^*}{r_r} \frac{Z_r}{Z_s} + \left(\frac{Z_r}{Z_s} + 1 \right) a = \frac{u_r^*}{r_s} + \left(\frac{r_r}{r_s} + 1 \right) a \quad (3.50)$$

$$u_s^* = u_r^* + r_r a + r_s a \quad (3.51)$$

$$a = \frac{u_s^* - u_r^*}{r_r + r_s} \quad (3.52)$$

Substituting Eqs 3.52 and 3.46 into Eqs 4.48, gives,

$$u_r = \frac{u_r^*}{r_r} r_r = (b - a + a) r_r = \left(\frac{u_r^*}{r_r} + \frac{u_s^* - u_r^*}{r_r + r_s} \right) r_r = u_r^* + \frac{u_s^* - u_r^*}{r_r + r_s} r_r \quad (3.53)$$

Substituting Eqs 3.52 and 3.47 into Eqs 4.49, gives,

$$u_s = \frac{u_s^*}{r_s} r_s = \left(b \frac{Z_r}{Z_s} + a - a \right) r_s = \left(\frac{u_s^*}{r_s} - \frac{u_s^* - u_r^*}{r_r + r_s} \right) r_s = u_s^* - \frac{u_s^* - u_r^*}{r_r + r_s} r_s \quad (3.54)$$

For the planet displacement in the x and y directions,

$$\begin{aligned} x_{pi} &= x_{pi}^* - x_{pi-ideal} \\ &= x_{pi}^* - \left[-\cos \left(\frac{u_s^* - u_r^*}{r_r + r_s} + \theta_{original-planet-i} \right) r_c + \cos(\theta_{original-planet-i}) r_c \right] \end{aligned} \quad (3.55)$$

$$\begin{aligned} y_{pi} &= y_{pi}^* - y_{pi-ideal} \\ &= y_{pi}^* - \left[\sin \left(\frac{u_s^* - u_r^*}{r_r + r_s} + \theta_{original-planet-i} \right) r_c - \sin(\theta_{original-planet-i}) r_c \right] \end{aligned} \quad (3.56)$$

In this research, MATLAB programs were developed to generate and solve the dynamic equations of the overall system which was presented in Eq 3.41 with substitution of Eqs 3.53-56.

3.5. SUMMARY OF CHAPTER

In this chapter, a generalized lumped mass dynamic model of the single stage planetary gear set is developed based on Kahraman's model³⁷ with major modifications. The overall system is considered separately as three sub-systems, namely a sun gear - planet gear pair, a ring gear - planet gear pair and a carrier arm - planet gear pair. Each sub-system is isolated from the others and after equations of motion have been obtained for each sub-system, the overall equations are combined using matrix techniques. In the first two sub systems, the rigid gear bodies are connected by damping and stiffness along the gear mesh action line, which also simulates the combined gear error, run out functions and tooth separation phenomenon. In the third sub-system, planet gears are mounted on the carrier arm through the planet pin-bearing assembly which is simulated with introduced stiffness and damping features. The rotational motion of the planet gears is completely uncoupled from the carrier arm's motion. To combine the three sub-systems to form the overall equations of motion, four key terms (x_{pi}^* , y_{pi}^* , \ddot{u}_s^* , \ddot{u}_r^*) are defined and corresponding equations are developed (Section 3.4). By introducing these four terms the equations of motion for planet gears of two different rotations (one rotation is about sun gear centre, and another is about planet gear mounted point) can be combined.

The nomenclatures used in this chapter are given in the nomenclature list (pp.10-13 of this thesis). The matrix form of the overall equations of motion is developed and listed in Section 3.4.

The matrix form of the overall equations gives three advantages. First of all, adding and deleting any term in the sub-system equations can be done without difficulty and relative change can be made to the overall equations with convenience. Secondly, support flexibilities (such as shafts, bearings, and housing structures) can be combined into the overall equations on an overall scale rather than on a sub-system, which significantly simplifies the procedure to obtain both the overall and sub-system equations. Finally, every combination of torsional and /or transverse systems can be represented simply by deleting the relative rows and columns.

4. PITCH AND PROFILE EXCITATION

Transmission error, according to Harris⁴⁷ and Munro⁴⁸, is defined as a measure of departure from ideal (perfectly mounted rigid bodies with perfect geometry) motion transfer between the drive gear and pinion. Transmission error is one of the most important sources of vibration in geared systems and is usually due to the amplitude and phase deviations of the tooth profile from the true involute profile⁴⁹, as well as pitch, pressure angle and mounting (eccentricities and misalignments) errors.

In this research, transmission error is considered to be the primary feature that affects the vibration of planetary gear trains, and is further analyzed in this section. According to Ozguven and Houser⁵⁰, in high precision spur gears (which is the gear type in the planetary gear system studied in this research), the effect of pitch errors on the dynamic gear forces and stresses is not as important as the excitation due to mesh stiffness variation. For this reason, an approximate numerical approach is used to simulate the pitch errors for all the gear pairs. For the same reason and to simplify the overall equations, the same approach is used to simulate the gear profile errors. To reach a relatively accurate and realistic simulation of transmission error, a random (both amplitude and phase) impulse excitation is introduced into the simulation to represent the effect of impurity in lubrication of the meshing teeth. These three types of excitations are analyzed in section 4.1 for one spur gear pair. In order to simulate the excitations for the entire planetary gear system with n planet gears, the tooth meshing variation is introduced in section 4.2. The pitch, profile and random excitations of the planetary gear system are simulated and the numerical results are listed in section 4.3.

For the reason of simplification, the variations in pressure angle, mounting errors as well as tooth, gear body and supporting structure deformation are ignored for the simulation of transmission error in this research.

4.1. GEAR GEOMETRY ERRORS AND RANDOM EXCITATION FOR A SPUR GEAR PAIR

4.1.1. Pitch excitation of a spur gear pair

As analyzed in section 4, the theoretical pitch excitation model considers the spur gear pair (either sun gear - planet gear or ring gear - planet gear) as a single-degree-of-freedom lumped system shown in the simplified figure below (Figure 4-1). Each gear pair is represented by two rigid disks coupled along the line of action through a time varying mesh stiffness $k(t)$ and a time varying damping $c(t)$.

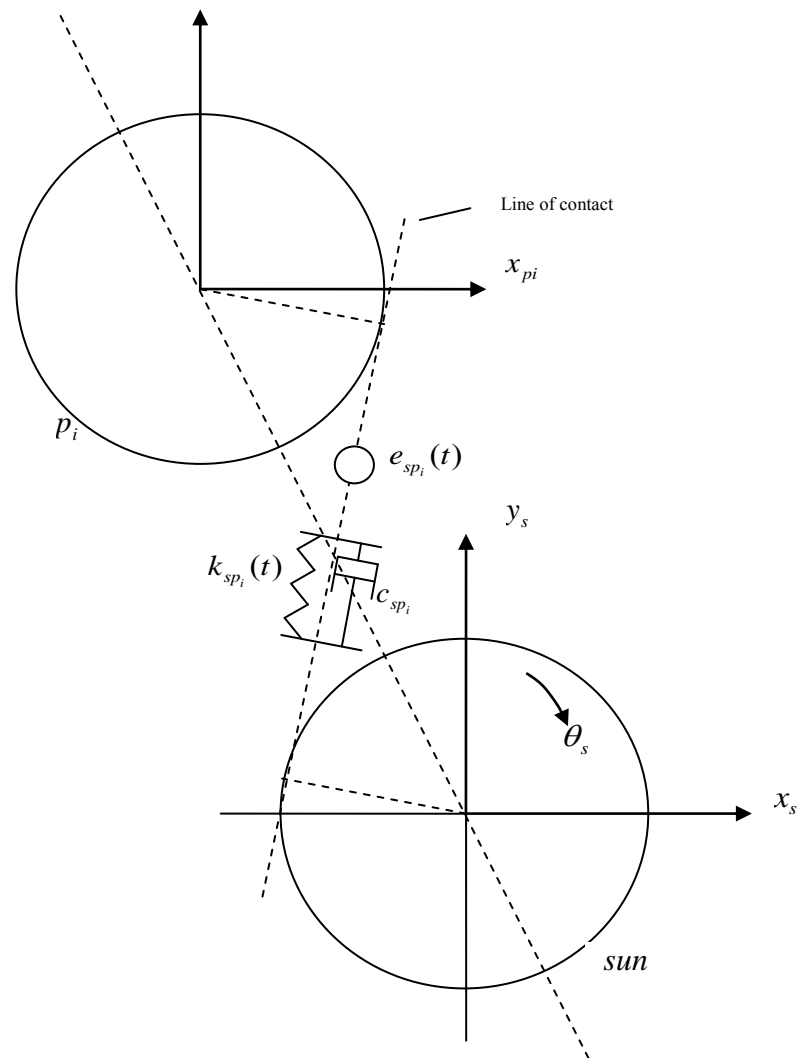


Figure 4-1 Torsional model of a spur gear pair (sun gear - planet gear, shown in this figure/ or ring gear - planet gear)

In this model, transmission errors are simulated by a displacement excitation at the mesh.

The pitch errors are simulated as a forcing function input into the model and are represented by a combination of an arbitrary number of harmonic terms as shown in Eqs 4.1^{51,52},

$$e_{pitch}(t) = \sum_{\substack{a=a \\ \alpha=1}}^{\substack{a=z \\ \alpha=26}} a \sin(\alpha * \theta_t) \quad (4.1)$$

where $e_{pitch}(t)$ denotes either pitch error of the sun gear, ring gear or planet gear; „a“ denotes the coefficient of pitch error amplitude, with a sum of all the coefficients from a to z less than 10 μm (the effect of geometrical error amplitude has been investigated by S. Jia, et al.⁵³); corresponding to coefficient „a“, coefficient α has values from 1 to 26 (with 26 values for coefficient „a“, from „a“ to „z“); θ_t denotes the number of teeth that have meshed (with a decimal form).

A typical numerical result of planet gear (32 teeth) pitch error is shown in Figure 4-2.

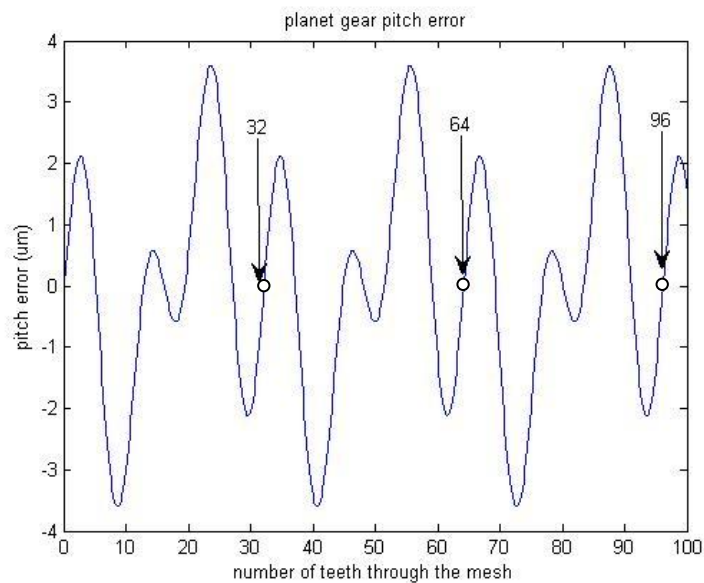


Figure 4-2 Planet gear pitch error (detailed program in Sec 7.4.4.1)

Figure 4-2 shows that the curve of the simulated planet gear pitch error is repeated once the planet gear rotates one revolution (32 teeth). The result shown in Figure 4-2 is based on Eqs 4.1 with three harmonics.

The numerical results of ring gear (83 teeth) pitch error is shown in Figure 4-3.

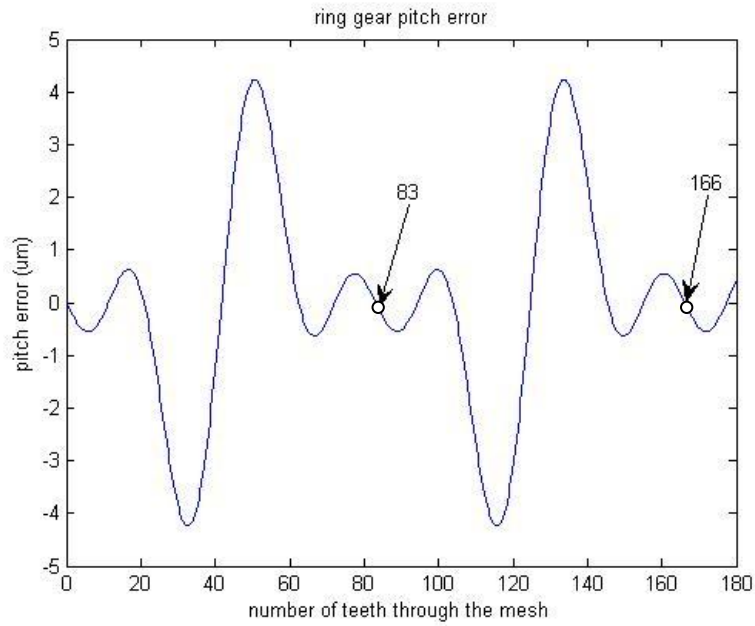


Figure 4-3 Ring gear pitch error (detailed program in Sec 7.4.4.2)

Figure 4-3 shows that the curve of the simulated ring gear pitch error is repeated once the ring gear rotates one revolution (83 teeth). The result shown in Figure 4-3 is also based on Eqs 4.1 with three harmonics.

The numerical results of sun gear (19 teeth) pitch error is shown in Figure 4-4.

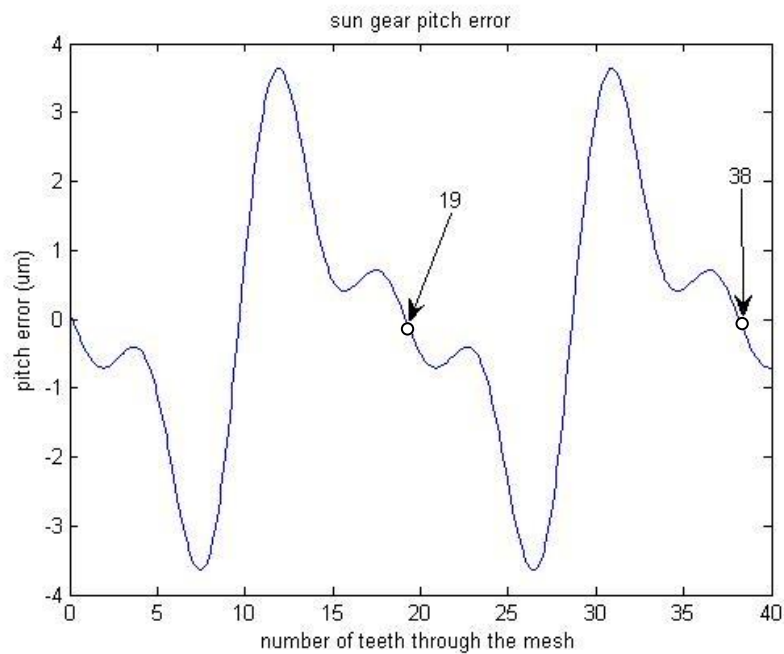


Figure 4-4 Sun gear pitch error (detailed program in Sec 7.4.4.3)

Figure 4-4 shows that the curve of the simulated sun gear pitch error is repeated once

the sun gear rotates one revolution (19 teeth). The result shown in Figure 4-4 is also based on Eqs 4.1 with three harmonics.

4.1.2. Profile excitation of a spur gear pair

All processes used in manufacturing gears cannot avoid the gears having deviation from the theoretical gear profile shown in Figure 4-5.

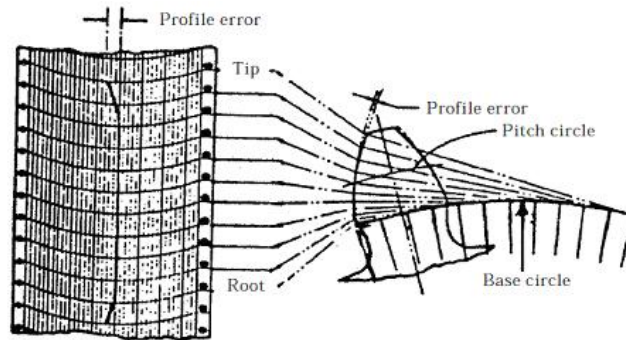


Figure 4-5 Relation between the profile error chart and the involute tooth profile⁵⁴

When two teeth are in mesh the profile error can be seen as in Figure 4-6.

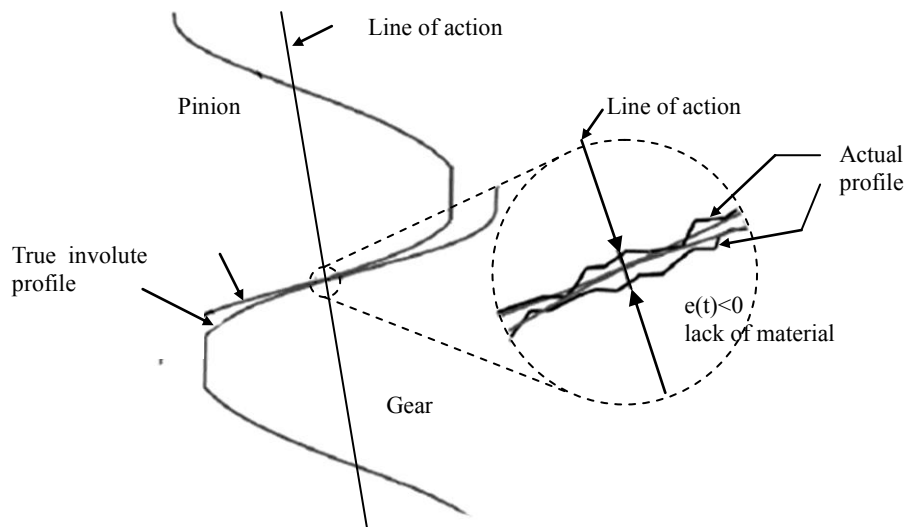


Figure 4-6 Profile error along the action line by reference⁵⁵

From Figure 4.6, it can be seen that the profile error of the pair of meshing teeth is the geometrical sum of the geometrical profile error of each of the two gears in mesh. In this research, an equation having the same structure as Eqs 4.1 is used to represent the profile error of one gear pair, shown in Eqs 4.2,

$$e_{profile}(t) = \sum_{\substack{a=a \\ \alpha=1}}^{\substack{a=z \\ \alpha=26}} a \sin(\alpha * \theta_t) \quad (4.2)$$

where $e_{profile}(t)$ denotes either profile error of the sun gear - planet gear mesh or the ring gear - planet gear mesh; „a“ denotes the coefficient of profile error amplitude, with a sum of all the coefficients from a to z less than $10 \mu m$ (the effect of geometrical error amplitude has been investigated by S. Jia, et al.⁵³); corresponding to coefficient „a“, coefficient α has values from 1 to 26 (with 26 values for coefficient „a“, from „a“ to „z“); θ_i denotes the number of teeth that have meshed (with a decimal form). This solution is suitable to model spur gear pairs having low contact ratio equal to 1 only; the solution suitable to model spur gear pairs with realistic contact ratio (>1) is examined in section 4.3.

The numerical results of an example sun gear - planet gear mesh profile error is shown in Figure 4-7.

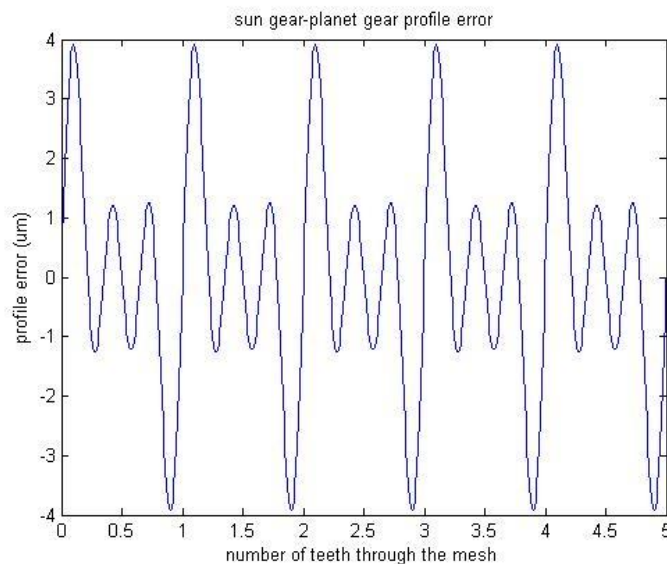


Figure 4-7 Sun gear - planet gear pair profile error (assumed contact ratio equal to 1)

Figure 4-7 shows that the curve of the simulated sun gear - planet gear pair profile error is repeated once for each new pair of teeth in mesh (assumed contact ratio equal to 1). The result shown in Figure 4-7 is based on Eqs 4.2 with three harmonics.

The numerical results of an example ring gear - planet gear mesh profile error is shown in Figure 4-8. Figure 4-8 shows that the curve of the simulated ring gear - planet gear pair profile error is repeated once for each new pair of teeth in mesh (assumed contact ratio equal to 1). The result shown in Figure 4-8 is again based on Eqs 4.2 with three harmonics.

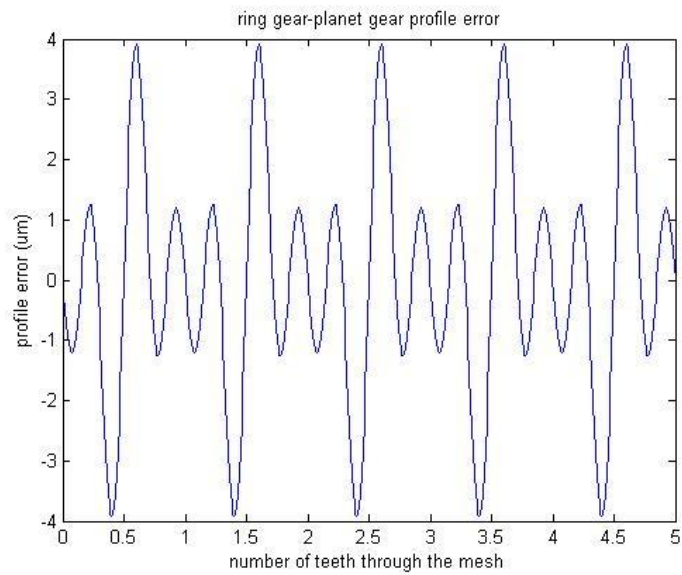


Figure 4-8 Ring gear - planet gear pair profile error (assumed contact ratio equal to 1)

4.1.3. Random excitation

In order to simulate the effect of impurities in lubrication and random impulses due to variation in the damaged tooth surface, a random (both amplitude and phase) impulse excitation is introduced in this section.

A random impulse excitation can be simulated as shown in Figure 4-9.

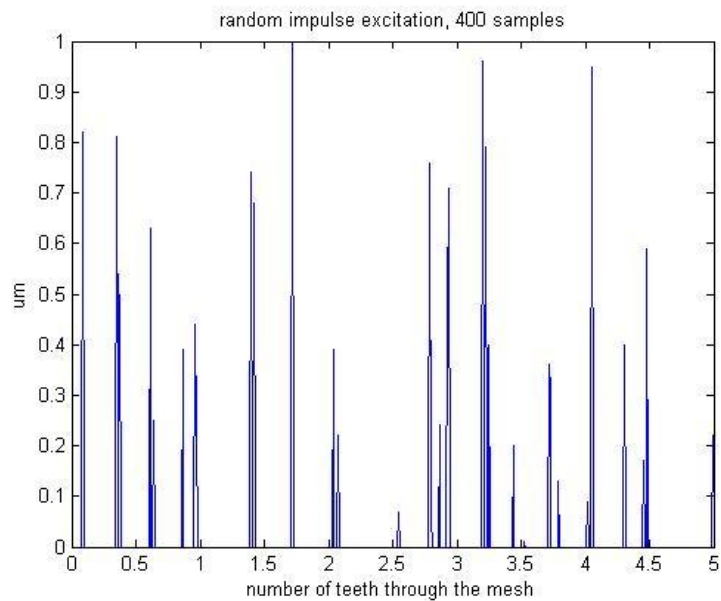


Figure 4-9 Random impulse excitation (400 samples) (detailed program in Sec 7.4.4.6)

4.2. TOOTH MESHING VARIATION

Planetary gear systems have multiple tooth meshes and those meshes have varying numbers of teeth in contact when the gears are in operation. As all the planet gears are generally under the same dynamic motion against the sun gear and ring gear, the numbers of teeth in contact all vary at the same frequency⁵⁶.

The time variations of numbers of teeth in contact at the multiple sun gear - planet gear meshes have an identical shape and same periodicity, however, the time variation of each pair generally have different phases. With the matching phase delays between pairs, the time variations of numbers of teeth in contact at the multiple ring gear - planet gear meshes also have an identical shape and same periodicity. The shape and periodicity functions for the multiple ring gear - planet gear meshes are different from the sun gear - planet gear meshes.

The phasing relationships analyzed in this research are based on the same method as in that by Parker and Lin⁵⁶ where variation functions of numbers of teeth in contact were introduced. In this section, functions $Y_{mrn}(X_{mr})$ and $Y_{msn}(X_{ms})$ represent the numbers of teeth in contact at the n th sun gear - planet gear and ring gear - planet gear meshes with zero load. The numerical values of $Y_{mrn}(X_{mr})$ and $Y_{msn}(X_{ms})$ are integers only. In the functions, X_{mr} and X_{ms} denote the number of mesh cycles in the sun gear - planet gear and ring gear - planet gear meshes respectively.

The development of equations representing the mesh phasing variation is shown in Table 4-1.

Symbol	Meaning	Equation	Value in this research
p_n	An integer that varies for each planet	--	0; 34; 68
z_r	Ring gear teeth number	--	83
z_s	Sun gear teeth number	--	19

Table 4-1 Development of equations representing mesh phasing variation

Symbol	Meaning	Equation	Value in this research
ψ_n	Circumferential angle of planets measured positive counter-clockwise	$\psi_n = P_n \frac{2\pi}{z_r + z_s}$	$0; \frac{2\pi}{3}; \frac{4\pi}{3}$
$rsn(1)$	Arbitrarily chosen first sun gear - planet gear mesh	0	0
$rsn(n)$	Relative phase between the n th sun gear - planet gear mesh and the arbitrarily chosen first sun gear - planet gear mesh (within the form of decimal less than 1)	$rsn(n) = -\frac{z_s \psi_n}{2\pi}$	$0; -\frac{1}{3}; -\frac{2}{3}$
$rrn(1)$	Arbitrarily chosen first ring gear - planet gear mesh	0	0
$rrn(n)$	Relative phase between the n th ring gear - planet gear mesh and the arbitrarily chosen first ring gear - planet gear mesh (within the form of decimal less than 1)	$rrn(n) = \frac{z_r \psi_n}{2\pi}$	$0; -\frac{1}{3}; -\frac{2}{3}$ or $0; \frac{2}{3}; \frac{1}{3}$

Table 4-1(continued) Development of equations representing mesh phasing variation

Figure 4-10 shows the mesh phasing variation of the sun gear - planet gear mesh, with $rsn(1)=0$ and $time=0$ corresponding to the pitch point contact at the first sun gear - planet gear mesh. The symbol „o“ denotes pitch point contact. The mesh phasing variation is based on the time variation of numbers of teeth in contact which differ from 1 to 2 (integers only) for all three sun gear - planet gear pairs. These variations of all three pairs have an identical shape and same periodicity with phase differences rsn between each other. Figure 4-11 shows the mesh phasing variation of the ring gear - planet gear mesh, with $rrn(1)=0$ and $time=0$ corresponding to the pitch point contact at the third ring gear - planet gear mesh. The mesh phasing variation is also based on the time variation of numbers of teeth in contact. The ring gear - planet gear mesh has higher contact ratio than sun gear - planet gear mesh. Numbers of teeth in contact differ from 2 to 3 (integers only) for all three ring gear - planet gear pairs. These variations of all three pairs also have an identical shape and same periodicity with phase differences rrn between each other. It should be noticed that $rsn(i)$ equals $rrn(i)$ for $i = 1,2,3$.

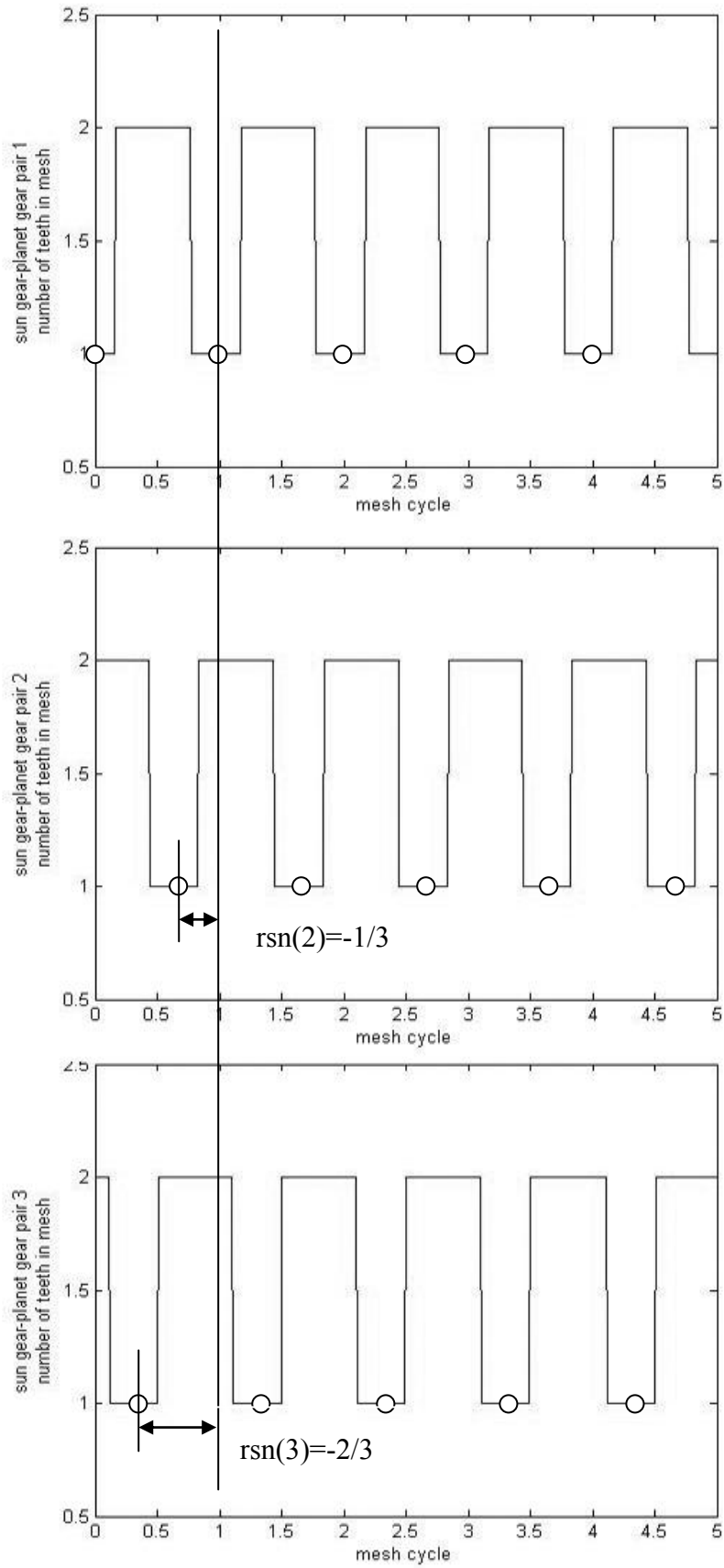


Figure 4-10 Mesh phasing variation of sun gear - planet gear meshes (top figure, mesh 1; middle figure, mesh 2; bottom figure, mesh 3)

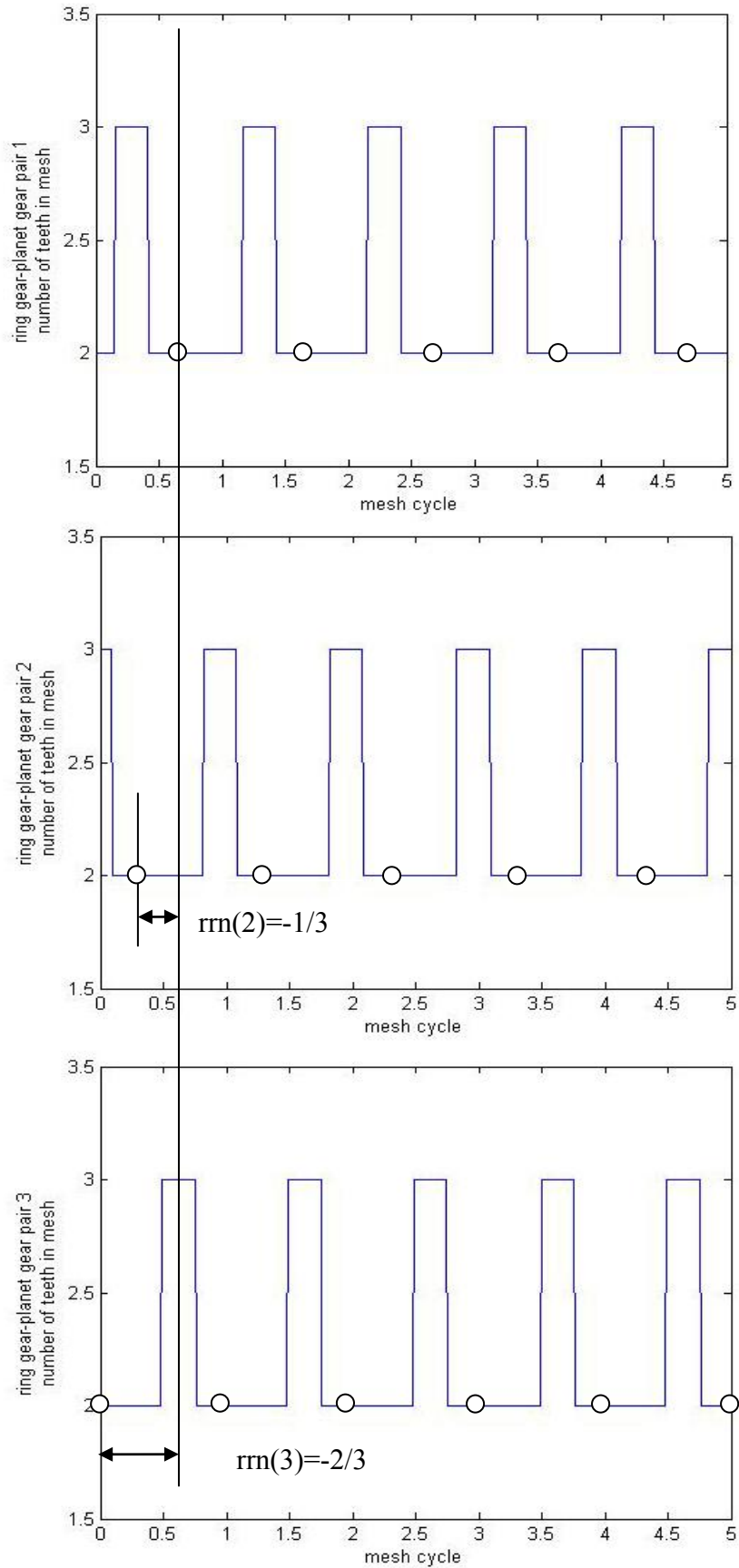


Figure 4-11 Mesh phasing variation of ring gear - planet gear meshes (top figure, mesh 1; middle figure, mesh 2; bottom figure, mesh 3)

In order to calculate the phase difference between the sun gear - planet gear mesh and the ring gear - planet gear mesh and to form the shape of each teeth mesh variation, a detailed mesh figure can be drafted as shown in Figure 4-12.

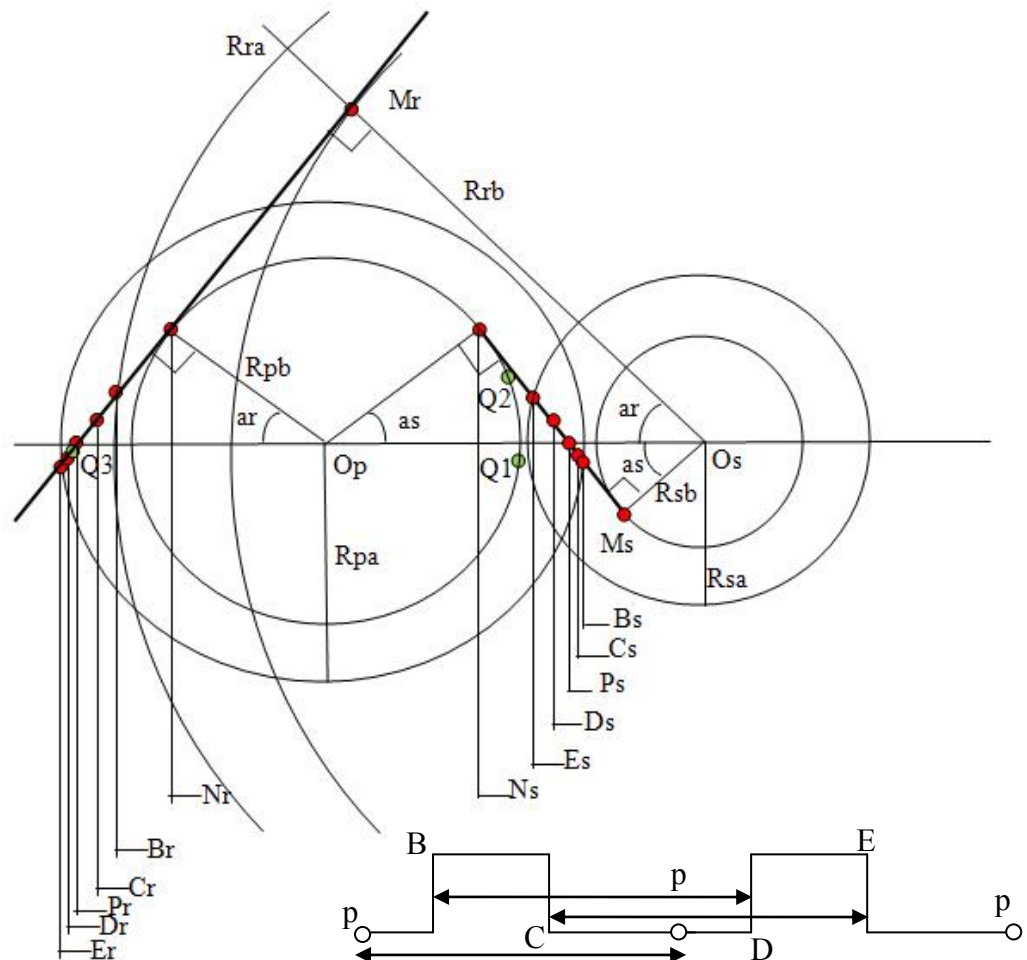


Figure 4-12 Detailed mesh representative of the planetary gear system

A description of symbols contained in Figure 4-12 and the corresponding gear mesh parameters are listed in Table 4-2.

Symbol	Meaning	Equation	Value
O_s	Origin of sun gear	--	--
z_s	Sun gear teeth number	--	19
α_s	Pressure angle	--	20°
m	Module	--	16
p	Circular pitch	$p = \pi m$	50.2655 mm

Table 4-2 Symbols contained in Figure 4-12 and the corresponding gear mesh parameters

Symbol	Meaning	Equation	Value
d_s	Pitch diameter of sun gear	$d_s = mz_s$	304 mm
h_{sa}	Tooth addendum height of sun gear	$h_{sa} = h_a^* m, h_a^* = 1$	16 mm
h_{sf}	Tooth dedendum height of sun gear	$h_{sf} = (h_a^* + c^*) m$; $c^* = 0.25$	20 mm
h_s	Tooth height of sun gear	$h_s = h_{sa} + h_{sf}$	36 mm
c_s	Tooth tip clearance of sun gear	$c_s = c^* m$	4 mm
R_{sa}	Addendum circle diameter of sun gear	$R_{sa} = \frac{d_s + 2^* h_{sa}}{2}$	168 mm
R_{sf}	Root circle radius of sun gear	$R_{sf} = \frac{d_s - 2^* h_{sf}}{2}$	132 mm
R_{sb}	Base circle radius of sun gear	$R_{sb} = d_s \cos \alpha_s$	142.8333 mm
O_p	Origin of planet gear	--	--
z_p	Planet gear teeth number	--	32
α_p	Pressure angle	--	20°
d_p	Pitch diameter of planet gear	$d_p = mz_p$	512 mm
h_{pa}	Tooth addendum height of planet gear	$h_{pa} = h_a^* m, h_a^* = 1$	16 mm
h_{pf}	Tooth dedendum height of planet gear	$h_{pf} = (h_a^* + c^*) m$; $c^* = 0.25$	20 mm
h_p	Tooth height of planet gear	$h_p = h_{pa} + h_{pf}$	36 mm
c_p	Tooth tip clearance of planet gear	$c_p = c^* m$	4 mm
R_{pa}	Addendum circle diameter of planet gear	$R_{pa} = \frac{d_p + 2^* h_{pa}}{2}$	272 mm
R_{pf}	Root circle radius of planet gear	$R_{pf} = \frac{d_p - 2^* h_{pf}}{2}$	236 mm
R_{pb}	Base circle radius of planet gear	$R_{pb} = d_p \cos \alpha_p$	240.5613 mm
z_r	Ring gear teeth number	--	83
α_r	Pressure angle	--	20°
d_r	Pitch diameter of ring gear	$d_r = mz_r$	1328 mm
h_{ra}	Tooth addendum height of ring gear	$h_{ra} = h_a^* m, h_a^* = 1$	16 mm

Table 4-2 (continued) Symbols contained in Figure 4-12 and the corresponding gear mesh parameters

Symbol	Meaning	Equation	Value
h_{rf}	Tooth dedendum height of ring gear	$h_{rf} = (h_a^* + c^*)m$ $c^* = 0.25$	20 mm
h_r	Tooth height of ring gear	$h_r = h_{ra} + h_{rf}$	36 mm
c_r	Tooth tip clearance of ring gear	$c_r = c^* m$	4 mm
R_{ra}	Addendum circle diameter of ring gear	$R_{ra} = \frac{d_r + 2^* h_{ra}}{2}$	680 mm
R_{rf}	Root circle radius of ring gear	$R_{rf} = \frac{d_r - 2^* h_{rf}}{2}$	644 mm
R_{rb}	Base circle radius of ring gear	$R_{rb} = d_r \cos \alpha_r$	623.9559 mm
B	Point, where second tooth enters contact	--	--
C	Point, where first tooth exits contact	--	--
P	Point, where second tooth at pitch point	--	--
D	Point, where third tooth enters contact	--	--
E	Point, where second tooth exits contact	--	--
$M_s E_s$	Length, shown in Figure 4-12	$M_s E_s = \sqrt{R_{sa}^2 - R_{sb}^2}$	88.4458 mm
$B_s N_s$	Length, shown in Figure 4-12	$B_s N_s = \sqrt{R_{pa}^2 - R_{pb}^2}$	126.9419 mm
$M_s N_s$	Length, shown in Figure 4-12	$M_s N_s = (R_{sb} + R_{pb}) \tan \alpha_s$	139.5442 mm
$B_s E_s$	Length, shown in Figure 4-12	$B_s E_s = M_s E_s + B_s N_s - M_s N_s$	75.8435 mm
$M_s P_s$	Length, shown in Figure 4-12	$M_s P_s = R_{sb} \tan \alpha_s$	51.9871 mm
$M_s B_s$	Length, shown in Figure 4-12	$M_s B_s = \sqrt{R_{sa}^2 - R_{sb}^2} - B_s E_s$	12.6023 mm
$B_s P_s$	Length, shown in Figure 4-12	$B_s P_s = M_s P_s - M_s B_s$	39.3848 mm
p_{sb}	Base pitch	$p_{sb} = p \cos \alpha_s$	47.2341 mm
$B_s C_s$	Length, shown in Figure 4-12	$B_s C_s = B_s E_s - p_{sb}$	28.6094 mm
$B_s D_s$	Length, shown in Figure 4-12	$B_s D_s = p_{sb}$	47.2341 mm

Table 4-2 (continued) Symbols contained in Figure 4-12 and the corresponding gear mesh parameters

Symbol	Meaning	Equation	Value in this research
$M_r N_r$	Length, shown in Figure 4-12	$M_r N_r = O_s O_p * \sin \alpha_r$	139.5442 mm
$N_r E_r$	Length, shown in Figure 4-12	$N_r E_r = \sqrt{R_{pa}^2 - R_{pb}^2}$	126.9419 mm
$M_r B_r$	Length, shown in Figure 4-12	$M_r B_r = \sqrt{R_{ra}^2 - R_{rb}^2}$	159.4209 mm
$B_r E_r$	Length, shown in Figure 4-12	$B_r E_r = M_r N_r + N_r E_r - M_r B_r$	107.0652 mm
$M_r P_r$	Length, shown in Figure 4-12	$M_r P_r = R_{rb} \tan \alpha_r$	227.1014 mm
$B_r P_r$	Length, shown in Figure 4-12	$M_r P_r = M_r P_r - M_r B_r$	67.6804 mm
p_{rb}	Base pitch	$p_{rb} = p \cos \alpha_r$	47.2341 mm
$B_r C_r$	Length, shown in Figure 4-12	$B_r C_r = B_r E_r - p_{rb}$	107.0180 mm
$B_r D_r$	Length, shown in Figure 4-12	$B_r D_r = p_{rb}$	47.2341 mm
Q_1	Image of P_s when the contact line $M_s N_s$ is wrapped on the planet base circle	--	--
tb	Planet tooth thickness at the base circle	$tb = m * (\pi / 2 + 2 / \alpha_s)$	26.7327 mm
Q_2	Point, an arc-length tb away from Q_1	--	--
Q_3	Point, the first point in the ring gear - planet gear contact region $B_r E_r$ that is an integer number of base pitches away from Q_2	--	--
$P_s P_r$	Length, shown in Figure 4-12	$P_s P_r = R_{pb} \tan \alpha_s + R_{pb} (\pi - \alpha_s - \alpha_r) + R_{pb} \tan \alpha_r$	762.9 mm
$Q_2 B_r$	Length, shown in Figure 4-12	$Q_2 B_r = P_s P_r - B_r P_r - tb$	668.5 mm
$B_r Q_3$	Length, shown in Figure 4-12	$B_r Q_3 = p_{rb} - p_{rb} [\text{dec}(Q_2 B_r / p_{rb})]$	40 mm
$P_r Q_3$	Length, shown in Figure 4-12	$P_r Q_3 = B_r Q_3 - B_r P_r $	27.6804 mm
rrs	Phase difference between sun gear - planet gear mesh and ring gear - planet gear mesh;	$ rrs = P_r Q_3 / p_{rb}$	0.5859 mesh circle

Table 4-2 (continued) Symbols contained in Figure 4-12 and the corresponding gear mesh parameters

As calculated in Table 4-2, the shape of functions $Ymrn(Xmr)$ and $Ymsn(Xms)$ are

fully defined by terms B_sE_s , B_sP_s , B_sC_s , B_sD_s , B_rE_r , B_rP_r , B_rC_r , and B_rD_r .

The mesh phasing variation analysis is completed with the phase difference rrs . To determine the sign of rrs , Table 4-3 is used.

Ring gear - planet gear contact progression	$rrs < 0$	$rrs > 0$
From B_r to E_r	From B_r to P_r to Q_r to E_r	From B_r to Q_r to P_r to E_r
From E_r to B_r	From E_r to P_r to Q_r to B_r	From E_r to Q_r to P_r to B_r

Table 4-3 Determining the sign of rrs ⁵⁶

Figure 4-13 shows the phase difference between sun gear - planet gear mesh and ring gear - planet gear mesh rrs .

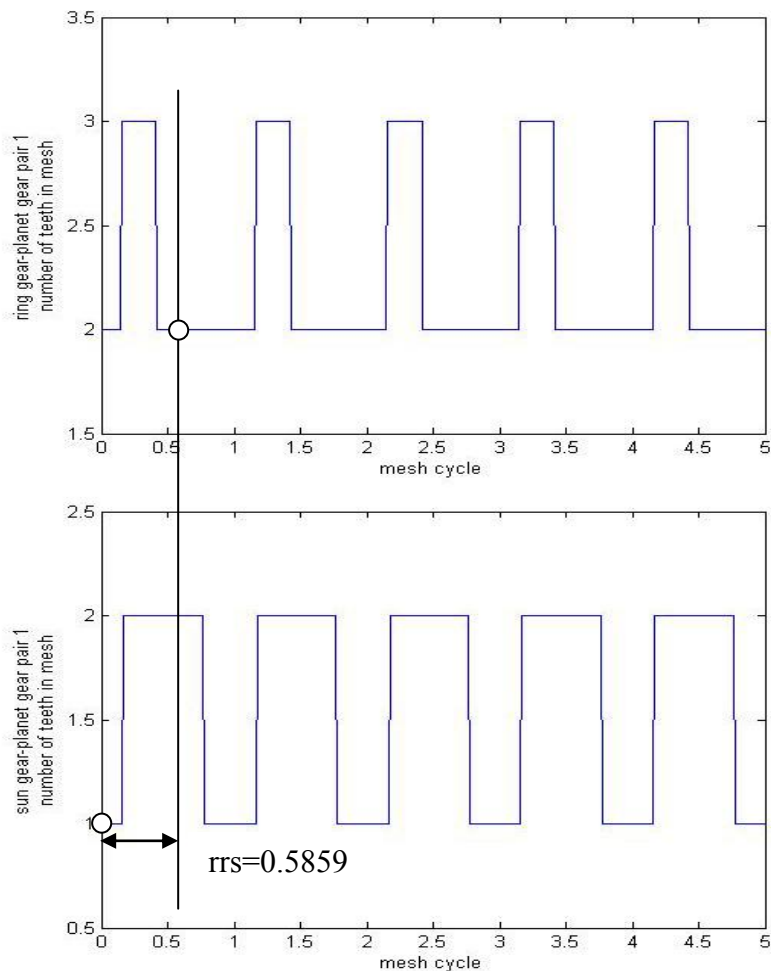


Figure 4-13 Phase difference between sun gear - planet gear mesh and ring gear - planet gear mesh

4.3. SIMULATION OF PITCH AND PROFILE EXCITATION WITH RANDOM IMPULSE FOR PLANETARY GEAR SYSTEMS

As defined in section 4.1, a numerical model for assumed contact ratio spur gear pair was introduced and two pitch and profile simulations were carried out as shown in Figure 4-7 and Figure 4-8. However this model is not suitable for gear pairs having a contact ratio greater than 1, such as the sun gear - planet gear pairs and ring gear - planet gear pairs in this research. To solve this problem, the combination of techniques introduced in section 4.1 and section 4.2 must be made.

As shown in Figure 4-10, also detailed in Figure 4-14, the second pair of teeth enters contact at approximate 0.2 mesh circle and exits contact at approximate 1.8 mesh circle. Approximately 0.4 mesh circle after the first gear pair exits contact (at 0.8 mesh circle) the third gear pair enters contact (at 1.2 mesh circle). Therefore during the mesh circle between 1.2 and 1.8, there are two gear pairs in contact (second pair and third pair). This periodicity repeats in the entire sun gear - planet gear mesh. The same occurs to the ring gear - planet gear pair as shown in Figure 4-11 where the number of gear pairs in mesh differs from two to three.

As defined in section 4.1, every tooth mesh has some profile error and as generally caused by the method of manufacture, an identical profile error can occur with all the meshes in the same gear pair. When only one pair of teeth is in mesh, the profile error carried by this pair of teeth solely (with other errors rather than tooth profile error) affects the dynamic motion of the transmission. When two (shown in Figure 4-10) or more pair (shown in Figure 4-11) of teeth are in mesh, the profile errors of each gear pair will interfere with each other as shown in Figure 4-15. In Figure 4-15, the different contact areas of two meshing gear pairs have unequal profile errors.

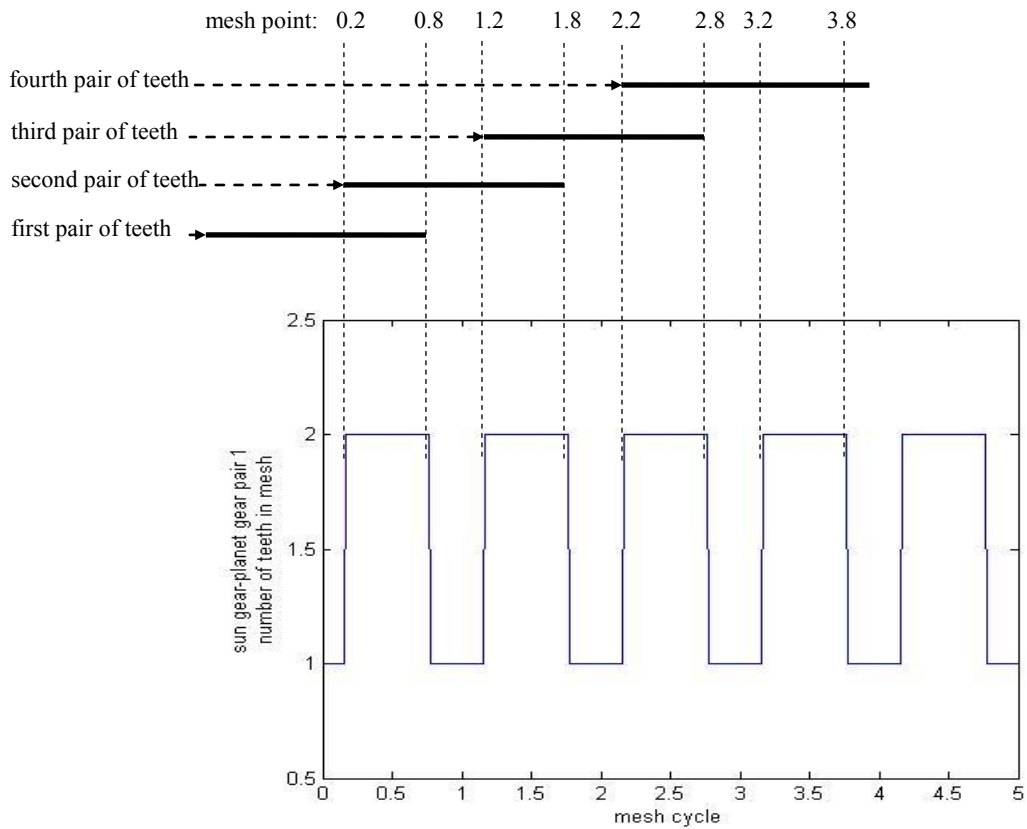


Figure 4-14 Number of teeth in mesh, the 1st sun gear - planet gear pair

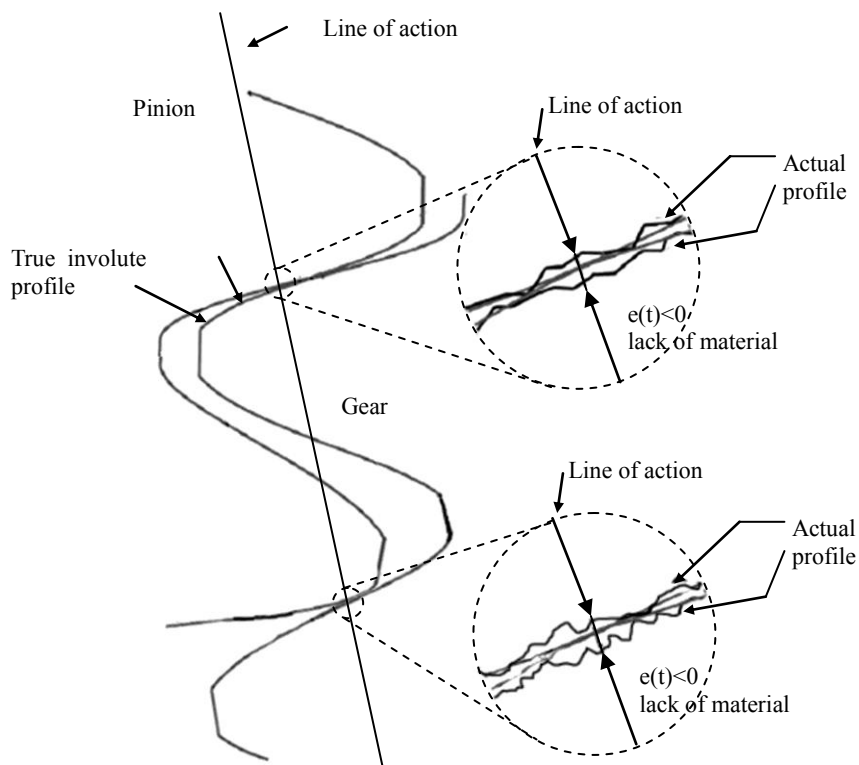


Figure 4-15 Profile error along the action line, two pairs of teeth in contact

In this research, the geometric sum of different profile errors is used when a number of profile errors exist at the same time when more than one pair of teeth are in contact. The combined profile error will have the same value as the largest amount of excess material (positive profile error) or smallest amount of reduction of material (negative profile error); in another words, the combined profile error has the same value as the largest numerical value among all the profile errors when they occur at the same time.

The numerical results of the sun gear - planet gear mesh profile error (with same profile error values of each pair of teeth to those shown in Figure 4-7) are shown in Figure 4-16.

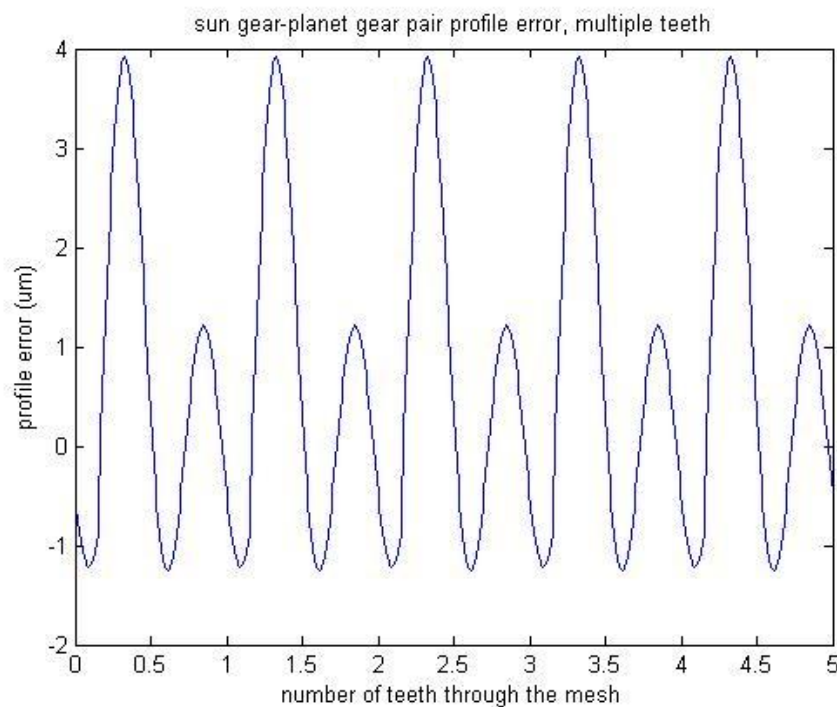


Figure 4-16 Sun gear - planet gear pair profile error with consideration of tooth meshing variation, first pair

The numerical results of the ring gear - planet gear mesh profile error (with same profile error values of each pair of teeth to those shown in Figure 4-8) are shown in Figure 4-17.

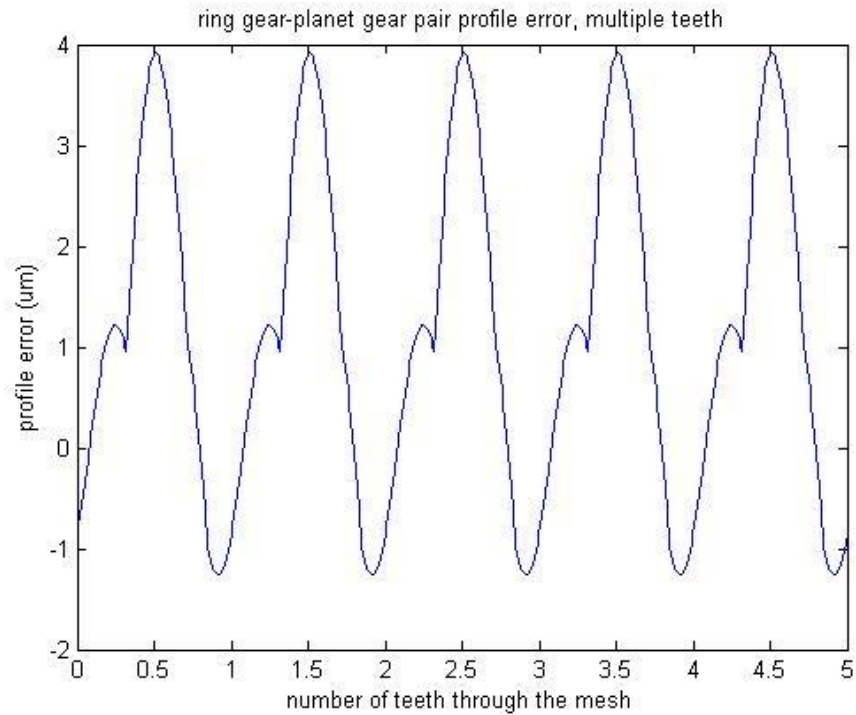
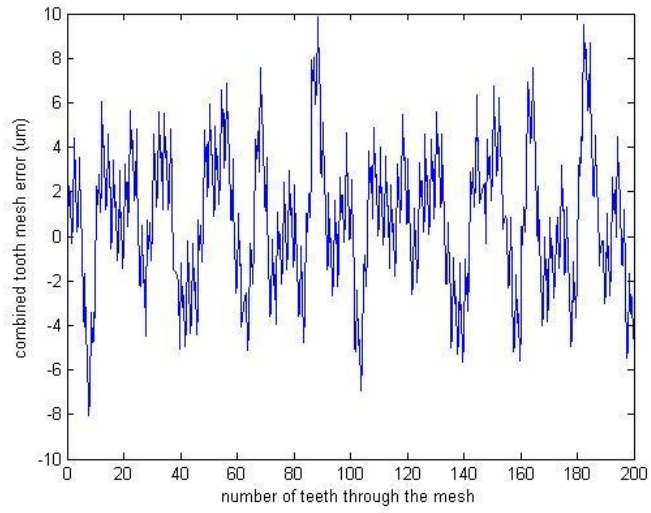


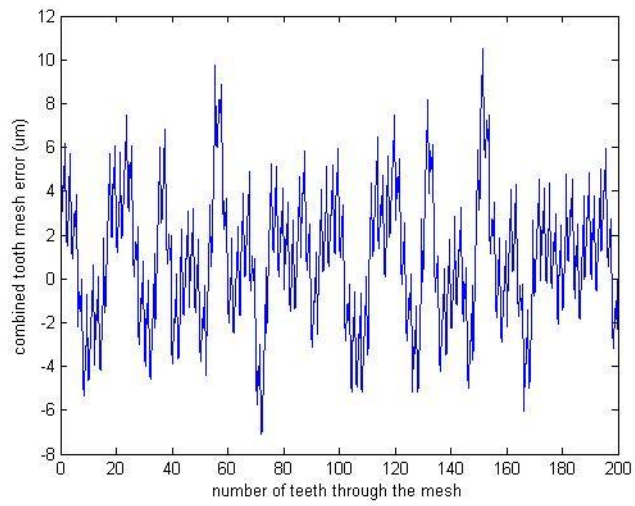
Figure 4-17 Ring gear - planet gear pair profile error with consideration of tooth meshing variation, first pair

To obtain the combined sum of the pitch errors (both sun gear pitch error and planet gear pitch error; or both ring gear pitch error and planet gear pitch error), profile errors (sun gear - planet gear pair profile error or ring gear - planet gear pair profile error) and random impulse excitation, the simple numerical sum is used.

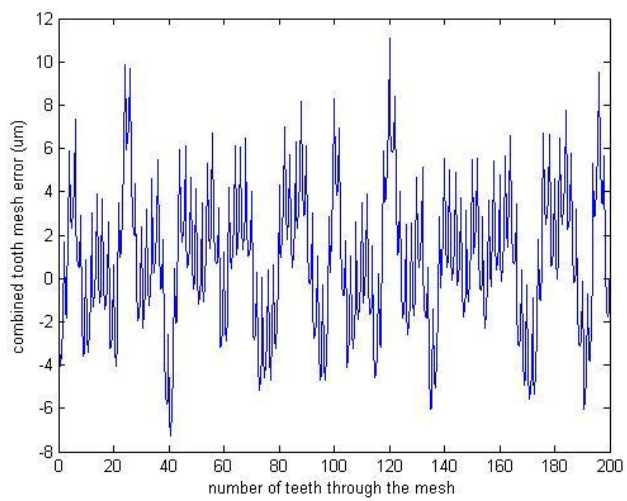
The combined tooth mesh error is shown in Figure 4-18 for sun gear - planet gear pairs and in Figure 4-19 for ring gear - planet gear pairs respectively.



(a)

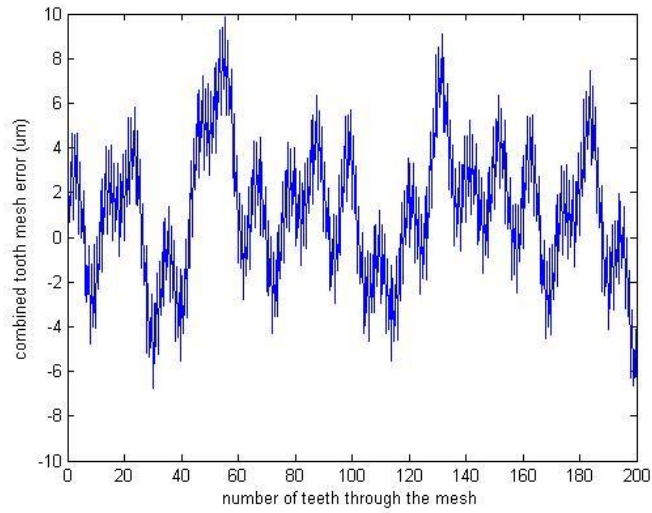


(b)

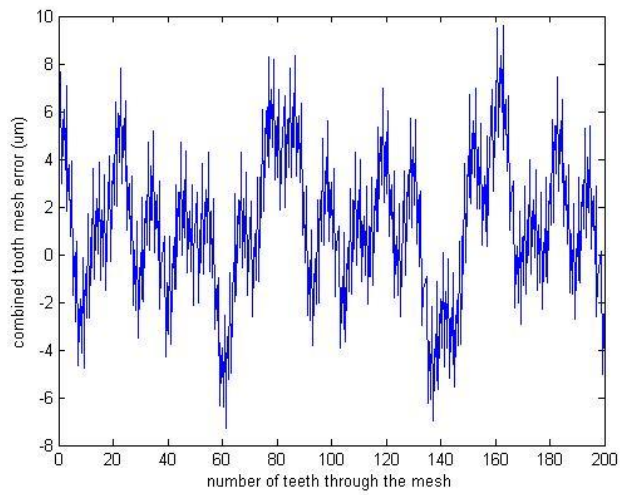


(c)

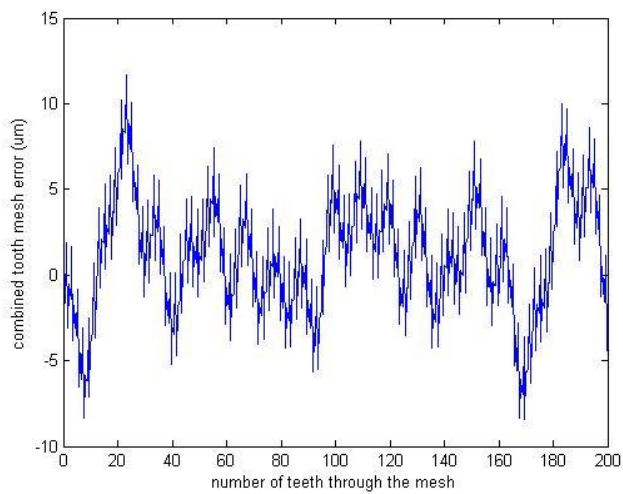
Figure 4-18 Combined gear error excitation for sun gear - planet gear pairs; (a) for first pair; (b) for second pair; (c) for third pair;



(a)



(b)



(c)

Figure 4-19 Combined gear error excitation for ring gear - planet gear pairs; (1) for first pair; (2) for second pair; (3) for third pair;

4.4. SUMMARY OF CHAPTER

For a simplified simulation of gear transmission error, only pitch and profile excitations with random pulses are developed in this thesis.

Both pitch and profile errors are simulated as a forcing function input into the gear dynamic model by a combination of an arbitrary number (3, for numerical simulation) of harmonic terms in the case of single teeth pair in mesh and contact ratio assumed to be one at all time (detailed equation: Eq 4.1 and Eq 4.2).

When more than one pair of teeth are in mesh (contact ratio is greater than one), a method is used to sum the total profile errors as it will have the same value as the largest amount of excess material (positive profile error) or smallest amount of reduction of material (negative profile error).

Tooth mesh variation is analyzed in terms of time variation of number of teeth in mesh. The pitch and profile excitations of the multiple gear pairs in the planetary gear set are simulated with introduced random pulses.

5. TOOTH MESH STIFFNESS ANALYSIS

5.1. COMBINED TORSIONAL MESH STIFFNESS OF MESHING GEARS

Based on the method used by Sirichai⁵⁷ and Wang⁵⁸, the combined torsional mesh stiffness was defined by Jia, Howard and Wang³⁹ as the ratio of the torque applied to the pinion and the relative angular rotation between the pinion and the gear shaft circles. There is no contribution to the combined torsional mesh stiffness from the relative angular rotation or displacement of both shafts as they are considered separately in the dynamic system.

In this research, the common formulation of combined torsional mesh stiffness developed in Jia's work⁴⁰ is used with modifications. The development is briefly shown as follows.

When two gears are in mesh, the contact force between meshing teeth applies a torque T to both of the gears and a resulting angular displacement will occur if the gears are not assumed perfectly rigid. The angular displacements can be expressed as,

$$\theta_p = \frac{T_p}{K_p} \quad (5.1)$$

$$\theta_g = \frac{T_g}{K_g} \quad (5.2)$$

The transmission ratio of the meshing gears is defined as,

$$Tratio = \frac{Z_g}{Z_p} \quad (5.3)$$

Therefore the total displacement referenced to the pinion is,

$$\theta = \theta_p + \theta_g \frac{Z_g}{Z_p} \quad (5.4)$$

The torque applied to the gear can be expressed in terms of the torque applied to the pinion as,

$$T_g = T_p \frac{Z_g}{Z_p} \quad (5.5)$$

Substituting Eqs 5.1, 5.2 and 5.5 into Eqs 5.4, gives,

$$\theta = \frac{T_p}{K_p} + \frac{1}{K_g} \frac{Z_g}{Z_p} T_p \frac{Z_g}{Z_p} = T_p \left[\frac{1}{K_p} + \frac{1}{K_g} \left(\frac{Z_g}{Z_p} \right)^2 \right] \quad (5.6)$$

If the effects of teeth bending and gear body torsional displacement are both included as springs in series, the refined form of Eqs 5.6 is shown as,

$$\theta = T_p \left[\frac{1}{K_{Tp}} + \frac{1}{K_{Bp}} + \frac{1}{K_{Tg}} \left(\frac{Z_g}{Z_p} \right)^2 + \frac{1}{K_{Bg}} \left(\frac{Z_g}{Z_p} \right)^2 \right] \quad (5.7)$$

where subscript *T* and *B* denotes tooth bending and body torsional displacement terms respectively.

When defining the torsional stiffness of teeth as a linear stiffness *k* multiplied by the pitch circle radius squared *r*², the torsional stiffness of the body defined as a linear stiffness multiplied by the root circle radius squared *r_f*² and the torque applied at the meshing point defined as a contact force multiplied by the pitch circle, the Eqs 5.7 can be rewritten to give,

$$\theta = \frac{F}{r_p} \left[\frac{1}{k_{Tp}} + \frac{1}{k_{Tg}} \right] + \frac{F}{r_{pf}} \left[\frac{1}{k_{Bp}} + \frac{1}{k_{Bg}} \right] \quad (5.8)$$

When two gears are in mesh, the contact force can be expressed as in Eqs 5.9 as it is along the line of action which is at a tangent to the base circle of the two gears.

$$K = \frac{F \times r_{pb}}{\theta} \quad (5.9)$$

Substituting Eqs 5.8 into Eqs 5.9 gives,

$$K = \frac{r_{pb}}{\frac{1}{r_p} \left[\frac{1}{k_{Tp}} + \frac{1}{k_{Tg}} \right] + \frac{1}{r_{pf}} \left[\frac{1}{k_{Bp}} + \frac{1}{k_{Bg}} \right]} \quad (5.10)$$

As defined in Jia's work [5.3], tooth stiffness and body stiffness can be expressed as,

$$k_T = \frac{3 \times E \times I}{\left(\frac{h}{2} \right)^3} \quad (5.11)$$

$$k_B = \frac{E \times b \times r_{shaft}}{r_f - r_{shaft}} \quad (5.12)$$

where E represents Young's Modulus, tooth inertia I is defined as $I = b \times s^3 / 12$ with b denotes the gear face width and S denotes tooth thickness.

Substituting Eqs 5.11 and 5.12 into Eqs 5.10 gives the expression of torsional mesh stiffness as developed in Jia's work⁴⁰.

$$K_1 = \frac{r_{pb}}{\frac{a_1}{r_p} \left[\frac{\left(\frac{h_p}{2}\right)^3}{3 \times E \times I_p} + \frac{\left(\frac{h_g}{2}\right)^3}{3 \times E \times I_g} \right] + \frac{b_1}{r_{pf}} \left[\frac{r_{pf} - r_{ps}}{E \times b \times r_{ps}} + \frac{r_{gf} - r_{gs}}{E \times b \times r_{gs}} \right]} \quad (5.13)$$

$$K_2 = \frac{r_{pb}}{\frac{a_2}{2r_p} \left[\frac{\left(\frac{h_p}{2}\right)^3}{3 \times E \times I_p} + \frac{\left(\frac{h_g}{2}\right)^3}{3 \times E \times I_g} \right] + \frac{b_2}{r_{pf}} \left[\frac{r_{pf} - r_{ps}}{E \times b \times r_{ps}} + \frac{r_{gf} - r_{gs}}{E \times b \times r_{gs}} \right]} \quad (5.14)$$

where a and b are constant coefficients calculated by numerical methods from FEA results over 16 pairs of meshing with very different parameters chosen⁴⁰. Also in Jia's work⁴⁰, a_1 was calculated to be 2.7462, a_2 1.9479, b_1 2.2932, and b_2 2.2853, respectively. Shown in Jia's work⁴⁰, the numerical results by using Eqs 5.13 and 5.14 gave reasonable accuracy compared to FEA results.

An assumption made in this research is that the second pair of teeth and the third pair of teeth in mesh have an equal effect, $Emesh$, on changing the mesh stiffness. This can be expressed as,

$$\frac{a_1}{1 + Emesh} = \frac{a_2}{2} \quad (5.15)$$

$$\frac{a_1}{1 + Emesh + Emesh} = \frac{a_3}{3} \quad (5.16)$$

Solving Eqs 5.15 and 5.16 gives $a_3 = 1.7755$.

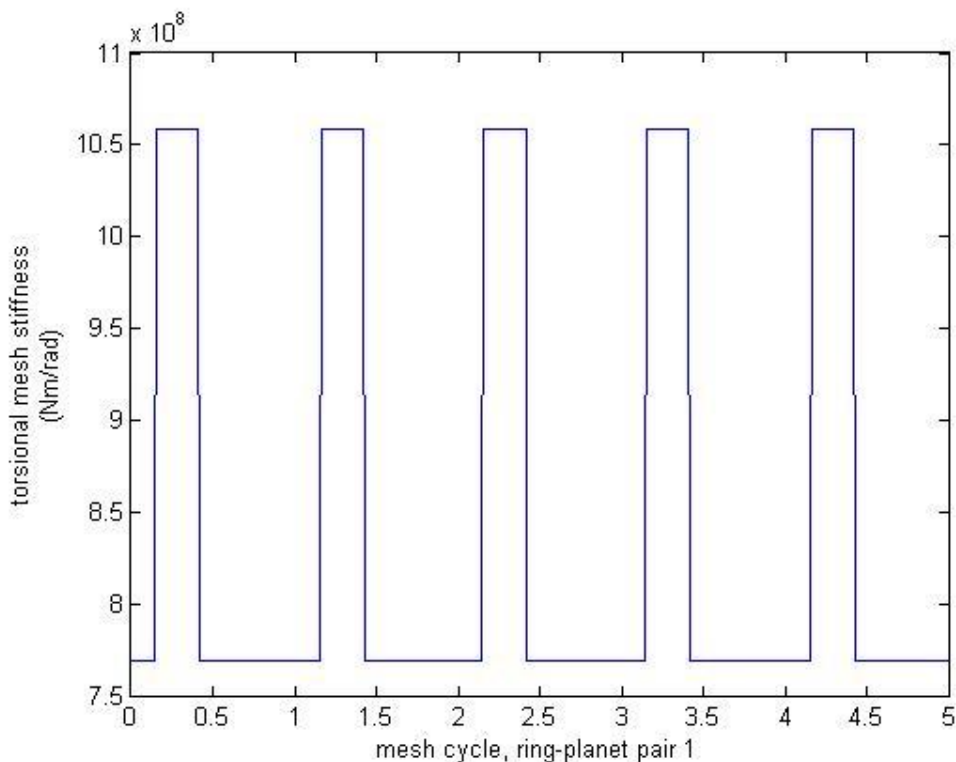
By the same method, b_3 was calculated to be 2.2827.

5.2. SIMULATION OF MESH STIFFNESS WITHOUT TOOTH FAULTS

Based on the equations introduced in section 5.1 and tooth meshing variation analysis in section 4.2, the simulations of sun gear - planet gear and ring gear - planet gear mesh stiffness are obtained using an input set of variables as listed in section 7.2.

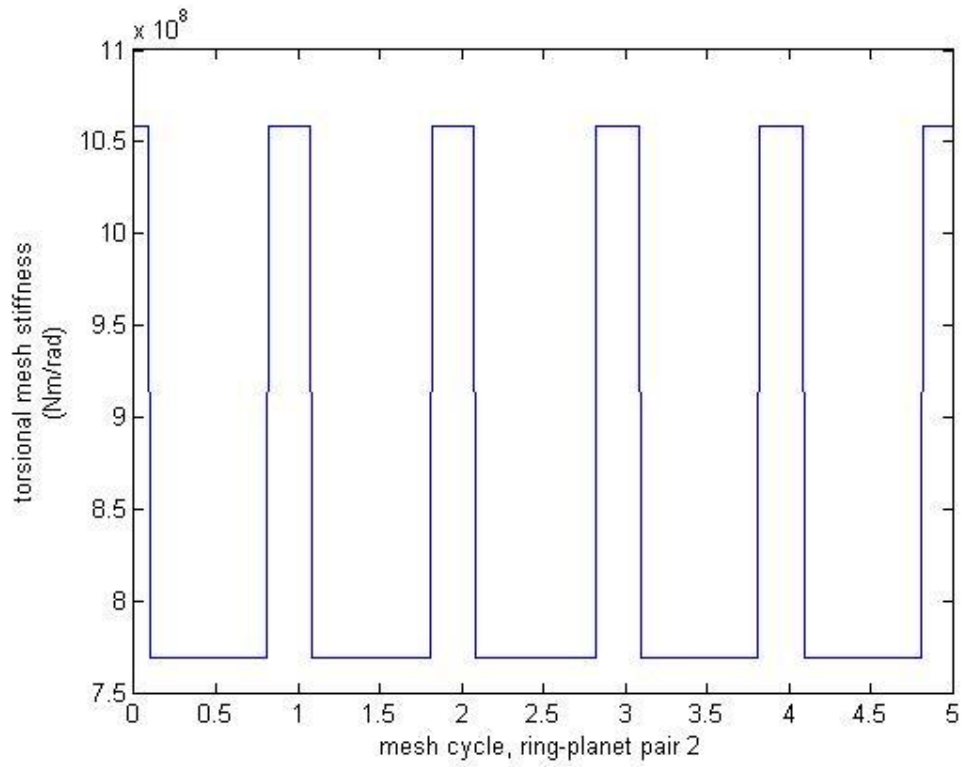
The values of mesh stiffness in this research are kept constant so the mesh stiffness diagrams have lines instead of curves similar to that in Jia's work⁴⁰. This is for the purpose of reducing computational time. More realistic simulations can also be obtained by using the program (Sec 7.5) developed in this research with a modification on the curve simulation equations (explained in Sec 7.5), however, the required computational time will be significantly increased.

The resulting time varying mesh stiffness is shown in Figure 5-1.

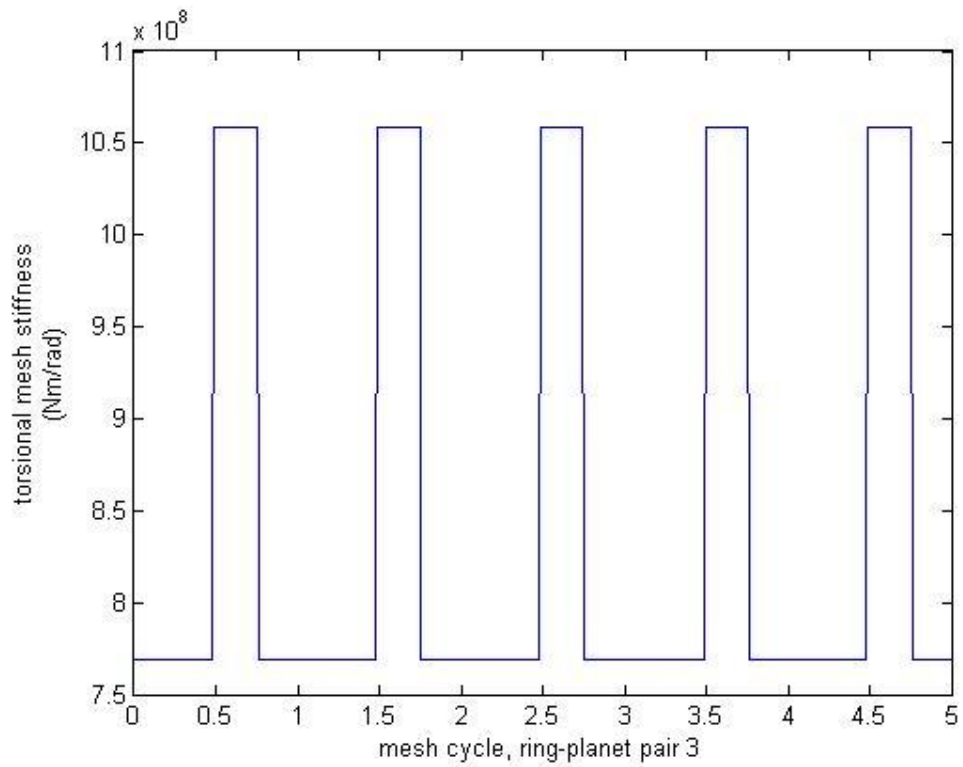


(a)

Figure 5-1 Torsional mesh stiffness of ring-planet pair (a, b, c) and sun-planet pair (d, e, f)

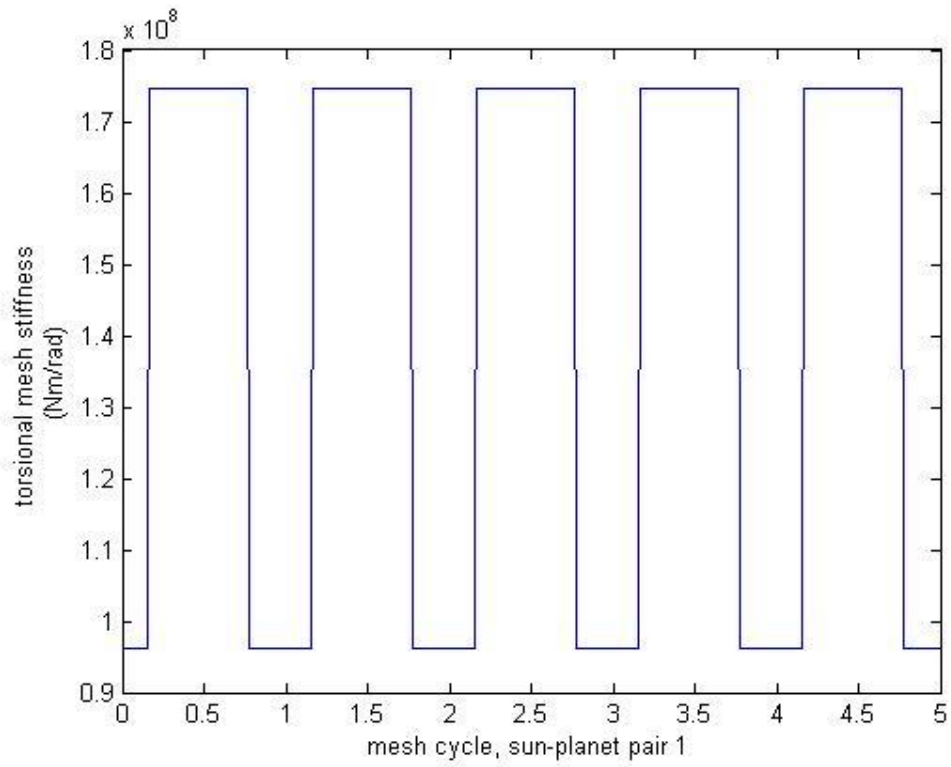


(b)

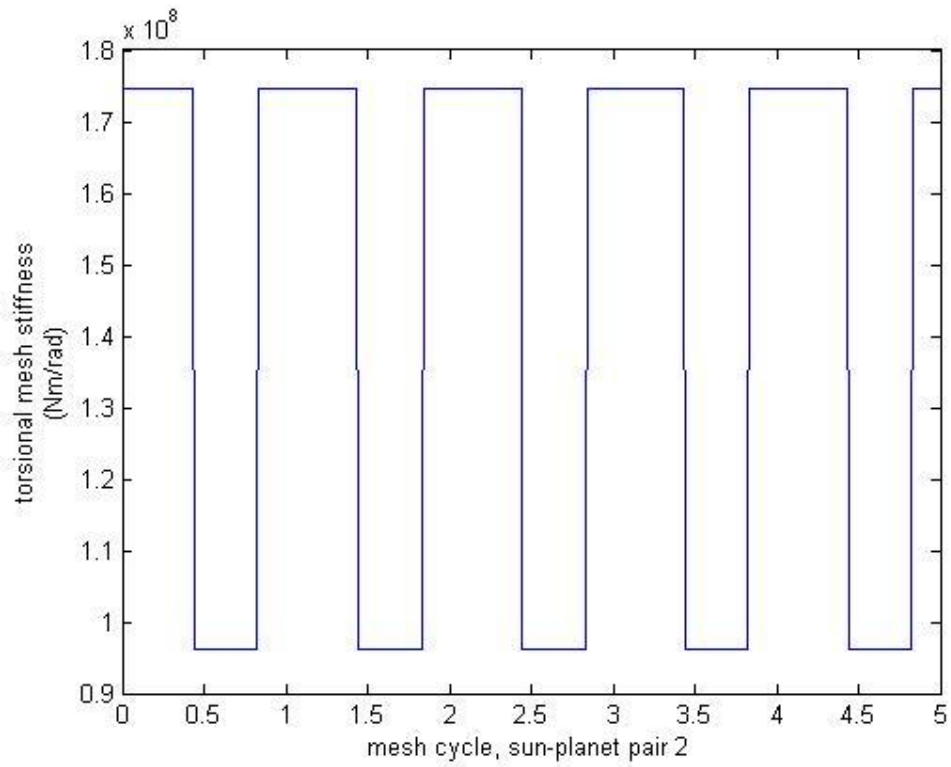


(c)

Figure 5-1 (continued) Torsional mesh stiffness of ring-planet pair (a, b, c) and sun-planet pair (d, e, f)

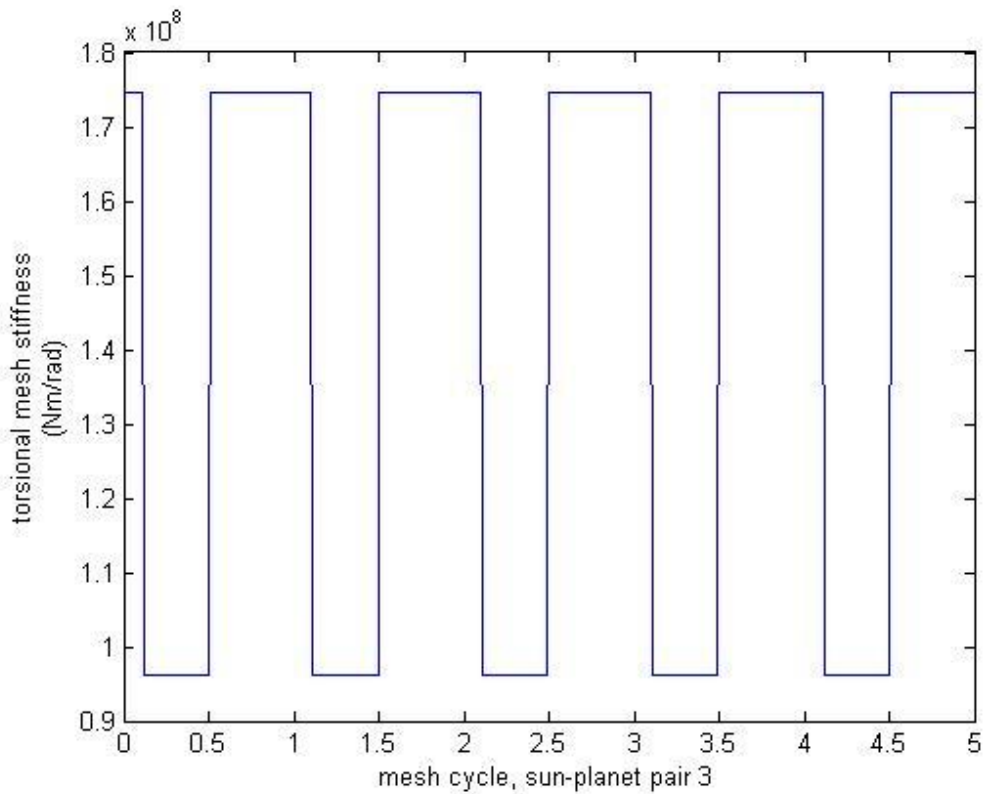


(d)



(e)

Figure 5-1 (continued) Torsional mesh stiffness of ring-planet pair (a, b, c) and sun-planet pair (d, e, f)



(f)

Figure 5-1 (continued) Torsional mesh stiffness of ring-planet pair (a, b, c) and sun-planet pair (d, e, f)

The time varying mesh stiffness results shown in Figure 5-1 perfectly match the time variation of number of teeth in contact analyzed in section 4.2. They also show the mesh phase differences between each sun gear - planet gear pair and between each ring gear - planet gear pair, as well as between sun gear - planet gear pairs and ring gear - planet gear pairs. More importantly the time varying mesh stiffness results show that the ring gear - planet gear mesh has much higher stiffness than sun gear - planet gear mesh. Even the lowest mesh stiffness ($7.6873e+008$ Nm/rad) in the ring gear - planet gear mesh is much higher than the highest value ($1.7448e+008$ Nm/rad) in the sun gear - planet gear mesh. This leads the conclusion that the ring gear teeth are much stiffer than the sun gear teeth.

5.3. MODELLING OF TOOTH CRACK

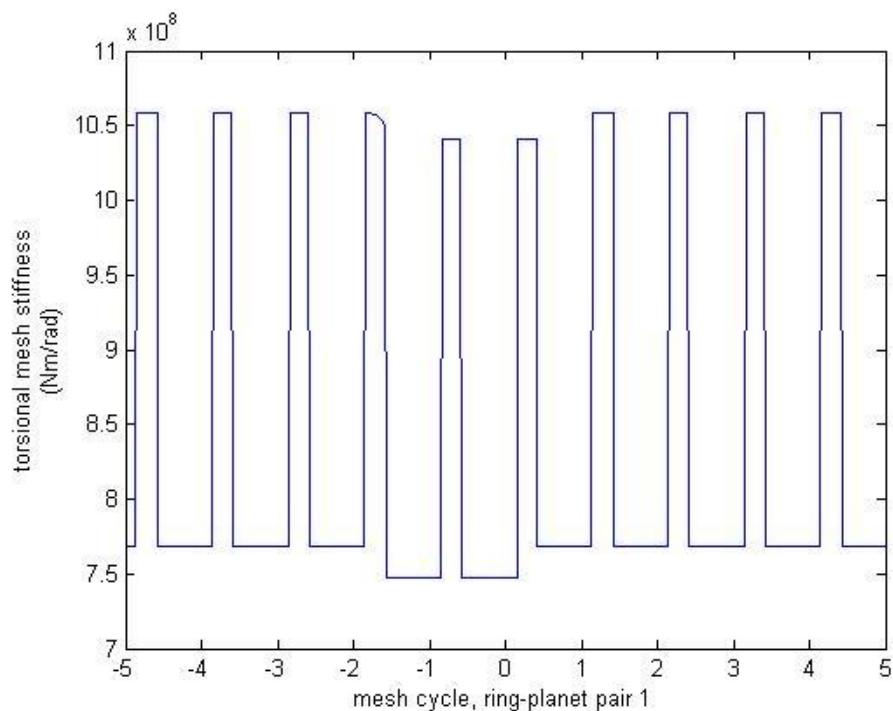
In this research the modelling of a tooth crack is conducted in two steps: calculation of the constant value of torsional mesh stiffness change and simulation of the cracked

mesh stiffness curve.

When a tooth with a crack is in mesh, the torsional mesh stiffness is less than that without tooth damage due to the reduced tooth thickness at the point the crack occurs. The change of tooth thickness will affect the rigidity of the tooth as it is taken into account in Eqs 5.13 and 5.14. In this research, localized tooth root cracks can be introduced by inputting the crack length (equivalent length along root circle) to the relative tooth in the MATLAB program. An arbitrary arrangement of number of cracks, locations of cracks, as well as crack length respectively can be easily simulated by simply placing the relative inputs into the program (see Sec 7.5).

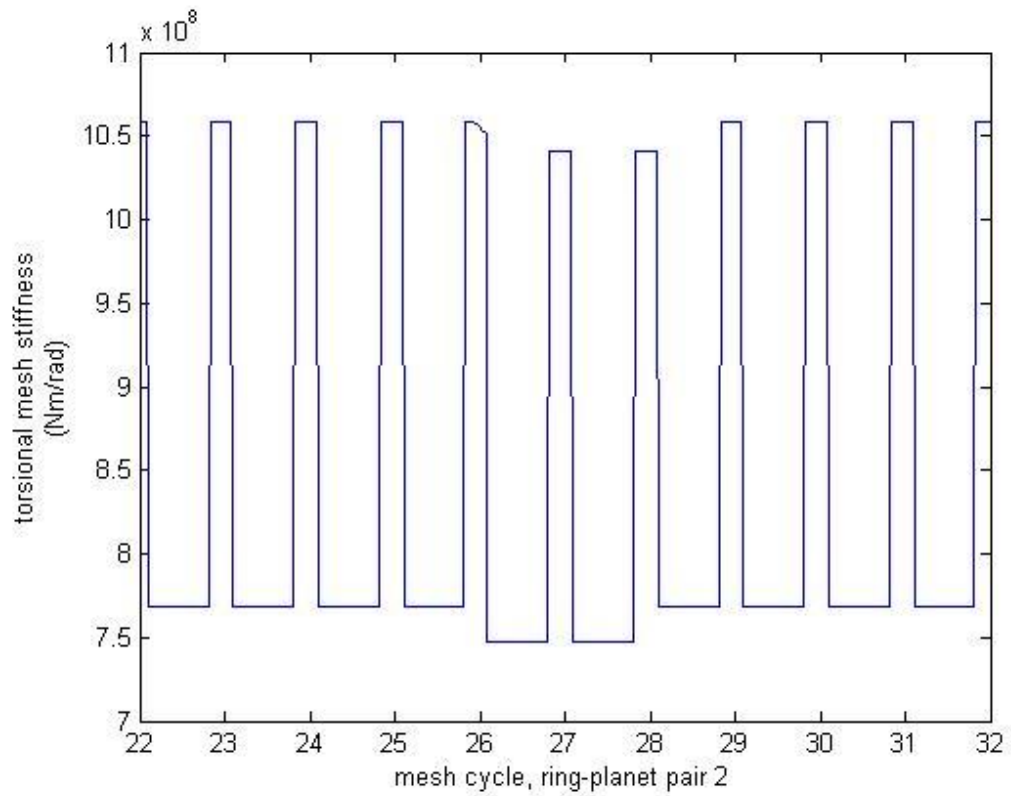
The resulting cracked mesh stiffness curve can also be simulated by simply changing the curve equations in the program (see Sec 7.5). The curve demonstrates the resulting time varying mesh stiffness while the cracked tooth is in mesh.

Figure 5-2 shows the torsional mesh stiffness of the ring-planet pair with a crack (length, 5% of tooth thickness based on the root circle; width, 100% of tooth face width) on the 83rd tooth of the ring gear.

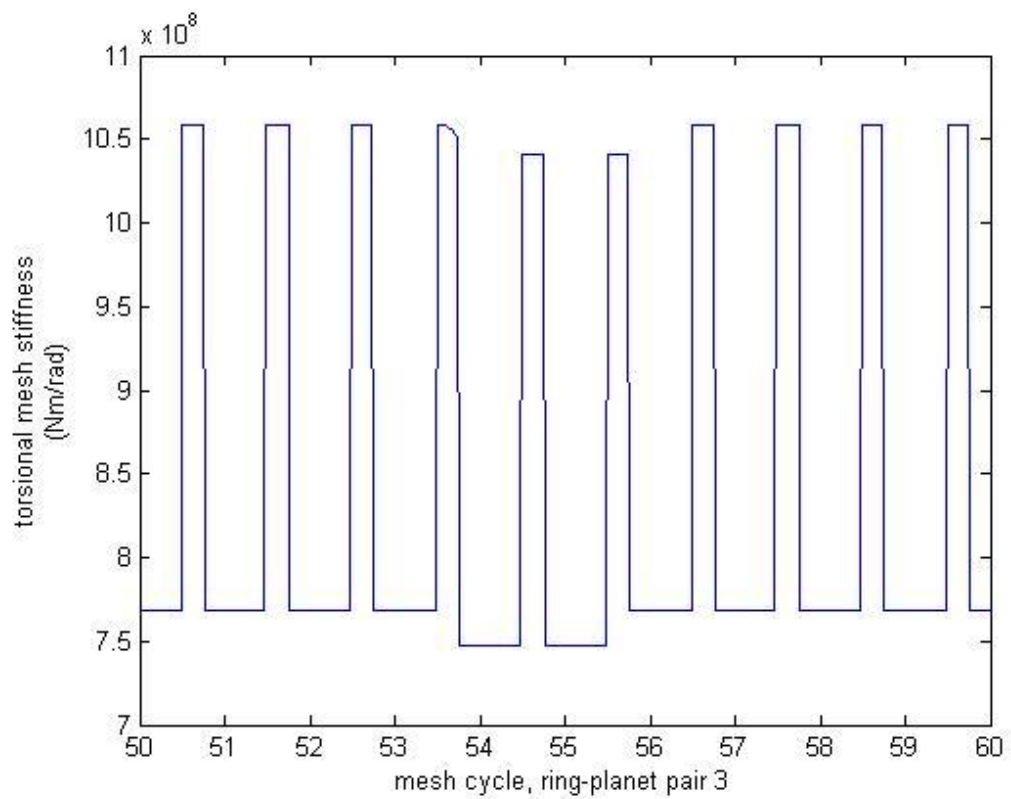


(a)

Figure 5-2 Torsional mesh stiffness of ring-planet pairs with a crack on the 83rd tooth of the ring gear



(b)



(c)

Figure 5-2 (continued) Torsional mesh stiffness of ring-planet pairs with a crack on the 83rd tooth of the ring gear

The resulting cracked (5% of tooth thickness based on the root circle) mesh stiffness in Figure 5-2 shows that the stiffness change is small (approximately 2% of undamaged tooth mesh stiffness), the change is introduced gradually rather than suddenly, and the stiffness change occurs from the point the cracked tooth entered contact until the crack left contact (in this case, the cracked tooth left contact). In conclusion, small tooth cracks change the mesh stiffness slightly, gradually and widely (depending on the location of crack).

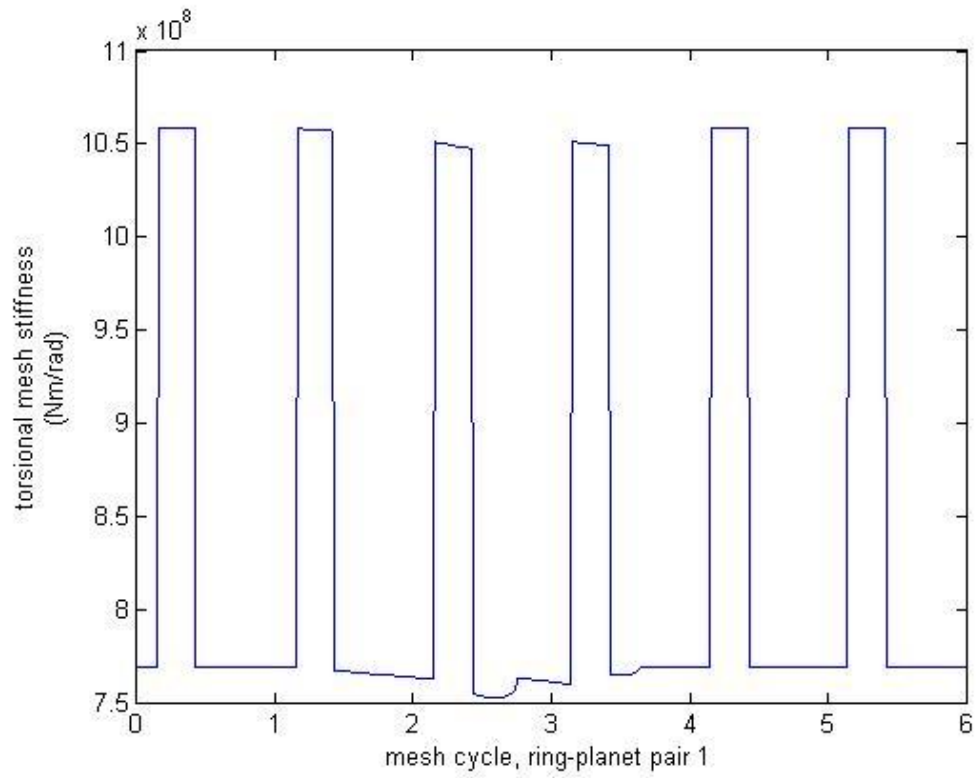
5.4. MODELLING OF TOOTH SPALLING

In this research the modelling of spalling is conducted by taking four factors into account. They are the location of the spall (central position of spall along the center line of tooth face width), the width of spall (equivalent effective radius), the depth of spall (average or maxima deduction on the mesh stiffness, in terms of percentage) and the curve function including the former three factors as inputs.

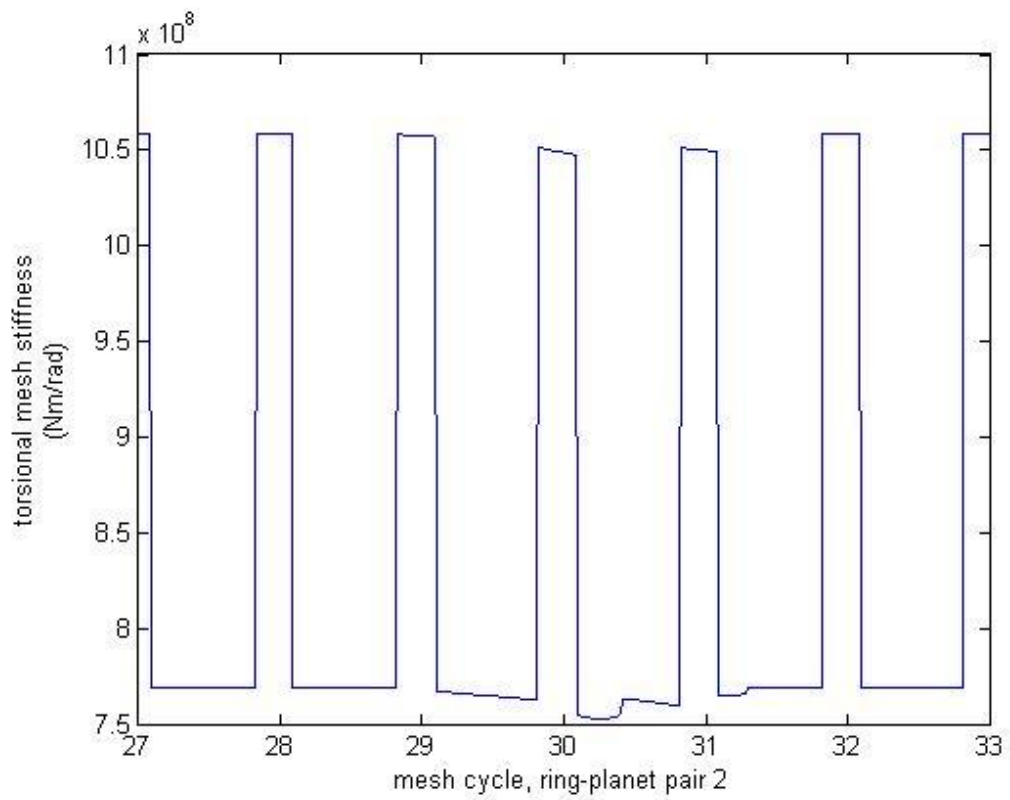
An arbitrary arrangement of number of spalls, locations of spalls, width of spalls, depth of spalls, as well as the calculated stiffness curve can be easily simulated by simply placing the relative inputs into the program (see Sec 7.5).

The stiffness reduction due to a spall is calculated as the stiffness change at the point of location of the spall (central position) where the thickness of the tooth reduces. The calculation can be conducted using Eqs 5.13, 5.14 and 5.19. It is to be noticed that the tooth thickness change used in the equations is an equivalent change at the root circle in terms of percentage.

Figure 5-3 shows the torsional mesh stiffness of ring-planet pairs with a spall (located at the point 60% of the contact line along the tooth surface; 10% equivalent radius; 0.4mm reduction on full depth spall; match curve function of $\cos^{\frac{1}{5}}$) on the 3rd tooth of ring gear and a smaller spall (5% equivalent radius and 0.2mm reduction) on the 4th tooth.

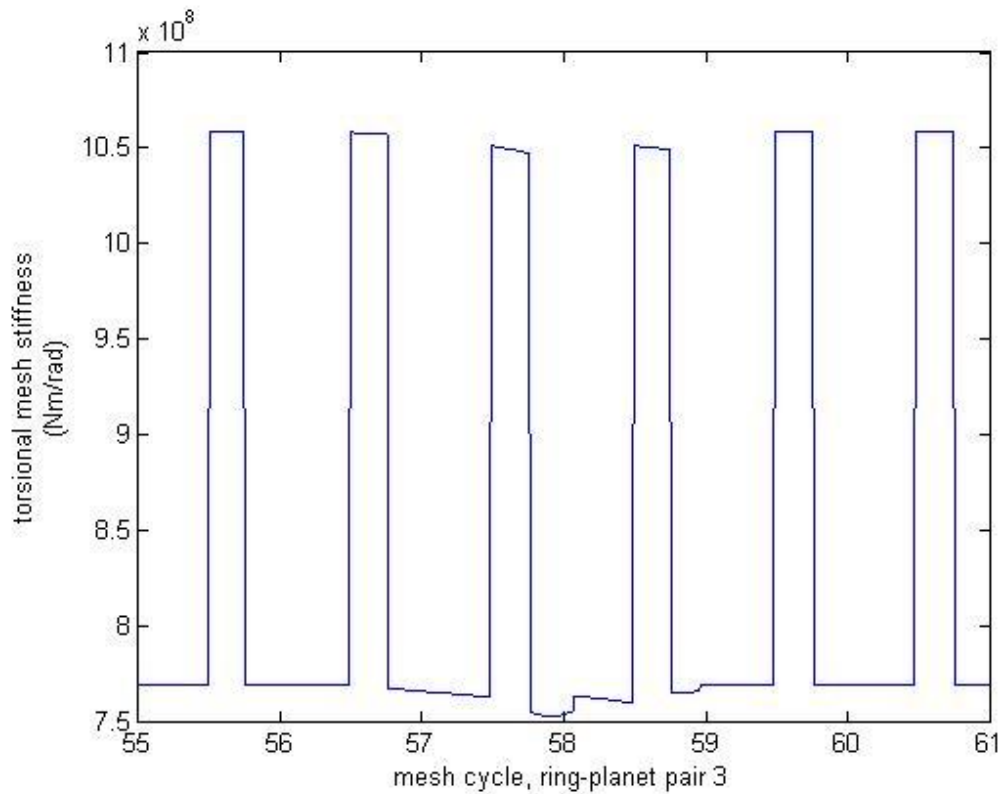


(a)



(b)

Figure 5-3 Torsional mesh stiffness of ring-planet pairs with two spalls



(c)

Figure 5-3 (continued) Torsional mesh stiffness of ring-planet pairs with two spalls

The resulting mesh stiffness (with two spalls) in Figure 5-3 shows that the stiffness change is very small (approximately 1% of undamaged tooth mesh stiffness for smaller spall, 5% equivalent radius and 0.2mm reduction), the change is introduced gradually rather than suddenly, and the stiffness change occurs from the point the spalled tooth entered contact until the spall left contact. In conclusion, tooth spalls change the mesh stiffness slightly (generally much smaller change than those with tooth cracks), gradually (generally more gradually than those with tooth cracks) and locally (depending on the equivalent radius of spall).

5.5. SUMMARY OF CHAPTER

In this paper, the common formulation of combined torsional mesh stiffness (defined by Jia, Howard and Wang³⁹) developed in Jia's work⁴⁰ was used with modifications to suit tooth mesh with contact ratio up to 3. Eqs 5.17 to 5.19 give the expression of torsional mesh stiffness. As these equations are based on FEA results, contact

stiffness is assumed to be contained by adjusting the coefficients (a and b) (to get satisfied results which are similar with the FEA results).

$$K_1 = \frac{r_{pb}}{\frac{a_1}{r_p} \left[\frac{\left(\frac{h_p}{2}\right)^3}{3 \times E \times I_p} + \frac{\left(\frac{h_g}{2}\right)^3}{3 \times E \times I_g} \right] + \frac{b_1}{r_{pf}} \left[\frac{r_{pf} - r_{ps}}{E \times b \times r_{ps}} + \frac{r_{gf} - r_{gs}}{E \times b \times r_{gs}} \right]}, \quad a_1 = 2.7462, b_1 = 2.2932, \quad (5.17)$$

$$K_2 = \frac{r_{pb}}{\frac{a_2}{2r_p} \left[\frac{\left(\frac{h_p}{2}\right)^3}{3 \times E \times I_p} + \frac{\left(\frac{h_g}{2}\right)^3}{3 \times E \times I_g} \right] + \frac{b_2}{r_{pf}} \left[\frac{r_{pf} - r_{ps}}{E \times b \times r_{ps}} + \frac{r_{gf} - r_{gs}}{E \times b \times r_{gs}} \right]}, \quad a_2 = 1.9479, b_2 = 2.2853, \quad (5.18)$$

$$K_3 = \frac{r_{pb}}{\frac{a_3}{3r_p} \left[\frac{\left(\frac{h_p}{2}\right)^3}{3 \times E \times I_p} + \frac{\left(\frac{h_g}{2}\right)^3}{3 \times E \times I_g} \right] + \frac{b_3}{r_{pf}} \left[\frac{r_{pf} - r_{ps}}{E \times b \times r_{ps}} + \frac{r_{gf} - r_{gs}}{E \times b \times r_{gs}} \right]}, \quad a_3 = 1.7755, b_3 = 2.2827. \quad (5.19)$$

The phasing relationships between mesh pairs were analyzed based on the teeth number variations previously developed.

The modelling of tooth cracks was conducted in two steps: calculation of the constant value of torsional mesh stiffness change and simulation of the cracked mesh stiffness curve. Reduction in tooth thickness at the point where the crack occurs causes the reduced mesh stiffness for the cracked tooth compared with the undamaged tooth.

The modelling of spalling was conducted by taking four factors into account. They are the location of the spall (central position of spall along the center line of tooth face width), the width of spall (equivalent effective radius), the depth of spall (average or maxima reduction on the mesh stiffness, in terms of percentage) and the curve function including the former three factors as inputs.

Using the MATLAB simulation program developed in this research, an arbitrary arrangement of cracks and spalls can be simulated with easy control of parameters.

It should be noticed that the methods (Sec 5.3 & 5.4) used in this research for tooth fault modelling are based on the calculated/equivalent stiffness variations and assumed curves. The simulation results are greatly affected by how accurate and

realistic the inputs are, especially the time varying mesh stiffness curves. However, by choosing parameters carefully and eventually using FEA to generate time varying mesh stiffness within one mesh cycle as well as time varying mesh stiffness curves with tooth faults as samples, these methods can be used to gain satisfying simulations with high accuracy for a range of arbitrary tooth faults with relatively low computational time.

6. LARGE LOW SPEED, HIGH TORQUE PLANETARY SPUR GEAR SYSTEMS- BUCKET WHEEL RECLAIMER DESIGN

In this section, the major modelling parameters of a typical bucket wheel reclaimer are introduced, including detailed arrangement, detailed parameters and relative calculations which are needed for this research.

6.1. BUCKET WHEEL RECLAIMER DESIGN

A bucket wheel reclaimer (or bucket wheel excavator) forms an important part of continuous mining operations, especially for surface mining equipment as shown in Figure 6-1.

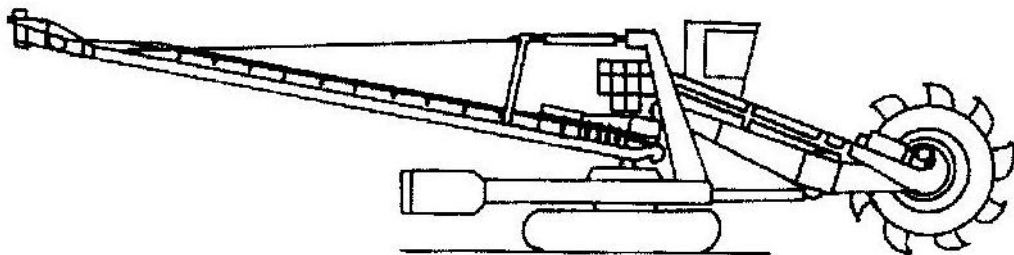


Figure 6-1 Compact bucket wheel reclaimer⁵⁹

Bucket wheel reclaimers vary in design to suit the needs of operational conditions and can range from small sized machines with a capacity of 100 cubic meters per hour to large machines with a capacity over 12500 cubic meters per hour⁶⁰.

In Western Australia, compact bucket wheel reclaimers similar to that shown in Figure 6-1 are widely used in mining operations such as for transferring iron ore. In this research, all the modelling is made for one typical design of compact bucket wheel reclaimer which is introduced with detailed arrangement and parameters in the rest of this section.

6.2. BUCKET WHEEL DRIVE

The compact bucket wheel reclaimer will be assumed to be driven by a slip ring AC induction motor. The motor is connected to the multistage reduction gearbox via an elastic coupling. A planetary gear box is connected after the reduction gearbox and supporting the bucket wheel via a flange, bolted to the carrier arm.

6.3. THE MOTOR

For the type of bucket wheel reclaimers under analysis in this research, the speed of rotation of the bucket wheel is in the range of 6rpm. The gearbox speed reduction ratio is 157.2789, (see section 6.5 and 6.6) including the multistage reduction gearbox and the planetary gearbox, requiring a motor with an operation speed of 950 rpm.

The speed of an AC induction motor is given by,

$$n = \frac{120f}{p} \quad (6.1)$$

where n is the speed of motor, f is the supply frequency in Hz and p is the number of poles. To supply 950 rpm at 50 Hz, a 6-pole motor is needed.

In the modelling of this research, specifications of the motor are based on a squirrel cage, three phase induction motor with a rated power of 450KW provided by ABB⁶¹.

The full load torque of the drive system is taken to be at 950rpm, and is calculated as,

$$T_{fl} = \frac{450 * 1000 * 0.96}{950 * \frac{2\pi}{60}} = 4342.4Nm \quad (6.2)$$

$$T_{start-up} = 2.3 * T_{fl} = 9987.6Nm \quad (6.3)$$

$$T_{maximum} = 2.6 * T_{fl} = 11290Nm \quad (6.4)$$

The inertia of the motor was estimated to be 20 kgm^2 .

The assumed torque-speed curve of the motor is shown in Figure 6-2.

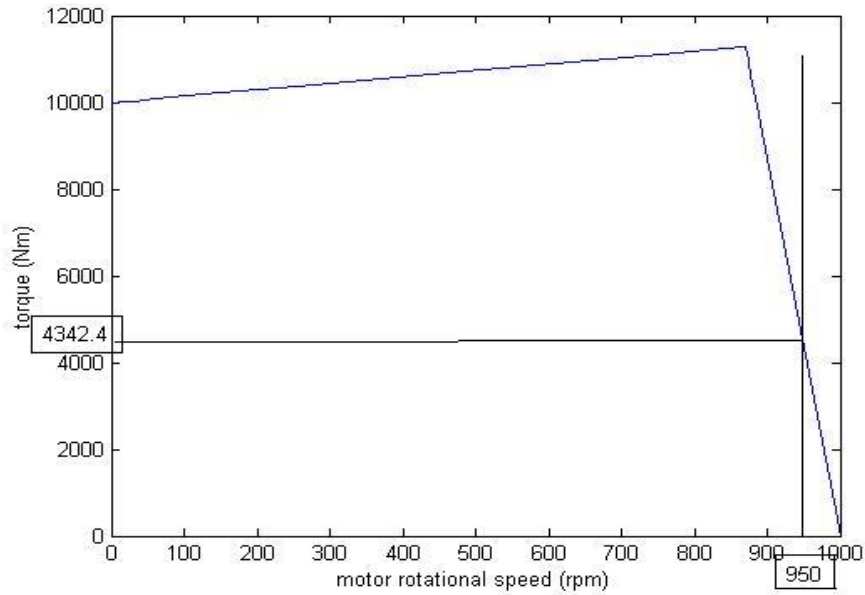


Figure 6-2 Torque-speed curve for a 450kw induction motor

6.4. FLUID COUPLING

The torque provided from the induction motor can be transient and very large. In that case, damage to the motor and gearboxes may occur. In order to avoid damage and absorb vibration and shock, a fluid coupling is generally employed to transfer the input torque from the motor to the reduction gearbox. A fluid coupling will also provide a more gentle acceleration of the rotational parts⁶².

Due to the nature of fluid couplings, they cannot operate at 100% efficiency⁶³. The slip between input and output during normal operation is generally in a range of 1 to 3 percent⁶⁴. In this research the coupling is assumed to have a slip of 3% at full load condition. The slip of a fluid coupling is calculated by,

$$S = \frac{\dot{\theta}_{motor} - \dot{\theta}_{gearbox}}{\dot{\theta}_{motor}} \quad (6.5)$$

and the damping of the coupling is represented by,

$$C_{coupling} = q_{cc} * \dot{\theta}_{motor} \quad (6.6)$$

where q_{cc} is the damping coefficient with a value of 15.

6.5. REDUCTION GEAR BOX

In order to reduce the input rotational speed of the system from approximately 950rpm (motor speed) to the bucket wheel operational speed in the range of 6 rpm, a reduction gear box is needed.

A typical gearbox arrangement of a compact bucket wheel reclaimer is shown in Figure 6-3.

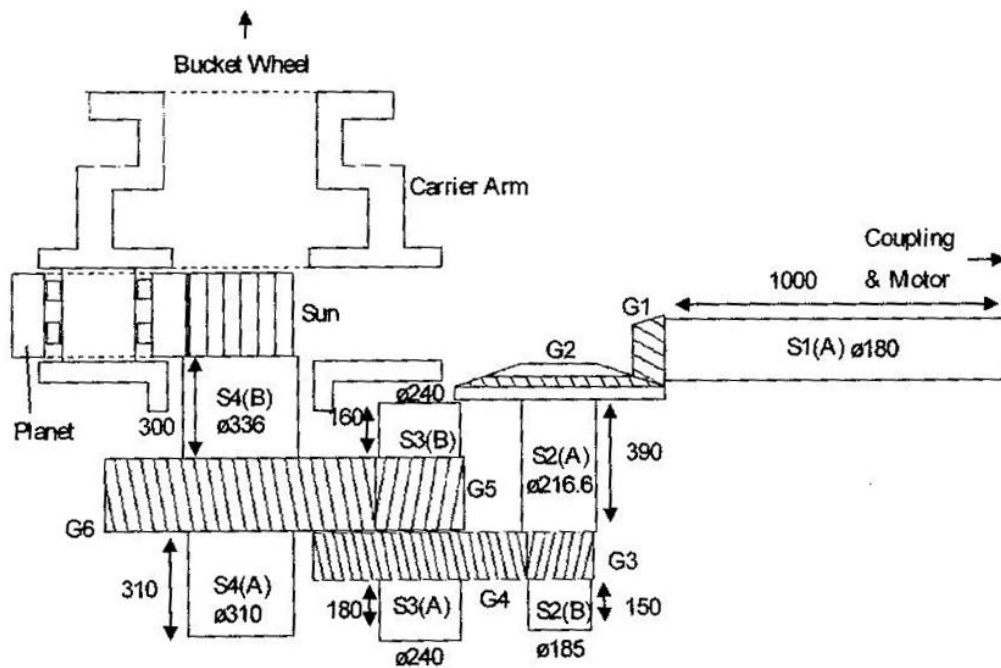


Figure 6-3 A typical gearbox arrangement of the bucket wheel drive (reduction gear box with gears G1 to G6, and a planetary gear box)⁶⁵

The gears selected for the reduction gear box have parameters as listed in Table 6-1.

Gear number	Module	Number of teeth	Pressure angle	Helix angle
G1	12 (mean)	13	20	30
G2	12 (mean)	38	20	30
G3	9	21	20	12
G4	9	68	20	12
G5	12	21	20	10
G6	12	65	20	10

Table 6-1 Parameters of reduction gears

This reduction gear box gives a total reduction ratio of

$$ReductionRatio = \frac{38}{13} \times \frac{68}{21} \times \frac{65}{21} = 29.2971 \quad (6.7)$$

It should be noticed that specifications other than the total reduction ratio of the reduction gearbox are not a concern in this research.

6.6. PLANETARY GEAR BOX

As shown in Figure 6-3 a planetary gearbox is connected between the reduction gearbox and the bucket wheel to provide a low speed and large torque transaction with a relatively compact gear arrangement.

The selected sun gear, ring gear and planet gears of the planetary gearbox have the parameters as listed and calculated in Table 6-2.

Parameters	Symbol	Sun gear	Planet gear	Ring gear
Module	m	16	16	16
Number of teeth	z	19	32	83
Pressure angle (°)	α	20	20	20
Face width (mm)	b	245	245	245
Pitch diameter (mm)	$d=m*z$	304	512	1328
Addendum (mm)	$h_a = h_a^* m = m$	16	16	16
Dedendum (mm)	$h_f = (h_a^* + c^*)m$ $= 1.25m$	20	20	20
Tooth height (mm)	$h = h_a + h_f$	36	36	36
Addendum circle Diameter (mm)	$d_a = d + 2h_a$	336	544	1360
Dedendum circle Diameter (mm)	$d_a = d - 2h_f$	264	472	1288
Base circle Diameter (mm)	$d_b = d \cos \alpha$	285.6666	481.1226	1247.9
Circular pitch (mm)	$p = \pi m$	50.2655	50.2655	50.2655
Base pitch (mm)	$p_b = p \cos \alpha$	47.2341	47.2341	47.2341

Table 6-2 Parameters of planetary gears

Parameters	Symbol	Sun gear	Ring gear	Planet gear
Tooth thickness (mm)	$s = \frac{\pi m}{2}$	25.1327	25.1327	25.1327
Centre distance (mm)	$a = \frac{m}{2}(z_s + z_p)$	0.4080	-----	0.4080

Table 6-2(continued) Parameters of planetary gears

The planetary gear ratios are calculated by Table 6-3 as below,

	Sun gear	Planet gears	Ring gear	Carrier arm
Step 1 Lock all gears and carrier arm; Rotate all parts as one through +1	+1	+1	+1	+1
Step 2 Lock carrier arm; Rotate ring gear through -1	-(83/32)* (-32/19)	-(83/32)	-1	0
Step 3 Sum step 1 and step 2	5.3684	-1.5938	0	+1

Table 6-3 The Tabular Method for the planetary gear ratios

In Table 6-3, the rotational speed ratio (5.3684 to 1) between sun gear and carrier arm is shown with the ring gear being locked which simulates the conditions of the bucket wheel reclaimer drive. The ratio associated with the reduction gearbox ratio (29.2971 in Eqs 6.7) provides a total speed reduction ratio of 157.2792:1 (5.3684*29.2971) from the motor to the bucket wheel. This design keeps the rotational speed of the bucket wheel in the range of 6rpm (950/157.2792=6.04 rpm).

In this research, to simplify the modelling and the calculation of the mass and inertia of the sun gear, ring gear, planet gears and carrier arm, they are assumed to be hollow cylinders.

The mass of a hollow cylinder⁶⁶ is given by,

$$mass = \pi b \rho \left[\left(\frac{d}{2} \right)^2 - \left(\frac{d_i}{2} \right)^2 \right] \quad (6.8)$$

where ρ is the density of material, where d for the gears is the pitch diameter and for the carrier arm is the outer diameter, and where d_i denotes shaft diameter for sun gear and planet gears, host diameter for ring gear, and inner diameter for carrier arm.

The inertia of a hollow cylinder is,

$$inertia = \frac{1}{2} m \left[\left(\frac{d}{2} \right)^2 + \left(\frac{d_i}{2} \right)^2 \right] = \frac{1}{2} \pi b \rho \left[\left(\frac{d}{2} \right)^4 - \left(\frac{d_i}{2} \right)^4 \right] \quad (6.9)$$

6.7. BUCKET WHEEL AND LOAD MATERIAL

The wheel body of the bucket wheel is simplified and approximated to be modeled as a hollow cylinder with dimensions r_{wout} for outer radius, r_{win} for inner radius, and l_w for length. The bucket wheel is bolted to the carrier arm for simplification and the shaft can be modeled with shaft mass and inertia.

The mass of the wheel body is therefore calculated as,

$$mass_w = \pi \rho_w (r_{wout}^2 - r_{win}^2) l_w \quad (6.10)$$

and the inertia of the wheel body is calculated as,

$$inertia_w = \frac{1}{2} \pi \rho_w (r_{wout}^4 - r_{win}^4) l_w \quad (6.11)$$

A number n_b of buckets are mounted on the outer circle of the wheel body. Every bucket is modeled as a quarter cylinder with hollow centers, having outer width of w_{bout} , outer radius of r_{bout} , inner width of w_{bin} , and inner radius of r_{bin} .

The mass of a single bucket is therefore calculated as,

$$mass_b = \frac{1}{4} \pi \rho_b (r_{bout}^2 w_{bout} - r_{bin}^2 w_{bin}) \quad (6.12)$$

and the inertia of a single bucket about the centre of carrier arm is calculated as,

$$inertia_b = \frac{1}{4} \frac{1}{2} \pi \rho_b (r_{bout}^4 w_{bout} - r_{bin}^4 w_{bin}) + \frac{1}{4} \pi \rho_b (r_{bout}^2 w_{bout} - r_{bin}^2 w_{bin}) r_{wout}^2 \quad (6.13)$$

The mass of a full bucket of ore is calculated as,

$$mass_o = \frac{1}{4} \pi \rho_o r_{bin}^2 w_{bin} \quad (6.14)$$

and the inertia of a full bucket of ore about the centre of carrier arm is calculated as,

$$inertia_o = \frac{1}{4} \frac{1}{2} \pi \rho_o r_{bin}^4 w_{bin} + \frac{1}{4} \pi \rho_o r_{bin}^2 w_{bin} r_{wout}^2 \quad (6.15)$$

When the bucket wheel is in operation, not all the buckets are full of ore. An approximated loading condition is introduced here to simulate the mass and inertia of loaded ore. The ore loading condition coefficient is,

$$Olcc = \sum n_o p_o \quad (6.16)$$

where p_o denotes the percentage of ore in a single bucket and n_o is the number of buckets with the same loading condition.

6.8. SUMMARY OF CHAPTER

The major components of the typical compact bucket wheel reclaimer used in this thesis are summarized in Figure 6-4.

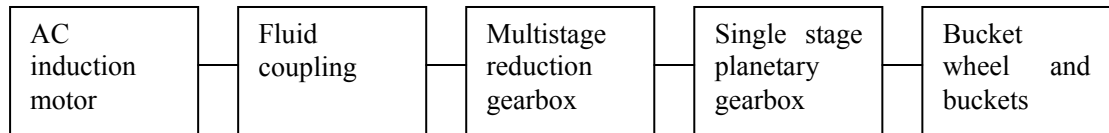


Figure 6-4 Major components used in this thesis

The major parameters are summarized in Table 6-4.

Component	Symbol	Parameter	Value
AC induction motor	n	speed of motor	950 rpm
	p	number of poles	6
	f	supply frequency	50 Hz

Table 6-4 Major parameters of the bucket wheel reclaimer components

Component	Symbol	Parameter	Value
AC induction motor	T_{fl}	full load torque	4342.4 Nm
	$T_{start-up}$	start-up torque	9942.9 Nm
	$T_{maximum}$	maximum torque	11240 Nm
	--	inertia of the motor	20 kgm^2
Fluid coupling	q_{cc}	damping coefficient	15
Reduction gear box	<i>ReductionRatio</i>	reduction ratio	29.2971
Planetary gear box	--	mass of sun gear	98.9691 kg
	--	mass of ring gear	2015.1 kg
	--	mass of carrier arm	3699.2 kg
	--	mass of planet gear	284.2189 kg
	--	inertia of sun gear	1.4760 kgm^2
	--	inertia of ring gear	1224.4 kgm^2
	--	inertia of carrier arm	1849.6 kgm^2
	--	inertia of planet gear	11.9417 kgm^2
	--	reduction ratio	5.3681
Bucket wheel and load material	r_{wout}	outer radius	2 m
	r_{win}	inner radius	1 m
	l_w	length	0.1 m
	$mass_w$	mass of bucket wheel body	7398.5 kg
	$inertia_w$	inertia of bucket wheel body	18496 kgm^2
	$mass_b$	mass of a single bucket	1277.8 kg
	$inertia_b$	inertia of a single bucket	6048.3 kgm^2
	$mass_o$	mass of a full bucket of ore	3664.6 kg
	$inertia_o$	inertia of a full bucket of ore	16312 kgm^2
	$Olcc$	loading condition coefficient	3*0.8+1*0.6+1*0.1

Table 6-4(continued) Major parameters of the bucket wheel reclaimer components

7. GENERALISED SOFTWARE MODEL

In this thesis, all the calculations and simulations are conducted using the MATLAB program. The MATLAB program was developed using symbolic math and written in M-files. The entire program includes 49 mfiles with most inputs listed in one mfile and a few located in other mfiles.

In this chapter, the flow chart of the overall software model is illustrated and the overall inputs are listed. MATLAB programs used for each chapter (Chapter 3 to Chapter 9) are introduced with corresponding flow chart where it is applicable. The detailed code of each MATLAB program is listed in Appendix 13.1.

7.1. FLOW CHART OF PROGRAMS

This flow chart divides the entire programs into 4 levels. The first level represents the input and output level, which is shown using single-line circles and texted arrows. The second level contains programs for sub-system level calculations and simulations, which are presented using rounded corner rectangles. The third level is the sub-system overall level, which is shown using double-line circles. There are 8 groups of third level programs. The fourth level is the main program which contains the ODE function and solver. It is shown using a triple-line circle.

Between each part there are line-arrows, which represents the connections and data flow directions.

This overall flow chart represents the detail down to the level of a single program and hence does not include the code level within the single program.

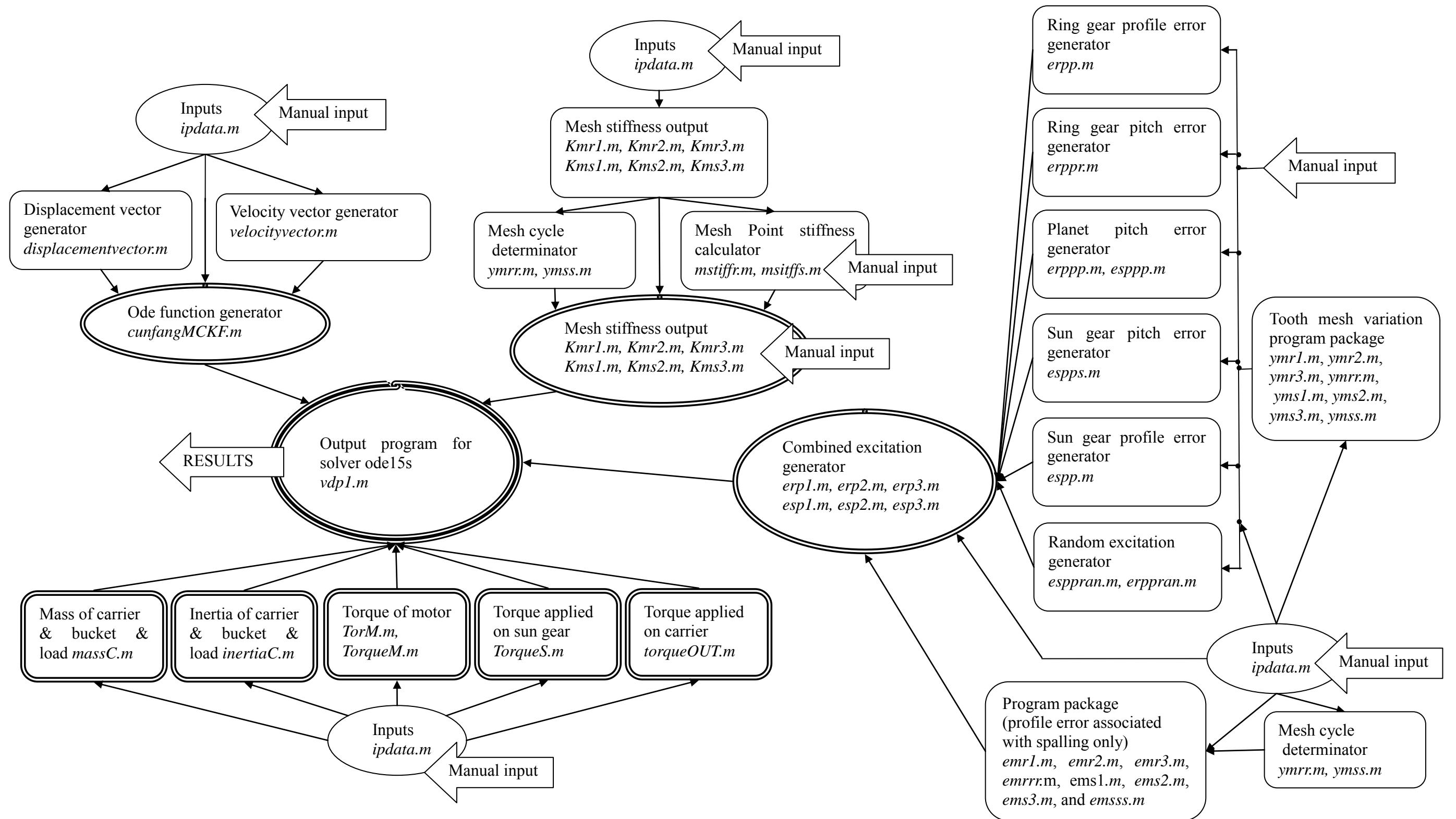


Figure 7-1 Flow chart of program developed in this research

7.2. INPUT

The program developed to introduce input values into the program is named *ipdata.m*. It includes all inputs needed in the entire program except displacement factors of action line of mesh (Sec 7.3), setting for profile and pitch excitation (Sec 7.4), and settings for tooth faults (Sec 7.5).

The value of each input can be arbitrary; however, realistic values are needed to gain realistic results.

The inputs employed in this research are listed in Table 7-1.

Input	Symbol	Value	Meaning
ipdata(1)	z_s	19	teeth number of sun gear
ipdata(2)	z_p	32	teeth number of planet gear
ipdata(3)	z_r	83	teeth number of ring gear
ipdata(4)	α_s	20	pressure angle, sun gear, degrees
ipdata(5)	α_r	20	pressure angle, ring gear, degrees
ipdata(6)	m	16/1000	Module
ipdata(7)	n	3	number of planets
ipdata(8)	B/b	245/1000	face width (m)
ipdata(9)	r_c	calculated	centre distance of sun & planet / design radial distance between the centers of planet gear and carrier arm
ipdata(14)	--	82/1000	sun gear shaft radius (m)
ipdata(15)	--	136/1000	planet gear shaft radius (m)
ipdata(16)	--	880/1000	ring gear host radius (m)
ipdata(21)	E	$210 \cdot 10^9$	Young's Modulus (Pa)
ipdata(22)	ρ	7850	density of gear/carrier arm material (kg/m^3)
ipdata(23)	ρ_o	4700	density of ore (kg/m^3)
ipdata(31)	p	6	number of poles
ipdata(32)	f	50	supply frequency (Hz)
ipdata(33)	n	950	operating speed of motor (rpm)
ipdata(34)	--	450000	rated power of motor (Watts)

Table 7-1 List of inputs

Input	Symbol	Value	Meaning
ipdata(35)	--	29.2971	reduction gear box ratio
ipdata(36)	--	calculated	gear box ratio
ipdata(37)	--	20	inertia of motor (kgm^2)
ipdata(41)	--	5	output torque control ratio
ipdata(42)	--	12	number of buckets
ipdata(43)	--	5	corresponding to in(92), number of buckets with ore when in operation
ipdata(44)	--	calculated	starting up end point/loading up start point
ipdata(45)	--	calculated	loading up end point
ipdata(46)	--	calculated	unloading start point
ipdata(47)	--	calculated	unloading end point
ipdata(48)	--	calculated	single bucket load loading up/unloading period
ipdata(49)	--	calculated	overloading start point
ipdata(50)	--	calculated	overloading end point
ipdata(51)	cd	3	condition controller
ipdata(53)	SP_{sp_i}	1	SPsp controller
ipdata(54)	SP_{rp_i}	1	SPrp controller
ipdata(55)	--	0.001	differential step controller
ipdata(56)	--	0	shaft-frequency excitation controller
ipdata(61)	c_{sp_i}	10	damping of sun-planet meshing (Ns/m)
ipdata(62)	c_{rp_i}	10	damping of ring-planet meshing (Ns/m)
ipdata(63)	c_{px}	10^{10}	damping of planet-carrier connection in x direction (Ns/m)
ipdata(64)	c_{py}	10^{10}	damping of planet-carrier connection in y direction (Ns/m)
ipdata(65)	k_{px}	10^8	stiffness of planet-carrier connection in x direction (N/m)
ipdata(66)	k_{py}	10^8	stiffness of planet-carrier connection in y direction (N/m)
ipdata(67)	r_{cp_i}	calculated	centre distance of sun & planet / real radial distance between the centers of planet gear and carrier arm (m)
ipdata(71)	T_{rb}	0	torque from base to ring gear (Nm)
ipdata(72)	q_{cc}	15	coupling damping coefficient
ipdata(81)	r_{cin}	0/1000	inner radius of carrier arm (m)

Table 7-1(continued) List of inputs

Input	Symbol	Value	Meaning
ipdata(82)	r_{cout}	1	outer radius of carrier arm (m)
ipdata(83)	l_c	150/1000	average width of carrier arm (m)
ipdata(84)	r_{win}	1	inner radius of wheel (m)
ipdata(85)	r_{wout}	2	outer radius of wheel (m)
ipdata(86)	l_w	0.1	average width of wheel (m)
ipdata(87)	n_b	in(42)	number of buckets
ipdata(88)	r_{bout}	1	bucket dimension, outer radius (m)
ipdata(89)	w_{bout}	1.2	bucket dimension, outer width (m)
ipdata(90)	r_{bin}	0.95	bucket dimension, inner radius (m)
ipdata(91)	w_{bin}	1.1	bucket dimension, inner width (m)
ipdata(92)	$Olcc$	3.1	ore loading condition
ipdata(93)	--	0.8	single bucket ore drop
ipdata(94)	--	calculated	ore drop period
ipdata(95)	--	10	overloading rate
ipdata(101)	c_s	300	damping of sun gear support in x direction (Ns/m)
ipdata(102)	c_s	300	damping of sun gear support in y direction (Ns/m)
ipdata(103)	c_{st}	100	damping of sun gear support in torsional direction (Ns/m)
ipdata(104)	c_r	450	damping of ring gear support in x direction (Ns/m)
ipdata(105)	c_r	450	damping of ring gear support in y direction (Ns/m)
ipdata(106)	c_{rt}	10^6	damping of ring gear support in torsional direction (Ns/m)
ipdata(107)	c_c	500	damping of carrier arm support in x direction (Ns/m)
ipdata(108)	c_c	500	damping of carrier arm support in y direction (Ns/m)
ipdata(109)	c_{ct}	100	damping of carrier arm support in torsional direction (Ns/m)
ipdata(111)	k_s	10^7	stiffness of sun gear support in x direction (N/m)
ipdata(112)	k_s	10^7	stiffness of sun gear support in y direction (N/m)
ipdata(113)	k_{st}	0	stiffness of sun gear support in torsional direction (N/m)
ipdata(114)	k_r	10^8	stiffness of ring gear support in x direction (N/m)
ipdata(115)	k_r	10^8	stiffness of ring gear support in y direction (N/m)

Table 7-1(continued) List of inputs

Input	Symbol	Value	Meaning
ipdata(116)	k_{rt}	10^{10}	stiffness of ring gear support in torsional direction (N/m)
ipdata(117)	k_c	$5 \cdot 10^7$	stiffness of carrier arm support in x direction (N/m)
ipdata(118)	k_c	$5 \cdot 10^7$	stiffness of carrier arm support in y direction (N/m)
ipdata(119)	k_{ct}	0	stiffness of carrier arm support in torsional direction (N/m)
ipdata(201)	ψ_1	0	planet spacing 1 (rad)
ipdata(202)	ψ_2	$34/51 \cdot \pi$	planet spacing 2 (rad)
ipdata(203)	ψ_3	$68/51 \cdot \pi$	planet spacing 3 (rad)
ipdata(301)	--	0.00	angular error of the 1 st planet position on carrier arm (degree)
ipdata(302)	--	0.00	angular error of the 2 nd planet position on carrier arm (degree)
ipdata(303)	--	0.00	angular error of the 3 rd planet position on carrier arm (degree)

Table 7-1(continued) List of inputs

7.3. AUTOMATIC ASSEMBLY OF EQUATIONS OF MOTION (PROGRAM USED FOR CHAPTER 3)

The program presented here is aimed at developing a common generator of ODE (ordinary differential equations) functions automatically for the overall dynamic system. The arbitrary arrangement of planet gears and arbitrary parameter settings can be simply simulated by including the data listed in *ipdata.m*. Also additional details including reactions along the action line of mesh can be introduced without difficulty (only two terms *MDsp* and *MDrp* need to be changed, Sec 13.1.4). The flow chart for the ODE generation program is shown in Figure 7-2.

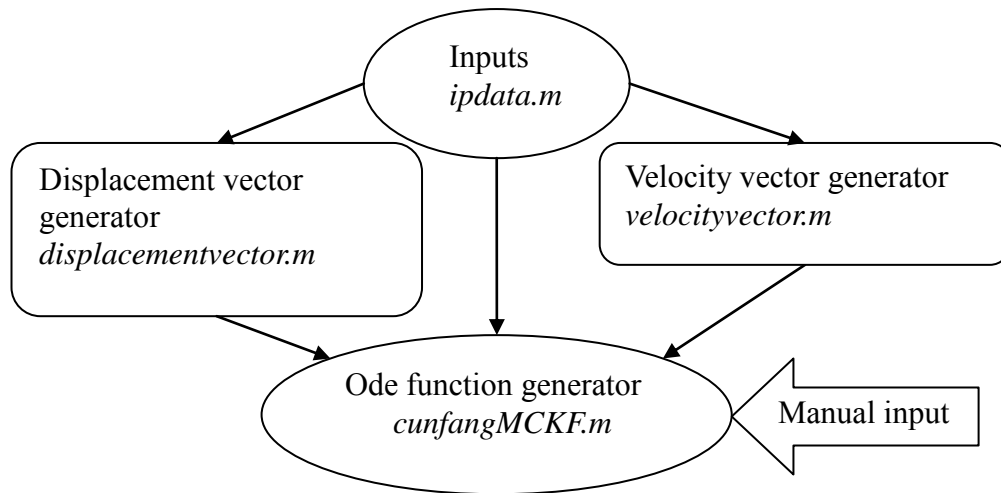


Figure 7-2 Flow chart of program for generation of ODE equations

Program *displacementvector.m* is developed to generate the displacement vector and optionally display each term in the displacement vector with associated physical meaning respectively (by using code after line 26).

Program *velocityvector.m* is developed to generate the velocity vector and optionally display each term in the velocity vector with associated physical meaning (by using code after line 26).

Program *cunfangMCKF.m* is developed to generate the ODE function⁶⁷. It requires *ipdata.m*, *displacementvector.m*, *velocityvector.m* and manual inputs (*MDsp* and *MDrp* at line 32, 103, 148, 173, 472, 543, 588, 614, 905, 939, 964, 1030, 1096, 1130, 1155, 1221, and governing equations at line 277, 285, 293, 301, 309, 317, 710, 718, 726, 734, 742, 750, 1288, 1296, 1304, 1312, 1320, 1332, and submission of Eqs3.53-56 at line 1380, 1394, 1410, 1424, 1440, 1500, 1514, 1533, 1547). The corresponding flow chart is shown in Figure 7-3.

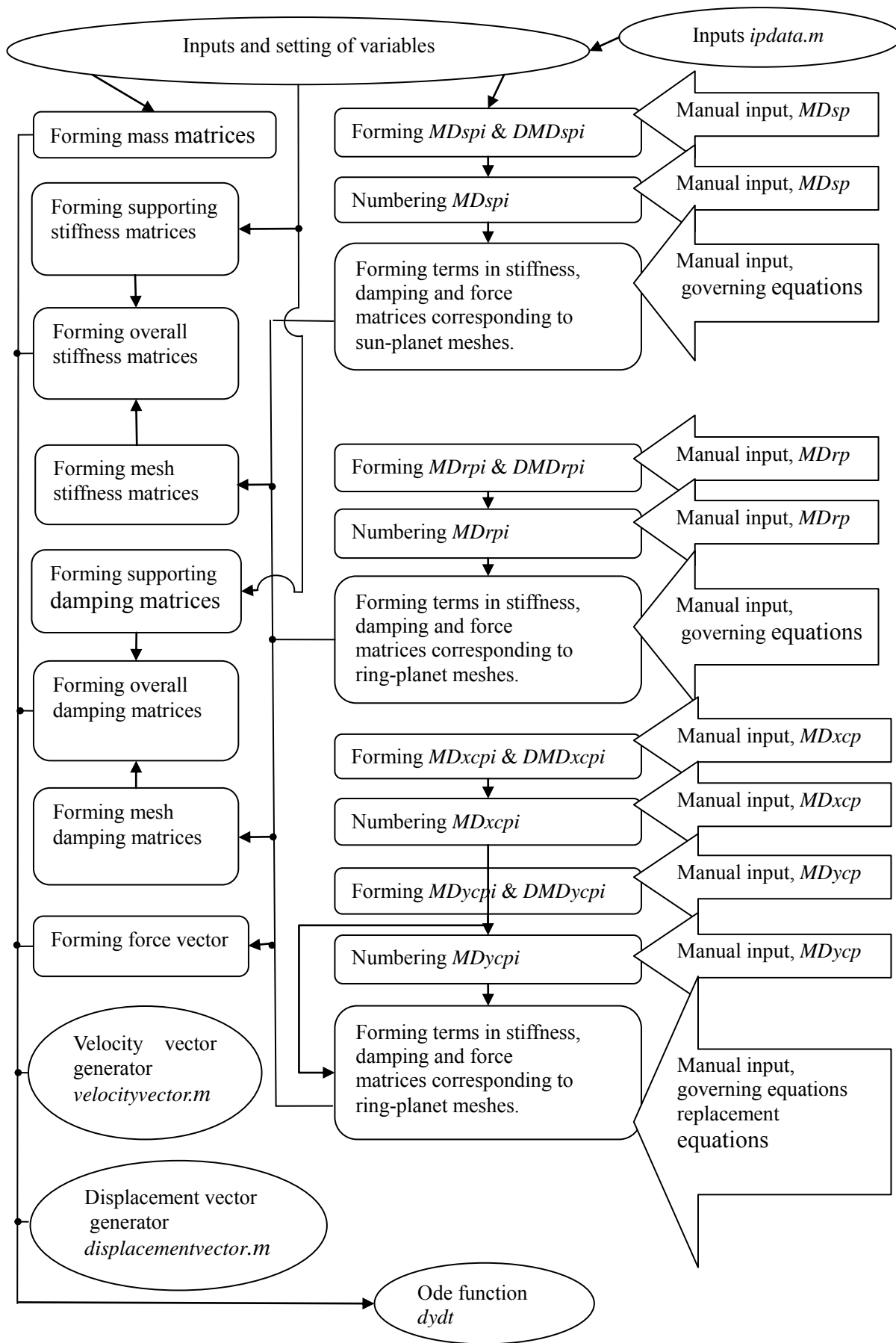


Figure 7-3 Flow chart of Ode function generator *cunfangMCKF.m*

7.4. GENERATION PROGRAM OF TRANSMISSION ERRORS (PROGRAM USED FOR CHAPTER 4)

7.4.1. PLANET GEAR PITCH ERROR

Programs *erppp.m* and *esppp.m* are developed to generate planet gear pitch error for ring-planet pairs and sun-planet pairs respectively. The same pitch error pattern is applied to all planet gears starting from the defined first tooth respectively.

It should be noticed that all coefficients used in each program should have the same corresponding value.

7.4.2. RING GEAR PITCH ERROR

Program *erppr.m* was developed to generate the ring gear pitch error for ring-planet pairs.

7.4.3. SUN GEAR PITCH ERROR

Program *espps.m* was developed to generate the sun gear pitch error for sun-planet pairs.

7.4.4. SUN GEAR - PLANET GEAR PAIR PROFILE ERROR

Program *espp.m* was developed to generate the assumed sun-planet profile error over the time of mesh for one pair of teeth.

7.4.5. RING GEAR - PLANET GEAR PAIR PROFILE ERROR

Program *erpp.m* was developed to generate the assumed ring-planet profile error over the time of mesh for one pair of teeth.

7.4.6. RANDOM EXCITATION

Programs *erpplan.m* and *esppran.m* were developed to model random excitation due to random tooth profile errors for ring-planet pairs and sun-planet pairs respectively.

7.4.7. TOOTH MESHING VARIATION

Program package (including *ymr1.m*, *ymr2.m*, *ymr3.m*, *ymrr.m*, *yms1.m*, *yms2.m*, *yms3.m*, and *ymss.m*) was developed to determine the number of teeth in mesh based on the time of meshing for all ring-planet and sun-planet pairs. It takes values in *ipdata.m* as inputs and gives out the number of teeth in mesh as a function of mesh cycle for different pairs respectively.

7.4.8. COMBINED PITCH AND PROFILE EXCITATION

A program package (including *erp1.m*, *erp2.m*, *erp3.m*, *esp1.m*, *esp2.m*, and *esp3.m*) was developed to generate the combined excitation due to pitch error, profile error and random features. It takes values in *ipdata.m* and outputs from programs listed in Sec 7.4.1 to 7.4.7 as inputs and gives out the combined excitation against mesh cycle for each pair in mesh respectively.

7.5. TOOTH MESH STIFFNESS (PROGRAM USED FOR CHAPTER 5)

The program used for chapter 5 was written to develop a common simulating method of torsional mesh stiffness of teeth in mesh. Features namely tooth mesh variation, equivalent root crack, localized spall, and arbitrary fault arrangement and resulting stiffness curves are included. The flow chart is shown in Figure 7-4.

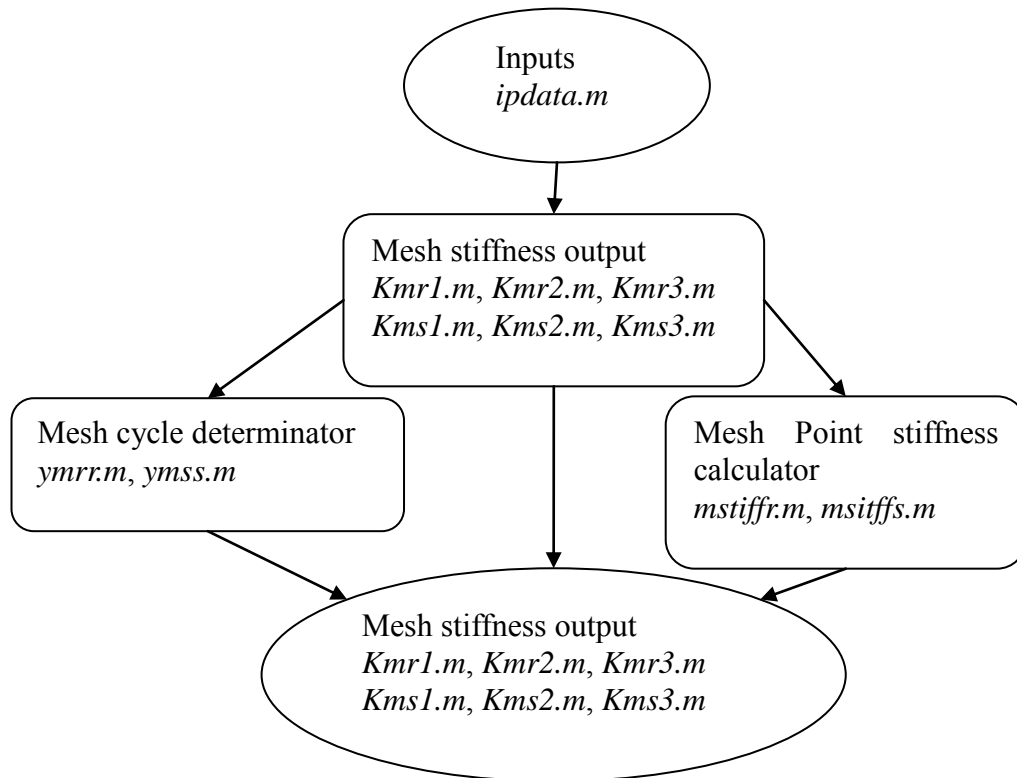


Figure 7-4 Flow chart of program used for tooth mesh stiffness

The program named Mesh Cycle Determinator takes the location of a mesh point along the mesh cycle as input and calculates whether or not the previous teeth are in mesh.

The program named Mesh Point Stiffness Calculator takes the location of a mesh point along the mesh cycle, number of teeth in mesh, which teeth are in mesh for both gears, and locations of mesh points along tooth meshing line as inputs and gives out a numerical result for torsional mesh stiffness at the mesh point. This program includes setting of tooth crack, tooth spall and assumed stiffness curves.

The program named Mesh Stiffness Output calculates the torsional mesh stiffness for the entire mesh period.

7.6. PROGRAM USED FOR CHAPTER 6

7.6.1. TORQUE-SPEED CURVE OF MOTOR

Program *TorM.m* was developed to generate the torque-speed curve of a motor. It takes the values listed in *ipdata.m* as inputs and calculates the motor torque against speed with units of rpm.

7.6.2. INERTIA OF CARRIER ARM WITH BUCKET WHEEL AND LOAD MATERIAL

Program *inertiaC.m* was developed to generate the inertia-displacement curve of the carrier arm with bucket wheel and load material. It takes the values listed in *ipdata.m* and real time torsional displacement of the carrier arm (result of ODE solver) as inputs and calculates the inertia against real time torsional displacement of the carrier arm. Cases such as those operating with or without load material, start loading, end loading and over load can be simulated by introducing corresponding values into *ipdata.m*.

7.6.3. MASS OF CARRIER ARM WITH BUCKET WHEEL AND LOAD MATERIAL

Program *massC.m* calculates the mass-displacement curve of the carrier arm with bucket wheel and load material. It takes the values listed in *ipdata.m* and real time torsional displacement of the carrier arm (result of ODE solver) as inputs and calculates the mass against real time torsional displacement of the carrier arm. Cases such as those operating with or without load material, start loading, end loading and over load can be simulated by introducing corresponding values into *ipdata.m*.

7.7. PROGRAM USED FOR CHAPTER 8

7.7.1. INPUT TORQUE

Program *TorqueS.m* was developed to simulate the input torque applied to the sun gear. It takes values listed in *ipdata.m* as inputs and calculates torque against speed of the sun gear with units of rpm.

7.7.2. OUTPUT TORQUE

Program *torqueOUT.m* was developed to simulate the output torque (value of torque due to load) applied to the carrier arm. It takes values listed in *ipdata.m* as inputs and calculates torque against real time torsional speed and displacement of the carrier arm (results of ODE solver). Cases such as those operating with or without load material, start loading, end loading and over load can be simulated by introducing corresponding values into *ipdata.m*.

7.7.3. SOLVER

Program *vdp1.m* was developed as required by the MATLAB solver *ode15s*. It needs the output of *cunfangMCKF.m* as part of the program and some find-replaces need to be done manually using the Edit-Find & Replace command .

7.8. PROGRAM USED FOR CHAPTER 9

7.8.1. RING-PLANET PROFILE ERROR ASSOCIATED WITH SPALLING

Program package (including *emr1.m*, *emr2.m*, *emr3.m*, and *emrrr.m*) generates the ring-planet profile error associated with spalling only. The type of tooth spalling simulated in this program package is a simplified case simulating the cutting off of material across the entire width of the tooth surface to introduce a platform in the mesh. The location of the centre line of the spalling (platform), width of the spalling (platform), maximum depth of the spalling, and the specific shape of the cross section of spalling can be arbitrarily simulated by introducing corresponding values into the program.

This package is also introduced into the Combined Pitch and Profile Excitation program as inputs.

7.8.2. SUN-PLANET PROFILE ERROR ASSOCIATED WITH SPALLING

Program package (including *ems1.m*, *ems2.m*, *ems3.m*, and *emsss.m*) was constructed to generate the sun-planet profile error associated with spalling only. The type of tooth spalling simulated in this program package is a simplified case representing the removal of material across the entire width of the tooth surface to introduce a platform in the mesh. The location of the centre line of the spalling (platform), width of the spalling (platform), maximum depth of the spalling, and the specific shape of the cross section of spalling can be arbitrarily simulated by introducing corresponding values into the program.

This package is also introduced into the Combined Pitch and Profile Excitation program as inputs.

7.9. SUMMARY OF CHAPTER

The MATLAB program was developed using symbolic math in order to generate the differential equations of a general model automatically, adjustable for different amounts of inputs automatically and was formed to be able to include more details or exclude existing details (e.g. interactive forces between mesh teeth, mount errors, etc.) with single modification on the inputs. Models with different numbers of planet gears with and without torsional/transverse responses can be easily simulated.

Every change on listed inputs can be automatically reflected into the overall equations of motion. Every change on the other inputs also can be automatically reflected into the overall equations of motion but may require some find-replace operations (22 in total, all listed in one m-file) to be done manually.

Practically all major changes or adding/deleting details on the model can be done within minutes before the program is ready to run. A one second simulation of a normal detailed model required approximately 6 hours computation with a PC equipped with Intel Core2Duo 3.0GHz CPU and 4GB RAM. To accelerate the computation, the MATLAB Compiler could be used in future work.

The MATLAB software requires the Symbolic Toolbox to run the programs

developed in this thesis. This is a major limitation as not all the versions of MATLAB include this toolbox (MATLAB version 7.1.0.246 was used in this research).

8. VIBRATION MODELLING WITH UNDAMAGED GEARS

In this chapter, the lumped mass modelling (developed over the former chapters) of the overall system including motor, coupling, reduction gearbox, planetary gearbox and simulated loading is built and analyzed with no damage on any gear components.

8.1. ASSUMPTIONS AND INPUT

In order to get a more realistic, more detailed and on the other hand a more computational efficient model, three groups of assumptions have been made respectively. In this section, assumptions which are related to undamaged gear models only, rather than matters concerned with input data values will be explained and corresponding input data or terms in the program will be specified in Table 8-1.

AN*	Explanation	Purpose	Value
1	Simulation is applied to large planetary gearbox with or without coupling and loading under operation condition of low speed, high torque (especially with load).	II	Variable inputs, mass, dimensions, and load
2	Due to AN 1, there is no backlash when gear system is in operation. Consequently MD_{sp} and MD_{rp} are zero or positive signed all the time. Teeth are assumed not to lose contact under any conditions.	I , III	Tooth separation phenomenon $SP_{sp} = 1$, $SP_{rp} = 1$
3	Only coupled torsional-transverse behavior of gear bodies is studied in a two dimensional model.	I	condition controller ipdata(51), cd=3
4	A single-stage planetary gear system contains one sun gear, one ring gear, one carrier arm and three equally spaced planet gears	III	number of planets n=3 planet spacing ipdata(201)=0 ipdata(202)= 34/51*pi ipdata(203)= 68/51*pi
5	Essential supporting shafts and bearings as well as gear casing are simulated on overall scale by introducing stiffness and damping terms	I , II , III	$[C_s]$ and $[k_s]$

Table 8-1 Assumptions and values of inputs associated with modelling with undamaged tooth
(*AN short for Assumption Number; I , more realistic; II , more detailed; III, more computational efficient)

AN*	Explanation	Purpose	Value
6	Geometric design of bucket wheel and carrier arm is kept as simple as possible. The wheel body of bucket wheel is simplified and approximately modeled as a hollow cylinder, relatively thin in length. Every bucket is modeled as a quarter cylinder with hollow centers.	III	Dimensions and density are chosen.
7	Tooth mesh friction is negligible.	III	
8	Gear mesh run out functions are set to zero.	III	$E_s = E_r = 0$ $E_{sp} = E_{rp} = 0$
9	Fluid coupling is modeled by using extra degree of freedom to simulate start up. In some cases (after starting up stage), fluid coupling is not modeled to simplify the model.	I , II , III	
10	Elements other than planetary gears are assumed to be perfectly rigid.	III	
11	Planetary gear bodies are assumed rigid and connected with mesh or supporting stiffness, damping as well as combined gear errors along the line of action.	III	
12	Associated with AN 11, planet gears are mounted on the carrier arm through the planet pin-bearing assembly which is simulated with introduced stiffness and damping features to simplify the equations of motion	III	
13	The rotational motion of the planet is completely uncoupled from the carrier arm's motion, as the zero friction force condition is the assumption to simplify the system (AN 7).	I , III	
14	Output torque is simulated by introducing load applied to the outer circle of the carrier arm including bucket wheel, buckets and loading material.	II , III	
15	Sun gear, ring gear and carrier arm are assumed to be perfectly concentric.	III	
16	An approximate numerical approach with three harmonics is used to simulate pitch and profile errors for all the gear pairs.	III	
17	Random pitch and profile errors are ignored.	III	
18	Supporting structure deformation is ignored for the simulation of transmission error in this research.	III	
19	Combined transmission error is on a scale of 10 μm	I	
20	All planet gears have the same pitch and profile error patterns.	III	

Table 8-1 (continued) Assumptions and values of inputs associated with modelling with undamaged tooth (*AN short for Assumption Number; I , more realistic; II , more detailed; III, more computational efficient)

AN*	Explanation	Purpose	Value
21	When more than one pair of teeth are in contact, the profile error is the same value as the largest excessive material or least lack of material.	I	
22	The second pair of teeth and the third pair of teeth in mesh have equal effect E_{mesh} on changing the mesh stiffness. (section 5.1)	III	
23	The values of mesh stiffness are kept constant so the mesh stiffness diagrams have lines instead of curves. More realistic simulations can also be obtained by using the program (Sec 7.5) developed in this research with a modification on the curve simulation equations.	I , III	
24	The coupling is assumed to have a slip of 3% at full load condition.	I , II	S=0.03
25	Reduction gear box ratio is assumed to ensure the output speed of planetary gear stage to be in the range of 6 rpm.	I	reduction gear box ratio ipdata(35) $ReductionRatio = 29.2971$
26	Sun gear, ring gear, planet gears, and carrier arm are assumed to be hollow cylinders in order to calculate the mass and inertia.	III	
27	An approximated loading condition is introduced to simulate the mass and inertia of loaded ore.	III	ore loading condition ipdata(92) $Olcc = 3.1$ single bucket ore drop ipdata(93)=0.8
28	Overload is simulated by increasing loading by overloading rate.	I	overloading rate ipdata(95)=10
29	Zero torque applied to ring gear from ring gear housing except reacting torque.	I , III	torque from base to ring gear ipdata(71) $T_{rb} = 0$
30	Zero stiffness applied to sun gear and carrier arm support in torsional direction.	III	stiffness of sun gear support in torsional direction ipdata(113) $k_{st} = 0$
31	Very high damping applied to planet-carrier connection in x and y direction.	I , III	damping of planet-carrier connection ipdata(63) and ipdata(64) $c_{px} = c_{py} = 10^4$ Ns/m

Table 8-1 (continued) Assumptions and values of inputs associated with modelling with undamaged tooth (*AN short for Assumption Number; I , more realistic; II , more detailed; III, more computational efficient)

AN*	Explanation	Purpose	Value
32	<p>Very high damping and stiffness applied to ring gear support in torsional direction. Ring gear is assumed to be fixed in torsional direction.</p> <p>Ring gear is assumed to be fixed onto the casing of the gear box.</p>	I , III	<p>damping of ring gear support in torsional direction ipdata(106)</p> $c_r = 10^6$ Ns/m <p>stiffness of ring gear support in torsional direction ipdata(116)</p> $k_r = 10^{10}$ N/m

Table 8-1 (continued) Assumptions and values of inputs associated with modelling with undamaged tooth (*AN short for Assumption Number; I , more realistic; II , more detailed; III, more computational efficient)

8.2. SIMULATION RESULTS

In this chapter three modelling cases of the undamaged gearbox are simulated. The first case represents the simulation where the bucket wheel, buckets and loading material are removed from the operational condition, and there is no combined gear error (transmission error) to simplify the model. The second case includes the bucket wheel, buckets and loading material (time variable, exists since loading up) to simulate the operational condition mainly during starting up and before loading up. There is also no combined gear error in order to limit computational time. The third case is the same as the second case except it has combined gear error. Results corresponding to case-1 are detailed and listed in this section. Differences between all three cases are discussed in Section 8.3.

For all the cases simulated in this thesis (including three cases in this chapter and case-4 in Chapter 9), synchronous signal averaging was used to analyze the vibration signals. After steady state rotational speed of the sun gear has been achieved, 4 revolutions of the sun gear, 2 revolutions of the planet gears and 1 revolution of the ring gear and the carrier arm are simulated for subsequent analysis due to the limitation of computational time (excess of 2 days was required for the simulation of one carrier arm revolution). Synchronous signal averaging was used to recover the vibration information relating to the components of interest where it is applicable. Frequency analysis was also employed.

One revolution of the sun gear was determined as when all sun teeth (in this thesis,

19 teeth) have been through the mesh (in this thesis, one of the three sun gear - planet gear meshes) once. One revolution of the ring gear was determined as when all ring teeth (in this thesis, 83 teeth) have been through the mesh (in this thesis, one of the three ring gear - planet gear meshes) once. One revolution of the carrier arm was defined as 360 degrees of carrier arm rotation about the ring gear which is assumed to be stationary. One revolution of a planet gear was defined as when all of the planet gear teeth have been through either one of the sun gear - planet gear meshes or the ring gear - planet gear meshes once.

The period of one revolution of each component shown in the figures uses the shaft position in degrees on the horizontal axis. For the sun gear, ring gear and planet gears signals, the term, shaft position, was defined to be the angular position of the shaft/gear about the corresponding mesh point rather than the axis of the shaft/gear. Zero degrees at the start corresponds to the start mesh point and 360 degrees denotes when the tooth mesh is back to the starting point. For the carrier arm signals, the term, shaft position, was defined to be the angular position of the carrier arm shaft about its own axis.

The following figures (Figure 8-1 to Figure 8-28) show the simulation results of case one from startup.

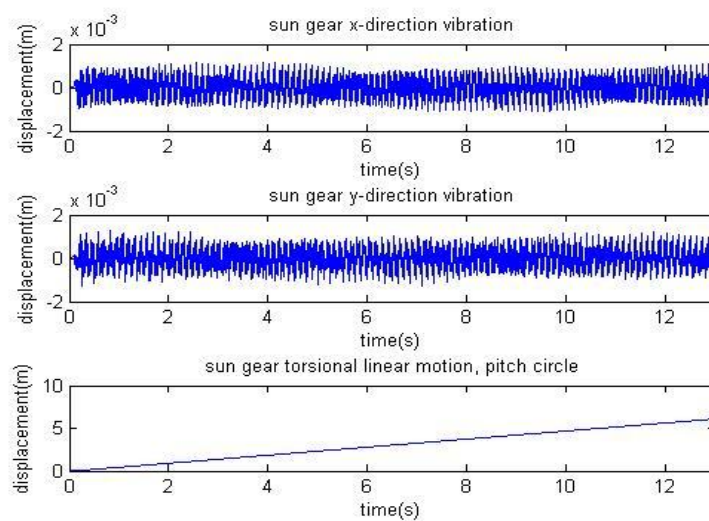


Figure 8-1 Case-1 sun gear time(s)-displacement(m)

Figure 8-1 shows the sun gear dynamic vibration signals including start up. The transverse signals shows that the steady state speed has been achieved within 0.3s. The torsional linear motion of the sun gear represents the circular motion of any point of the sun gear pitch circle along the pitch circle, and the linearity of the line indicates the steady state rotational speed.

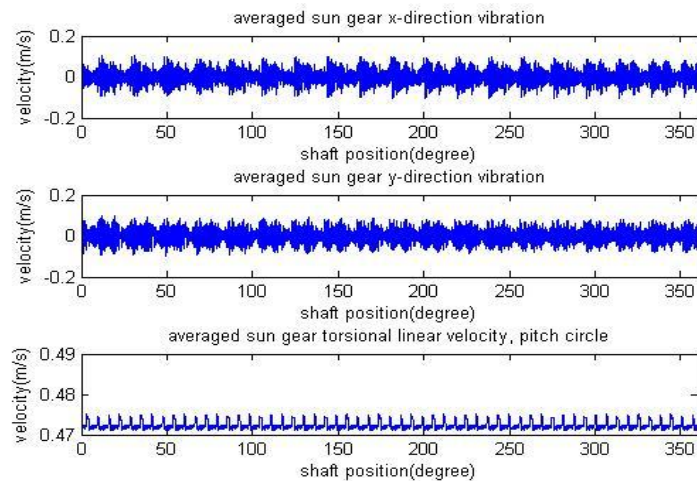


Figure 8-2 Case-1 sun gear averaged shaft position(degree)-velocity(m/s) vibration

There are 19 humps in the period of transverse signals shown in Figure 8-2, which is equal to the number of sun gear teeth. There are 57 pulses in the rotation velocity signal of sun gear (shown in Figure 8-2 and 8-3), which can be calculated as the number of sun gear teeth multiplied by the number of planet gears ($19 \times 3 = 57$, accuracy is affected by low number of revolutions used for averaging).

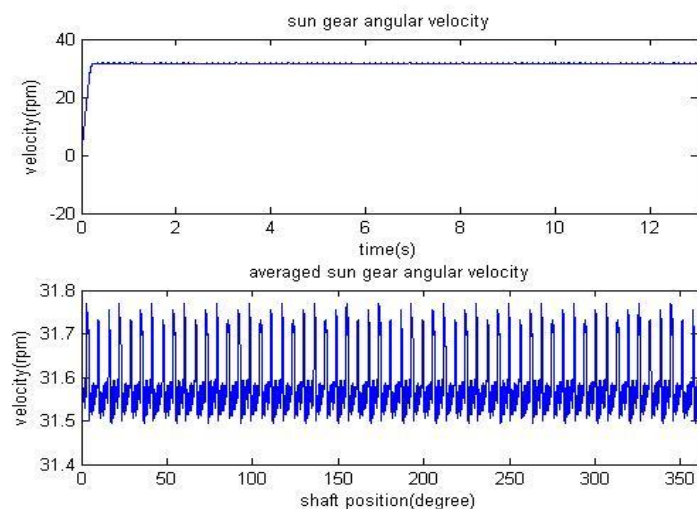


Figure 8-3 Case-1 sun gear time(s)-torsional velocity(rpm) and averaged shaft position(deg)-torsional velocity(rpm) vibration

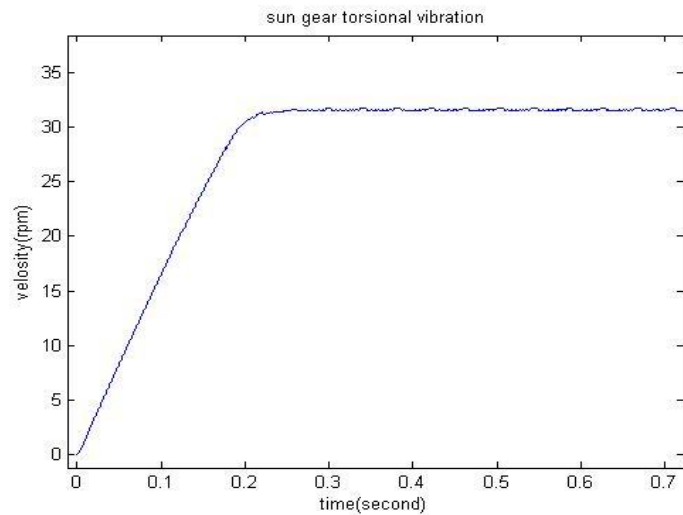


Figure 8-4 Case-1 enlarged figure shows starting up of sun gear time(s)-torsional velocity(rpm)

It is shown by Figure 8-3 that starting up can be simulated by the model developed in this thesis (enlarged figure shown in Figure 8-4). However, starting up can affect the results of signal averaging, frequency spectrum, and other methods used in detecting gear faults. In order to avoid the effect of starting up on signal processing, all signal processing used the vibration signal after steady state rotational speed had been obtained.

Figure 8-5, 8-6, 8-7 show the frequency spectrum from the sun gear x-direction, y-direction and torsional velocity vibration signals respectively. It can be seen that the former two show four harmonic frequencies but with very strong sideband effects. The latter one shows harmonic frequencies relatively more clearly. This shows that sun gear torsional vibration signal is superior than transverse signals for frequency analysis. The four harmonics should indicate the number of sun gear teeth multiplied by integers, however, low accuracy is obtained as only a small number of revolutions have been used for signal averaging.

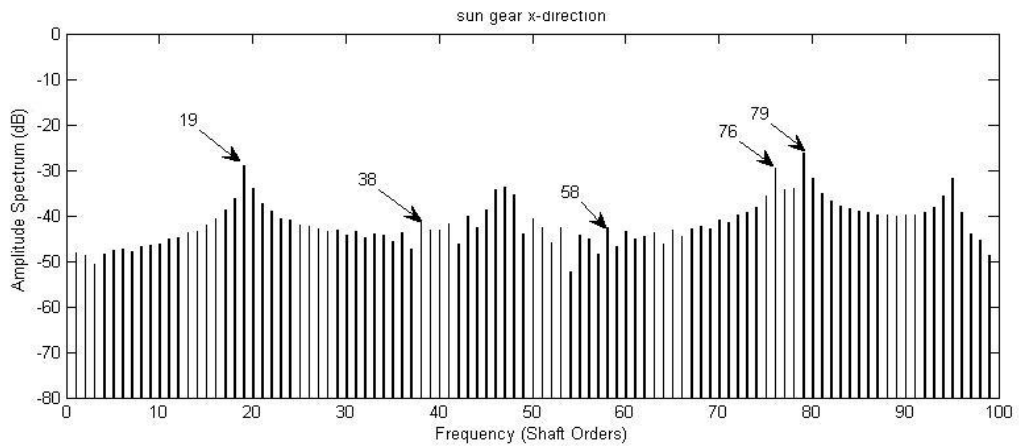
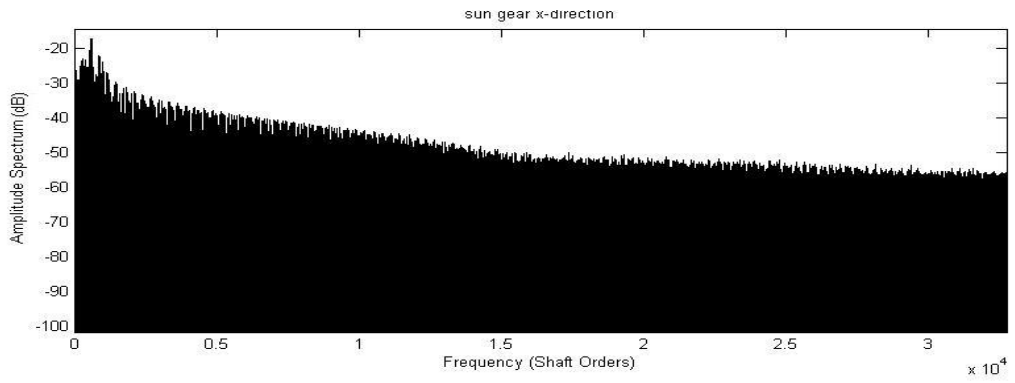


Figure 8-5 Case-1 Frequency spectrum of sun gear x direction velocity vibration

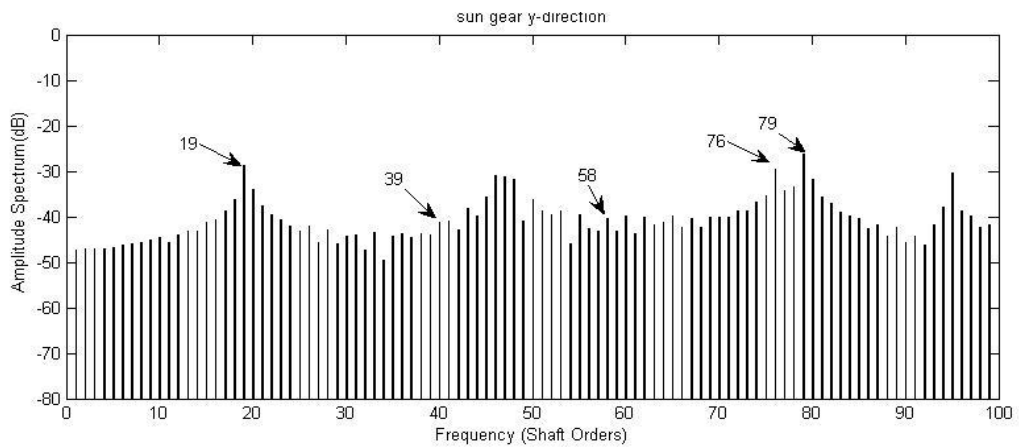
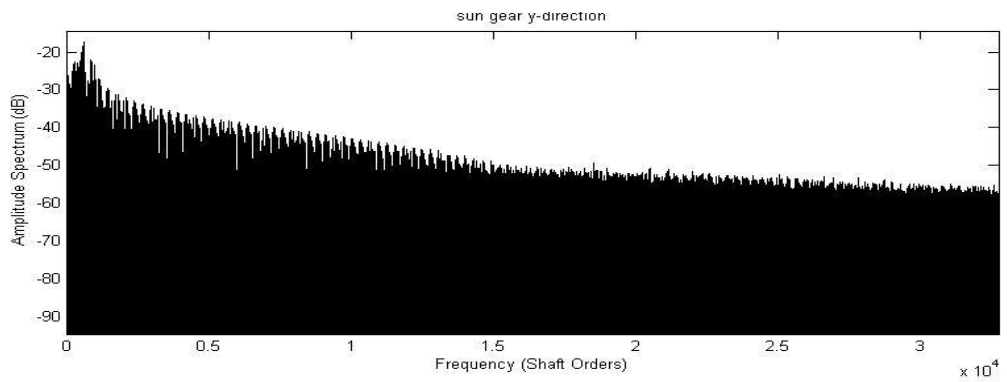


Figure 8-6 Case-1 Frequency spectrum of sun gear y direction velocity vibration

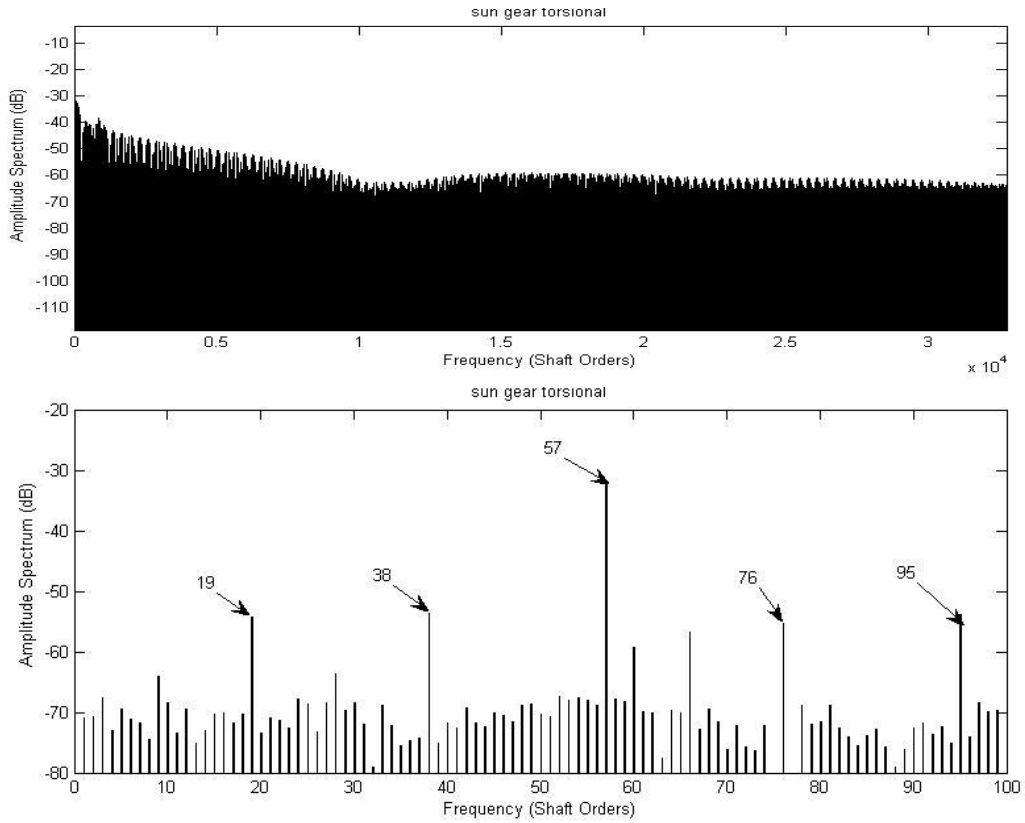


Figure 8-7 Case-1 Frequency spectrum of sun gear torsional velocity vibration

Figure 8-8 and 8-9 show ring gear vibrations as a function of time and shaft position. All signals fluctuate about zero as it is assumed and simulated that the ring gear is fixed to the gearbox host structure. However, Figure 8.8 shows that the ring gear rotates a small amount (0.1mm) under the action of the gearbox load as expected.

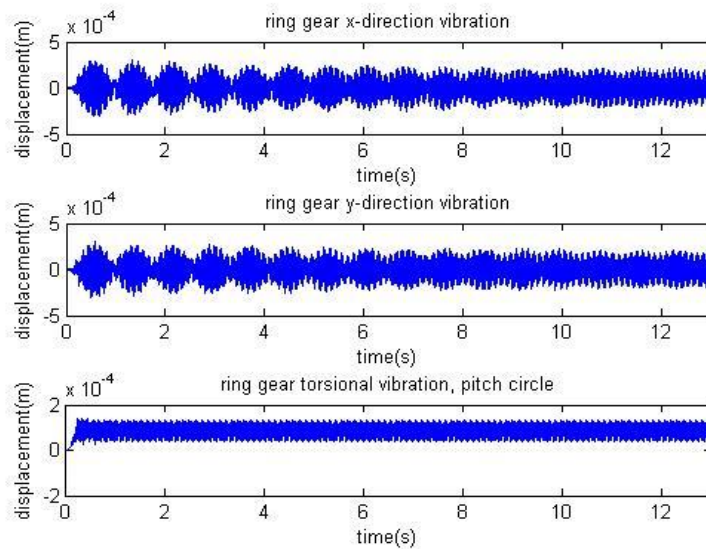


Figure 8-8 Case-1 ring gear time(s)-displacement(m)

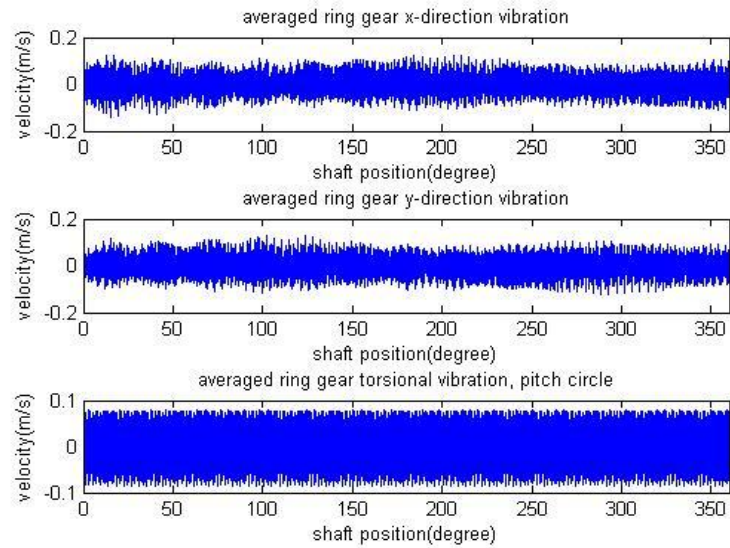


Figure 8-9 Case-1 ring gear averaged shaft position(degree)-velocity(m/s) vibration

Figure 8-10, 8-11, 8-12 show frequency spectrum from the ring gear x-direction, y-direction and torsional velocity vibration signals respectively. It can be seen that the former two show four harmonic frequencies but with very strong sideband effects. The latter one shows harmonic frequencies relatively more clearly. The Ring gear torsional vibration signal appears to be superior than transverse signals for frequency analysis. The harmonics should indicate the number of ring gear teeth multiplied by integers, which are 83, 166, 249, 332 as shown in Figure 8-12; however, low accuracy is obtained for transverse signals as only a small number of revolutions are used for signal averaging.

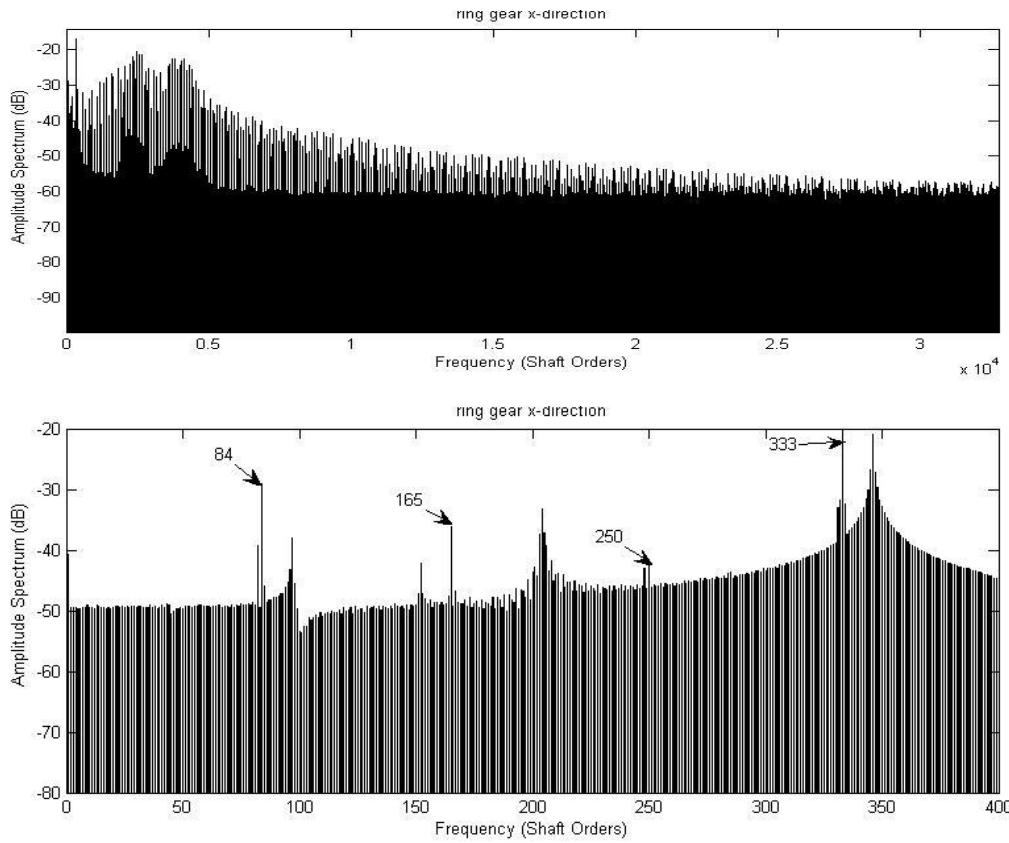


Figure 8-10 Case-1 Frequency spectrum of ring gear x direction velocity vibration

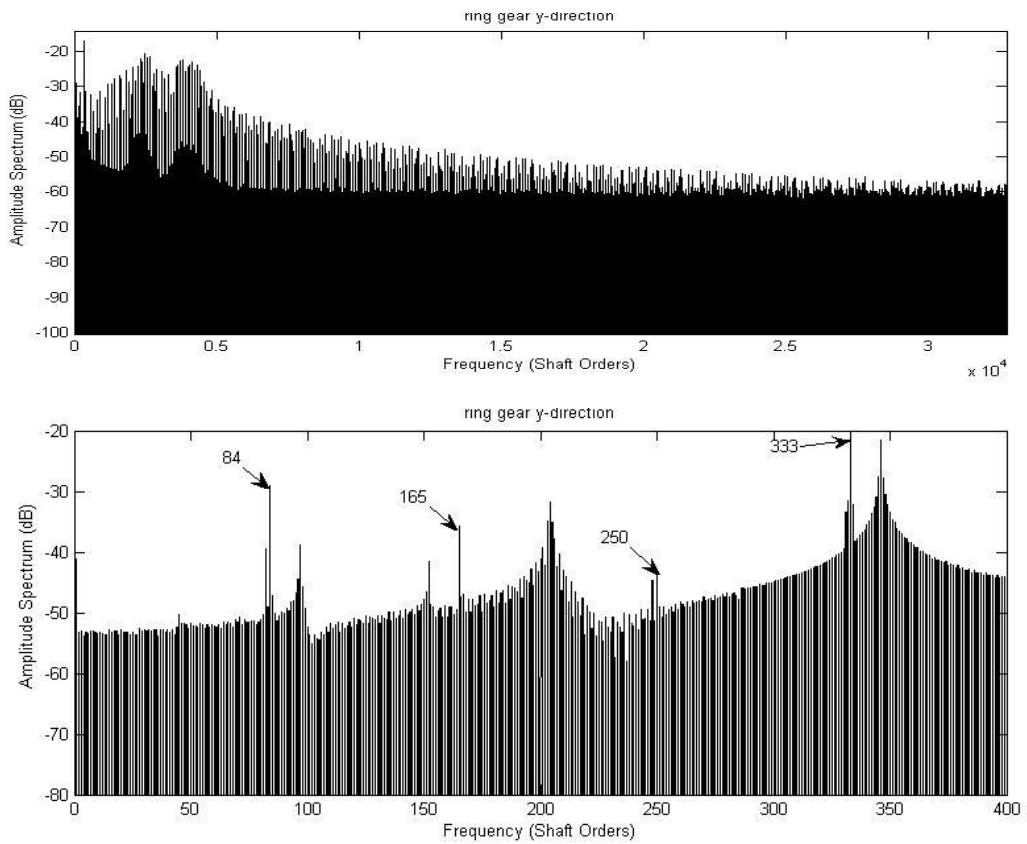


Figure 8-11 Case-1 Frequency spectrum of ring gear y direction velocity vibration

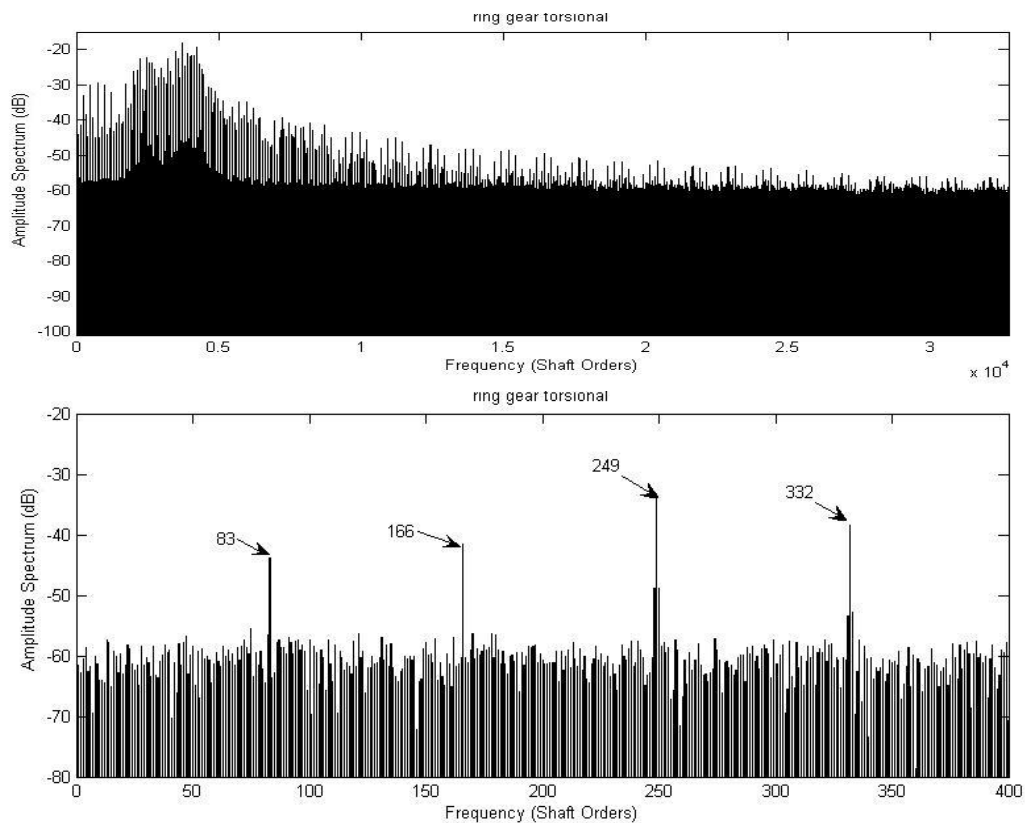


Figure 8-12 Case-1 Frequency spectrum of ring gear torsional velocity vibration

Figure 8-13 to 8-19 show results corresponding to the carrier arm. The transverse signals shows that steady state motion has been achieved within 0.3s in Figure 8-13. The torsional linear motion of the carrier arm represents the circular motion of the planet gear mount point on the carrier arm, and the linearity of the line indicates the steady state rotational speed. Starting up can be seen in Figure 8-15 with enlarged figure shown in Figure 8-16 for carrier arm.

There are 83 pulses in the carrier arm torsional velocity signal shown in Figure 8-15, which is equal to the number of ring gear teeth.

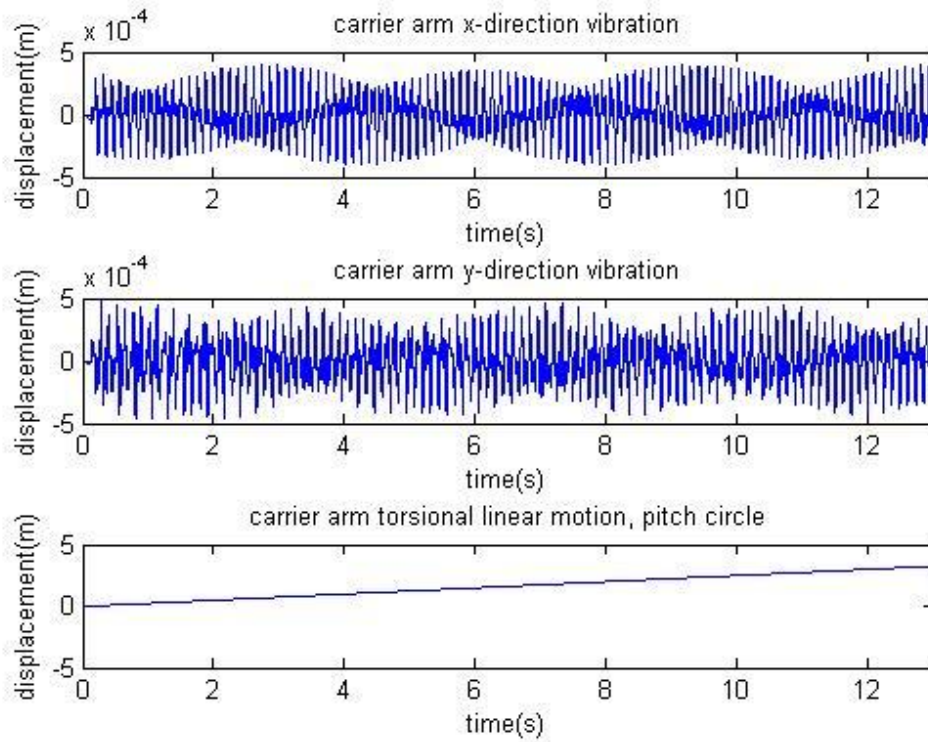


Figure 8-13 Case-1 carrier arm time(s)-displacement(m)

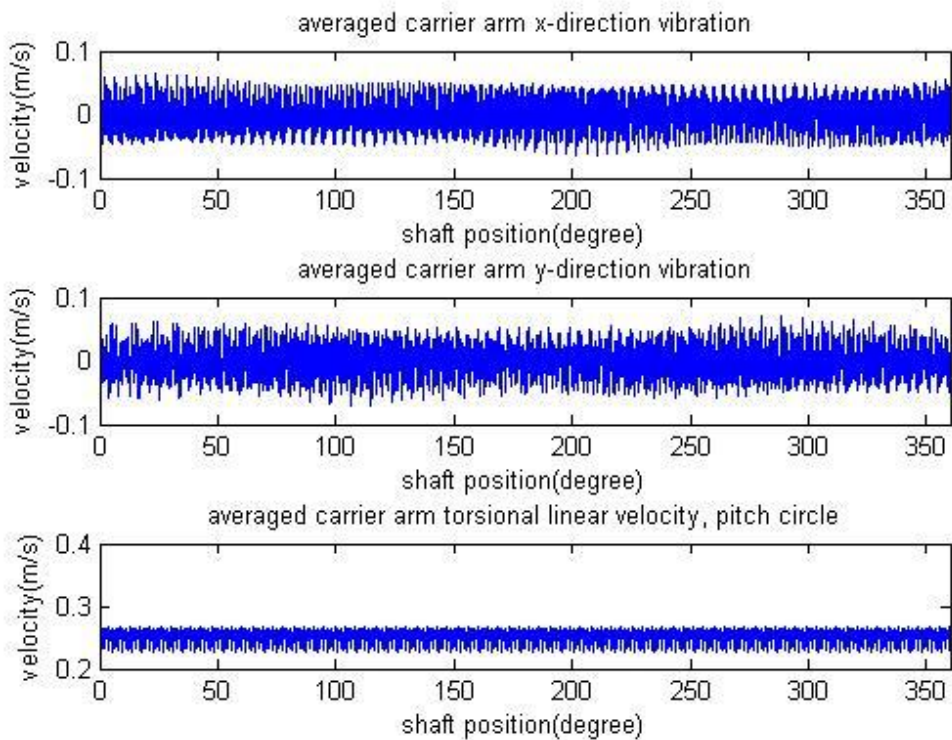


Figure 8-14 Case-1 carrier arm averaged shaft position(degree)-velocity(m/s) vibration

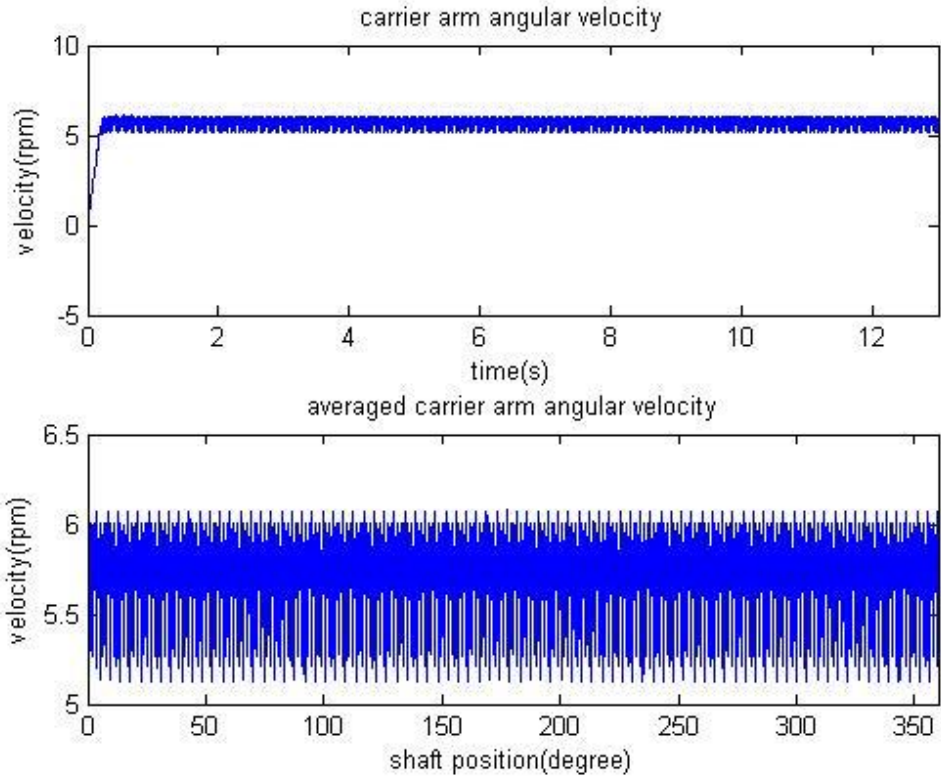


Figure 8-15 Case-1 carrier arm time(s)-torsional velocity(rpm) and averaged shaft position(deg)-torsional velocity(rpm) vibration

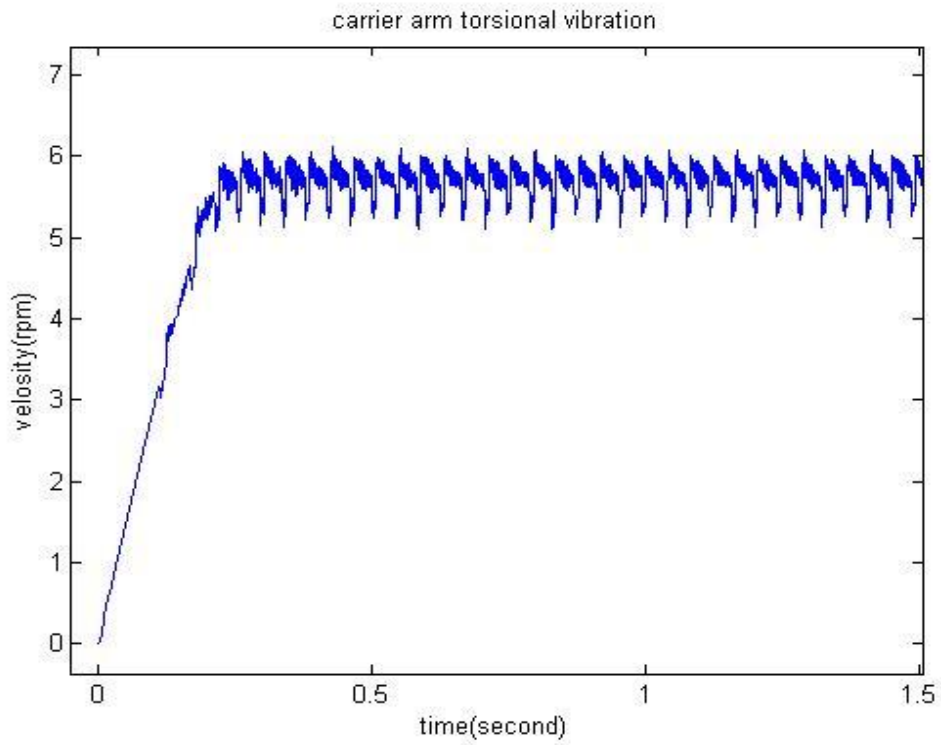


Figure 8-16 Case-1 enlarged figure shows starting up of carrier arm time(s)-torsional velocity(rpm)

Figure 8-17, 8-18, 8-19 show the frequency spectrum from the carrier arm x-

direction, y-direction and torsional velocity vibration signals respectively. It can be seen that the former two show four harmonic frequencies but with very strong sideband effects. The latter one shows harmonic frequencies more clearly. The harmonics should indicate the number of ring gear teeth multiplied by integers, which are 83, 166, 249, 332 as shown in Figure 8-19; however, low accuracy is obtained for transverse signals as only a small number of revolutions are used for signal averaging. The carrier arm torsional vibration signal is shown to be superior than the corresponding transverse signals for frequency analysis.

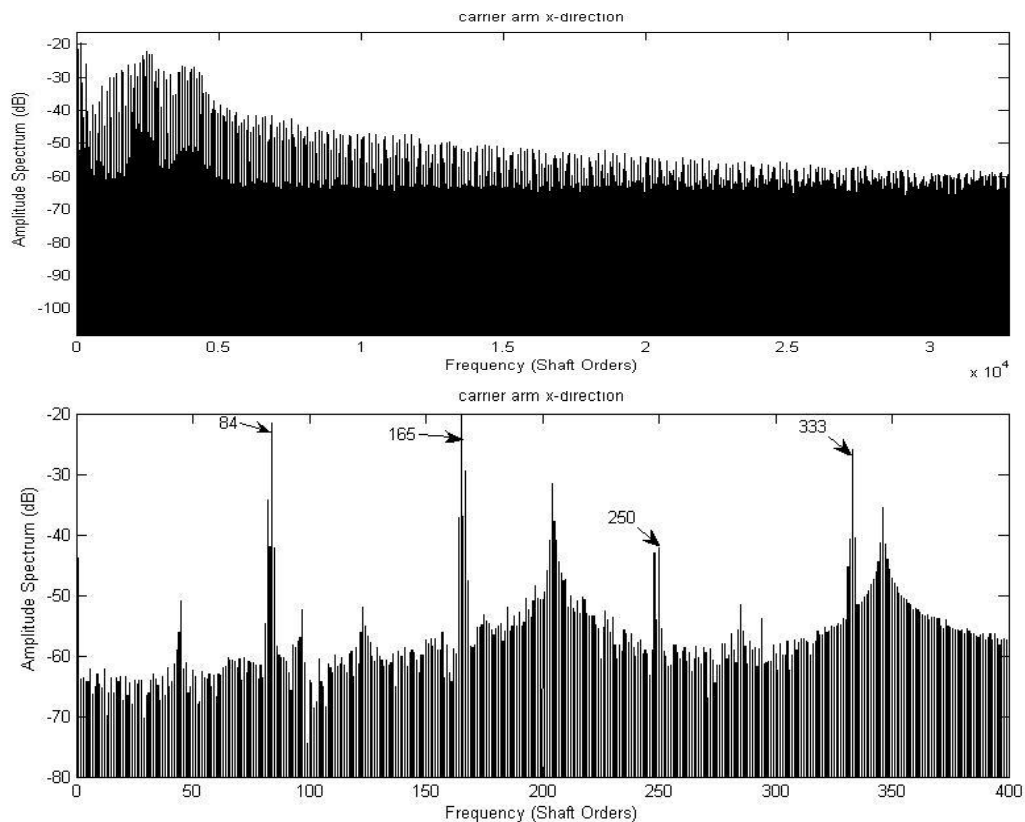


Figure 8-17 Case-1 Frequency spectrum of carrier arm x direction velocity vibration

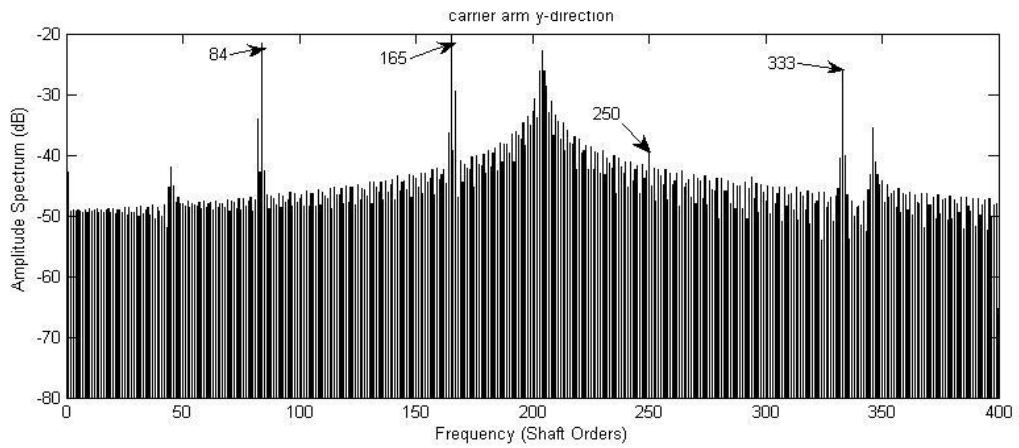
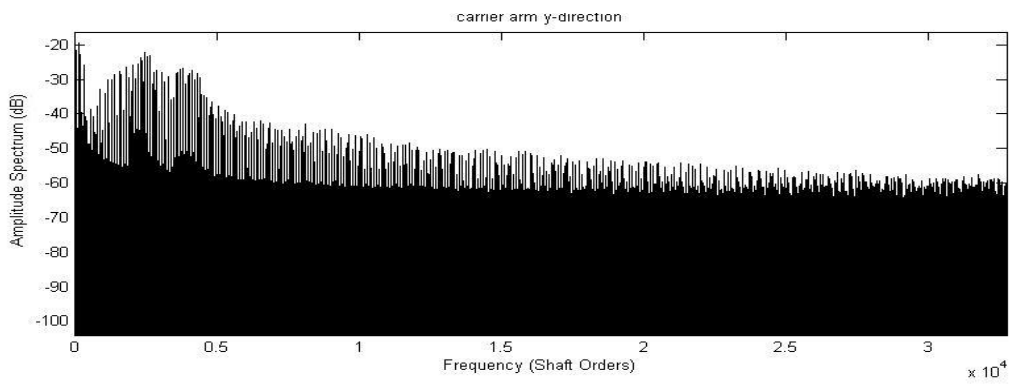


Figure 8-18 Case-1 Frequency spectrum of carrier arm y direction velocity vibration

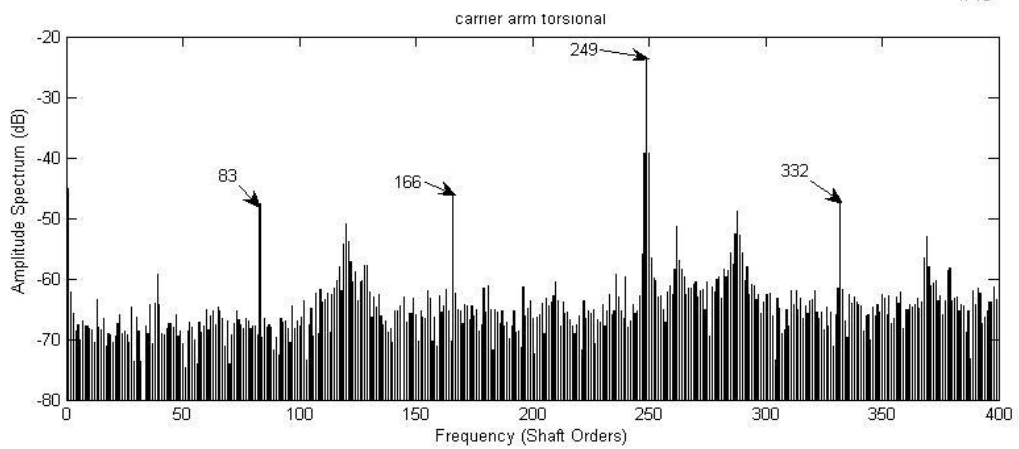
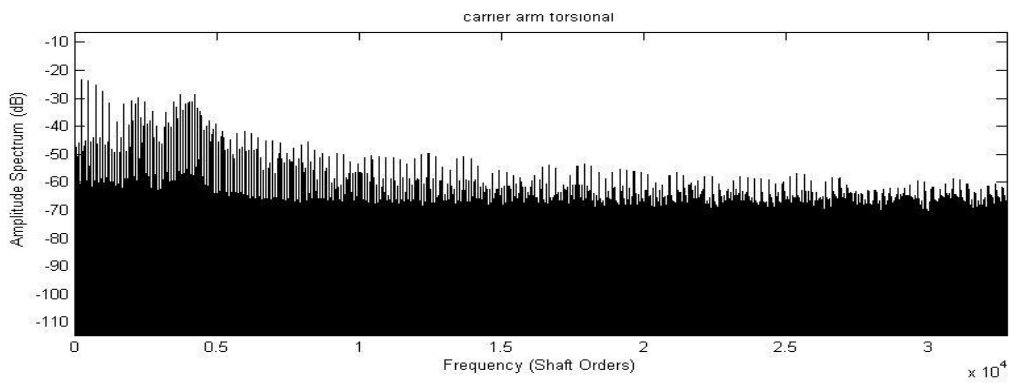


Figure 8-19 Case-1 Frequency spectrum of carrier arm torsional velocity vibration

Figure 8-20 to 8-26 show results corresponding to the planet gears. Figure 8-20, 8-21 and 8-22 show x direction motion about the sun gear centre, y direction motion about the sun gear centre and angular motion about the mount point of three planet gears respectively. The linearity of angular motion lines indicates the steady state rotational speed of planet gears about their mount points.

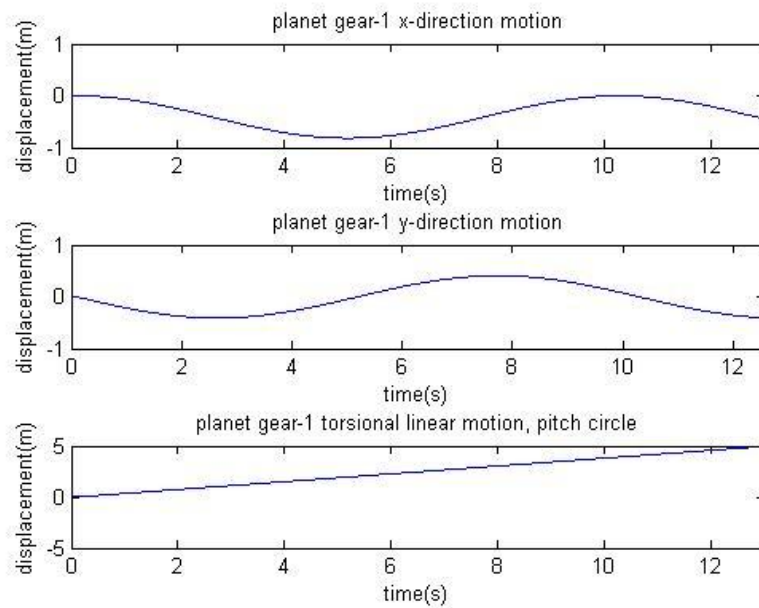


Figure 8-20 Case-1 planet gear-1 time(s)-displacement(m)

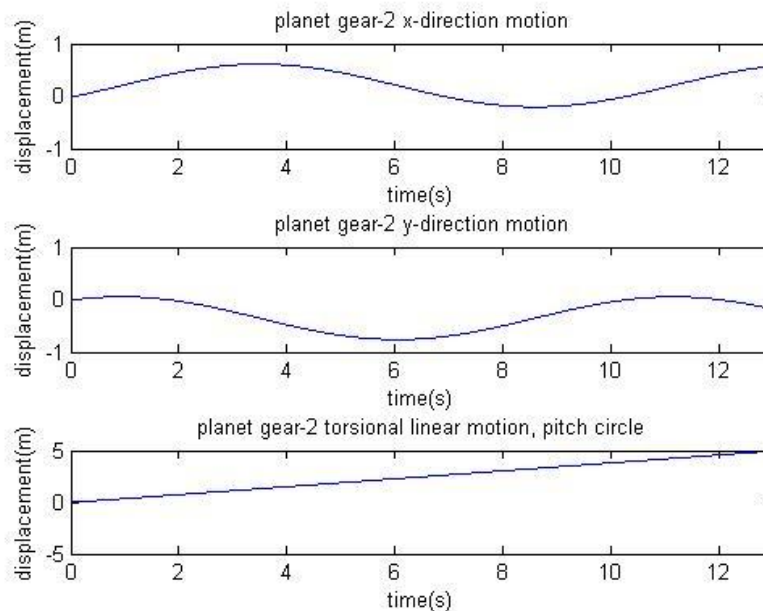


Figure 8-21 Case-1 planet gear-2 time(s)-displacement(m)

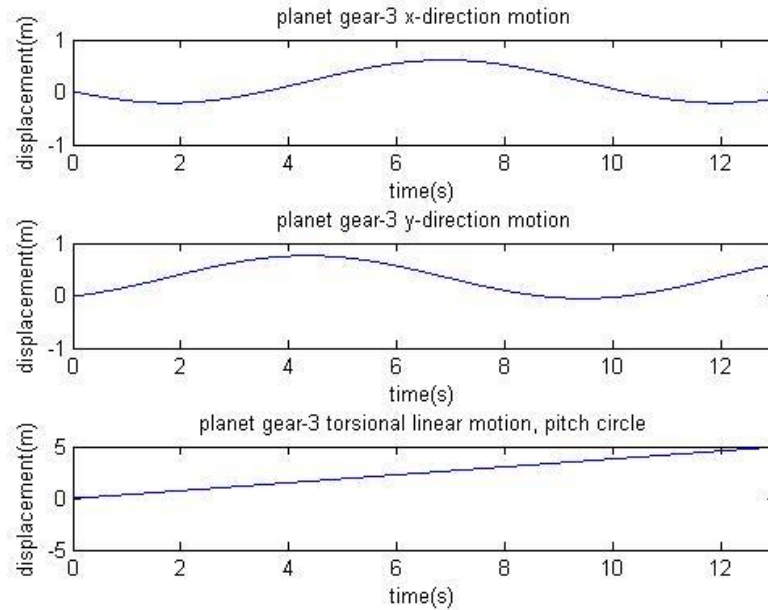


Figure 8-22 Case-1 planet gear-3 time(s)-displacement(m)

Figure 8-23 shows the averaged signals for the first planet gear. It can be seen that the synchronous signal averaging based on planet gear revolution (rotation about planet gears' mount points) is not practical on the x and y displacement signals as they oscillate about the sun gear centre with the carrier arm motion.

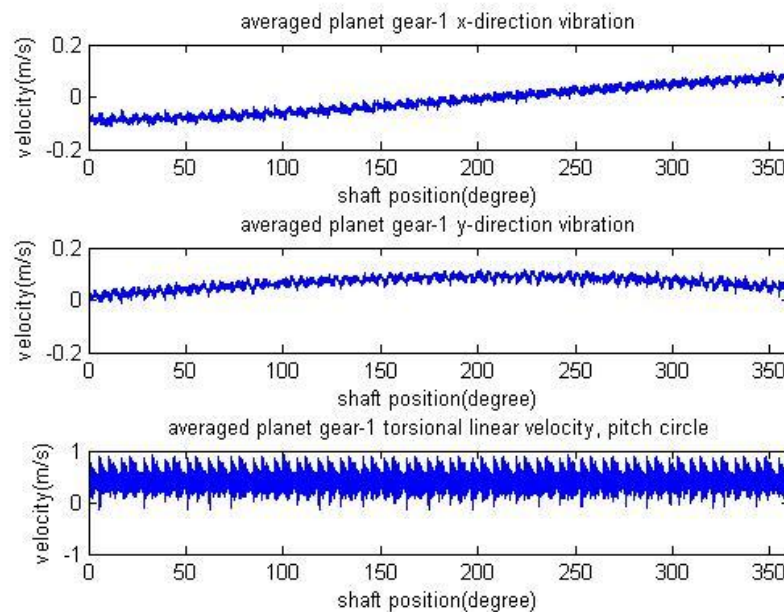


Figure 8-23 Case-1 planet gear-1 averaged shaft position(degree)-velocity(m/s) vibration

Figure 8-24, 8-25, and 8-26 show the frequency spectrum from the first planet gear

x-direction, y-direction and torsional velocity vibration signals respectively. The frequency spectrum from torsional signal shows four harmonic frequencies more clearly, more accurately indicating the number of planet gear teeth and with less sideband effects than those from transverse signals. Planet gear torsional vibration signal is seen to be superior than transverse signals for frequency analysis. Based on similar results on the sun gear, ring gear and carrier arm, a conclusion can be made that the torsional vibration signal is far superior than the transverse signals for frequency analysis for all rotating components of planetary gearboxes.

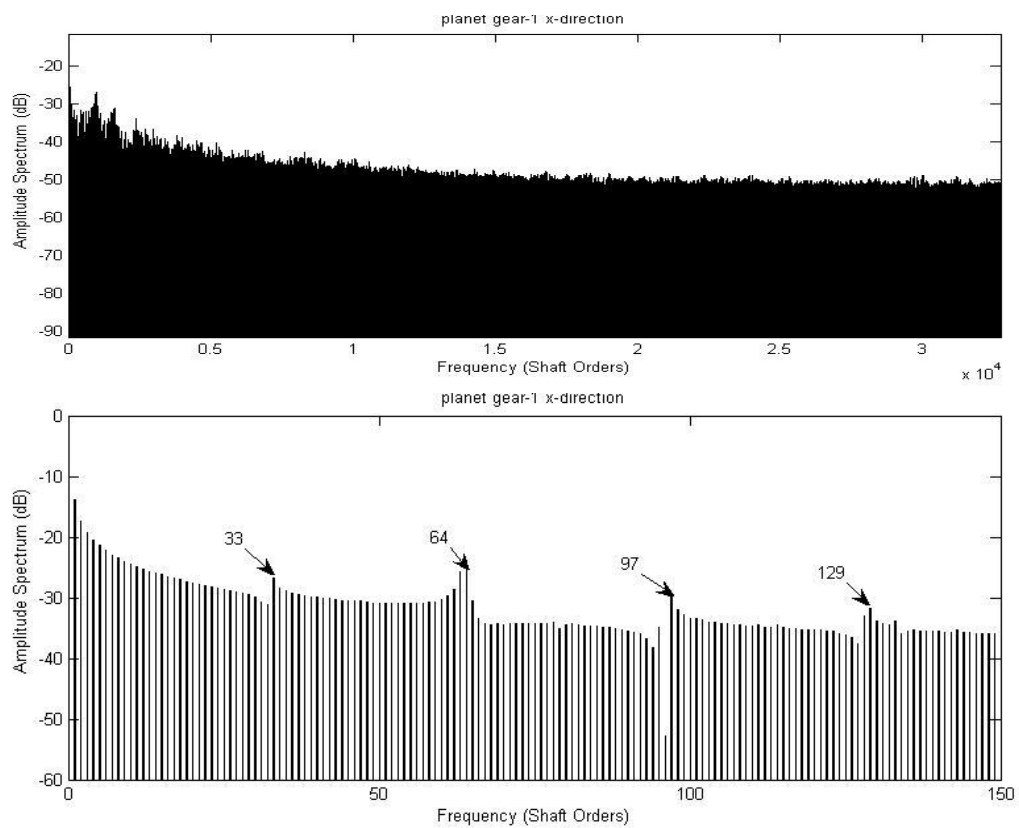


Figure 8-24 Case-1 Frequency spectrum of planet gear-1 x direction velocity vibration

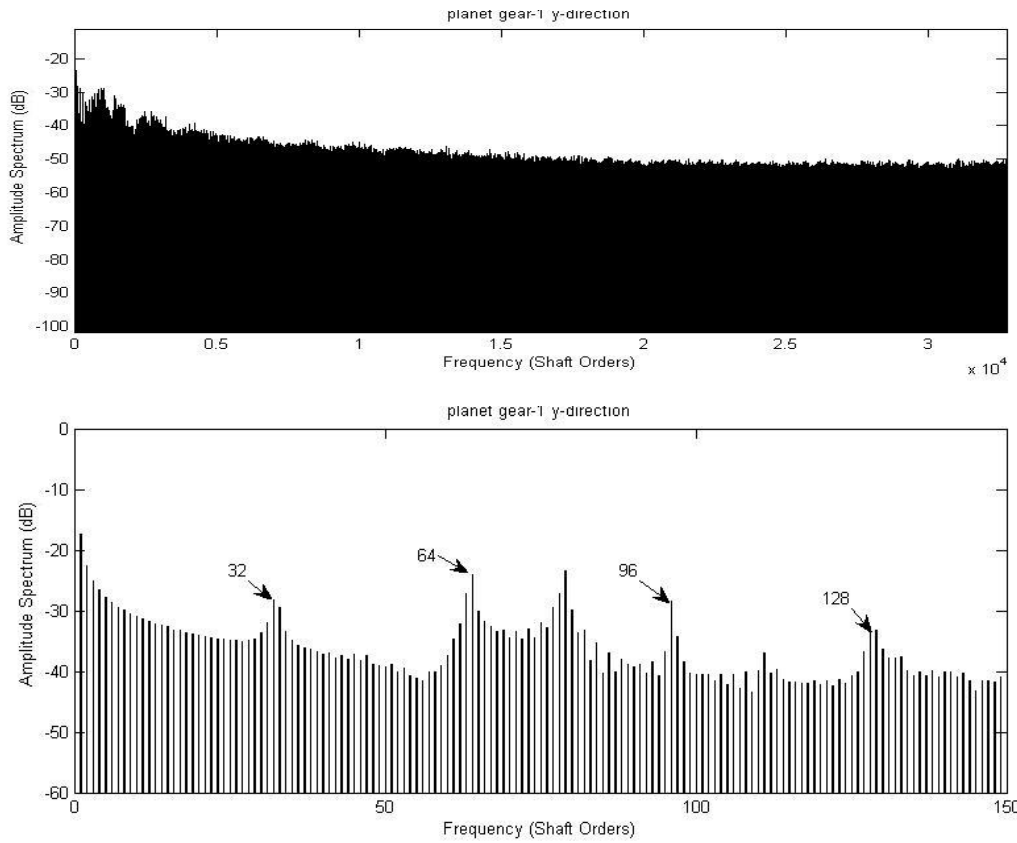


Figure 8-25 Case-1 Frequency spectrum of planet gear-1 y direction velocity vibration

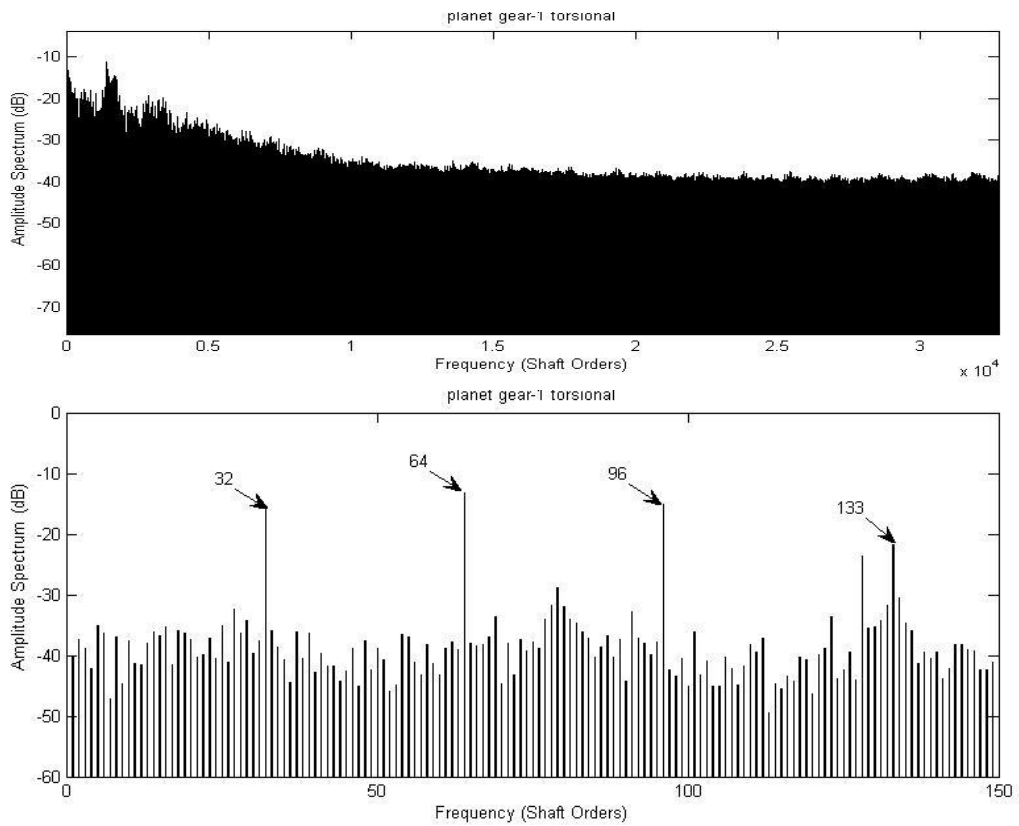


Figure 8-26 Case-1 Frequency spectrum of planet gear-1 torsional velocity vibration

8.3. COMPARISON OF CASE-1, CASE-2 AND CASE-3

Similar results are obtained in case-2 (Appendix 13.2) and case-3 compared to case-1 in Section 8.2. Only the major differences are listed and discussed as shown in the following figures.

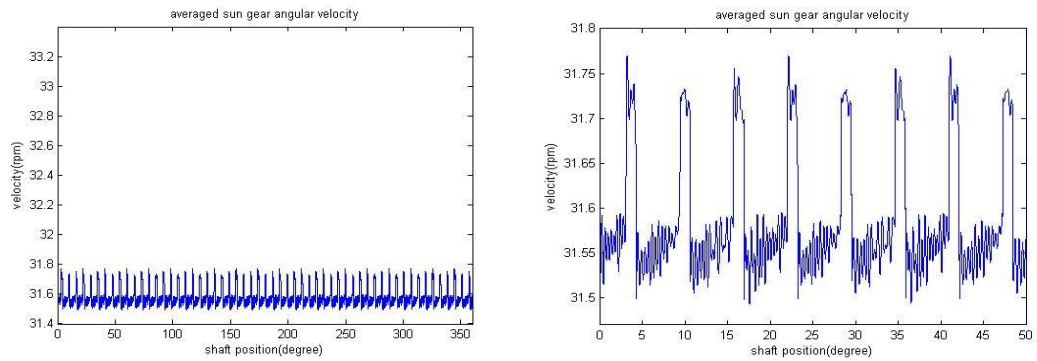


Figure 8-27 (a) (b) Case-1 averaged sun gear shaft position(degree)-torsional velocity(rpm) vibration and enlarged figure

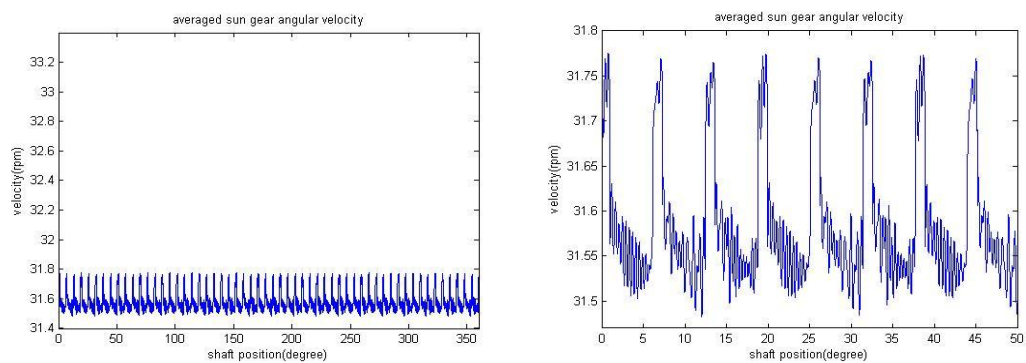


Figure 8-27 (c) (d) Case-2 averaged sun gear shaft position(degree)-torsional velocity(rpm) vibration and enlarged figure

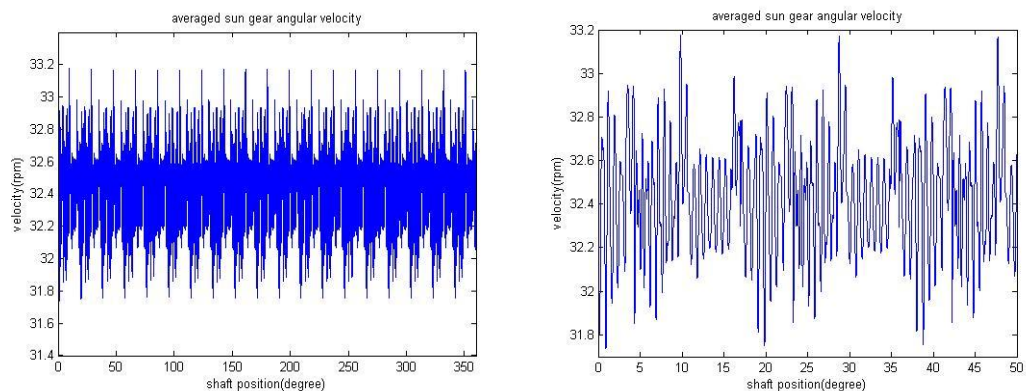


Figure 8-27 (e) (f) Case-3 averaged sun gear shaft position(degree)-torsional velocity(rpm) vibration and enlarged figure

Figure 8-27 (a) and (b) show averaged sun gear shaft position(degree)-torsional

velocity(rpm) vibration and enlarged figure in case-1. Very similar results (Figure 8-27 c and d) are shown in case-2 which has bucket wheel mass and inertia while case-1 does not. When combined gear error has been introduced into the simulation (case-3), the sun gear torsional speed is slightly increased and the tooth mesh cycle becomes unclear and the irregularity is increased and enhanced in the vibration signal compared to both case-1 and case-2.

Figure 8-28 shows the comparison of carrier arm velocity signals obtained in case-1, case-2 and case-3.

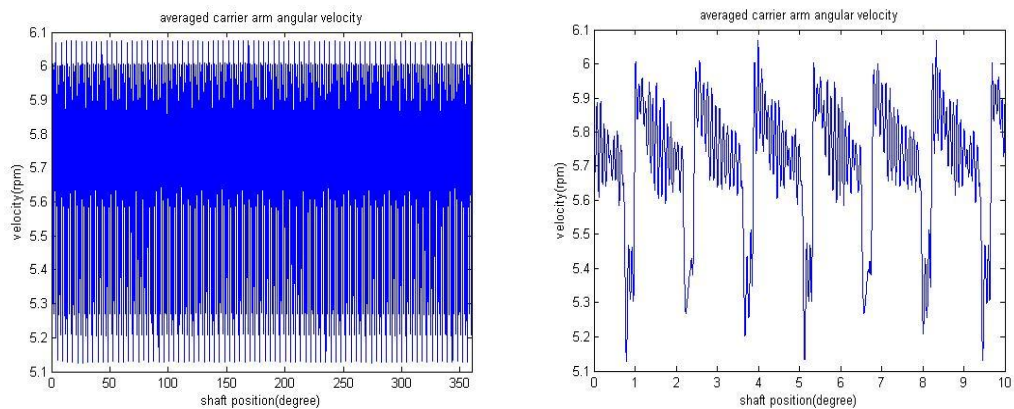


Figure 8-28 (a) (b) Case-1 averaged carrier arm shaft position(degree)-torsional velocity(rpm) vibration and enlarged figure

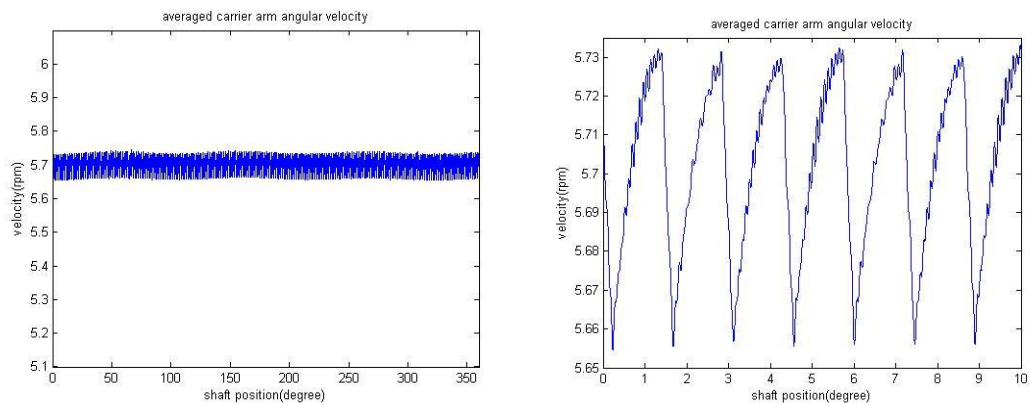


Figure 8-28 (c) (d) Case-2 averaged carrier arm shaft position(degree)-torsional velocity(rpm) vibration and enlarged figure

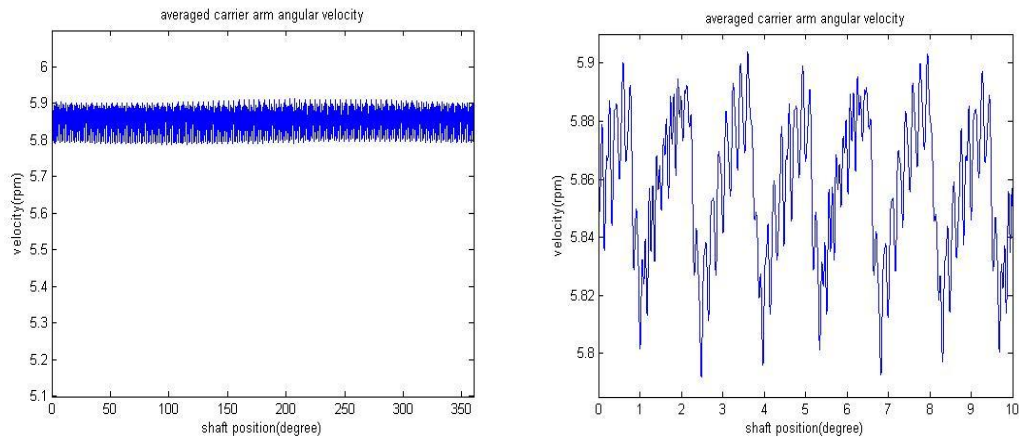


Figure 8-28 (e) (f) Case-3 averaged carrier arm shaft position(degree)-torsional velocity(rpm) vibration and enlarged figure

Figure 8-28 (a) and (b) show averaged carrier arm shaft position(degree)-torsional velocity(rpm) vibration and enlarged figure in case-1. As there is no bucket wheel mass and inertia included, the vibration signal varies in a large range from approximately 5 to 6 rpm and the signal is relatively noisy compared to case-2 which also has no combined gear error. The signal fluctuation range is reduced by a factor of 10 times when the large mass and inertia (bucket wheel) is included as for case-2. When the combined gear error has been introduced into the simulation (case-3), the carrier arm torsional speed is slightly increased and the signal irregularity is increased and enhanced in the vibration signal as compared to that of case-2.

Case-1 simulates the planetary gearbox without accessories (such as bucket wheel, buckets and other rotating components with high mass and inertia); the resulting signals are noisy and have big fluctuations which increase the difficulties for signal processing and fault detection. Case-2 and Case-3 have large mass and inertia terms by including bucket wheel and buckets, therefore they can simulate the overall system under operational conditions. Case-3 includes combined gear to be more realistic; however it requires longer computational time.

In Figure 8-29 it can be seen that even though very few revolutions had been averaged, there are 20 humps in the time period for the averaged sun gear x and y direction vibration signals in case-2 instead of 19 humps in case-1 while the sun gear has 19 teeth for both cases. Both torsional signals have $19 \times 3 = 57$ (number of the sun gear teeth multiplied by the number of planet gears) pulses shown in one carrier arm

revolution. This is due to the effectiveness of planet phasing and tooth mesh phasing, as discussed by several researchers including Parker's work^{56, 68}.

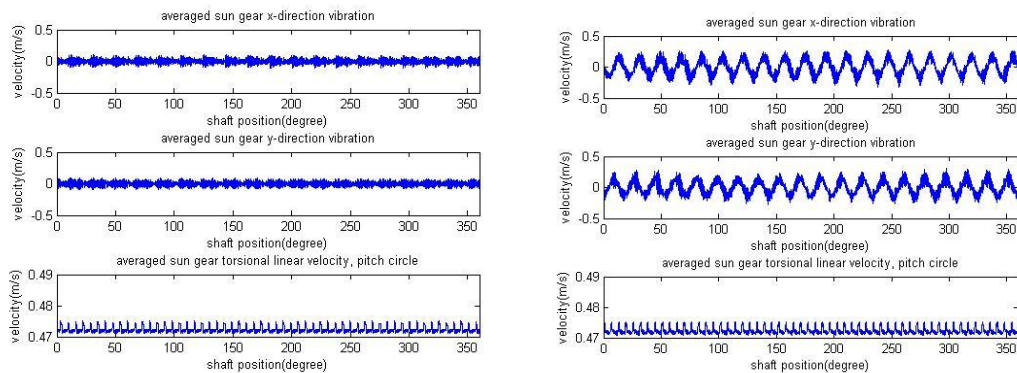


Figure 8-29 Comparison of sun gear signals of undamaged planetary gear set in case-1 and case-2 (left graph, case-1; right graph, case-2)

8.4. SUMMARY OF CHAPTER

The major findings in this chapter are summarized below.

Synchronous signal averaging is essential to recover the vibration information from time domain signals for further analysis such as frequency analysis. The number of revolutions used in the signal averaging process can affect the accuracy of the averaged signal and consequently affect the accuracy of further analysis results (as the number of revolutions used increases, the more accurate the results).

As shown in both the averaged signal and frequency spectrum figures (the later one has more clear information) the sun gear signals, ring gear signals and the planet gear signals have a number of pulses or a first mesh harmonic which indicates the number of gear teeth respectively. Also the carrier arm signals have a number of pulses or the first mesh harmonic indicating the number of ring gear teeth.

It is shown that the frequency spectrum from torsional signals is superior than those from transverse signals as it has less side band effects and it indicates the number of corresponding gear teeth more clearly.

The resulting signals in Case-1 vibrate in a large range and are relatively noisy

compared to the other two cases as the system does not include bucket wheel mass/inertia components. The signal fluctuation range is reduced by a factor of many times, which can be up to a level of tens, when the large mass and inertia components are included as for case-2. When the combined gear error has been introduced into simulation as for case-3, the signal irregularity is increased and enhanced in the vibration signal as compared to that of case-2. In conclusion, the addition of large mass and inertia components appears to constrain the vibration signals and increase the tooth mesh detectability and the addition of gear transmission error improves the realism of the model but also lowers the tooth mesh detectability.

9. VIBRATION MODELLING WITH GEAR FAULTS

Dynamic modelling of the planetary gear system with gear faults is introduced and the simulation results are analyzed in this chapter. In this research, single tooth faults (cracks and spalling) and also their combinations (Chapter 10) are included.

All three cases (Chapter 8, case-1 is without bucket wheel, buckets and combined gear error, case-2 includes bucket wheel and buckets but neglects the combined gear error, case-3 includes bucket wheel, buckets and combined gear error) are developed for the modelling of tooth faults with the major part based on case-2 for simulation of tooth cracks and in case-3 for simulation of spalling. Also comparisons are made with corresponding results in case-1. It should be noted that case-3 with tooth spalling is named as case-4.

As mentioned in Chapter 8, due to the limitation of computational time, only a small number of revolutions are used for signal averaging in this analysis (4 revolutions of the sun gear, 2 revolutions of the planet gears and 1 revolution of the ring gear and the carrier arm).

Simulation outputs from all models include the displacement and velocity signals of all degrees of freedom. Subsequent analysis includes signal averaging, FSA (Frequency Spectrum Analysis) and CWTA (Continuous Wavelet Analysis) carried out with all output signals except for the degrees of freedom of the second and third planet gear.

The calculation of planetary component speed ratios and contact ratios used in this chapter can be referred to in Table 3-1 and Table 6-3. One revolution of the sun gear is determined as when all sun teeth (in this thesis, 19 teeth) have been through the mesh (in this thesis, one of the three sun gear - planet gear meshes) once. One revolution of the ring gear is determined as when all ring teeth (in this thesis, 83 teeth) have been through the mesh (in this thesis, one of the three ring gear - planet gear

meshes) once. One revolution of the carrier arm is defined as 360 degrees of carrier arm rotation about the ring gear which is assumed to be stationary. One revolution of a planet gear is defined as when all of the planet gear teeth have been through either one of the sun gear - planet gear meshes or the ring gear - planet gear meshes once.

The period of one revolution of each component shown in the figures uses the shaft position in degrees on the horizontal axis. For the sun gear, ring gear and planet gears signals, the term, shaft position, is defined to be the angular position of the shaft/gear about the corresponding mesh point rather than the axis of the shaft/gear. Zero degrees at the start corresponds to the start mesh point and 360 degrees denotes when the tooth mesh is back to the starting point. For the carrier arm signals, the term, shaft position, is defined to be the angular position of the carrier arm shaft about its own axis.

9.1. MODEL WITH A LOCALISED TOOTH CRACK IN MESH

The most common method for tooth crack simulation is to introduce a localized change of mesh stiffness such as used in Jia's work⁴⁰. The tooth crack introduced in this thesis is assumed to be along the root circle only. A crack with five different lengths have been simulated using 5%, 20%, 40%, 60% and 80% of the tooth thickness along the root circle for the sun gear, ring gear and the first planet gear respectively. Results are listed and analyzed with two methods, FSA and CWTA, in this section.

9.1.1. CRACK ON SUN GEAR TOOTH

The tooth crack simulated on the sun gear is a single crack localized on the 19th tooth where the 1st tooth is defined to be the first tooth in mesh with the first planet gear at time zero.

Simulation outputs after signal averaging with a single 80% crack on the sun gear at the 19th tooth are shown in Figure 9-1. It can be seen from the figure that there are three humps in the period of one sun gear revolution as there are three planet gears. The number of humps shown here should be exactly equal to the number of planet gears.

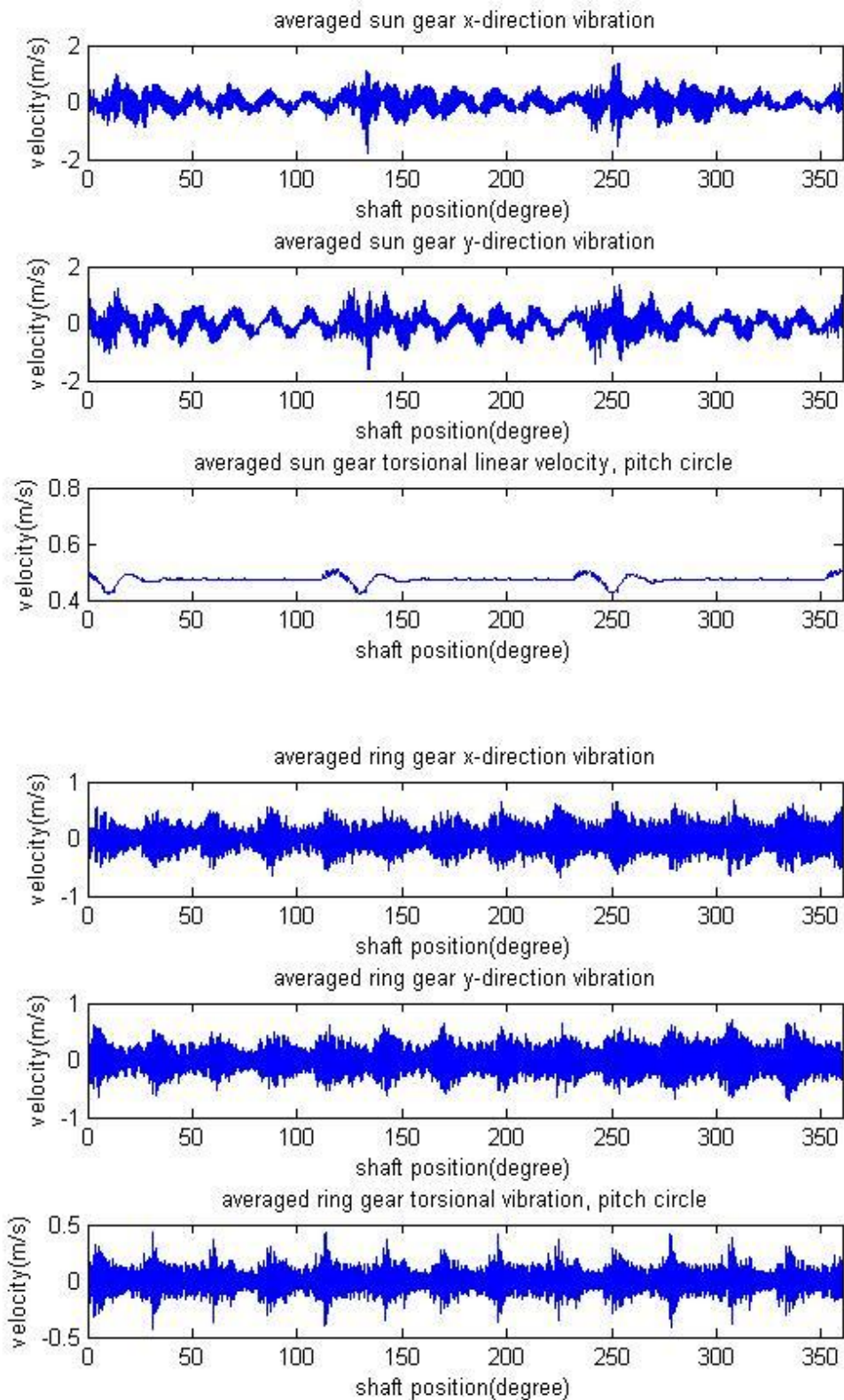


Figure 9-1 Simulation outputs after signal averaging with a single 80% crack on the sun gear at the 19th tooth

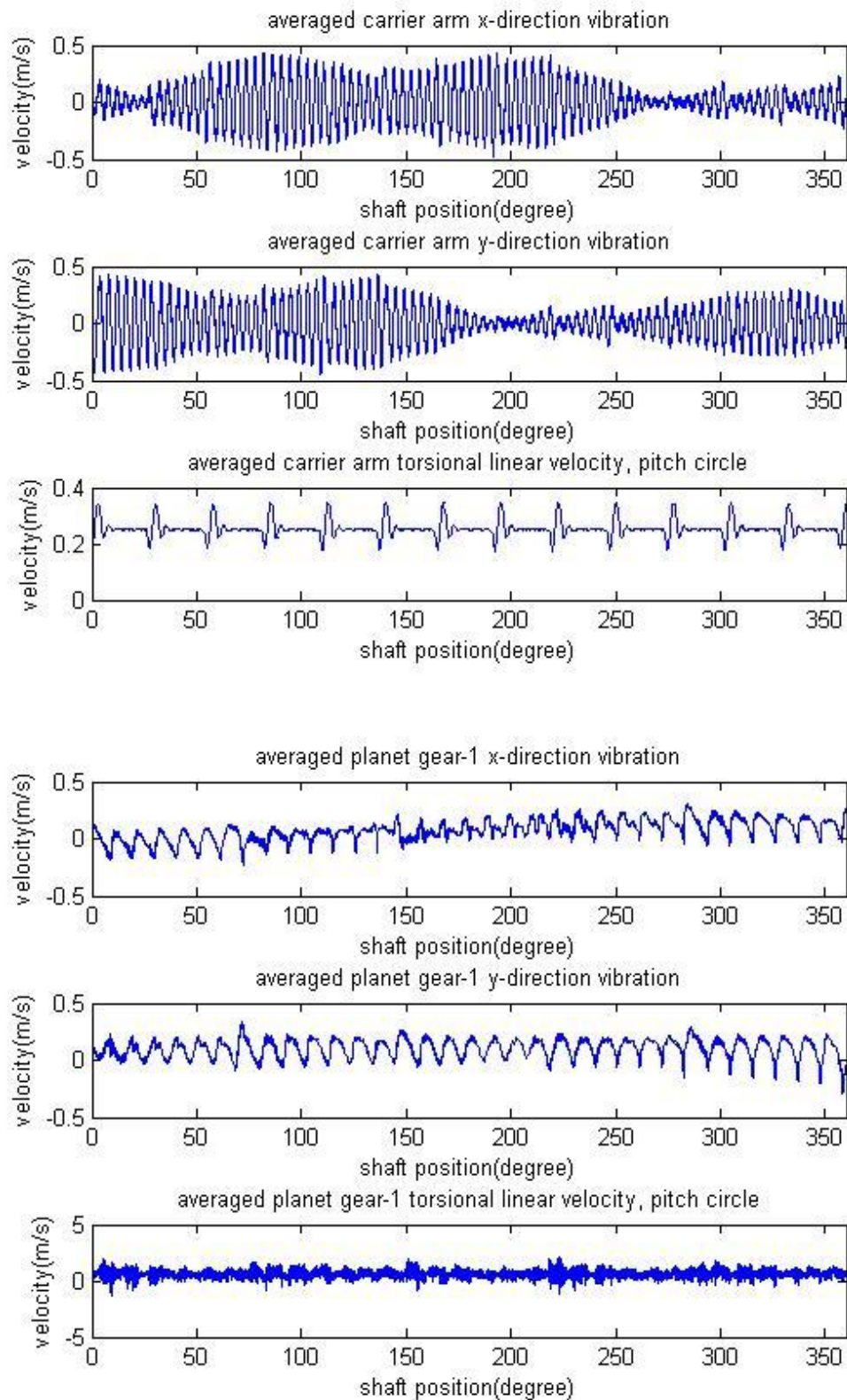


Figure 9-1(continued) Simulation outputs after signal averaging with a single 80% crack on the sun gear at the 19th tooth

Figure 9-1 also shows that there are 13 humps in the period of one ring gear

revolution and also 13 pulses in the period of one carrier arm revolution, which can be calculated as sun gear-carrier arm speed ratio minus 1 then multiplied by the number of planet gears (in this case, $(5.3684-1)*3=13.1052$). It should be noticed that the carrier arm x and y motions are affected by the transverse motions of the planet gears about their mount points rather than about the sun gear centre, so they appear to not be useful in indicating sun gear damage. The angular velocity signal of the planet gear-1 appears to show five disturbed points which can be calculated using Eq 9.1. It should be noted that the phasing of these disturbed points will be different for each revolution. After averaging of a large number of revolutions, the sun gear damage will not be evident in the planet vibration.

$$\text{NumberofDisturbances} = \text{NumberofPlanetGears} * \frac{\text{NumberofPlanetGearTeeth}}{\text{NumberofSunGearTeeth}} \quad (9.1)$$

It can be seen that the torsional signals are shown to be superior than the transverse signals except for those of the planet gears.

A comparison is made with the sun gear crack using results of a 5% crack on the sun gear (19th tooth), as well as for the case of the undamaged gear (Case-2, see Appendix 13.2), shown in Figure 9-2 (left column, undamaged; middle column, 5% crack; right column, 80% crack). It should be noticed that the figures in Figure 9-2 do not have the same scale as it is not easy to see details in large scale figures of signals with the 5% crack. It can be seen that the influence of the sun gear crack is clearly reflected on both the transverse and torsional vibration signals of the sun gear and ring gear, but only on the torsional vibration signal (especially for small cracks) of the planet gear and the carrier arm.

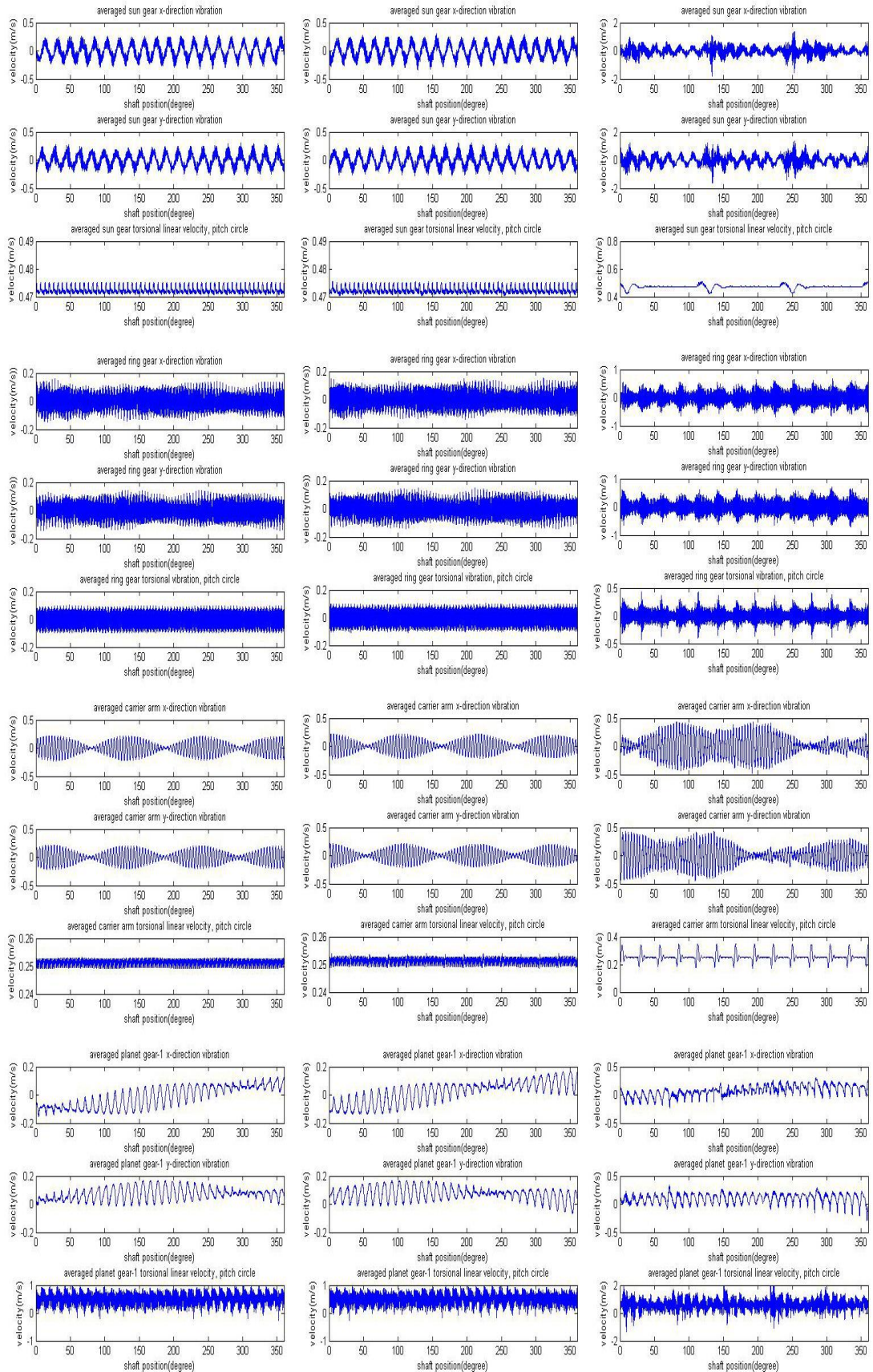


Figure 9-2 Comparison of results, undamaged, 5% cracked and 80% cracked sun gear 19th tooth

A grade system is introduced here to mark the vibration signals of the 12 degrees of freedom (listed as xs, ys, us, xr, yr, ur, xc, yc, uc, xp, yp, and up) from superior to weak (1st to 12nd) for detectability of the tooth fault. Based on the averaged signals, the grades for the sun gear crack are marked as shown in Table 9-1.

Fault type	Detectability of tooth fault			
	1 st	2 nd	3 rd	4 th
Sun gear tooth crack	us, uc	xr, yr, ur,	xs, ys, up	xc, yc, xp, yp

Table 9-1 Detectability of sun gear tooth crack based on averaged signals

The averaged signals can be used to detect large cracks as shown in Figure 9-1 and 9-2, however it appears difficult to detect early stage cracks. Frequency Spectrum Analysis (FSA) can be used to improve the early stage detectability.

FSA applied to Case-2 with the sun gear crack gives the results shown in Figure 9-3 to 9-14. Each figure shows the frequency range covering the first four mesh harmonics.

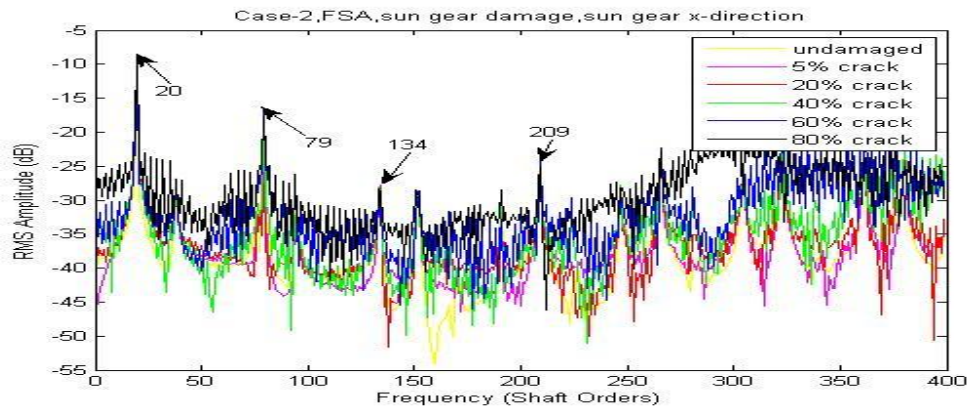


Figure 9-3 Case-2, FSA, sun gear damage, sun gear x-direction

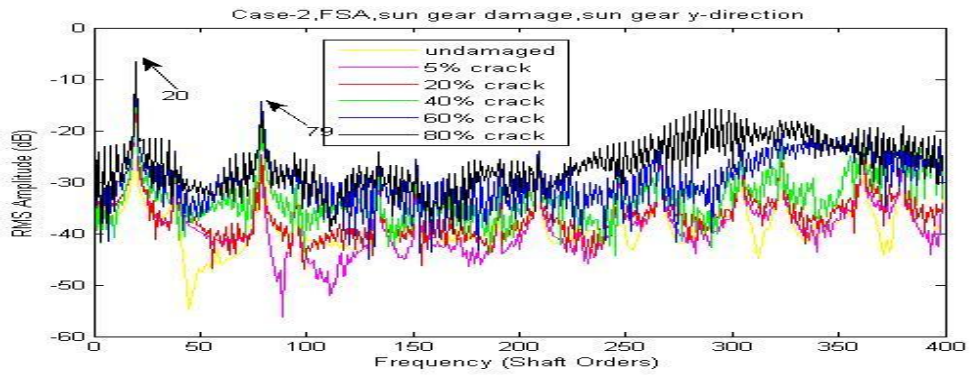


Figure 9-4 Case-2, FSA, sun gear damage, sun gear y-direction

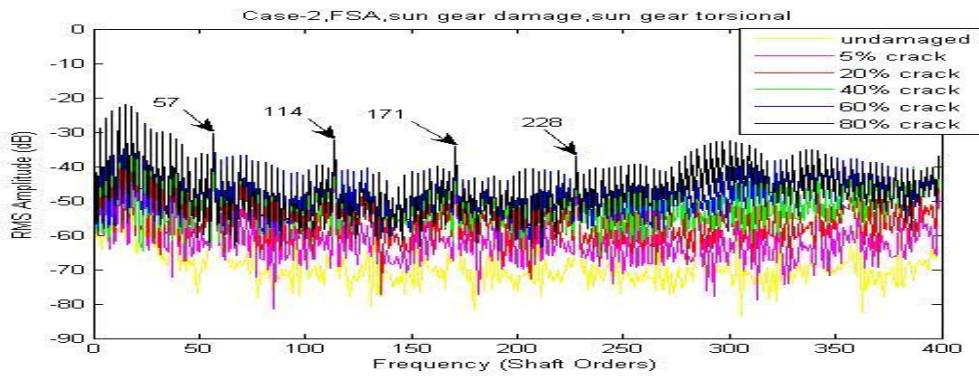


Figure 9-5 Case-2, FSA, sun gear damage, sun gear torsional

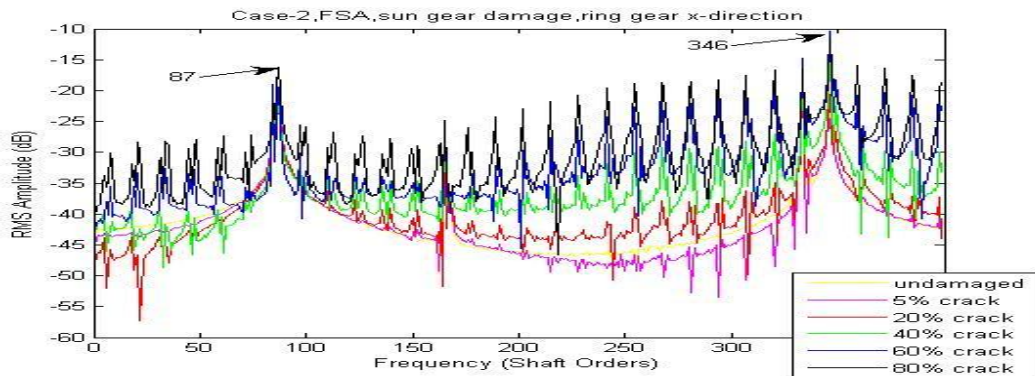


Figure 9-6 Case-2, FSA, sun gear damage, ring gear x-direction

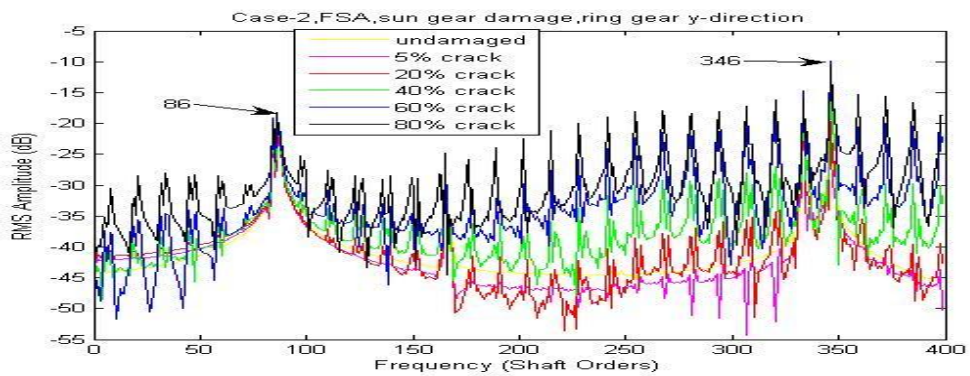


Figure 9-7 Case-2, FSA, sun gear damage, ring gear y-direction

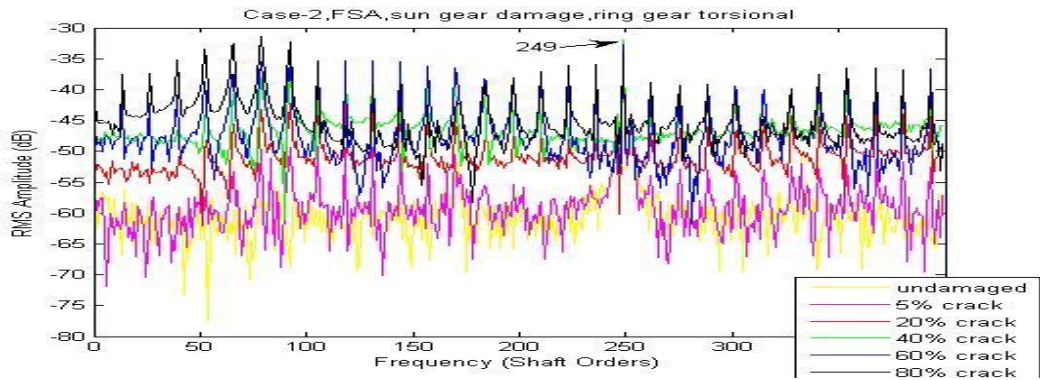


Figure 9-8 Case-2, FSA, sun gear damage, ring gear torsional

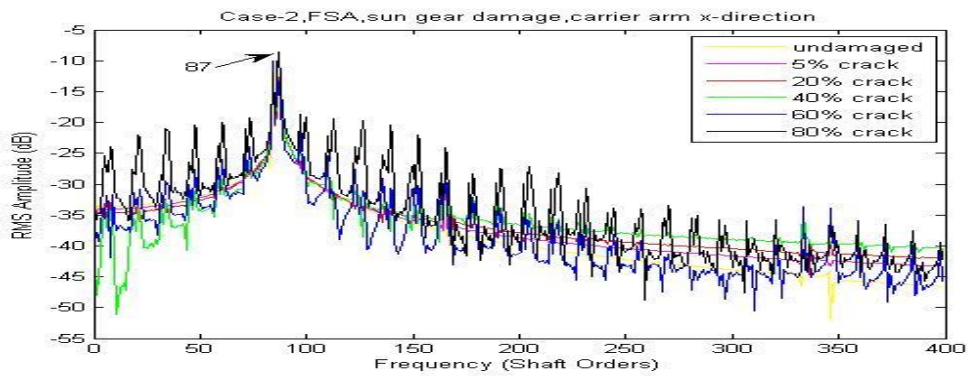


Figure 9-9 Case-2, FSA, sun gear damage, carrier arm x-direction

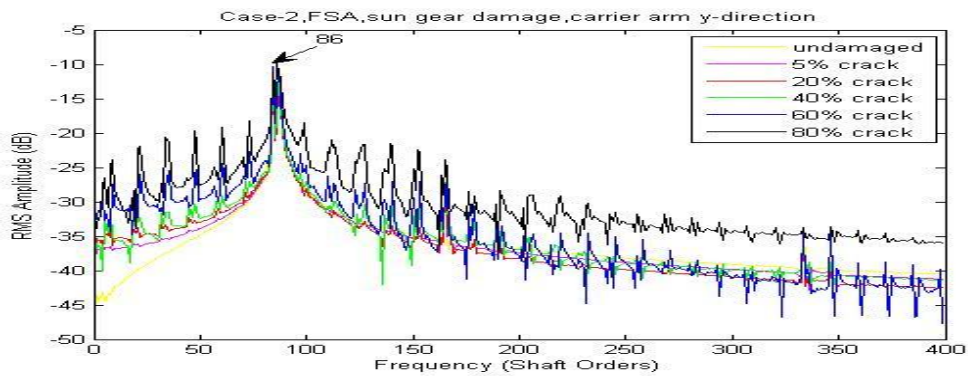


Figure 9-10 Case-2, FSA, sun gear damage, carrier arm y-direction

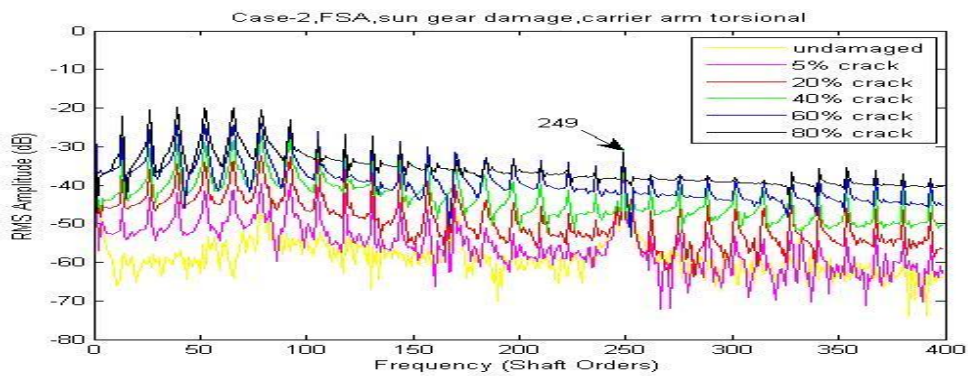


Figure 9-11 Case-2, FSA, sun gear damage, carrier arm torsional

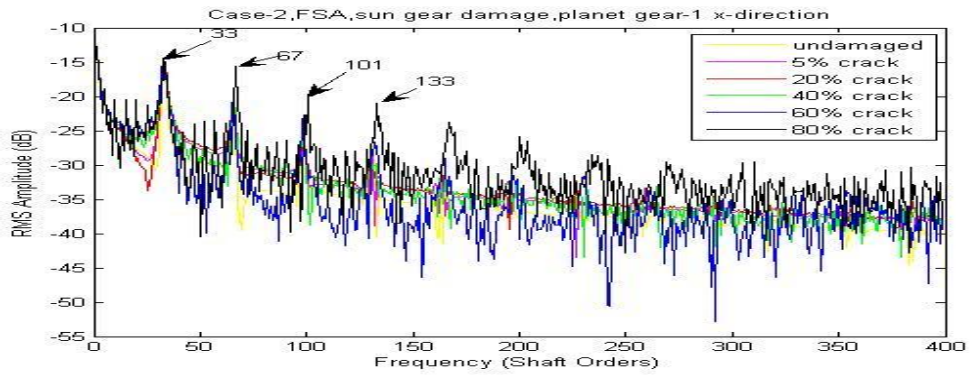


Figure 9-12 Case-2, FSA, sun gear damage, planet gear-1 x-direction

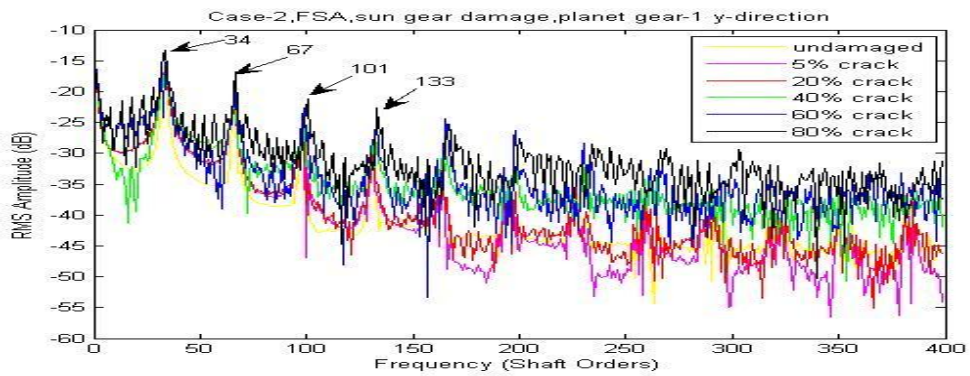


Figure 9-13 Case-2, FSA, sun gear damage, planet gear-1 y-direction

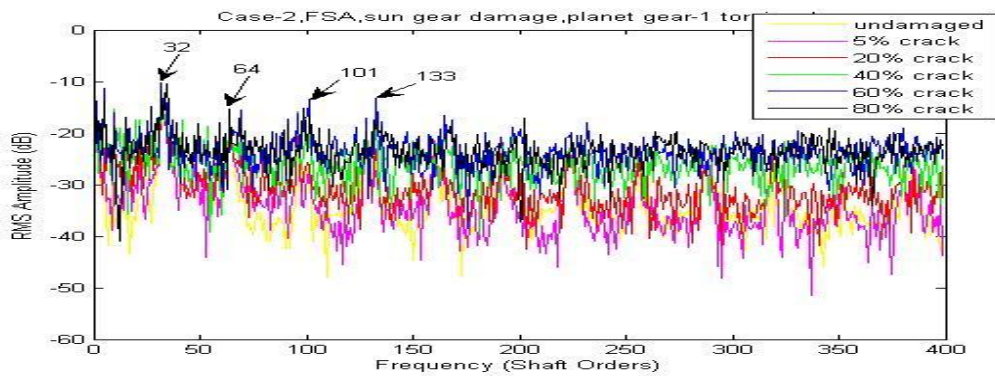


Figure 9-14 Case-2, FSA, sun gear damage, planet gear-1 torsional

Based on the FSA figures above, the detectability grades are marked as shown in Table 9-2 with discussion.

Detectability of sun gear tooth crack		Figure	Discussion		
			Low frequency lines	High frequency lines	Lines in details
1 st	uc	9-11	In very good order		
2 nd	us	9-5	In very good order	In good order	Little disorder
3 rd	ur	9-8	In good order with little disorder		
4 th	xr, yr	9-6,9-7	In good order		Some local disorder
5 th	up	9-14	In good order	Local disorder appears often	
6 th	xs, ys	9-3,9-4	Local disorder appears very often		
7 th	xc, yc	9-9, 9-10	In wrong order	In wrong order	In wrong order with local Disorder
8 th	xp, yp	9-12, 9-13	In chaos	In chaos	In chaos

Table 9-2 Detectability of sun gear tooth crack based on FSA

FSA method can slightly approve early stage detectability of sun gear tooth crack. More importantly it creates a way to refine the grade of detectability. This will give a big advantage in vibration signal selection for fault detection purposes. However, FSA is not able to locate the tooth faults. In order to do so, the CWTA was employed. The one dimensional wavelet analysis function using the Morlet wavelet was used with a step by step mode from 1 to 2001 with a step size of 50.

Based on the CWTA figures, the detectability grades are marked as shown in Table 9-3.

Detectability of sun gear tooth crack		Sensitive step range (total data points 2 ¹⁶)	Minimum clearly detectable crack	Noise on figure which affects detectability
1 st	uc	450 to 950 50 up	5% 5%~20%	Very clear in all step range
2 nd	us	1200 up	20%	Very clear in sensitive step range
3 rd	xc, yc	950 to 1550	20%~40%	Clear in sensitive step range
4 th	ur	50 to 900	20%~40%	Noisy
5 th	xr, yr	50 to 400	40%	Very noisy

Table 9-3 Detectability of sun gear tooth crack based on CWTA

Detectability of sun gear tooth crack		Sensitive step range (total data points 2^{16})	Minimum clearly detectable crack	Noise on figure which affects detectability
6 th	xs, ys	50 to 900	60%	Very noisy
7 th	up	50 to 900	60%	Extremely noisy
8 th	xp, yp	--	--	Unable to detect

Table 9-3(continued) Detectability of sun gear tooth crack based on CWTA

The CWTA results applied to carrier arm torsional vibration signals are compared with different sun gear cracks in Figure 9-15. As the most fault detectable CWTA signal, it provides very clear information of the faults' location at the very early stage which can be starting from 5% damage with confidence.

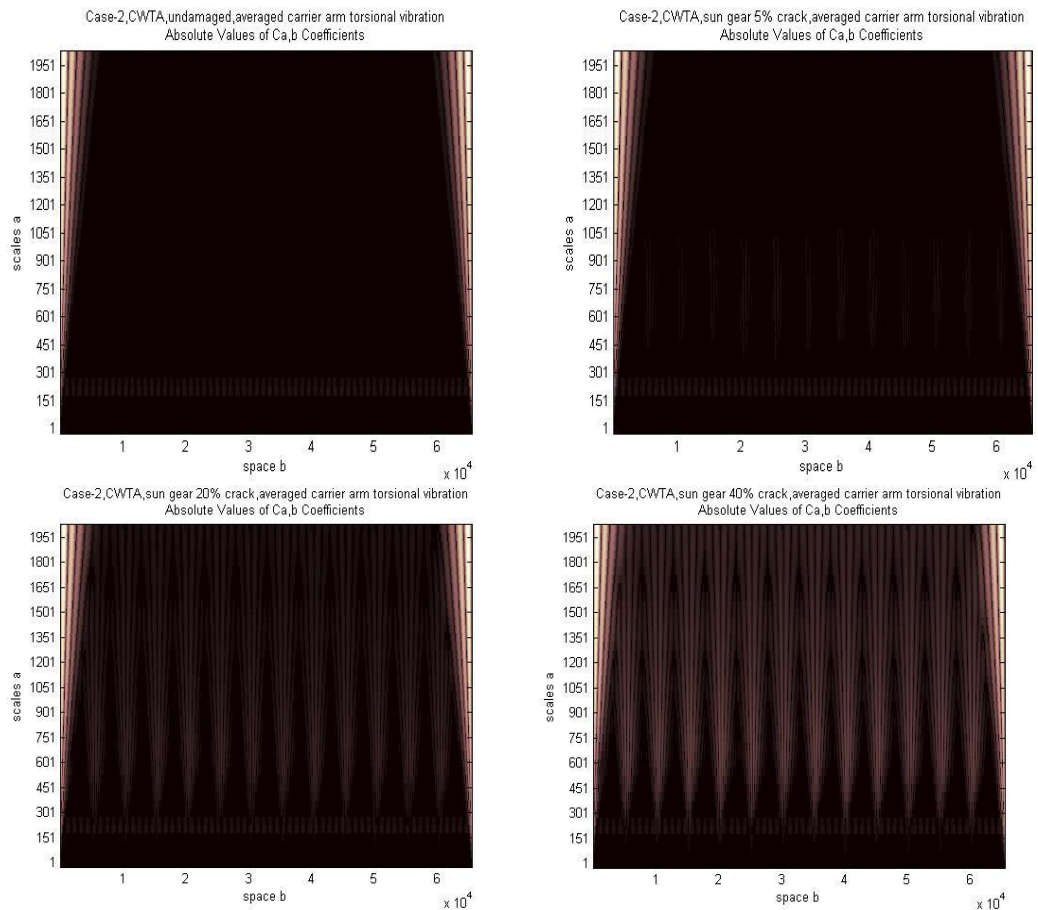


Figure 9-15 Case-2, CWTA, sun gear crack, averaged carrier arm torsional vibration

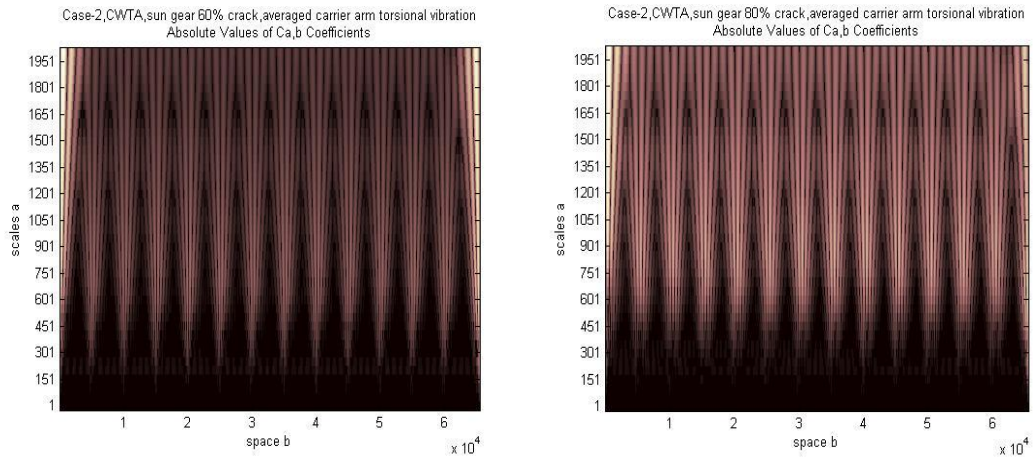


Figure 9-15 (continued) Case-2, CWTA, sun gear crack, averaged carrier arm torsional vibration

The CWTA results applied to sun gear torsional vibration signals are compared with different sun gear cracks in Figure 9-16. As the second most fault detectable CWTA signal, it provides very clear information of the faults' location at the very early stage which can be starting from 20% damage with confidence.

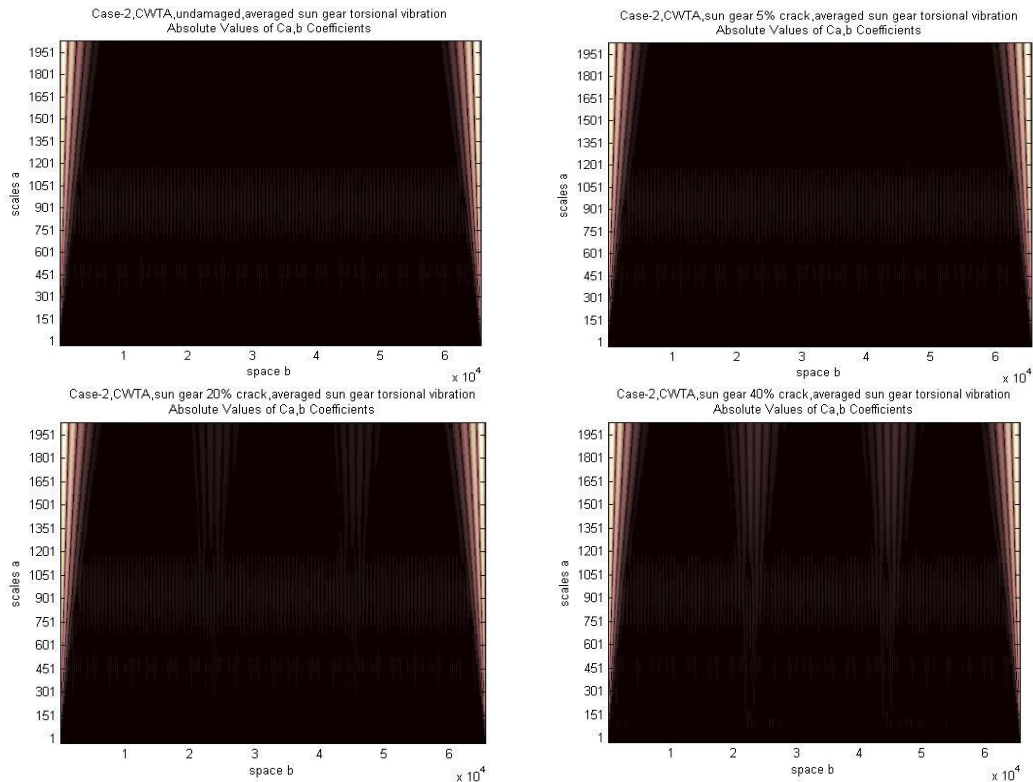


Figure 9-16 Case-2, CWTA, sun gear crack, averaged sun gear torsional vibration

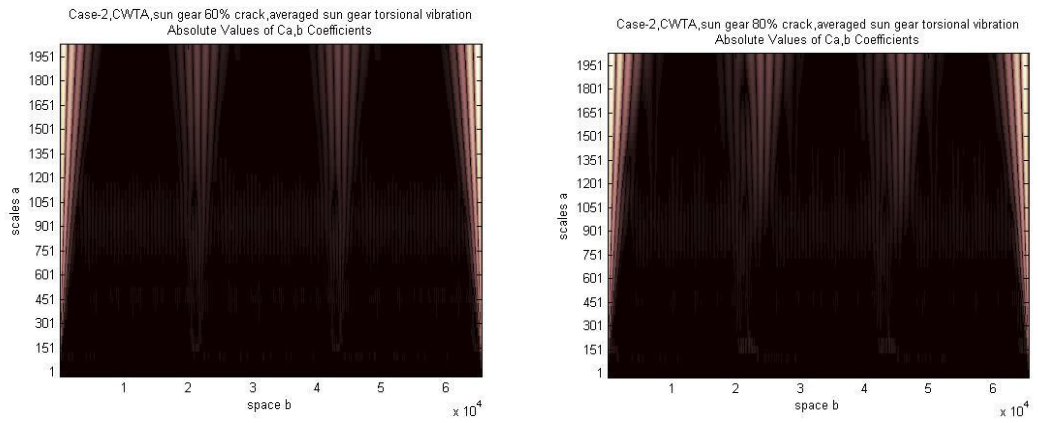


Figure 9-16 (continued) Case-2, CWTA, sun gear crack, averaged sun gear torsional vibration

In conclusion, the CWTA appears to be an efficient method to detect and locate the sun gear tooth cracks. It also provides information of fault detectability of vibration signals.

9.1.2. CRACK ON RING GEAR TOOTH

The tooth crack simulated on the ring gear was a single crack localized on the 83rd tooth where the 1st tooth is defined to be the first tooth in mesh with the first planet gear at time zero.

Simulation outputs after signal averaging with a single 80% crack on the 83rd tooth of the ring gear are shown in Figure 9-17.

It can be seen in Figure 9-17 that the averaged sun gear signals are not able to indicate the location of ring gear tooth fault as the disturbed points shown in the signals have different phases from different revolutions.

Figure 9-17 shows that there are 3 humps in the period of one ring gear revolution and one carrier arm revolution, which is equal to the number of planet gears. It should be noticed that the carrier arm x and y direction signals are affected by the transverse motions of the planet gears about their mount points rather than about the sun gear centre, so they appear to not be useful. The angular velocity signal of the planet gear-1 appears insensitive as well. It can be seen that the torsional signals are superior to the transverse signals except those of the planet gears.

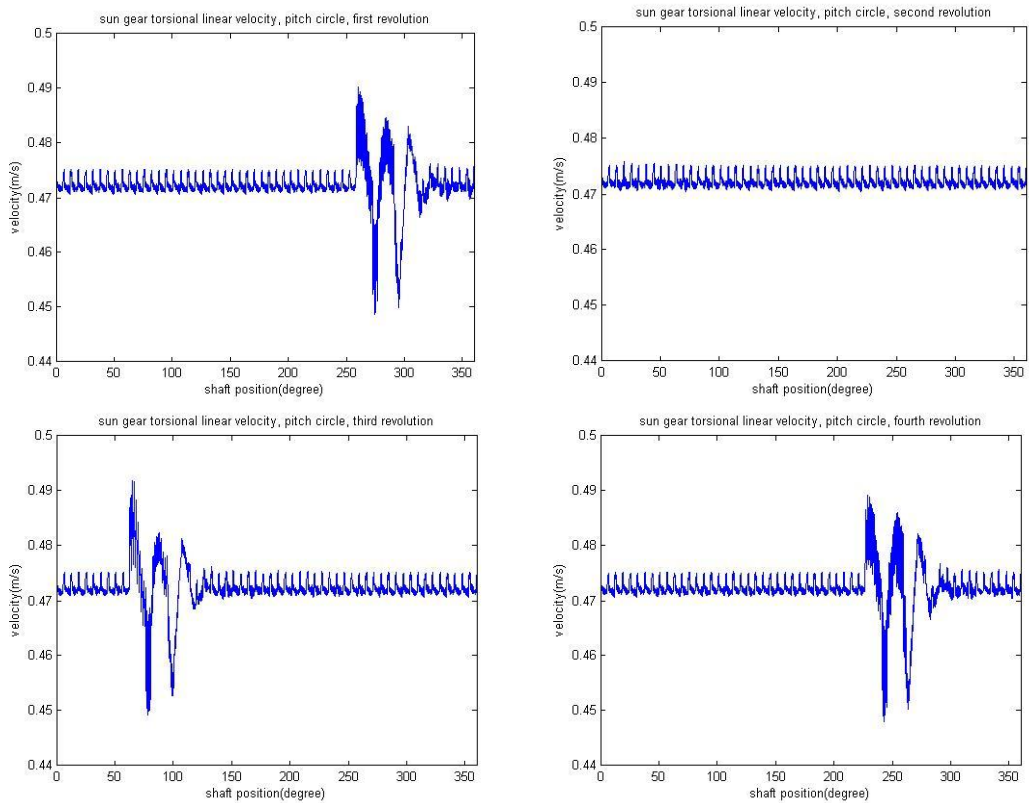
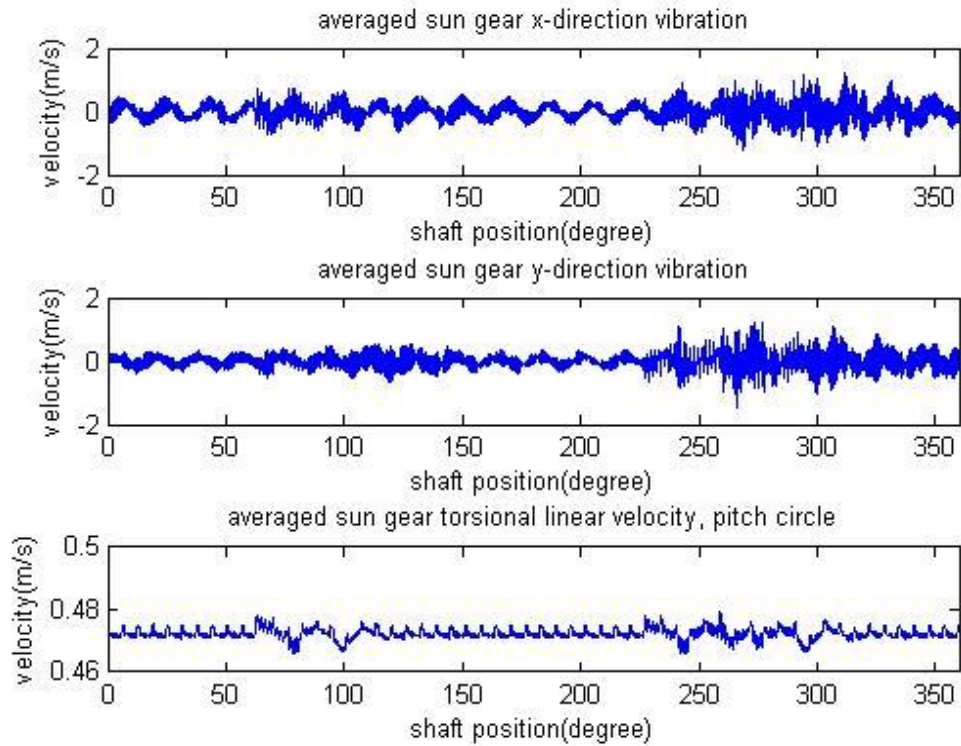


Figure 9-17 Simulation outputs after signal averaging with a single 80% crack on the 83rd tooth of the ring gear

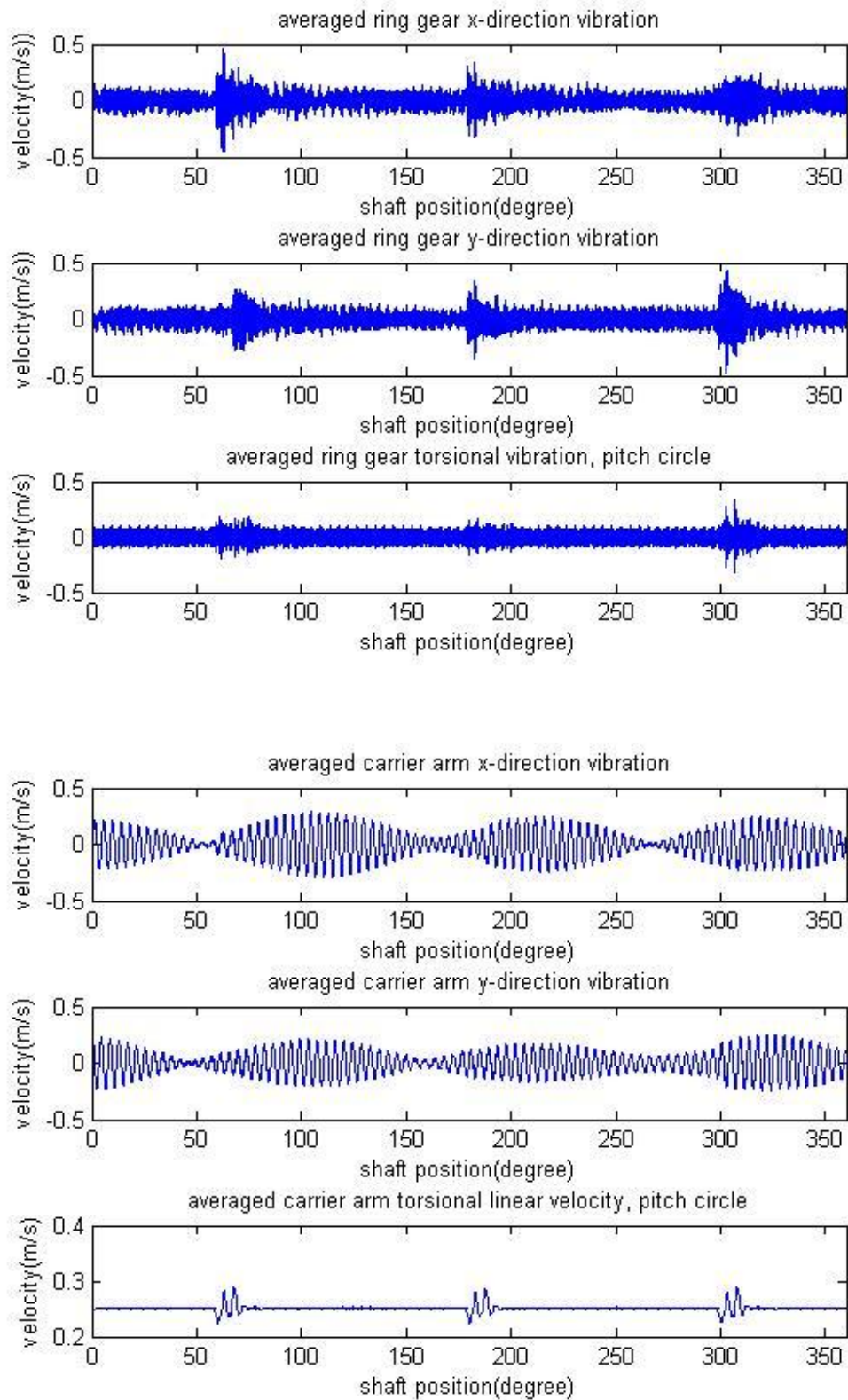


Figure 9-17(continued) Simulation outputs after signal averaging with a single 80% crack on the 83rd tooth of the ring gear

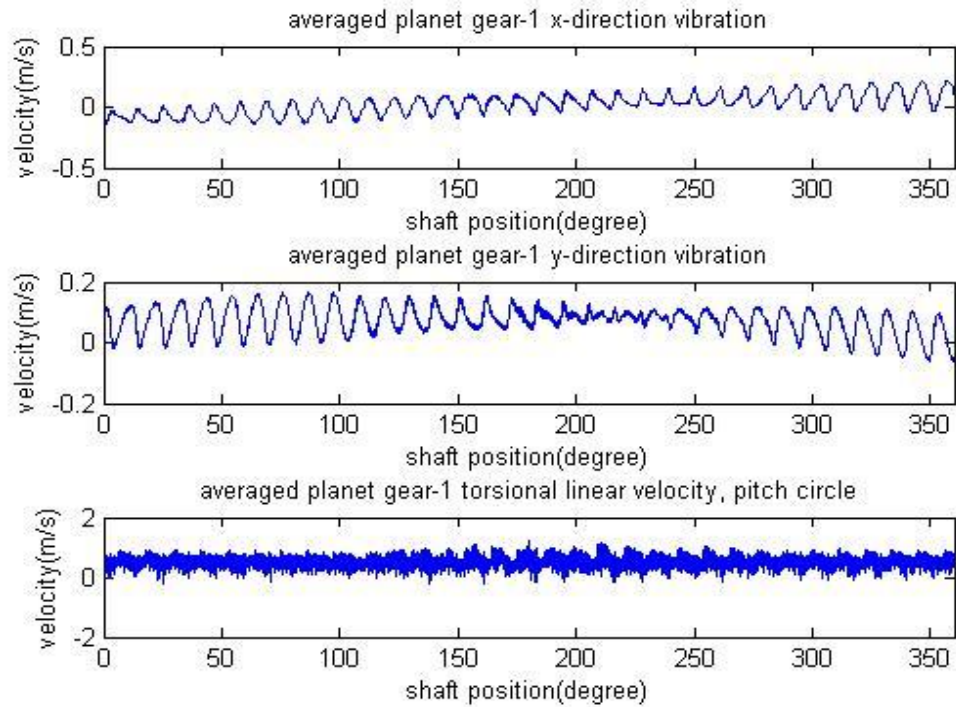


Figure 9-17(continued) Simulation outputs after signal averaging with a single 80% crack on the 83rd tooth of the ring gear

A comparison is made with the ring gear crack using results of a 5% crack on the ring gear (83rd tooth) as well as for the case of the undamaged gear (Case-2, see Appendix 13.2) shown in Figure 9-18 (left column, undamaged; middle column, 5% crack; right column, 80% crack). It should be noticed that the figures in Figure 9-18 do not have the same scale as it is not easy to see details in large scale figures with the 5% crack. It can be seen that the influence of the ring gear crack is clearly reflected on both the transverse and torsional vibration signals of the sun gear and ring gear components, but only on the torsional vibration signal (especially for small cracks) for the carrier arm and not at all for the planet gear vibration signals.

Based on the averaged signals, the detectability of the ring gear crack is marked as shown in Table 9-4.

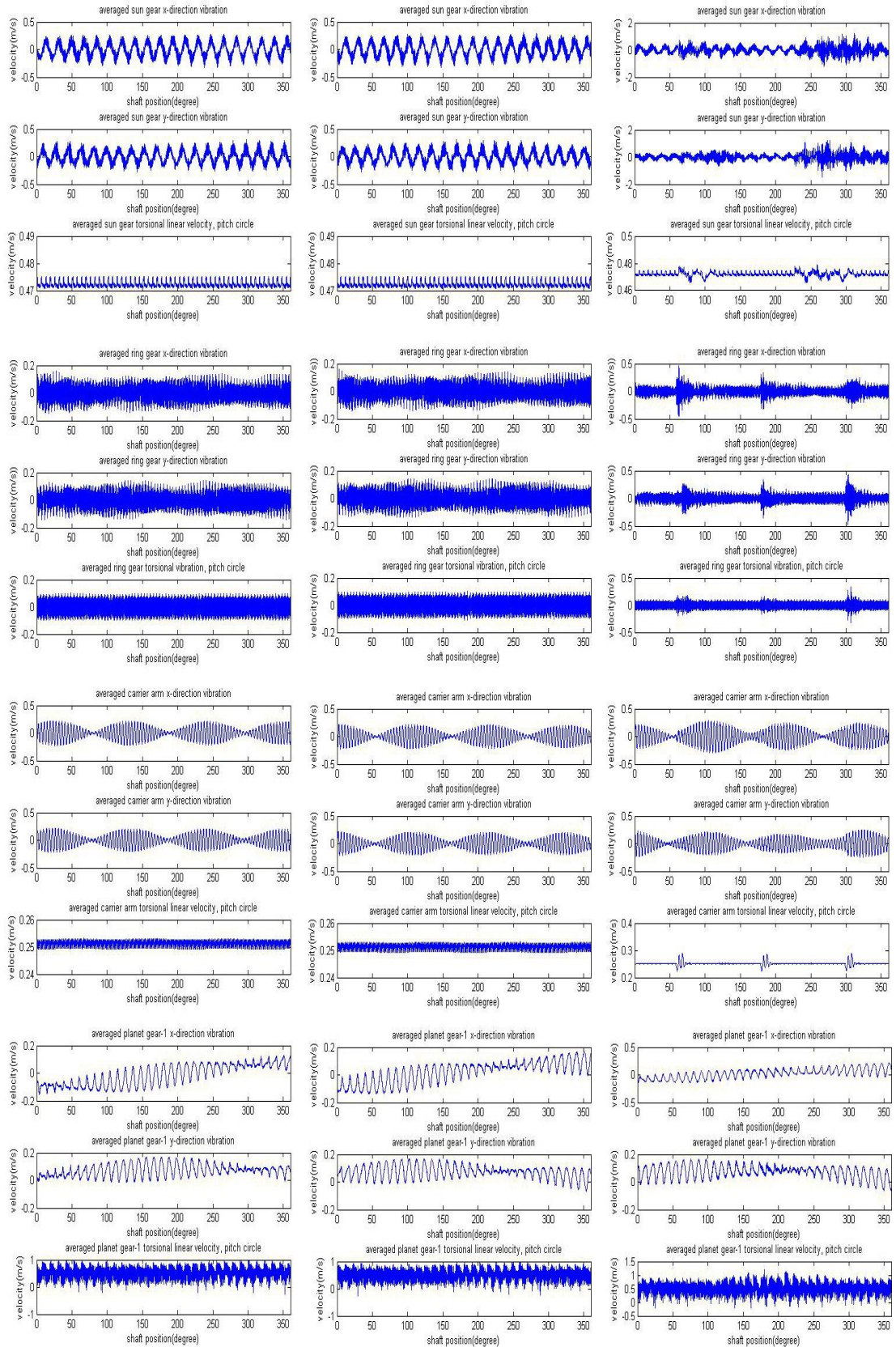


Figure 9-18 Comparison of results, undamaged, 5% cracked and 80% cracked ring gear 83rd tooth

Fault type	Detectability of tooth fault			
	1 st	2 nd	3 rd	4 th
Ring gear tooth crack	us, uc	xr, yr, ur,	xs, ys	xc, yc, xp, yp, up

Table 9-4 Detectability of ring gear tooth crack based on averaged signals

The averaged signal can be used to detect large cracks as shown in Figure 9-17 and 9-18, but it is hard to detect early stage cracks. Frequency Spectrum Analysis (FSA) can be used to improve the early stage detectability.

FSA applied to Case-2 with the ring gear crack gives the results shown in Figure 9-19 to 9-30. Each figure shows the frequency range covering the first four mesh harmonics.

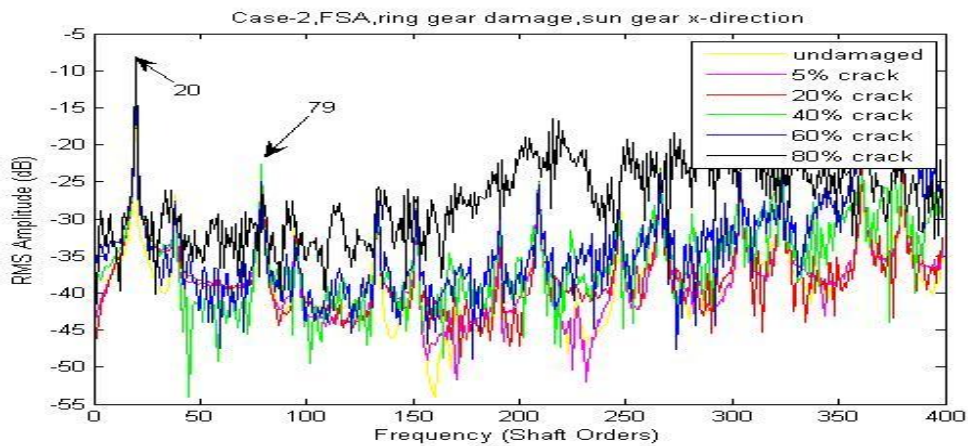


Figure 9-19 Case-2, FSA, ring gear damage, sun gear x-direction

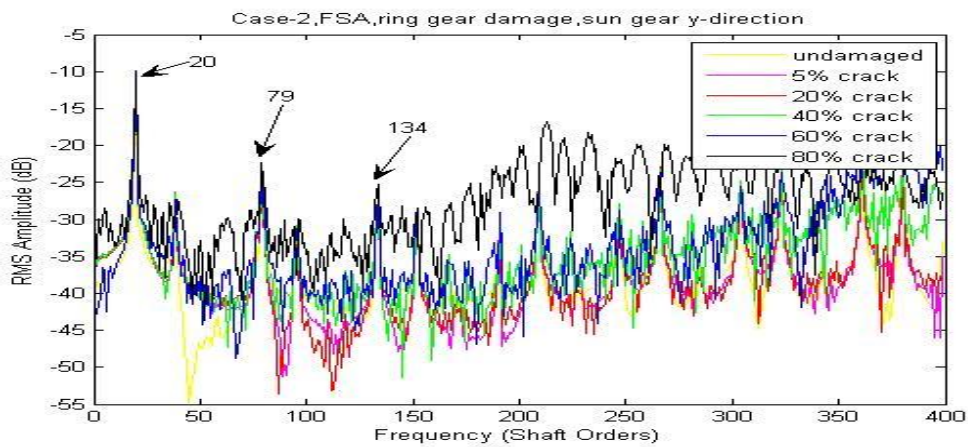


Figure 9-20 Case-2, FSA, ring gear damage, sun gear y-direction

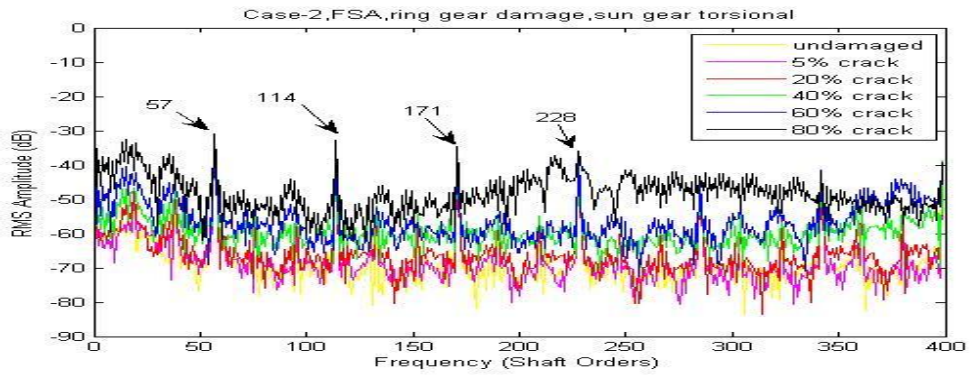


Figure 9-21 Case-2, FSA, ring gear damage, sun gear torsional

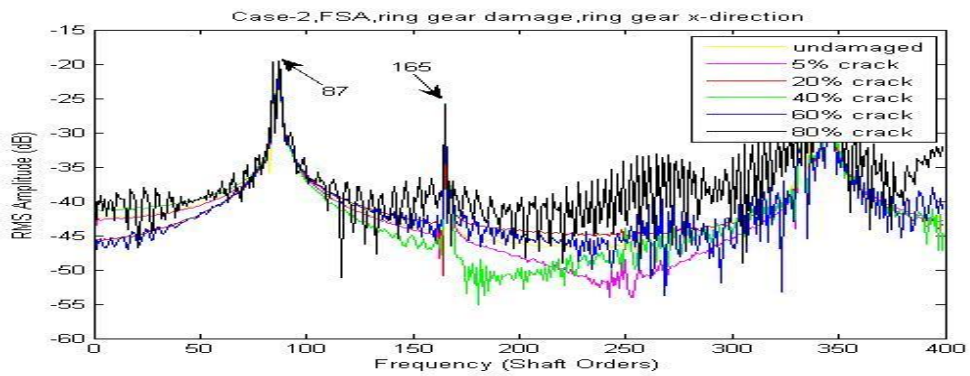


Figure 9-22 Case-2, FSA, ring gear damage, ring gear x-direction

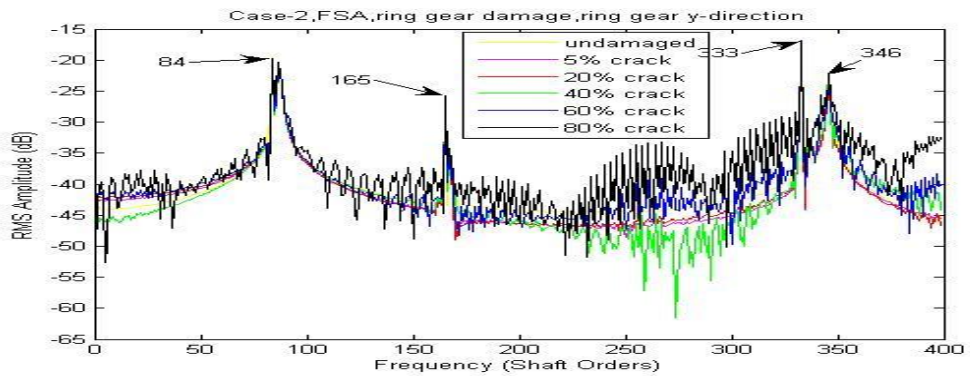


Figure 9-23 Case-2, FSA, ring gear damage, ring gear y-direction

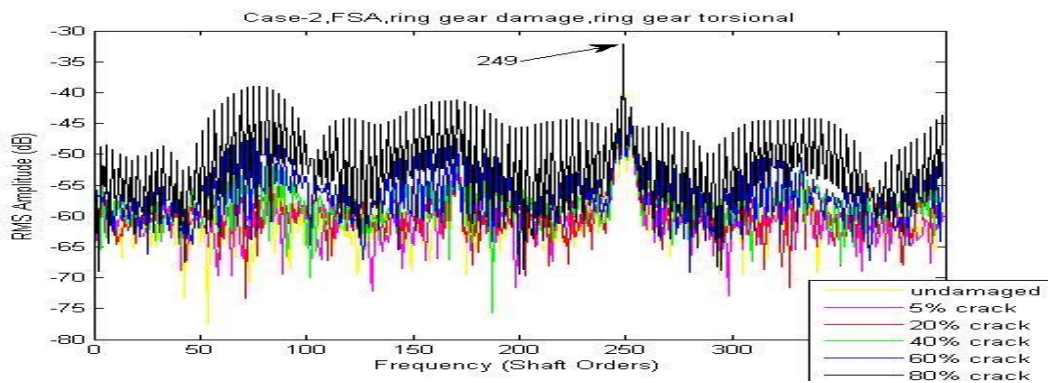


Figure 9-24 Case-2, FSA, ring gear damage, ring gear torsional

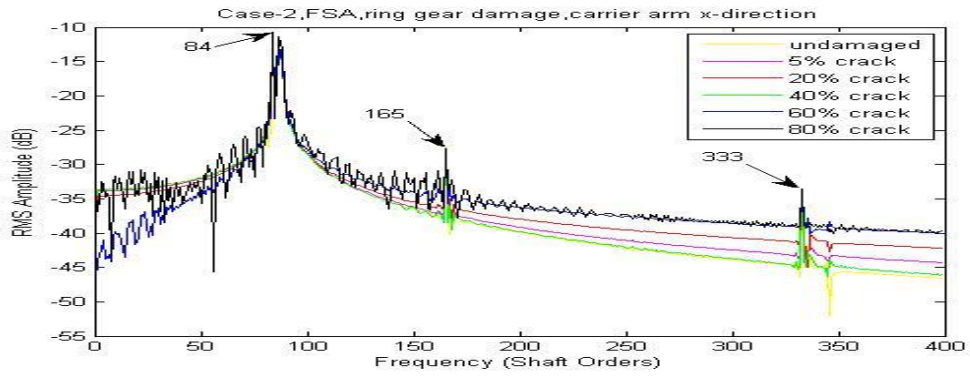


Figure 9-25 Case-2, FSA, ring gear damage, carrier arm x-direction

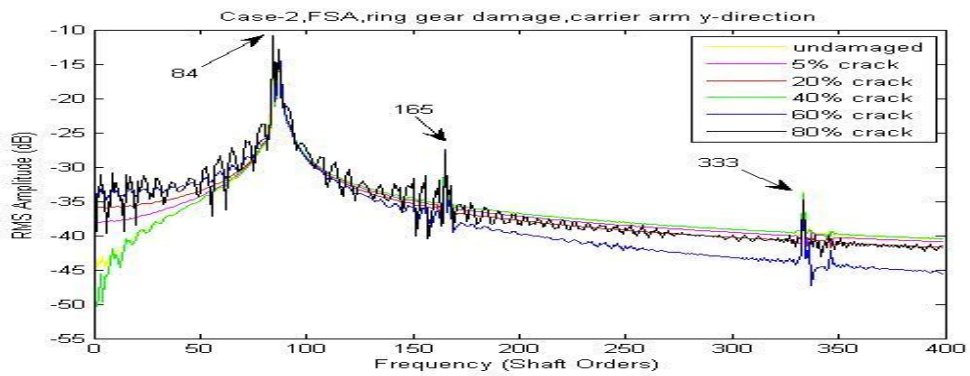


Figure 9-26 Case-2, FSA, ring gear damage, carrier arm y-direction

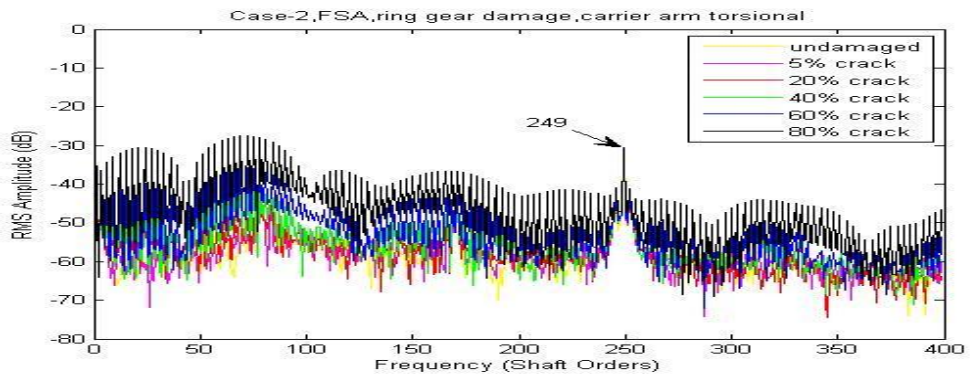


Figure 9-27 Case-2, FSA, ring gear damage, carrier arm torsional

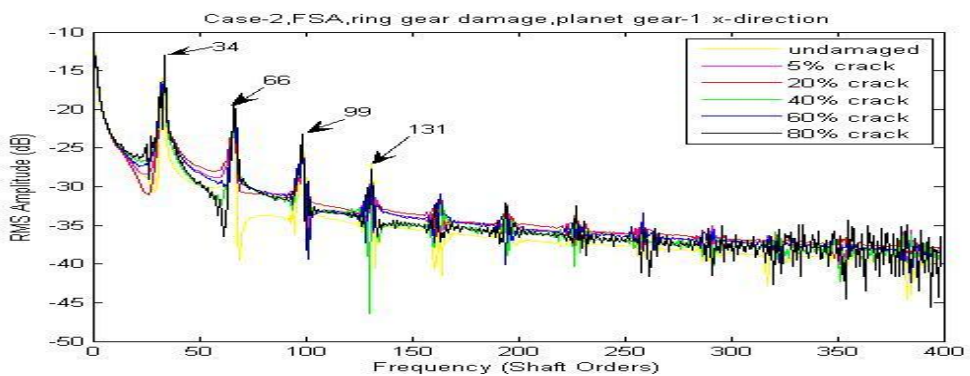


Figure 9-28 Case-2, FSA, ring gear damage, planet gear-1 x-direction

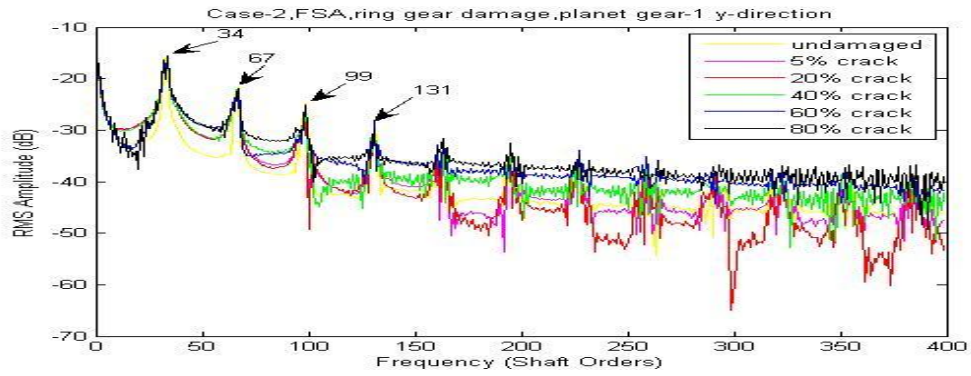


Figure 9-29 Case-2, FSA, ring gear damage, planet gear-1 y-direction

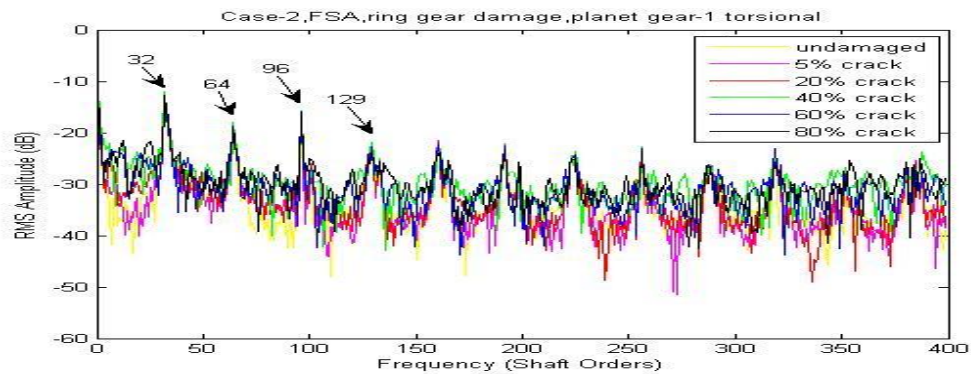


Figure 9-30 Case-2, FSA, ring gear damage, planet gear-1 torsional

Based on the FSA figures above, the detectability grades are marked as shown in Table 9-5 with discussion.

Detectability of ring gear tooth crack		Figure	Discussion		
			Low frequency lines	High frequency lines	Lines in details
1 st	uc, us	9-27,9-21	In very good order	In good order	Little disorder
2 nd	ur	9-24	In good order with little disorder		
3 rd	xr, yr	9-22,9-23	In good order		Some local disorder
4 th	up	9-30	In good order	Local disorder appears often	
5 th	xs, ys	9-19,9-20	Local disorder appears very often		
6 th	xc, yc	9-25,9-26	In wrong order	In wrong order	In wrong order with local disorder
7 th	xp, yp	9-28, 9-29	In chaos	In chaos	In chaos

Table 9-5 Detectability of ring gear tooth crack based on FSA

The FSA method can slightly improve early stage detectability of the ring gear tooth

crack. More importantly it creates a way to refine the grade of detectability. This will give a big advantage in vibration signal selection for fault detection purpose. However, FSA was not able to locate the tooth faults. In order to do so, the one dimensional wavelet analysis function using the Morlet wavelet was used with a step by step mode from 1 to 2001 with a step size of 50.

Based on the CWTA figures, the detectability grades are marked as shown in Table 9-6.

Detectability of ring gear tooth crack		Sensitive step range (total data points 2^{16})	Minimum clearly detectable crack	Noise on figure which affects detectability
1 st	uc	450 to 950	Below 40%	Very clear in all step range
2 nd	ur	1000 to 1600	Below 40%	Noisy
3 rd	xr, yr	1000 to 1600	Below 40%	Very noisy
4 th	us	1200 up	Below 80%	Very clear in sensitive step range
5 th	xc, yc	1050 to 1550	60%~80%	Clear in sensitive step range
6 th	xs, ys	50 to 300	60%	Very noisy
7 th	xp, yp, up	--	--	Unable to detect

Table 9-6 Detectability of ring gear tooth crack based on CWTA

The CWTA results applied to carrier arm torsional vibration signals are compared with different ring gear cracks in Figure 9-31. As it is the most fault detectable CWTA signal, it provides very clear information of the faults' location in mid-range which is below 40% damage.

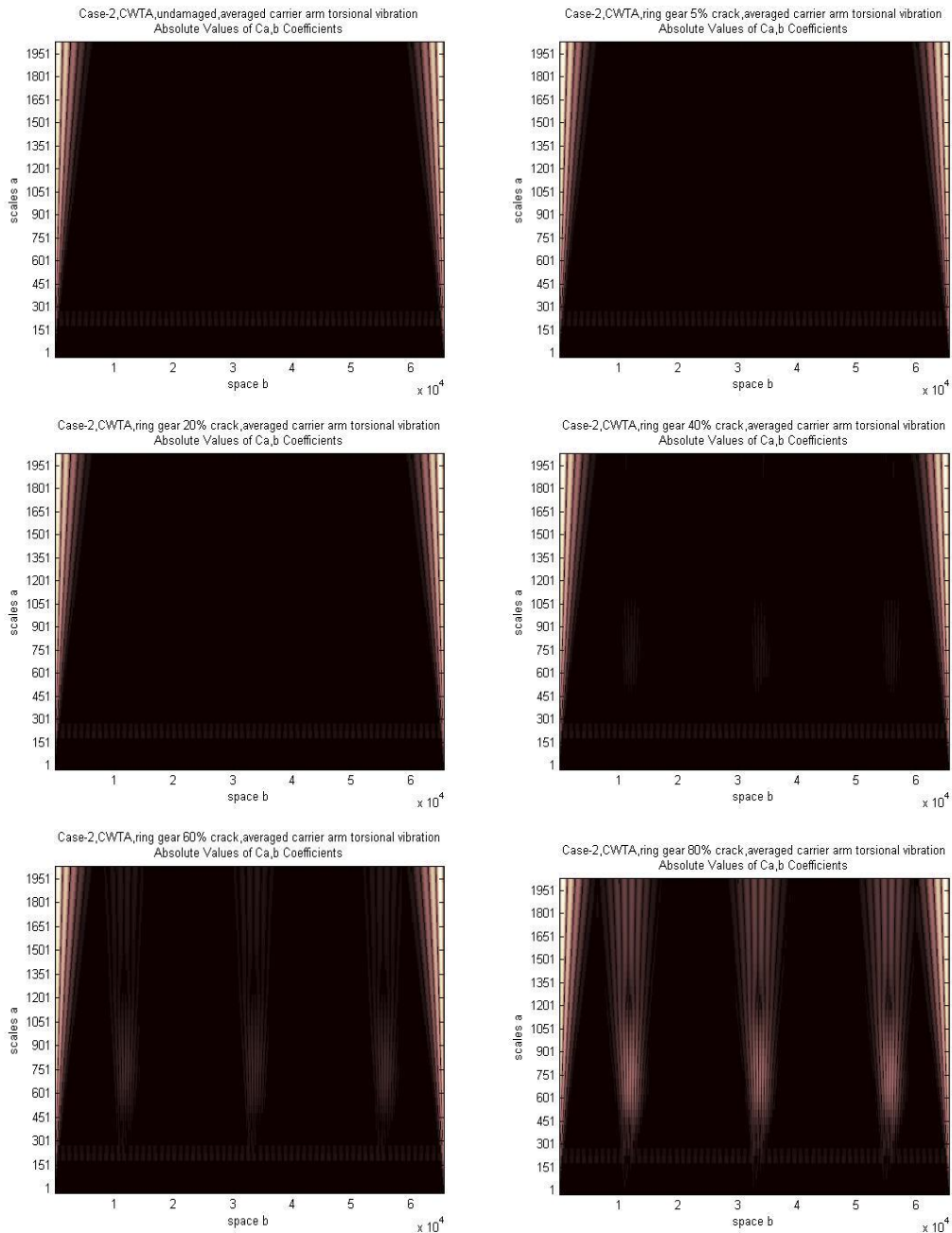


Figure 9-31 Case-2, CWTA, ring gear crack, averaged carrier arm torsional vibration

The CWTA results applied to ring gear torsional vibration signals are compared with different ring gear cracks in Figure 9-32. As the second most fault detectable CWTA signal, it provides information of the faults' location at early stage (20%~40%) though the signal is relatively noisy in all step ranges.

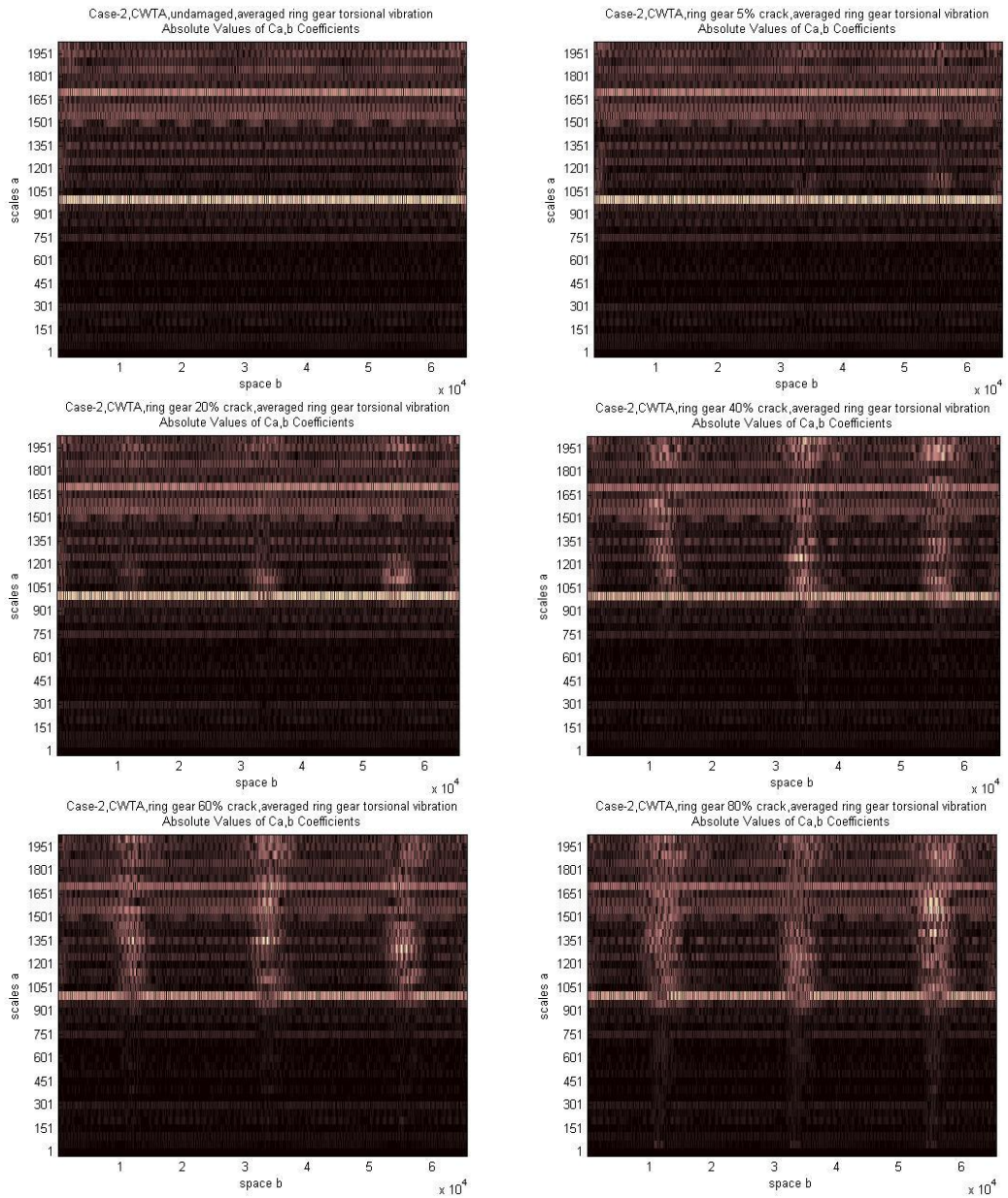


Figure 9-32 Case-2, CWTA, ring gear crack, averaged sun gear torsional vibration

In conclusion, the CWTA appears to be an efficient method to detect and locate the ring gear tooth cracks. It also provides information of fault detectability from the vibration signals.

9.1.3. CRACK ON PLANET GEAR TOOTH

The tooth crack simulated on the planet gear-1 is a single crack localized on the 32nd tooth where the 1st tooth is defined to be the first tooth in mesh with the sun gear at time zero.

Simulation outputs after signal averaging with a single 80% crack on the planet gear-1 at the 32nd tooth are shown in Figure 9-33. Figure 9-33 shows that there are humps with the period of one sun gear revolution which can be calculated as in Eq 9.2 ($19/(32/2)=1.1875$).

$$\text{NumberofHumps} = \frac{\text{NumberofSunGearTeeth}}{\text{NumberofPlanetGearTeeth} / 2} \quad (9.2)$$

These humps correspond to the damaged tooth progressing through both the sun gear - planet gear mesh and the ring gear - planet gear mesh in order. Due to the fact that they have different phases from different revolutions, the averaged signal is ineffective.

Figure 9-33 also shows that there are 3 bigger humps and 2 smaller humps in the period of one ring gear revolution and one carrier arm revolution, which can be calculated as in Eq 9.3 ($83/32=2.5938$). The bigger humps correspond to the sun gear - planet gear mesh and the smaller humps correspond to the ring gear - planet gear mesh.

$$\text{NumberofBiggerHumps} = \text{NumberofSmallerHumps} = \frac{\text{NumberofRingGearTeeth}}{\text{NumberofPlanetGearTeeth}} \quad (9.3)$$

It should be noticed that the carrier arm x and y vibration signals are affected by the transverse motions of the planet gears about their mount points rather than about the sun gear centre, so they appear to not be useful for planet damage detection.

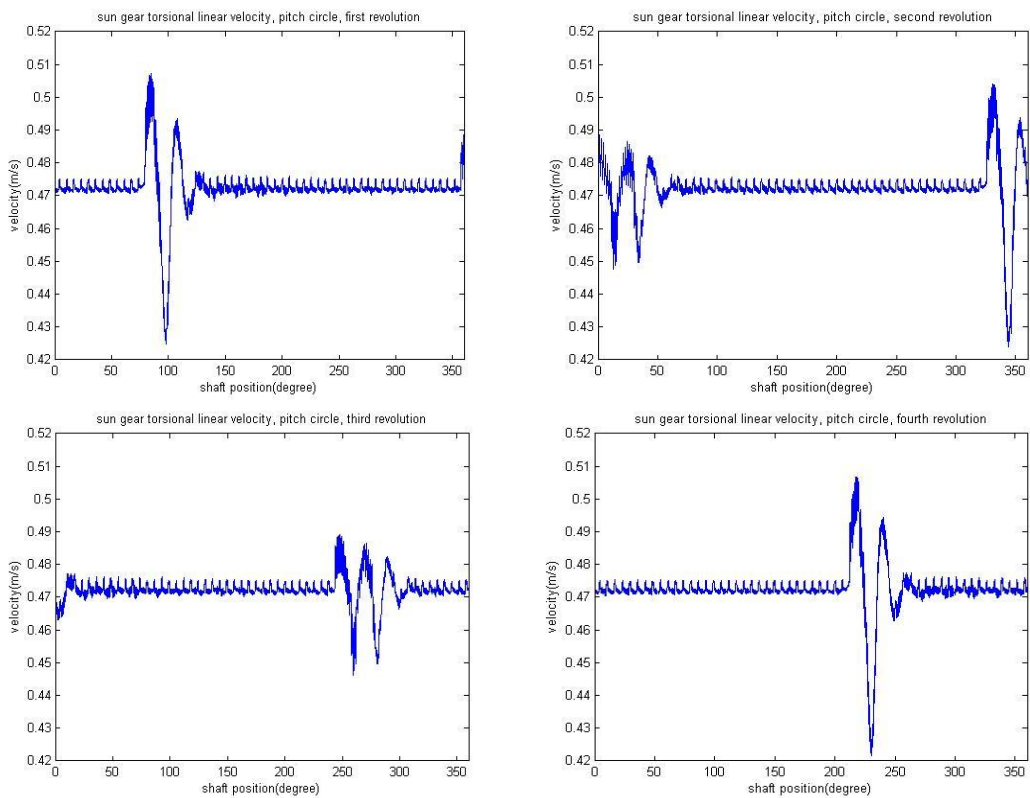
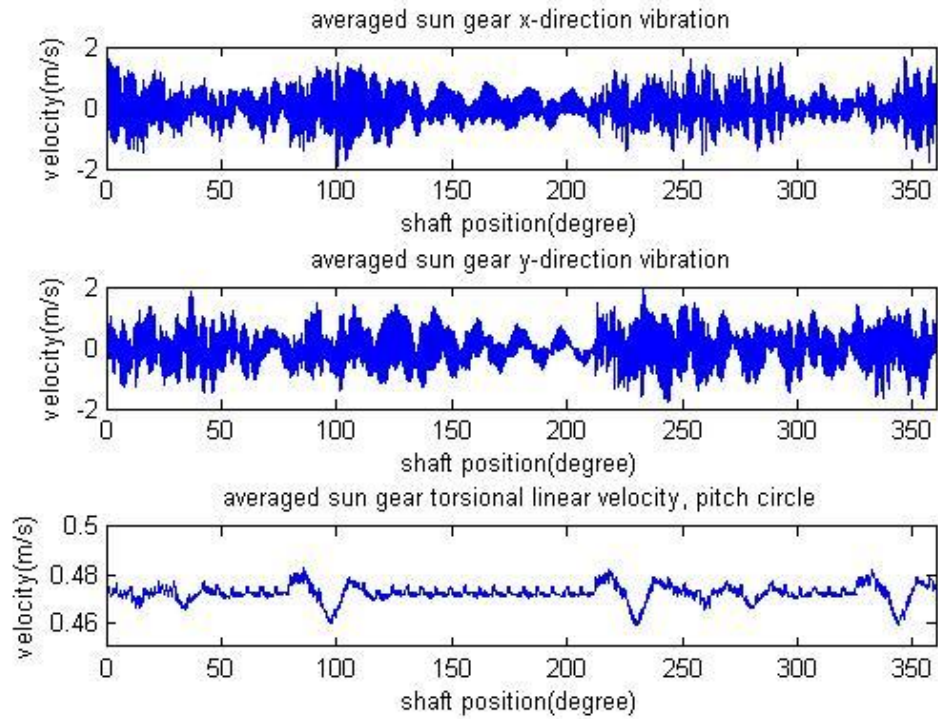


Figure 9-33 Simulation outputs after signal averaging with a single 80% crack on the planet gear-1 at the 32nd tooth

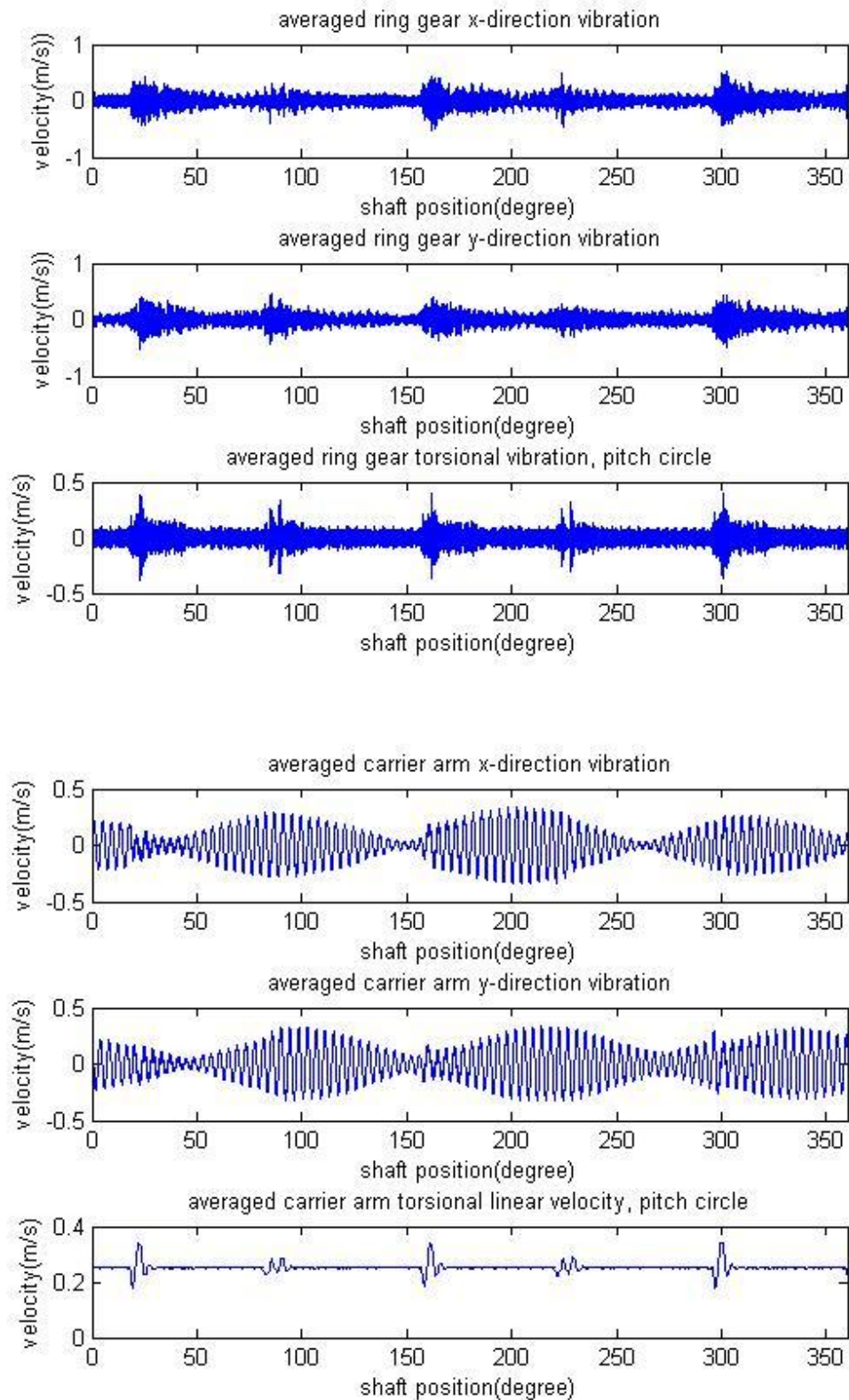


Figure 9-33(continued) Simulation outputs after signal averaging with a single 80% crack on the planet gear-1 at the 32nd tooth

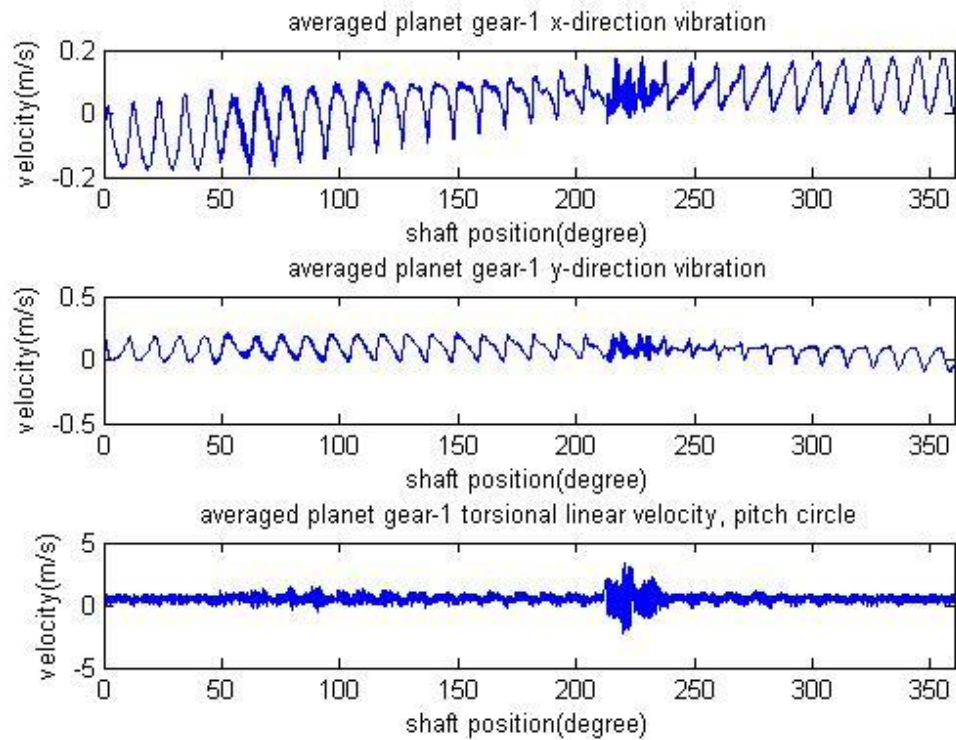


Figure 9-33(continued) Simulation outputs after signal averaging with a single 80% crack on the planet gear-1 at the 32nd tooth

Figure 9-33 also shows that there is an obvious deviation in the period of one planet gear revolution (the first planet gear) corresponding to the sun gear - planet gear mesh (where the crack has bigger effect on mesh stiffness change). A contact which is hardly noticeable (between 50 to 100 degrees) corresponding to the ring gear - planet gear mesh can also be seen.

A conclusion can be made that the torsional signals are superior than the transverse signals except those of the planet gears.

A comparison is made with the planet gear crack using results of a 5% crack on the planet gear-1 (32nd tooth) as well as for the case of the undamaged gear (Case-2, see Appendix 13.2) shown in Figure 9-34 (left column, undamaged; middle column, 5% crack; right column, 80% crack).

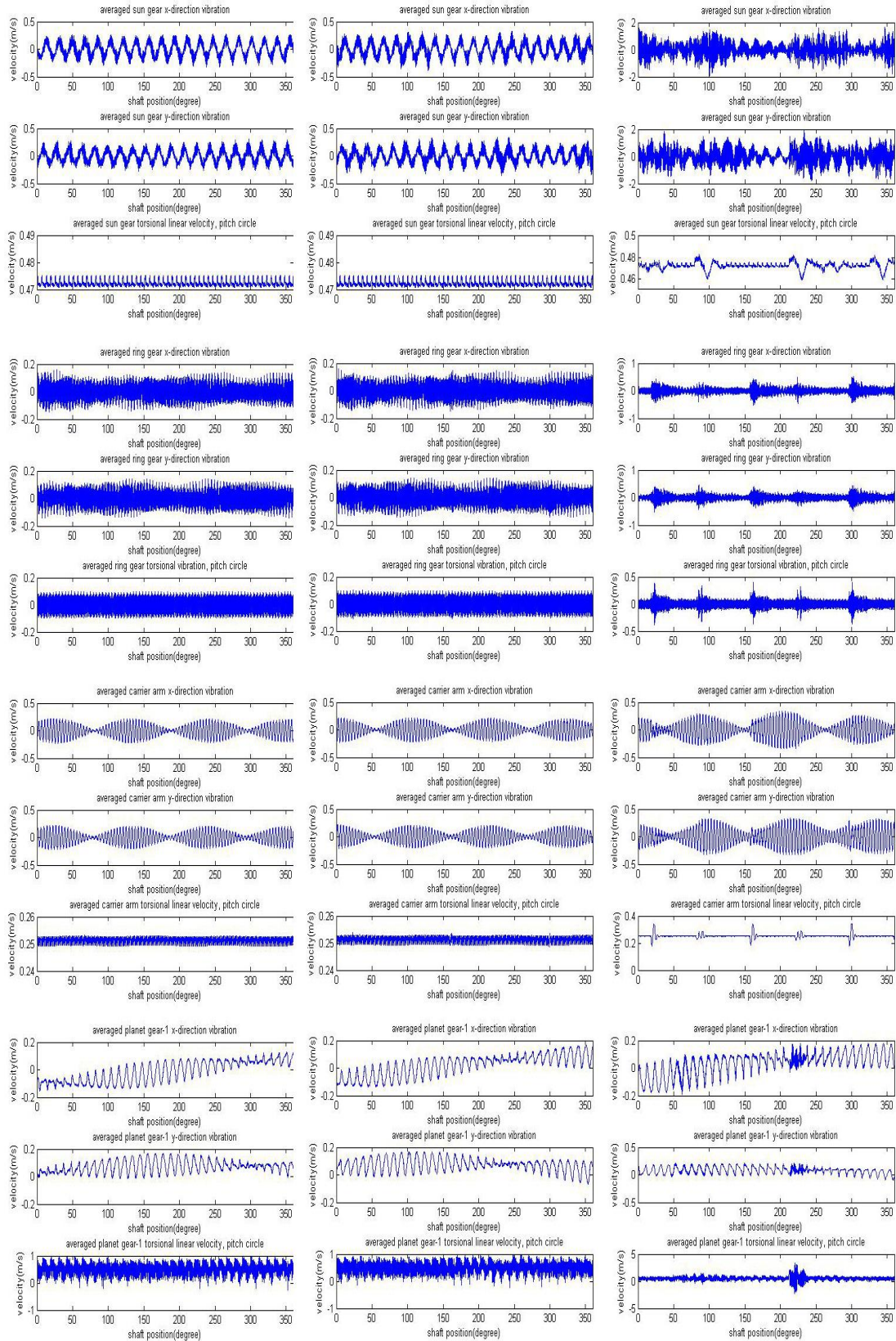


Figure 9-34 Comparison of results, undamaged, 5% cracked and 80% cracked planet gear-1 32nd tooth

It should be noticed that figures in Figure 9-34 do not have the same scale as it is not

easy to see details in large scale figures of the signals with the 5% crack. It can be seen that the influence of the planet gear crack is clearly reflected on both the transverse and torsional vibration signals of the sun gear, ring gear and planet gear-1, but only on the torsional vibration signal (especially for small cracks) for the carrier arm and not at all in the transverse signals of the carrier arm.

Based on the averaged signals, the detectability of planet gear-1 crack is marked as shown in Table 9-7.

Fault type	Detectability of tooth fault			
	1 st	2 nd	3 rd	4 th
Planet gear-1 tooth crack	us, ur, uc, up	xr, yr	xp, yp, xs, ys	xc, yc

Table 9-7 Detectability of planet gear-1 tooth crack based on averaged signals

The visualization of the averaged signal can be used to detect large cracks as shown in Figure 9-33 and 9-34. However it is not practicable for early stage detection. Frequency Spectrum Analysis (FSA) was used here to improve the early stage detectability.

FSA applied to Case-2 with the planet gear-1 crack gives the results shown in Figure 9-35 to 9-46. Each figure shows the frequency range covering the first four mesh harmonics.

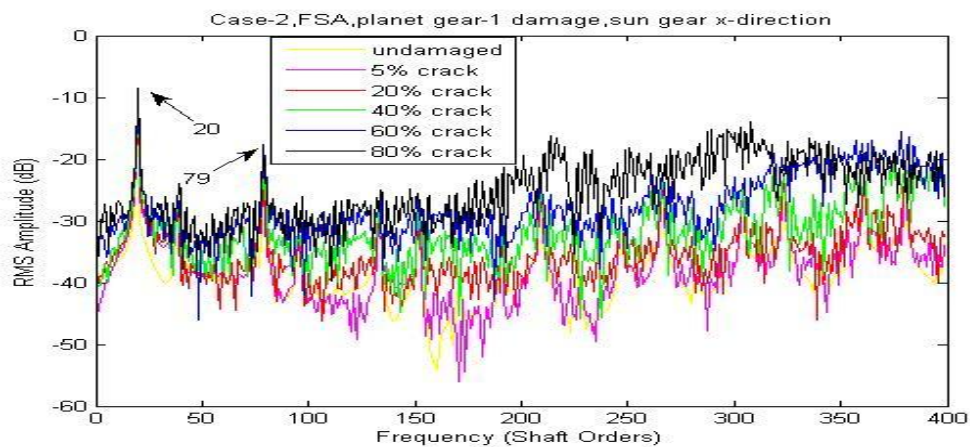


Figure 9-35 Case-2, FSA, planet gear-1 damage, sun gear x-direction

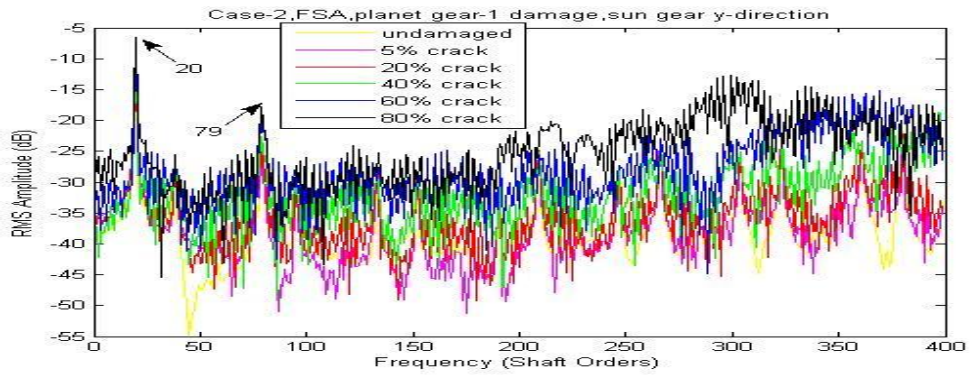


Figure 9-36 Case-2, FSA, planet gear-1 damage, sun gear y-direction

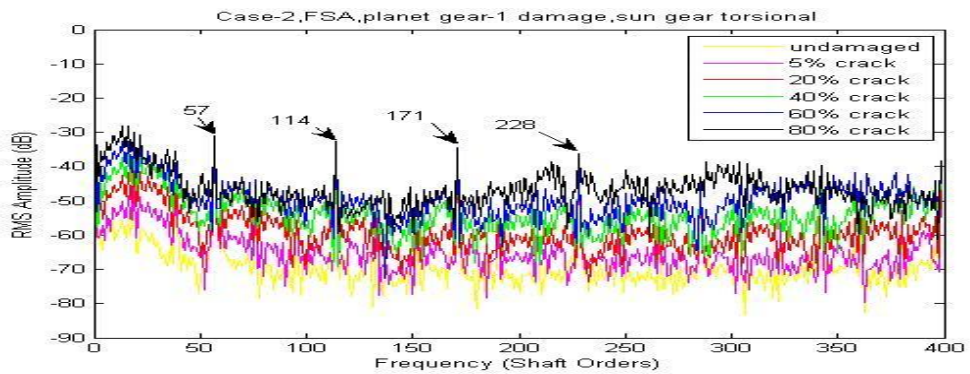


Figure 9-37 Case-2, FSA, planet gear-1 damage, sun gear torsional

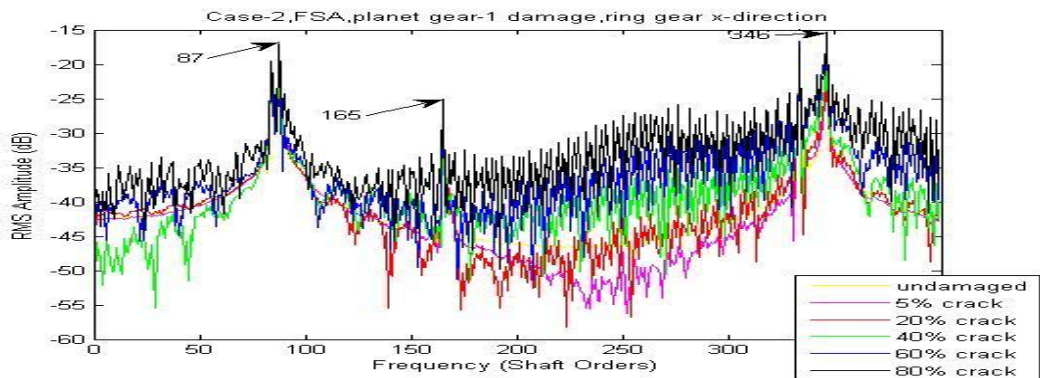


Figure 9-38 Case-2, FSA, planet gear-1 damage, ring gear x-direction

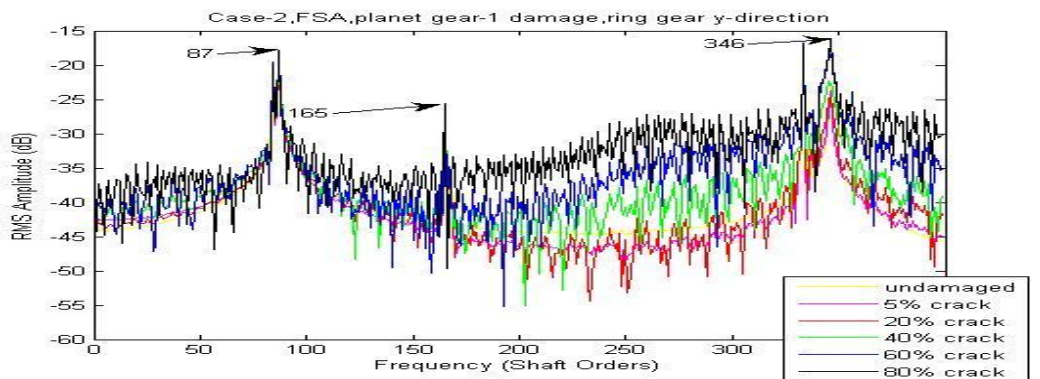


Figure 9-39 Case-2, FSA, planet gear-1 damage, ring gear y-direction

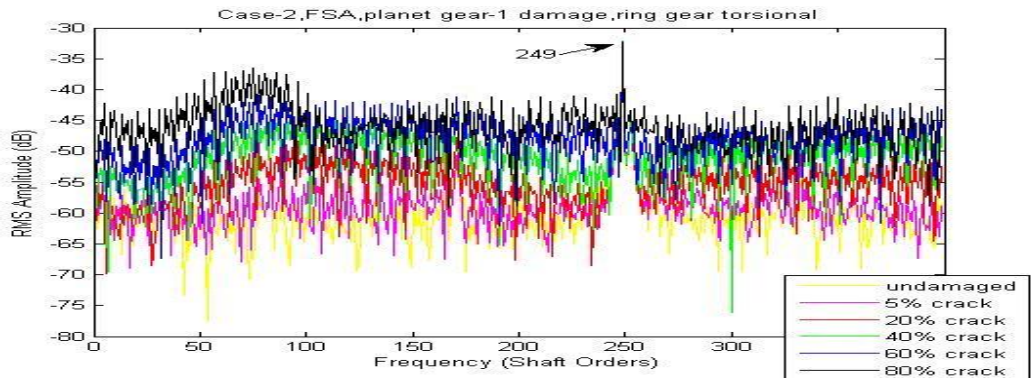


Figure 9-40 Case-2, FSA, planet gear-1 damage, ring gear torsional

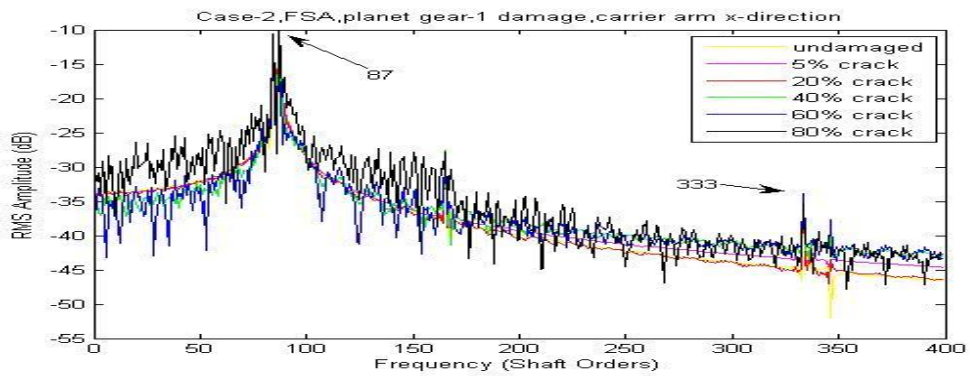


Figure 9-41 Case-2, FSA, planet gear-1 damage, carrier arm x-direction

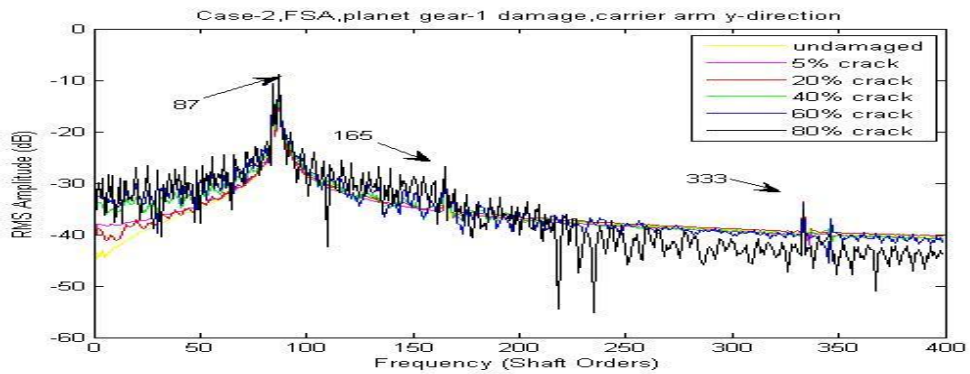


Figure 9-42 Case-2, FSA, planet gear-1 damage, carrier arm y-direction

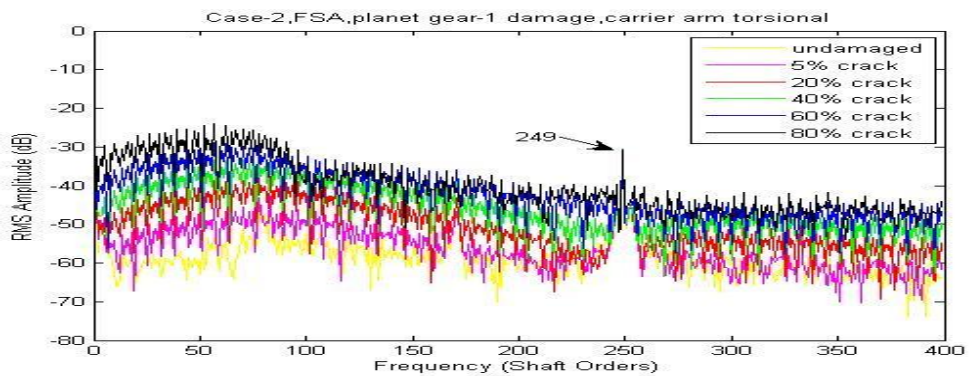


Figure 9-43 Case-2, FSA, planet gear-1 damage, carrier arm torsional

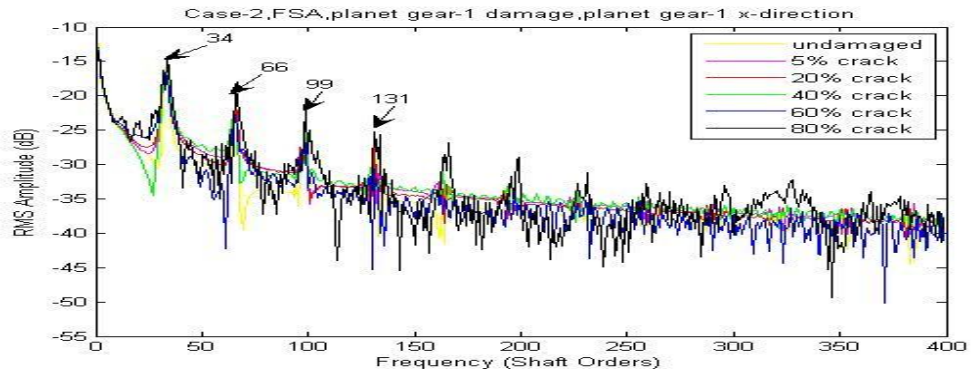


Figure 9-44 Case-2, FSA, planet gear-1 damage, planet gear-1 x-direction

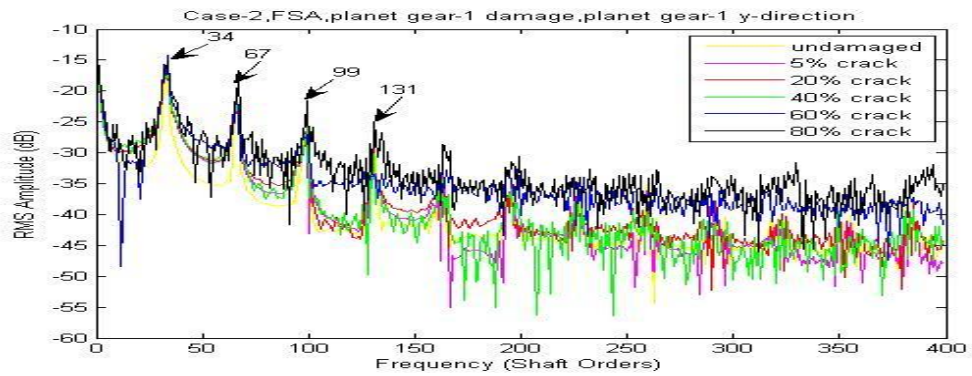


Figure 9-45 Case-2, FSA, planet gear-1 damage, planet gear-1 y-direction

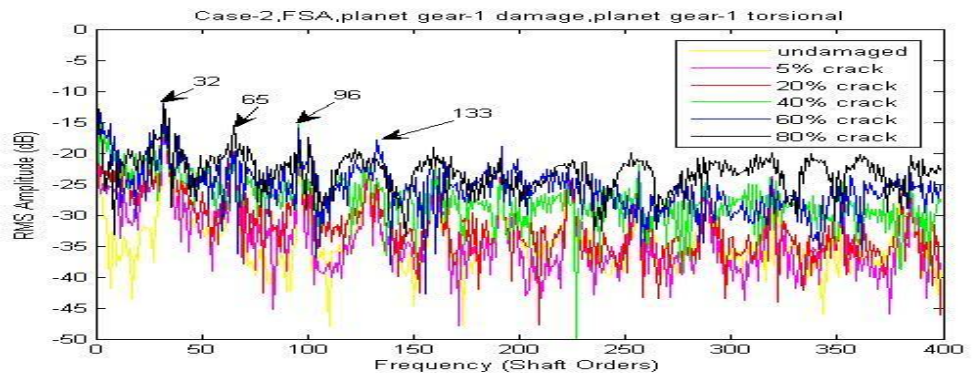


Figure 9-46 Case-2, FSA, planet gear-1 damage, planet gear-1 torsional

Based on the FSA figures above, the detectability grades are marked as shown in Table 9-8 with discussion.

Detectability of planet gear-1 tooth crack		Figure	Discussion		
			Low frequency lines	High frequency lines	Lines in details
1 st	uc	9-43	In very clear good order		
2 nd	up	9-46	In good order		
3 rd	ur	9-40	In good order with little disorder		
4 th	us	9-37	In good order	Some local disorder	In good order
5 th	xr, yr	9-38,9-39	In good order	Some local disorder	
6 th	xp, yp	9-44,9-45	In good order		Local disorder appears very often
7 th	xs, ys	9-35,9-36	Local disorder appears very often		
8 th	xc, yc	9-41,9-42	In wrong order	In wrong order	In wrong order with local disorder

Table 9-8 Detectability of planet gear-1 tooth crack based on FSA

FSA method can slightly improve early stage detectability of the planet gear tooth crack. More importantly it creates a way to refine the grade of detectability. This can give a big advantage in vibration signal selection for fault detection purpose. However, the FSA is not able to locate the tooth faults. In order to do so, CWTA can be employed. The one dimensional wavelet analysis function based on the Morlet wavelet was used with a step by step mode from 1 to 2001 with a step size of 50.

Based on the CWTA figures, the detectability grades are marked as shown in Table 9-9.

Detectability of planet gear-1 tooth crack		Sensitive step range (total data points 2^{16})	Minimum clearly detectable crack	Noise on figure which affects detectability
1 st	uc	350 to 950	Below 5%	Very clear in all step range
2 nd	us	2000 up 1100 to 2000	20% 40%	Very clear in sensitive step range
3 rd	ur	1000 to 1600	Below 40%	Noisy
4 th	xr, yr	1000 to 1600	40%	Very noisy
5 th	xc, yc	1050 to 1550	60%~80%	Clear in sensitive step range
6 th	xs, ys	100 to 600	80%	Very noisy
7 th	xp,yp, up	--	--	Unable to detect

Table 9-9 Detectability of planet gear-1 tooth crack based on CWTA

The CWTA results from the carrier arm torsional vibration signals are compared with different planet gear cracks in Figure 9-47. As the most fault detectable CWTA signal, it provides very clear information of the faults' location at the very early stage with 5% damage.

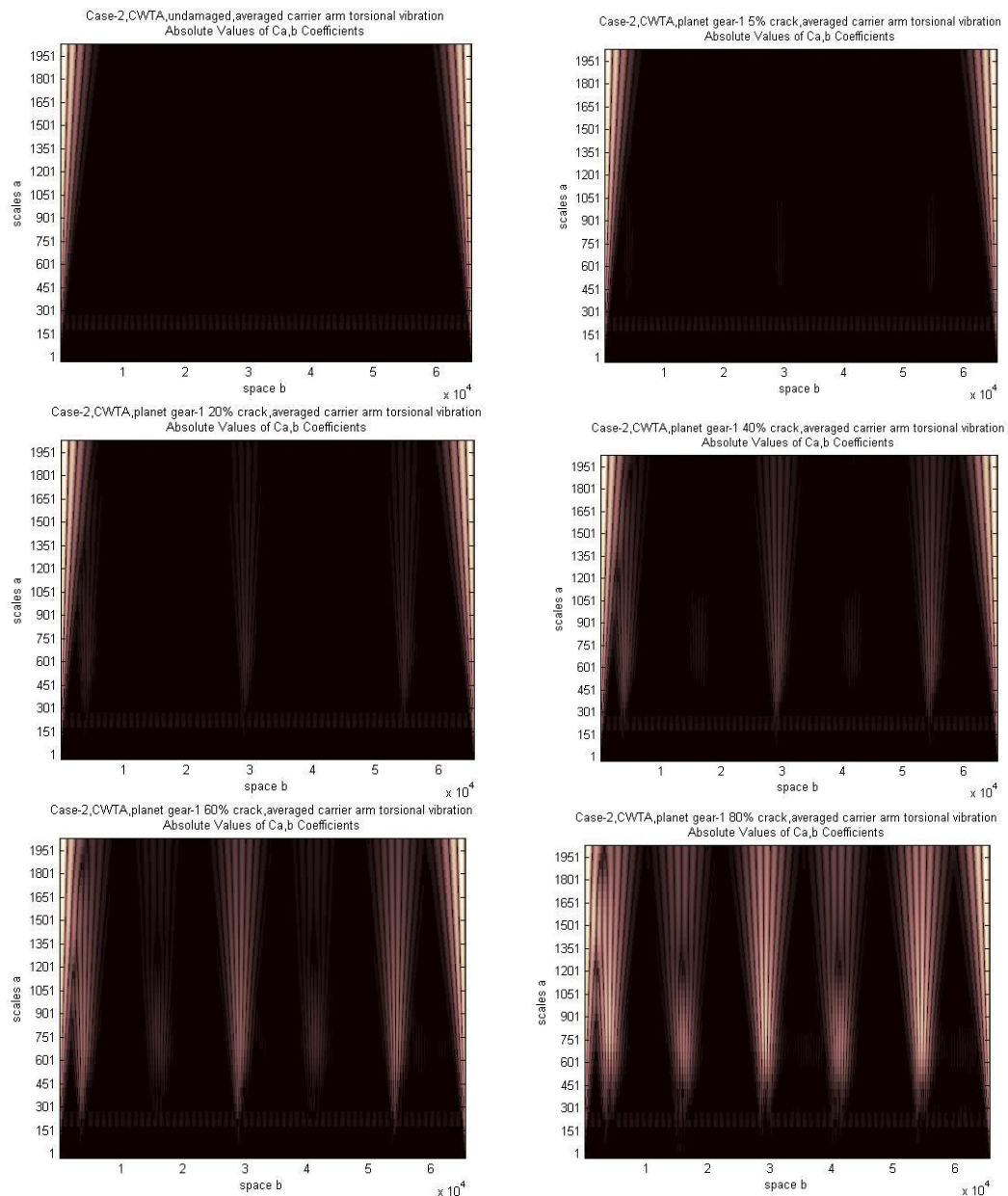


Figure 9-47 Case-2, CWTA, planet gear-1 crack, averaged carrier arm torsional vibration

The CWTA results for the sun gear torsional vibration signals are compared with different planet gear cracks in Figure 9-48. As the second most fault detectable CWTA signal, it provides clear information of the faults' location at the early stage (20%~40%) though the signal is relatively noisy outside the sensitive step range.

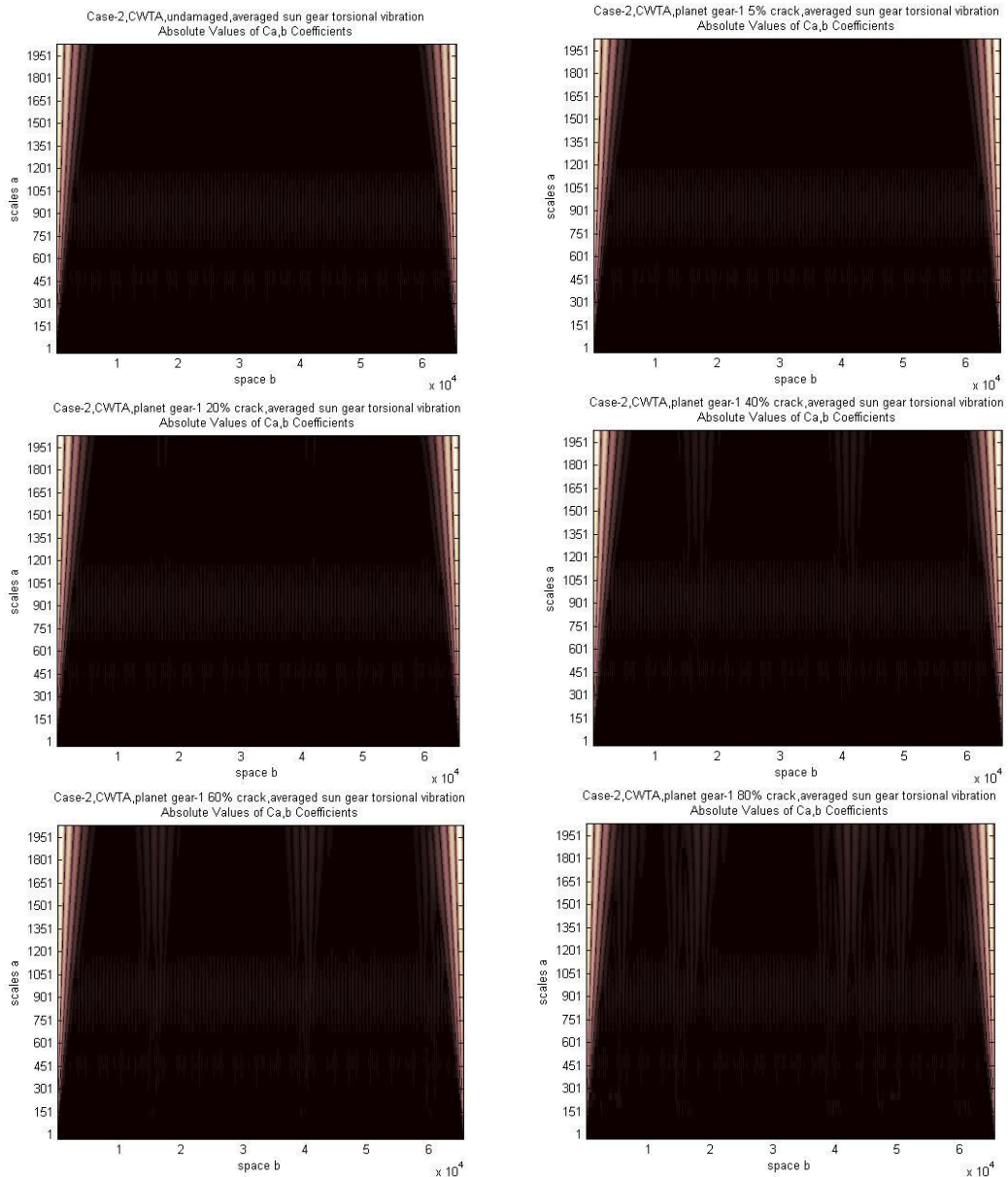


Figure 9-48 Case-2, CWTA, planet gear-1 crack, averaged sun gear torsional vibration

In conclusion, the CWTA is shown to be an efficient method to detect and locate the planet gear tooth cracks. It also provides information of fault detectability of vibration signals.

9.2. MODEL WITH A LOCALISED TOOTH SPALL IN MESH

Tooth spalling is simulated using both a change of mesh stiffness and a change of tooth profile. Spalling simulated in this thesis is considered to occupy the whole tooth width, with a controlled width along the teeth contact line, a controlled location along the tooth meshing area, controlled depth and programmed cross section profile. All spalls are assumed to be located in the tooth meshing area and the reduction of material gives a change of mesh stiffness and when the spall occurs across the whole width of the tooth, the tooth profile is changed. To limit the computation time, the change of mesh stiffness is based on an assumed function relative to all the dimensions of spalling but with low accuracy (high accuracy can be achieved by careful FEA analysis). A description of tooth spalling simulated in this thesis is shown in Figure 9-49.

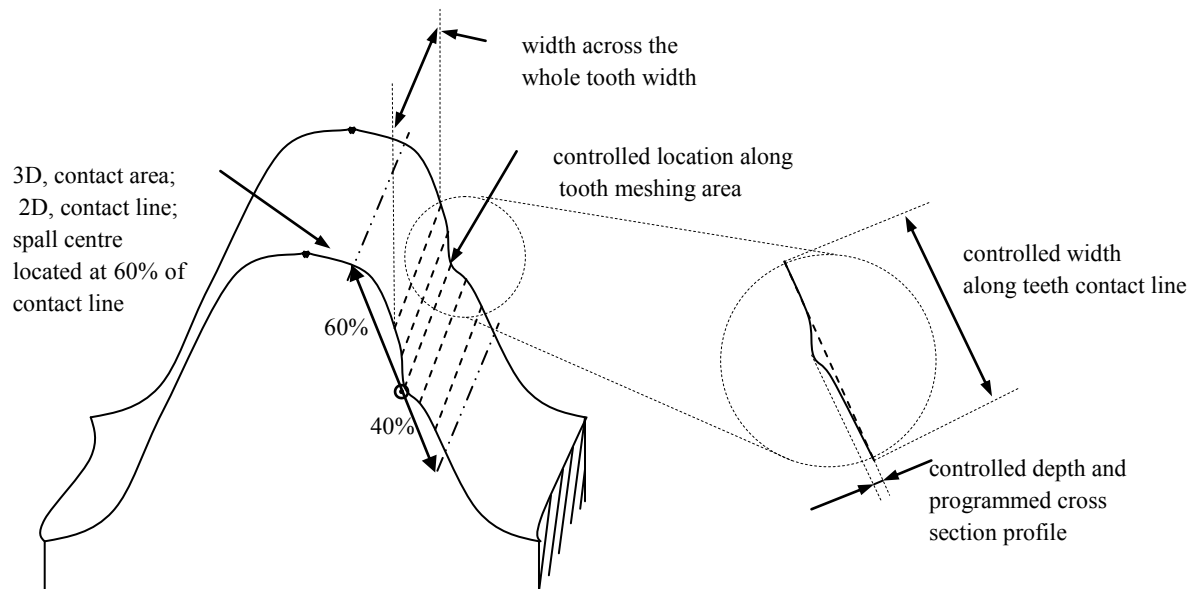


Figure 9-49 A description of tooth spalling

To simplify the overall model, the change of tooth profile is combined into the tooth profile error. Both methods of dealing with the stiffness change and tooth profile change have the ability to handle multiple spalls and even arbitrary setting of spalling.

Spalls with four different dimensions have been used namely $5e-5$, $10e-5$, $20e-5$ and

w20e-5 (indicate spalling depth in meter). They all have the same location on the teeth (center point of spall is at the 60% of contact line, see Figure 9-49) and the same cross section profile (based on Cosine function) across the entire tooth width. The first three have the same width of 10% of tooth contact line and the last one has a doubled width.

Results are listed and analyzed with two methods FSA and CWTA after signal averaging.

9.2.1. SPALL ON SUN GEAR TOOTH

The tooth spalling simulated on the sun gear was a single spall on the 19th tooth where the 1st tooth was defined to be the first tooth in mesh with the first planet gear at time zero.

Simulation outputs after signal averaging with a single w20e-5 spall on the sun gear at the 19th tooth are shown in Figure 9-50.

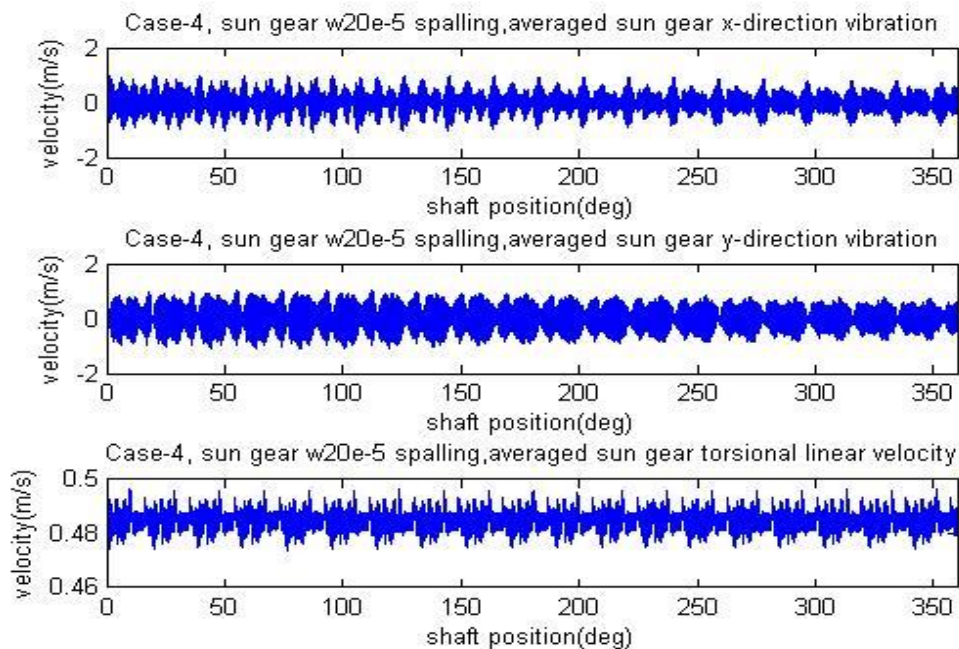


Figure 9-50 Simulation outputs after signal averaging with a single w20e-5 spall on the sun gear at the 19th tooth

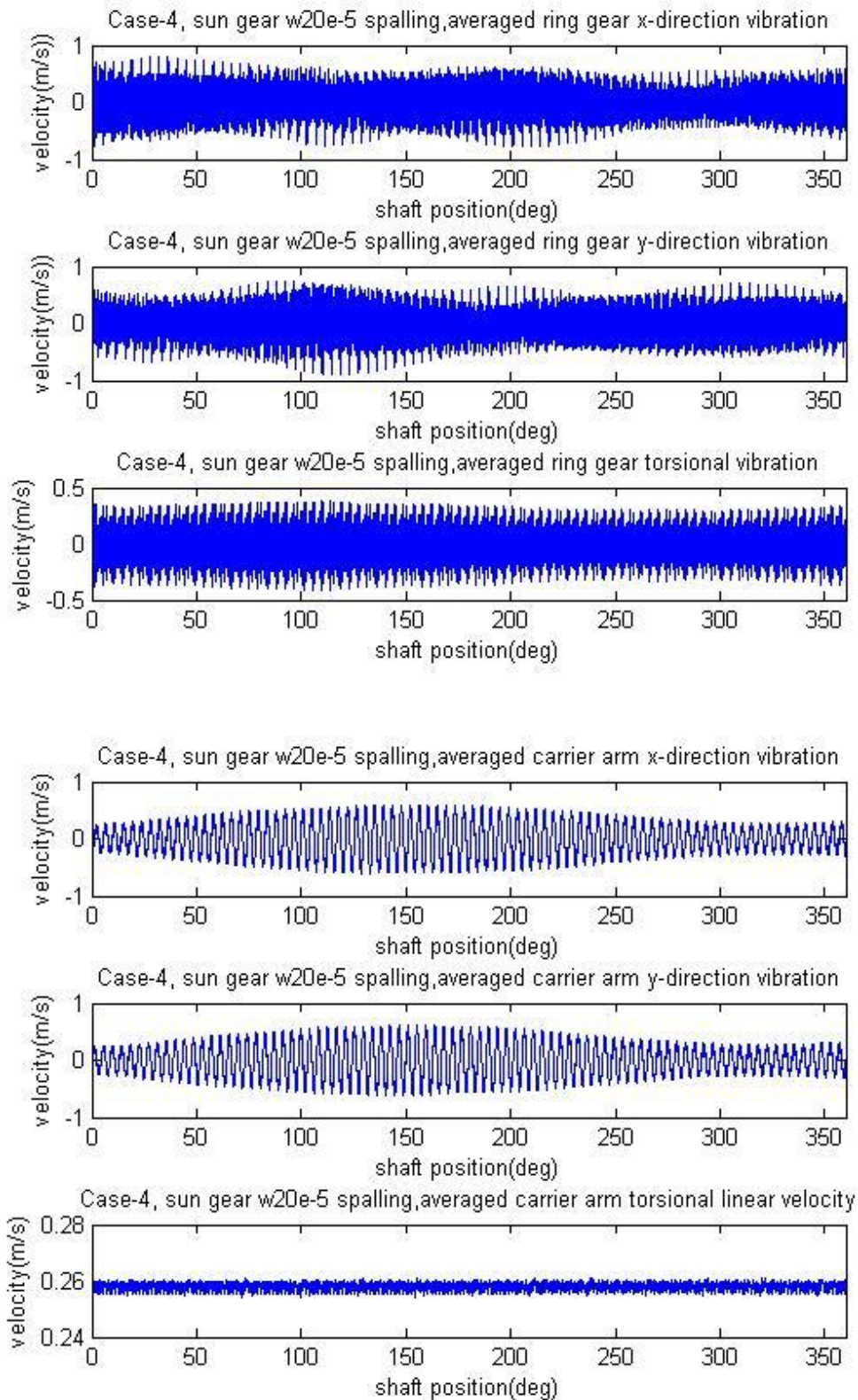


Figure 9-50(continued) Simulation outputs after signal averaging with a single w_{20e-5} spall on the sun gear at the 19th tooth

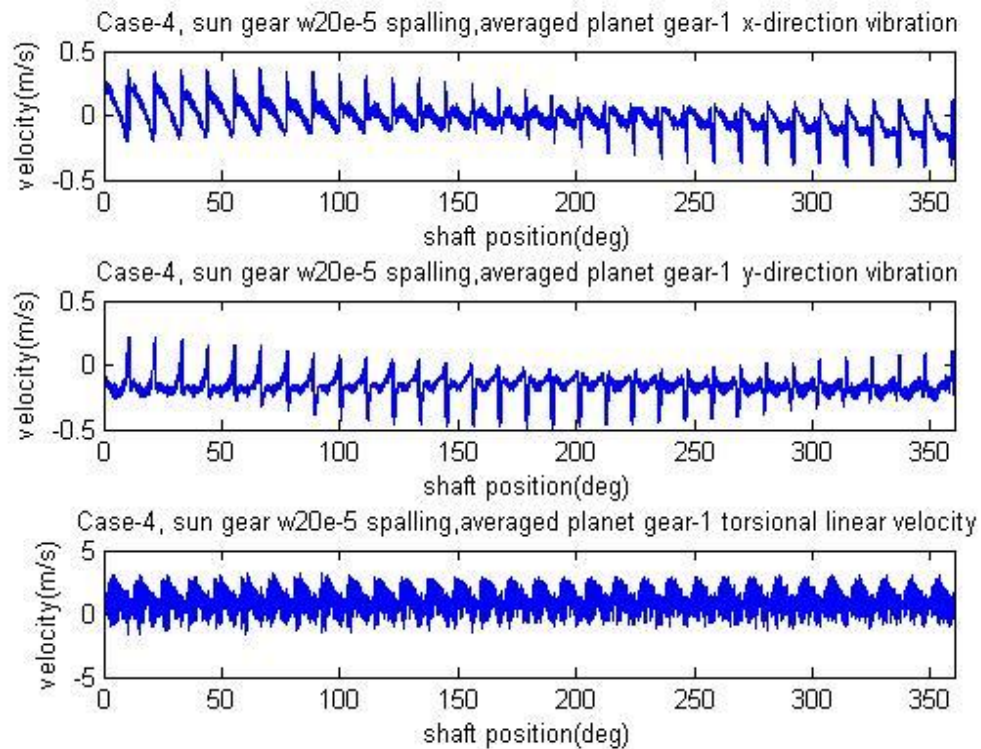


Figure 9-50(continued) Simulation outputs after signal averaging with a single $w20e-5$ spall on the sun gear at the 19th tooth

A comparison was made with the sun gear spalling using the results of a $5e-5$ spall on the sun gear (19th tooth) as well as a $10e-5$ spall shown in Figure 9-51 (left column, $5e-5$ spall; middle column, $10e-5$ spall; right column, $w20e-5$ spall). It can be seen that the influence of the sun gear spall is very hard to be seen from the averaged transverse and torsional signals. The only noticeable influence of the sun gear spall is shown in the figure of the carrier arm torsional velocity signal as there are 13 pulses (though they are very hard to notice) in the period of one carrier arm revolution (see in Figure 9-50). Based on the averaged signals, detectability grades can be marked where the carrier arm torsional signal appears to be superior than all other signals.

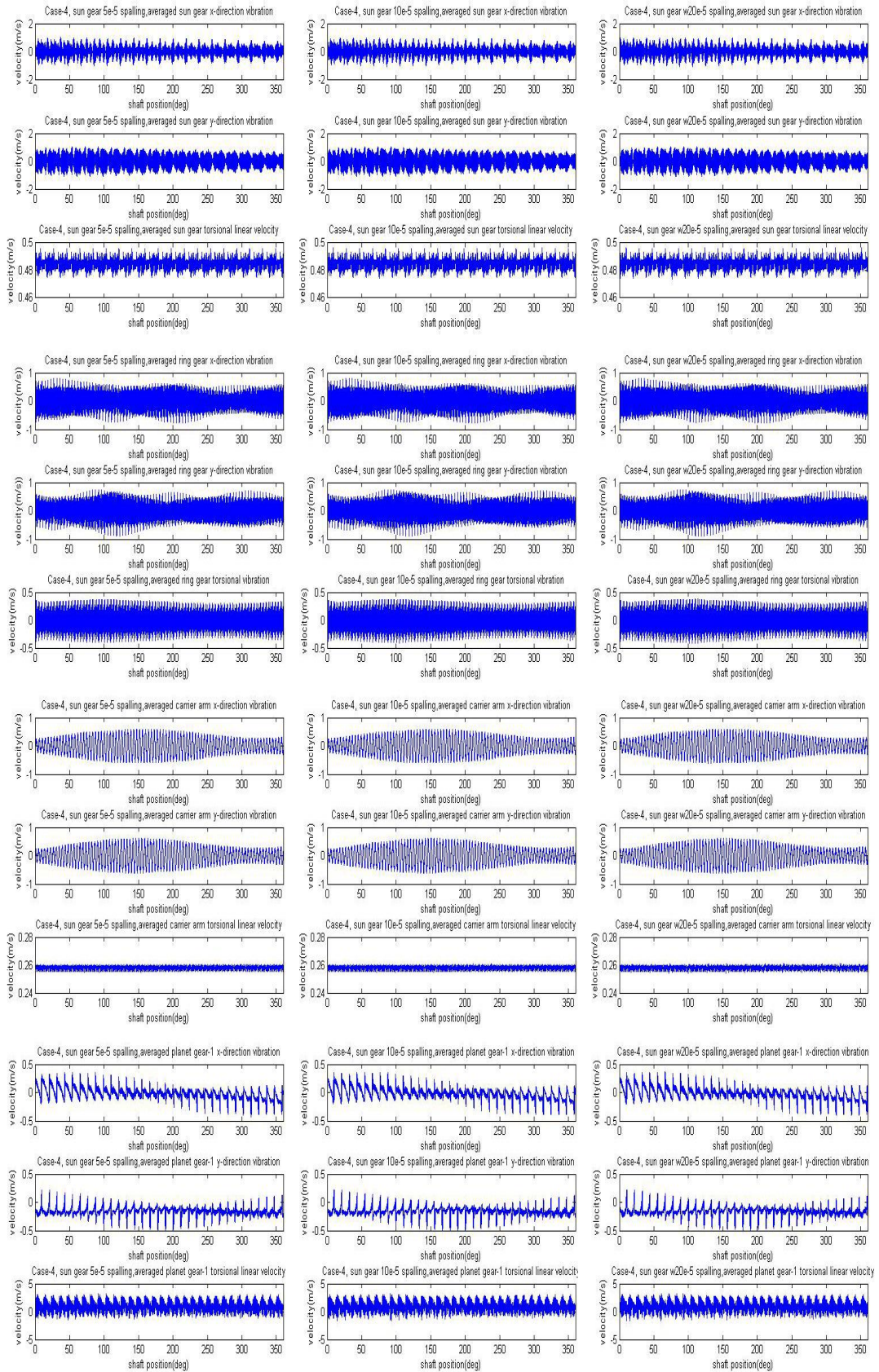


Figure 9-51 Comparison of results, 5e-5 spall, 10e-5 spall and w20e-5 spall on the sun gear 19th tooth

The averaged signal is expected to detect very large spalls as indicated for the detectability of sun gear tooth cracks, however, it is unlikely to be practicable for early stage detection of sun gear spalling as shown in Figure 9-51. Frequency Spectrum Analysis (FSA) was then used to improve the early stage detectability of sun gear tooth spalling.

The FSA applied to Case-4 with the sun gear spalling gives the results shown in Figure 9-52 to 9-63. Each figure shows the frequency range covering the first four mesh harmonics.

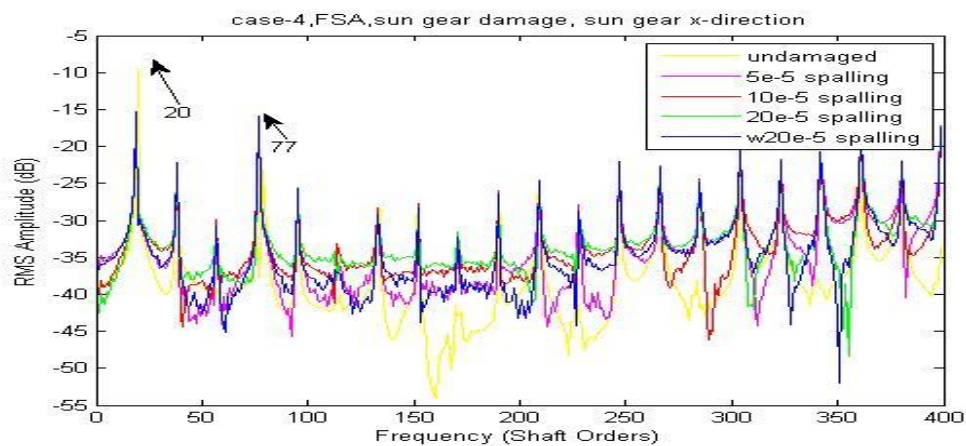


Figure 9-52 Case-4, FSA, sun gear damage, sun gear x-direction

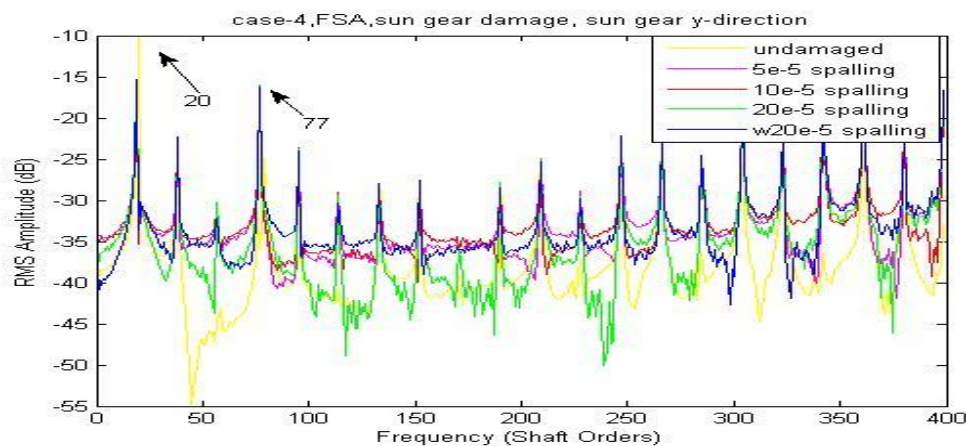


Figure 9-53 Case-4, FSA, sun gear damage, sun gear y-direction

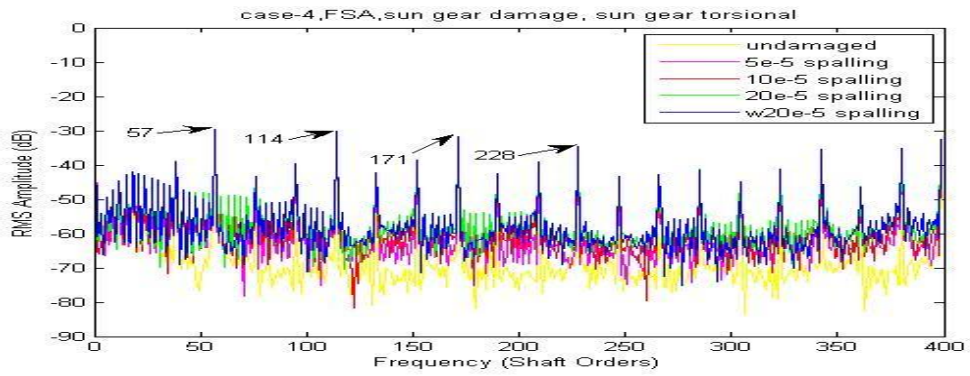


Figure 9-54 Case-4, FSA, sun gear damage, sun gear torsional

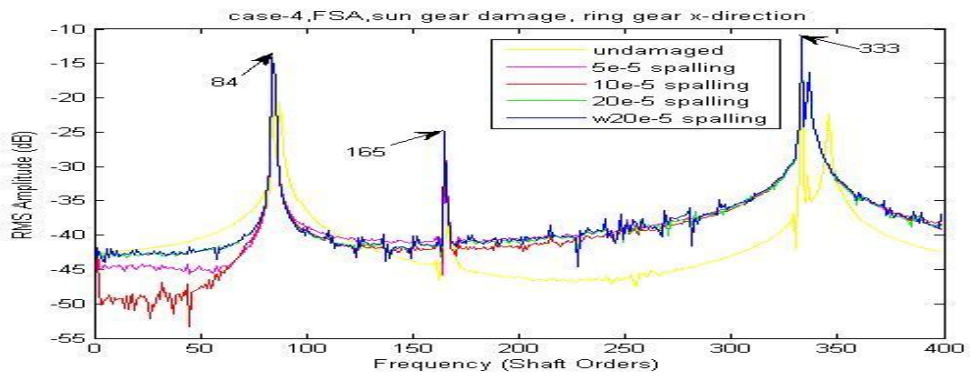


Figure 9-55 Case-4, FSA, sun gear damage, ring gear x-direction

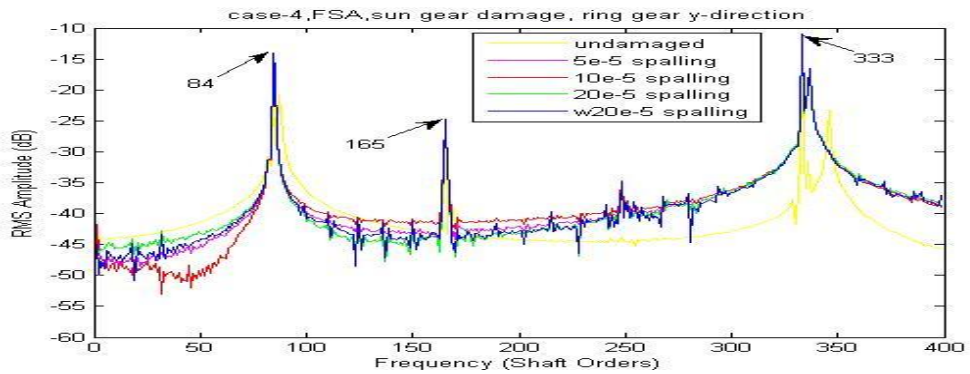


Figure 9-56 Case-4, FSA, sun gear damage, ring gear y-direction

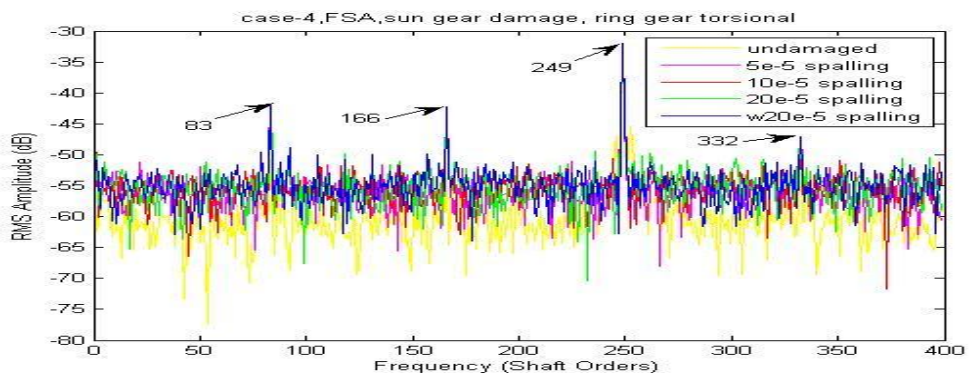


Figure 9-57 Case-4, FSA, sun gear damage, ring gear torsional

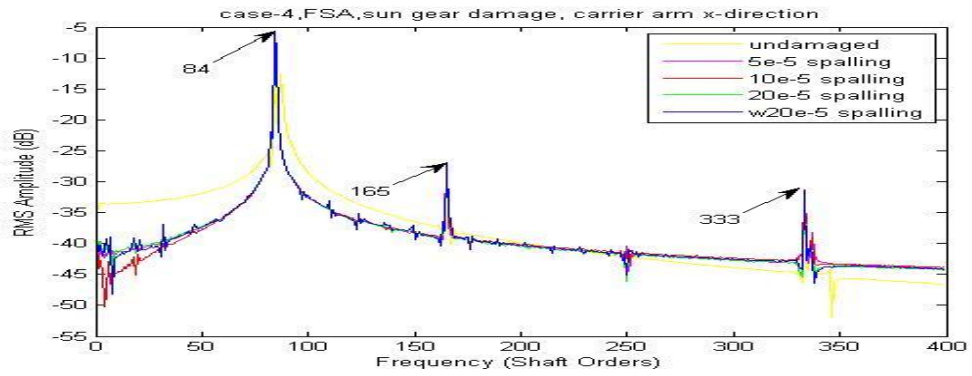


Figure 9-58 Case-4, FSA, sun gear damage, carrier arm x-direction

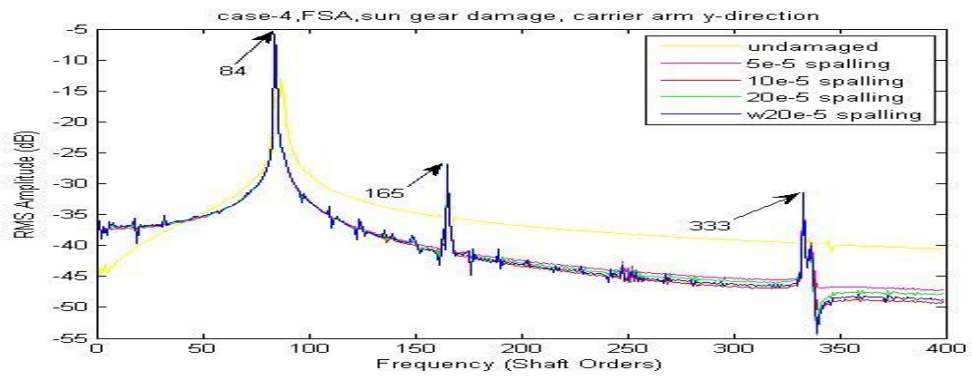


Figure 9-59 Case-4, FSA, sun gear damage, carrier arm y-direction

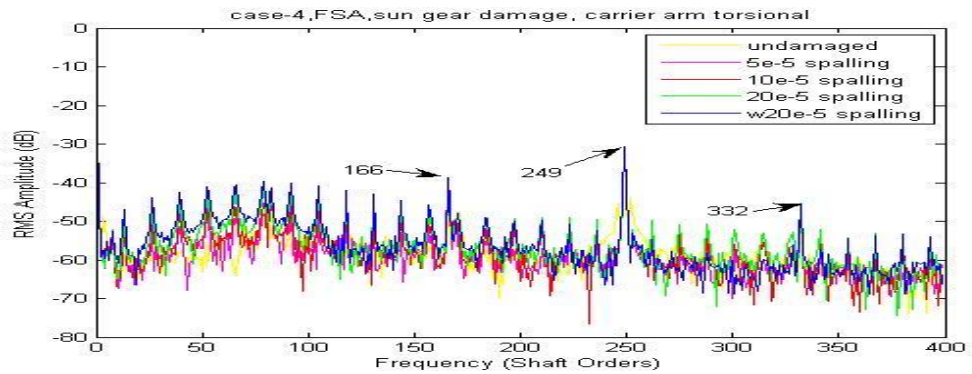


Figure 9-60 Case-4, FSA, sun gear damage, carrier arm torsional

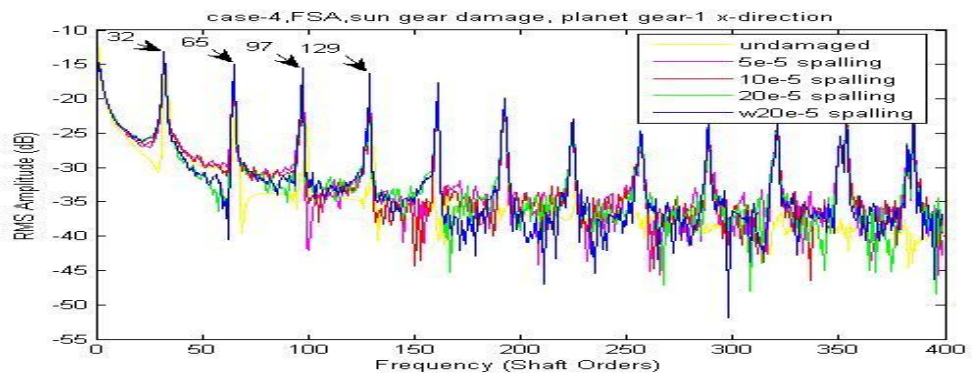


Figure 9-61 Case-4, FSA, sun gear damage, planet gear-1 x-direction

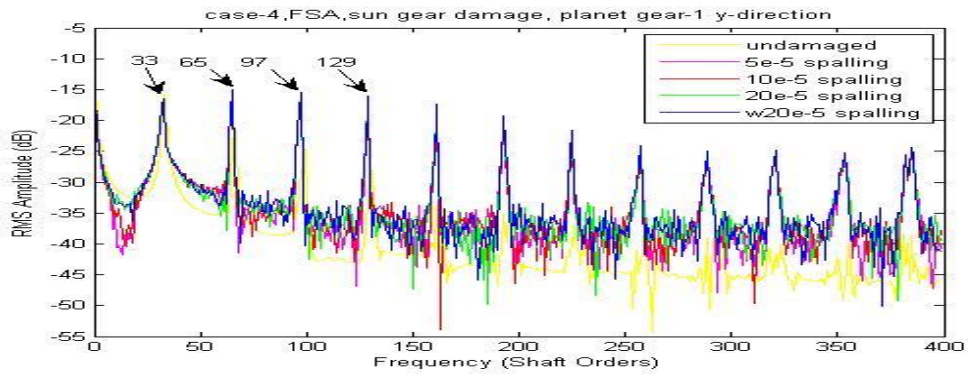


Figure 9-62 Case-4, FSA, sun gear damage, planet gear-1 y-direction

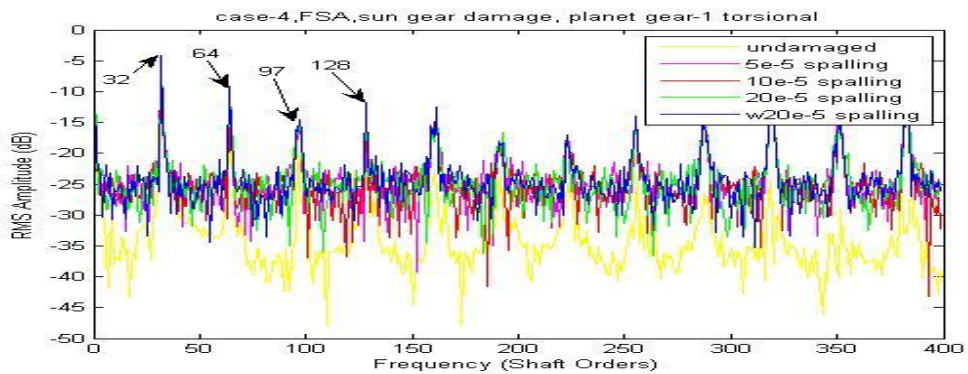


Figure 9-63 Case-4, FSA, sun gear damage, planet gear-1 torsional

Based on the FSA figures above, the detectability grades are marked as shown in Table 9-10 with discussion.

Detectability of sun gear tooth spalling		Figure	Discussion		
			Low frequency lines	High frequency lines	Lines in details
1 st	us	9-54	In good order with some local disorder		
2 nd	ur, uc, up	9-57, 9-60, 9-63	In order, but distance between lines is small or have unexpected disorder often		
3 rd	xs, ys	9-52, 9-53	Disorder happens very often		
4 th	xr,yr, xp,yp	9-55,9-56, 9-61,9-62	Mostly in disorder		
5 th	xc,yc	9-58,9-59	In wrong order with local disorder		

Table 9-10 Detectability of sun gear tooth spalling based on FSA

The previous results have shown that the FSA method can slightly improve the early stage detectability of the sun gear tooth spalling. More importantly it creates a way to

refine the grade of detectability which shows generally that the torsional signal is superior to the transverse signal for the sun gear spalling detection. However, the FSA was not able to locate the tooth fault. In order to do so, CWTA can be employed. The one dimensional wavelet analysis function using the Morlet wavelet can used with a step by step mode from 1 to 501 with a step size of 10.

Based on the CWTA figures, the detectability grades are marked as shown in Table 9-11.

Detectability of sun gear tooth spalling		Sensitive step range (total data points 2^{16})	Minimum clearly detectable spall	Noise on figure which affects detectability
1 st	uc	500 to 700	20e-5	Very clear in all step range
2 nd	us	1200 to 1900	w20e-5	Very clear in sensitive step range
3 rd	others	--	--	Unable to detect

Table 9-11 Detectability of sun gear tooth spalling based on CWTA

The CWTA results applied to the carrier arm torsional vibration signals are compared with different sun gear spalls in Figure 9-64 with a refined step range from 1 to 2001 (a step size of 50). The CWTA has been demonstrated to be the most fault detectable approach. It provides very clear information of the faults“location in very early stage which for the spall is below the 20e-5 damage level.

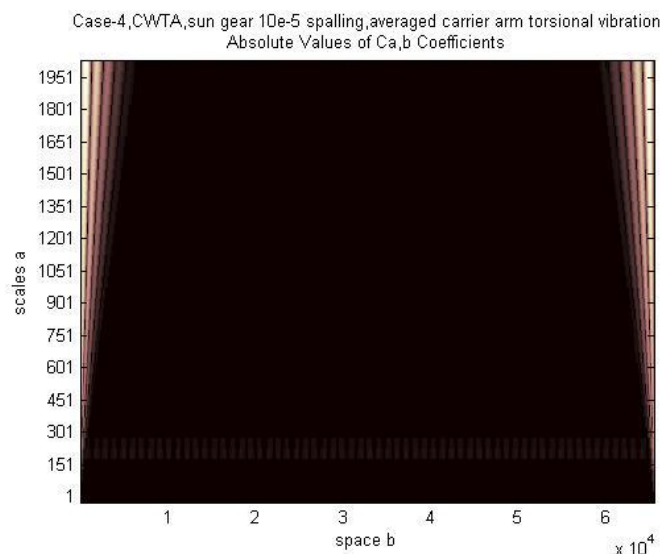


Figure 9-64 Case-2, CWTA, sun gear spall, averaged carrier arm torsional vibration

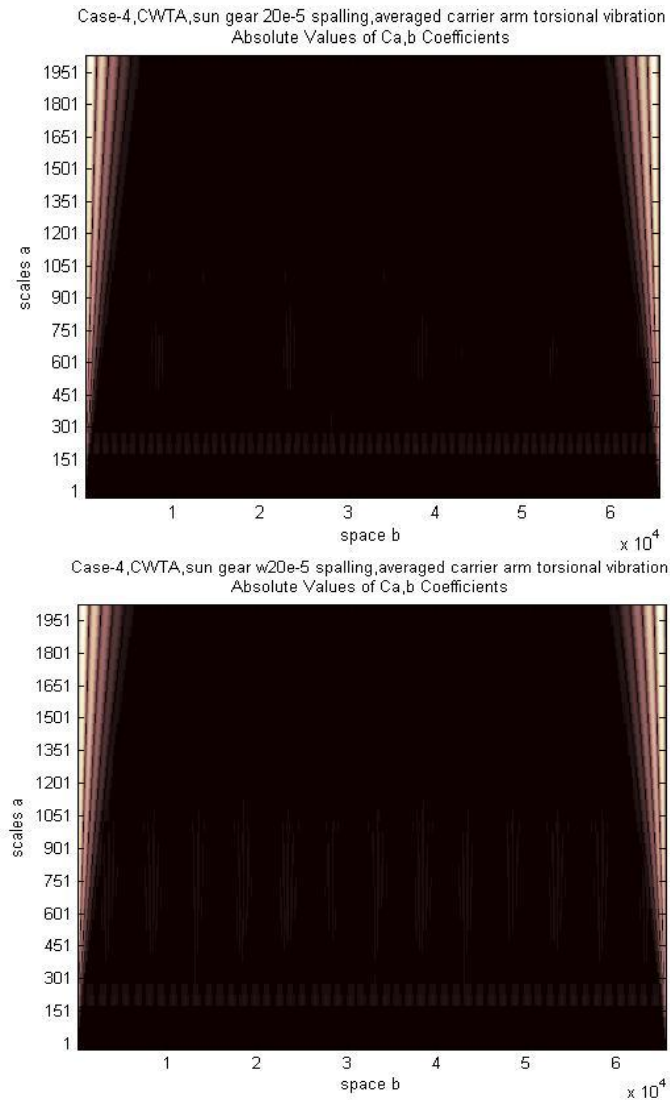


Figure 9-64(continued) Case-2, CWTA, sun gear spall, averaged carrier arm torsional vibration

The CWTA results from the sun gear torsional vibration signals are shown in Figure 9-65. As the second most fault detectable CWTA signal, it provides information of the faults' location starting from the w20e-5 damage level, though on this damage level the fault can not be fully detected.

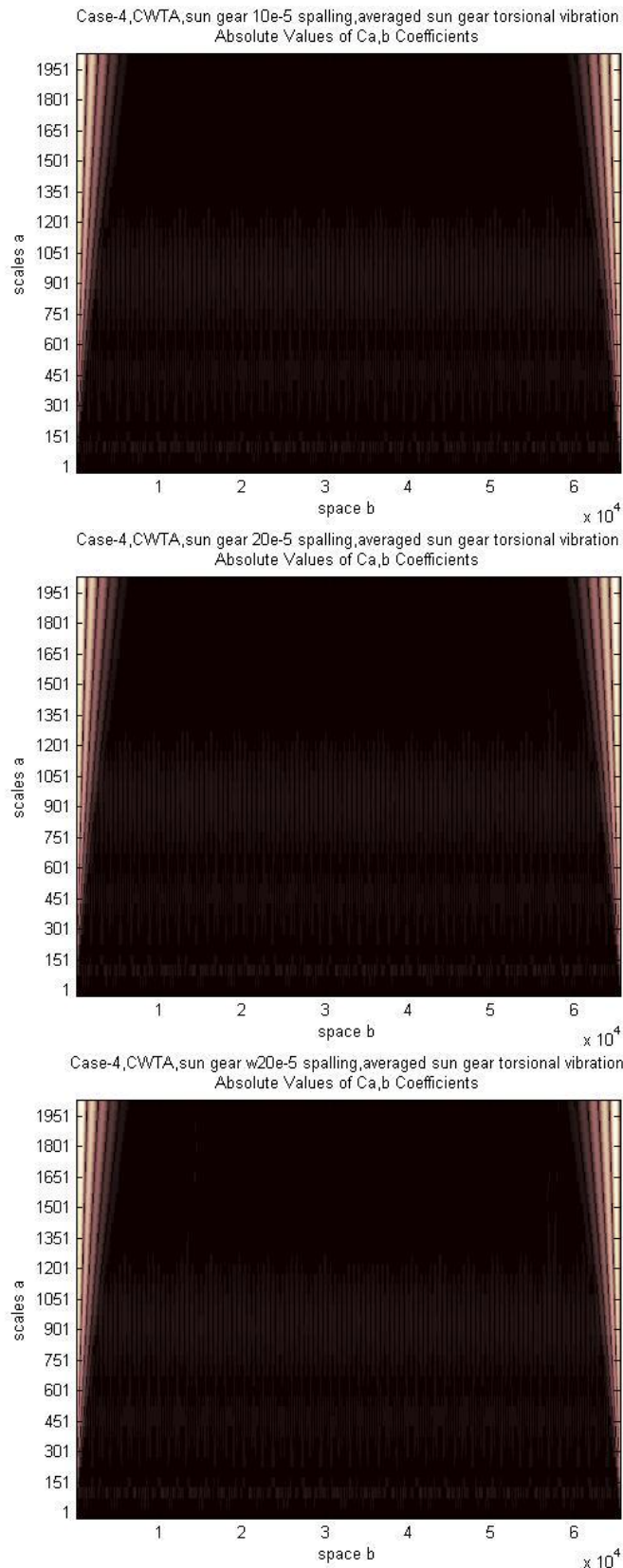


Figure 9-65 Case-2, CWTA, sun gear spall, averaged sun gear torsional vibration

In conclusion, the CWTA shows and locates the sun gear tooth spall damage using the sun gear and carrier arm torsional signals at an early stage.

9.2.2. SPALL ON RING GEAR TOOTH

The tooth spalling simulated on the ring gear was a single spall localized on the 83rd tooth where the 1st tooth was defined to be the first tooth in mesh with the first planet gear at time zero.

Simulation outputs after signal averaging with a single $w20e-5$ spall on the ring gear at the 83rd tooth are shown in Figure 9-66.

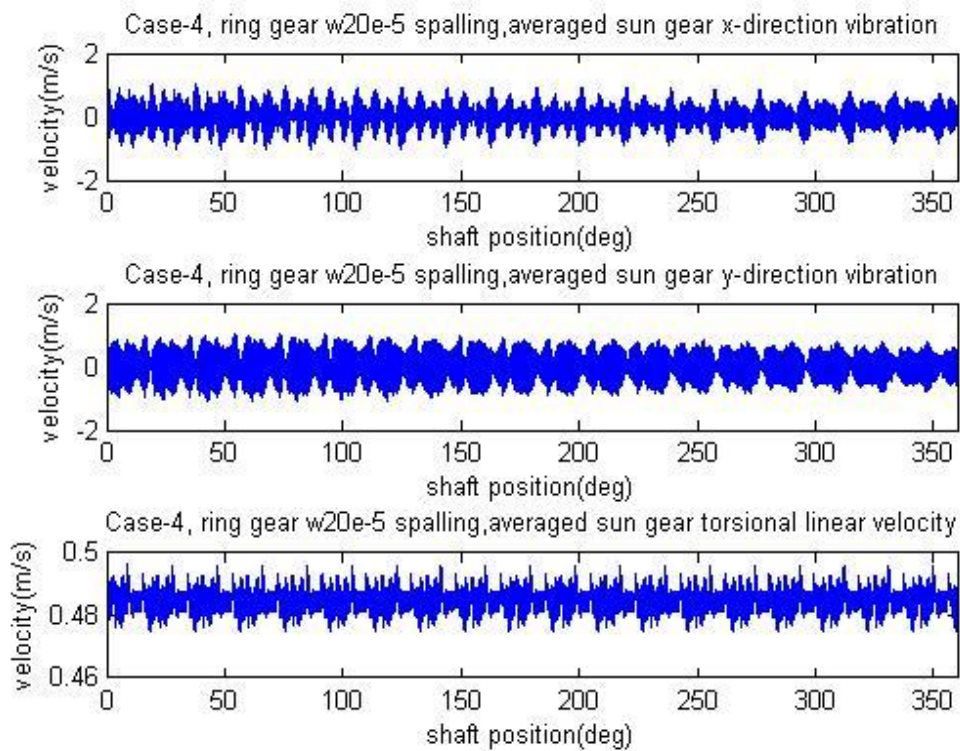


Figure 9-66 Simulation outputs after signal averaging with a single $w20e-5$ spall on the ring gear at the 83rd tooth

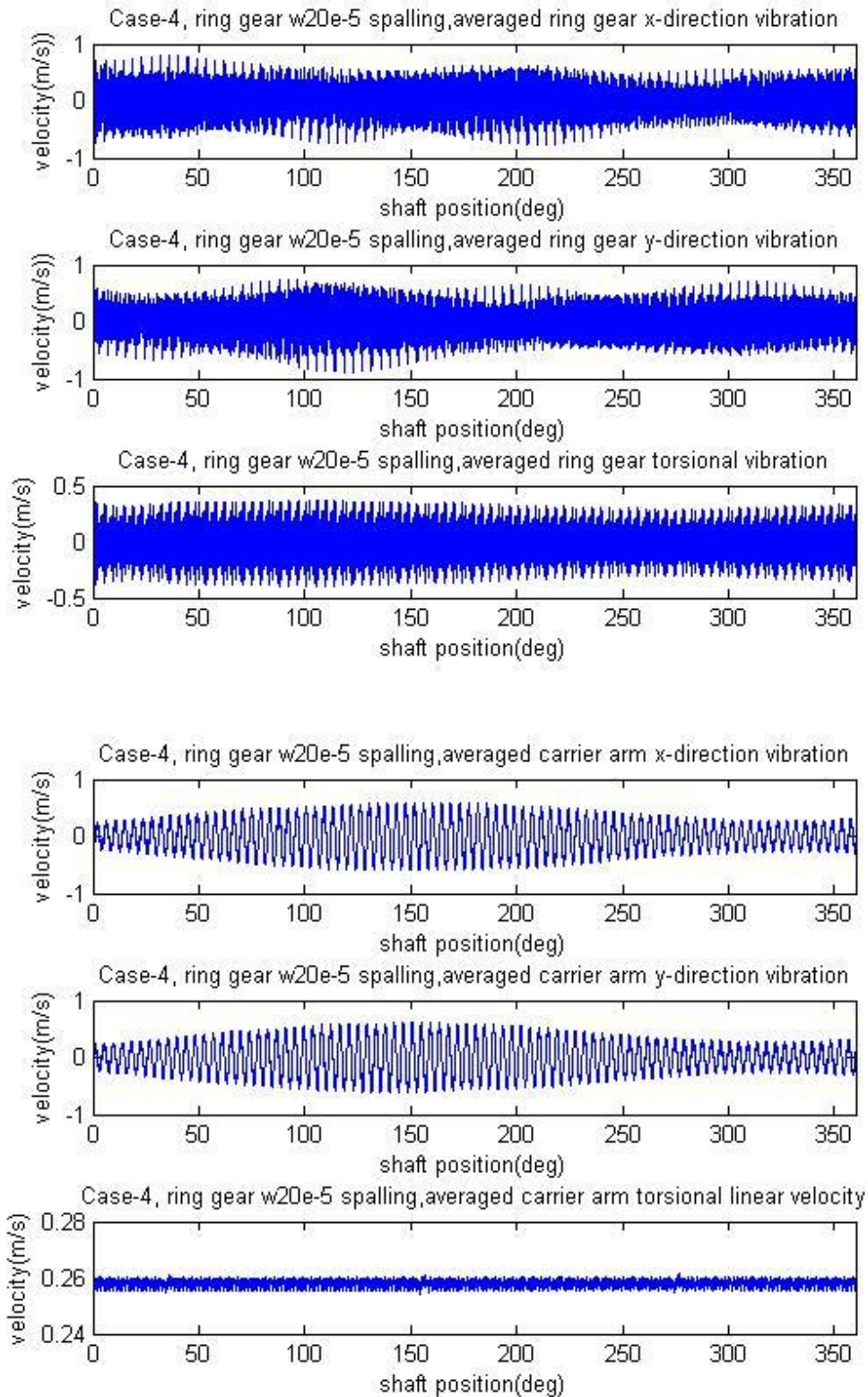


Figure 9-66(continued) Simulation outputs after signal averaging with a single w20e-5 spall on the ring gear at the 83rd tooth

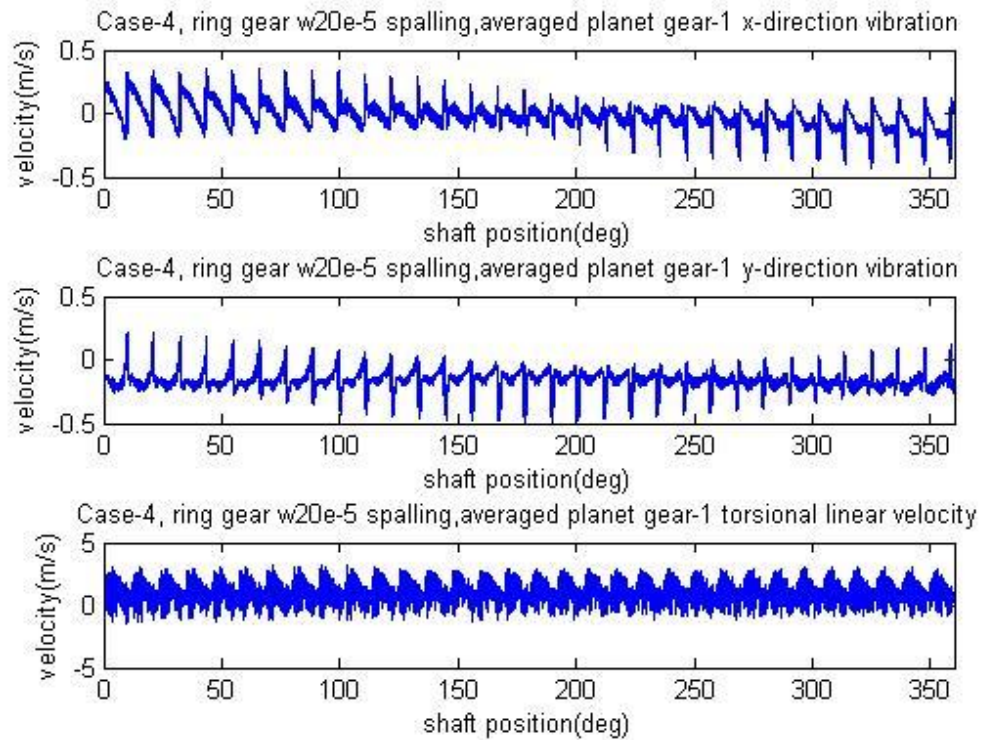


Figure 9-66(continued) Simulation outputs after signal averaging with a single w20e-5 spall on the ring gear at the 83rd tooth

A comparison was made with the ring gear spall using results of a 5e-5 spall on the ring gear (83rd tooth) as well as a 10e-5 spall shown in Figure 9-67 (left column, 5e-5 spall; middle column, 10e-5 spall; right column, w20e-5 spall). It can be seen that the influence of the ring gear spall is very hard to be seen from the averaged signals, including both transverse and torsional motions except for the carrier arm torsional velocity signal, which shows clearly 3 pulses in the period of one carrier arm revolution. Based on the averaged signals, detectability grades can be marked as the carrier arm torsional signal again appears to be superior than all other signals.

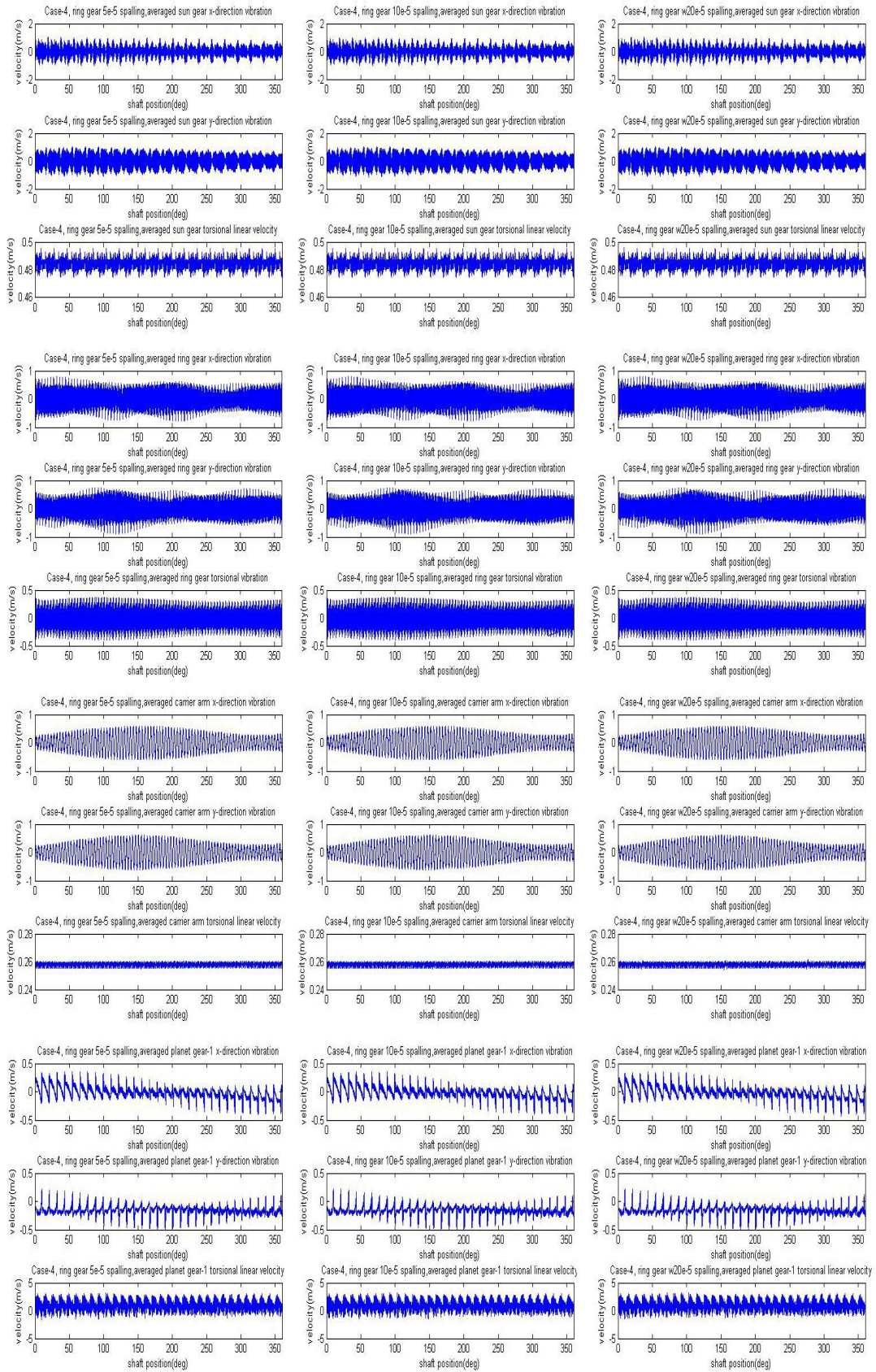


Figure 9-67 Comparison of results, 5e-5 spall, 10e-5 spall and w20e-5 spall on the ring gear at the 83rd tooth

The averaged signal is expected to detect very large spalls as it has already been proven to be able to detect ring gear tooth cracks, however, it is seen to not be sensitive for early stage ring gear spalling as shown in Figure 9-67. Frequency Spectrum Analysis (FSA) was then used to improve the early stage detectability.

The FSA applied to Case-4 with the ring gear spalling gives the results shown in Figure 9-68 to 9-79. Each figure shows the frequency range covering the first four mesh harmonics.

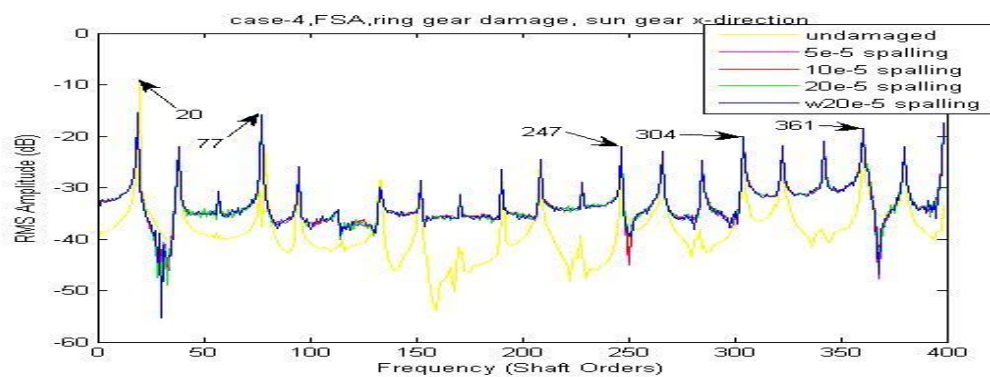


Figure 9-68 Case-4, FSA, ring gear damage, sun gear x-direction

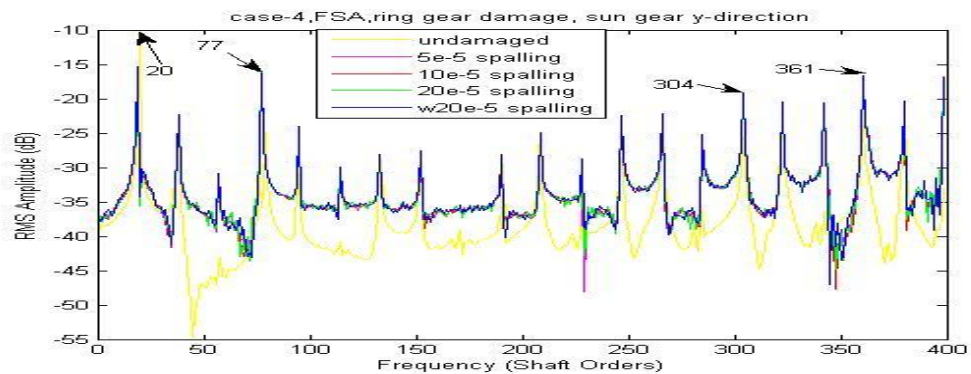


Figure 9-69 Case-4, FSA, ring gear damage, sun gear y-direction

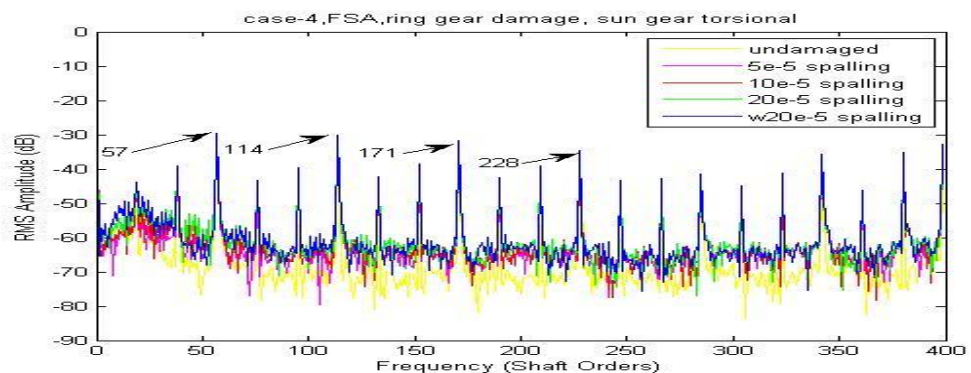


Figure 9-70 Case-4, FSA, ring gear damage, sun gear torsional

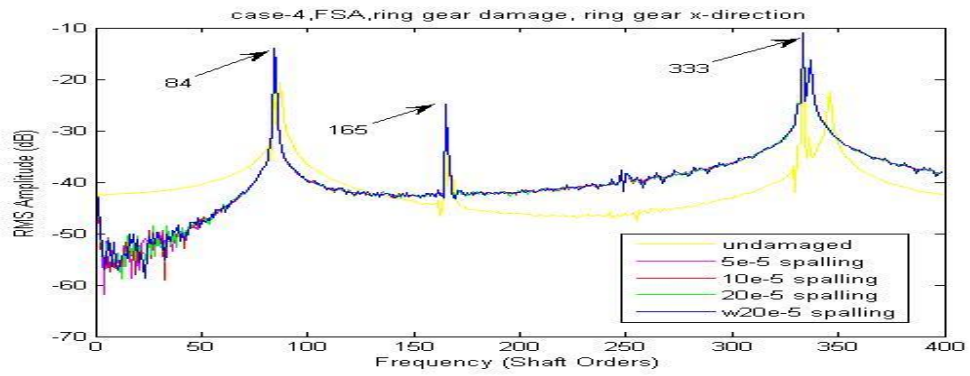


Figure 9-71 Case-4, FSA, ring gear damage, ring gear x-direction

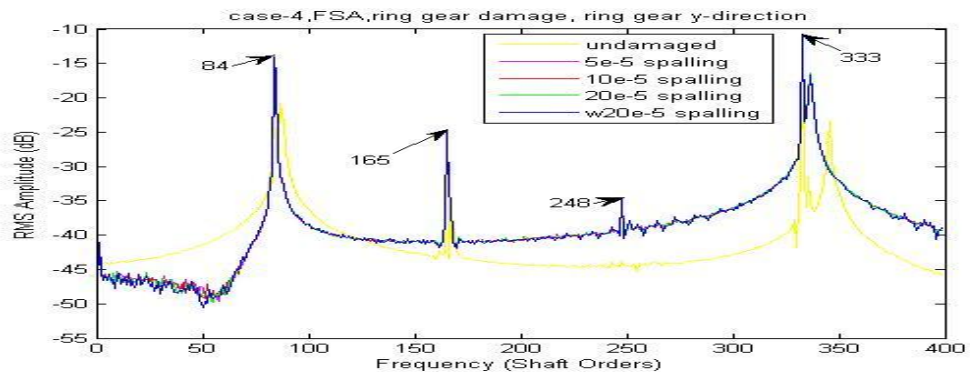


Figure 9-72 Case-4, FSA, ring gear damage, ring gear y-direction

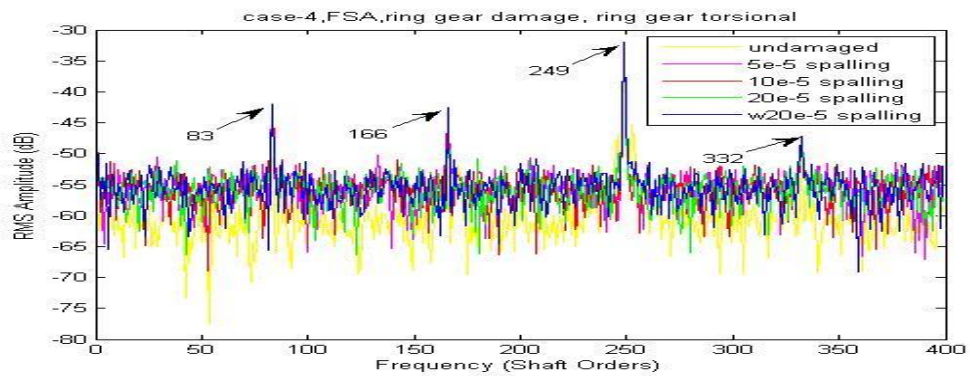


Figure 9-73 Case-4, FSA, ring gear damage, ring gear torsional

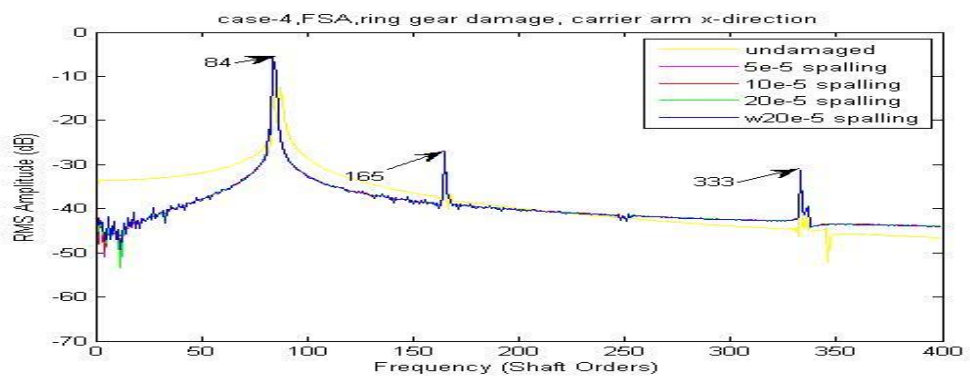


Figure 9-74 Case-4, FSA, ring gear damage, carrier arm x-direction

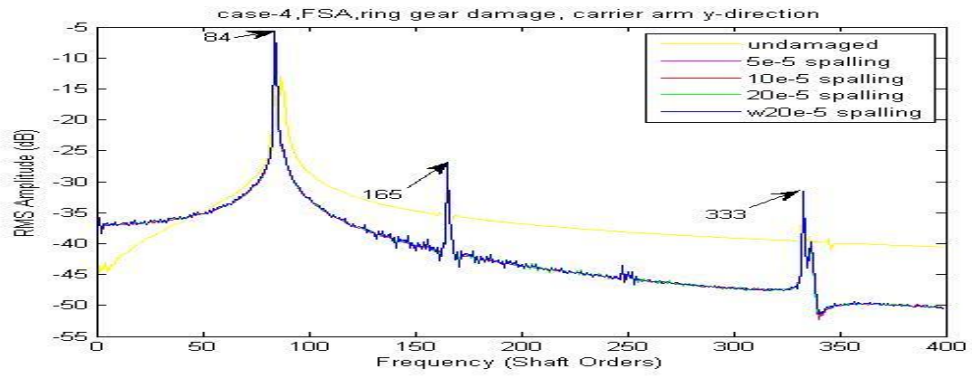


Figure 9-75 Case-4, FSA, ring gear damage, carrier arm y-direction

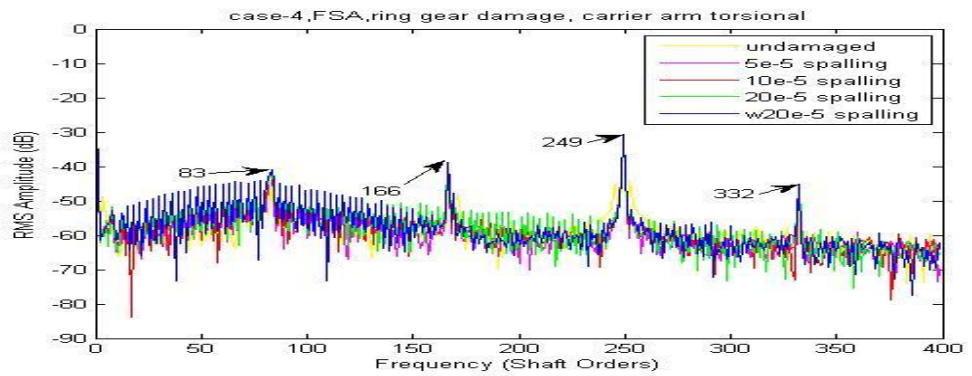


Figure 9-76 Case-4, FSA, ring gear damage, carrier arm torsional

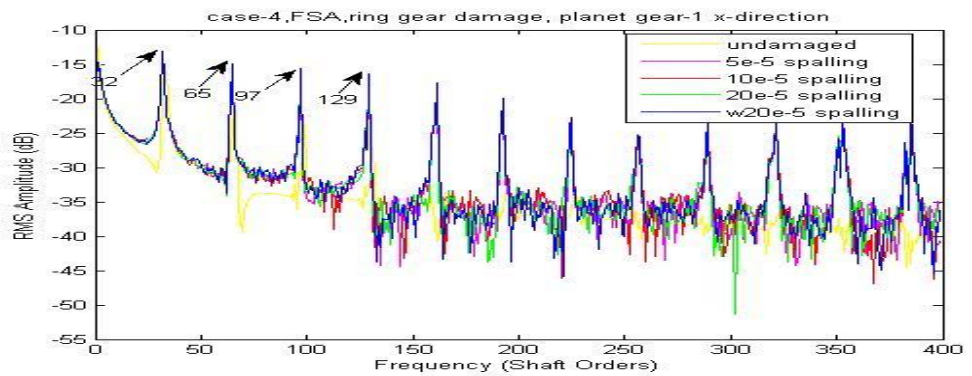


Figure 9-77 Case-4, FSA, ring gear damage, planet gear-1 x-direction

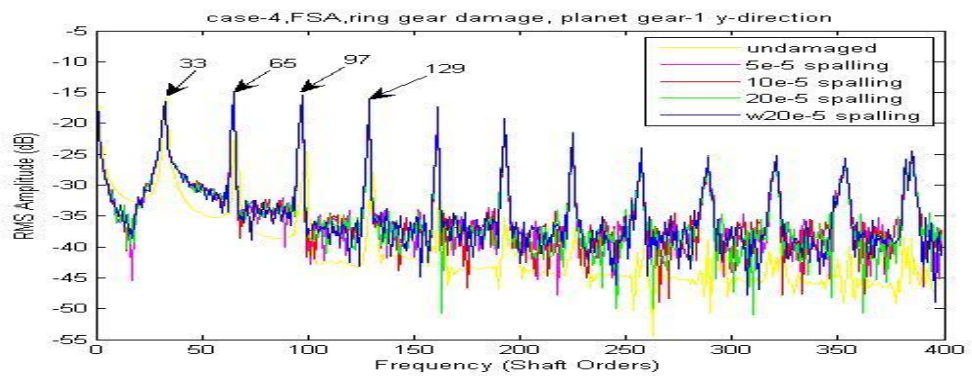


Figure 9-78 Case-4, FSA, ring gear damage, planet gear-1 y-direction

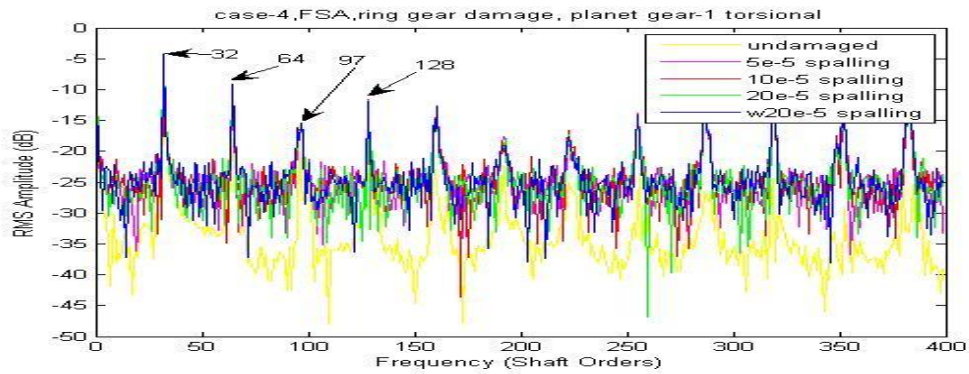


Figure 9-79 Case-4, FSA, ring gear damage, planet gear-1 torsional

Based on the FSA figures above, the detectability grades are marked as shown in Table 9-12 with discussion.

Detectability of ring gear tooth spalling		Figure	Discussion		
			Low frequency lines	High frequency lines	Lines in details
1 st	up	9-79	In good order with some local disorder		
2 nd	ur, us, uc	9-73, 9-70, 9-76	In order, but distance between lines is small or have unexpected disorder often		
3 rd	xs,ys xp,yp	9-68,9-69 9-77,9-78	Disorder happens very often		
4 th	xr,yr,	9-71,9-72	Mostly in disorder		
5 th	xc,yc	9-74,9-75	In wrong order with local disorder		

Table 9-12 Detectability of ring gear tooth spalling based on FSA

The FSA method can slightly improve the early stage detectability of the ring gear tooth spalling. More importantly it creates a way to refine the grade of detectability which shows generally that the torsional signal is superior to the transverse signal for the ring gear spalling detection. Also it is somewhat surprising that the planet gear transverse and torsional signals have significantly increased detectability. However, the FSA was not able to locate the tooth fault. In order to do so, the CWTA was further investigated. The one dimensional wavelet analysis function Morlet wavelet was used with a step by step mode from 1 to 501 with a step size of 10.

Based on the CWTA figures, the detectability grades are determined as shown in Table 9-13.

Detectability of ring gear tooth spalling		Sensitive step range (total data points 2^{16})	Minimum clearly detectable spall	Noise on figure which affects detectability
1 st	uc	300 to 800	$10e-5 \sim 20e-5$	Very clear in all step range
2 nd	others	--	--	Unable to detect

Table 9-13 Detectability of ring gear tooth spalling based on CWTA

The CWTA results applied to the carrier arm torsional vibration signals are compared with different ring gear spalls in Figure 9-80 with both the original step range and a refined step range from 1 to 2001 in steps of 50. As the most fault detectable CWTA signal, it provides very clear information of the faults' location in the very early stage starting from below the $20e-5$ damage level with confidence. It can also be seen that step size of the CWTA can affect the results as the use of a smaller step size improves the analysis.

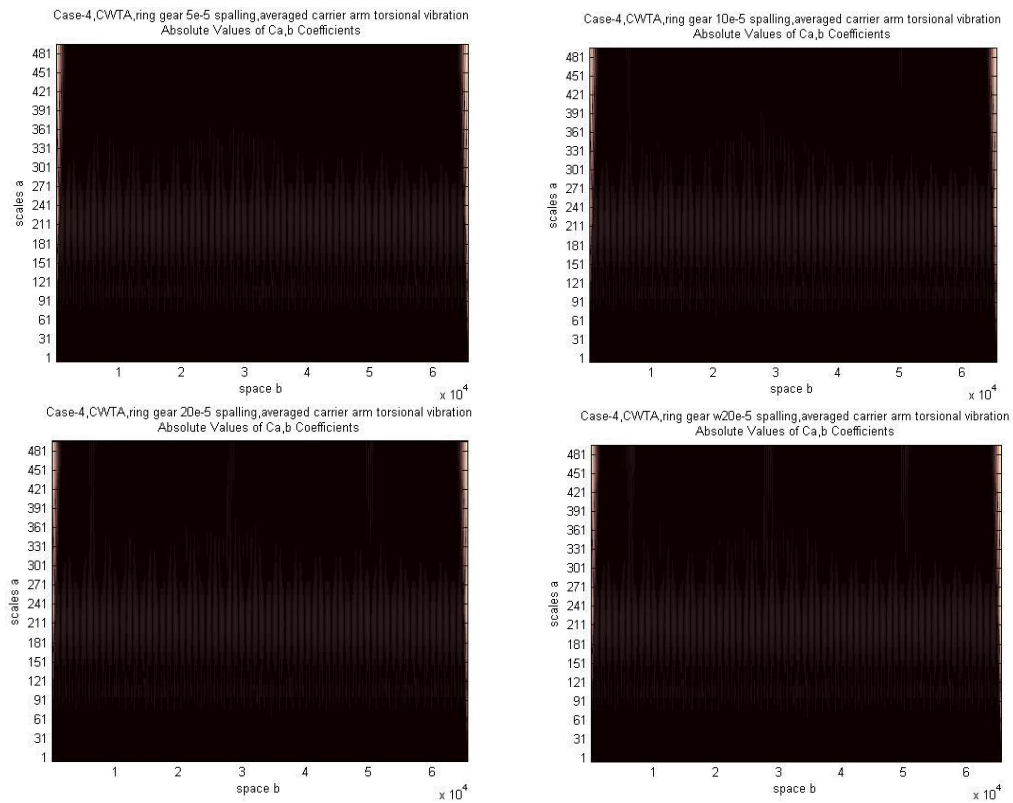


Figure 9-80 Case-2, CWTA, ring gear spall, averaged carrier arm torsional vibration

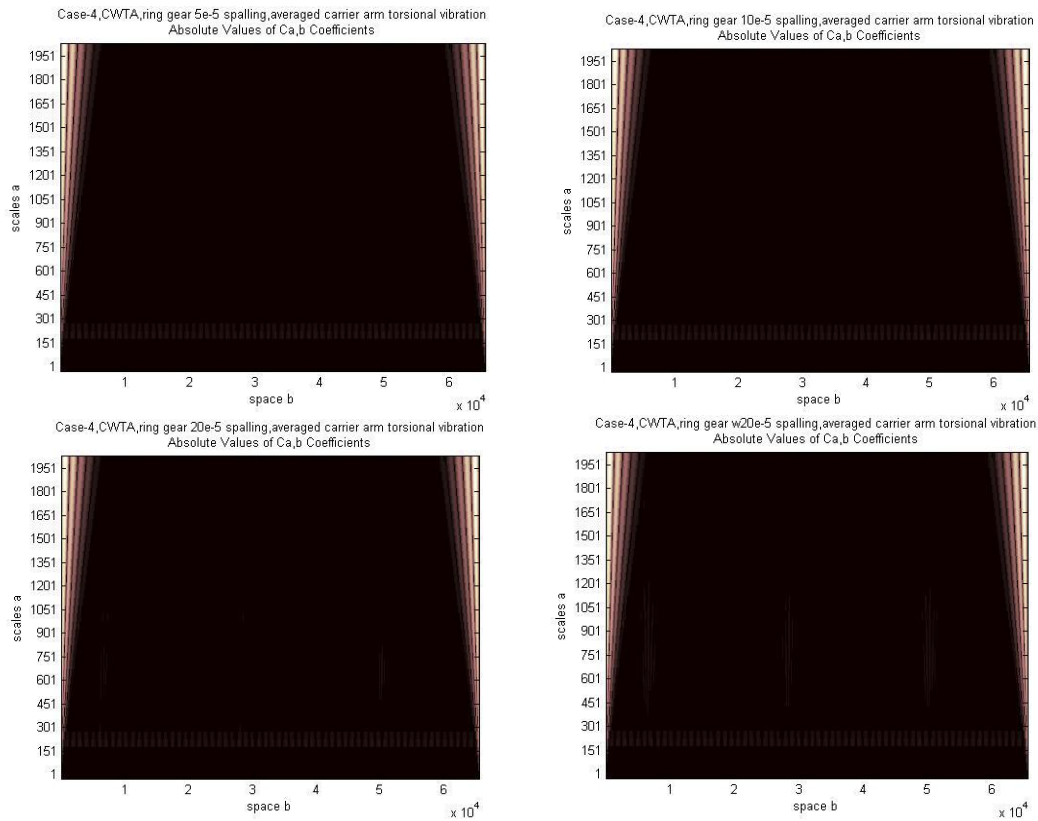


Figure 9-80(continued) Case-2, CWTA, ring gear spall, averaged carrier arm torsional vibration

In conclusion, the CWTA applied to the carrier arm torsional signals appeared to be an effective method to detect and locate ring gear tooth spalling at an early damage stage.

9.2.3. SPALL ON PLANET GEAR TOOTH

The tooth spalling simulated on the planet gear-1 was a single spall localized on the 32nd tooth where the 1st tooth was defined to be the first tooth in mesh with the sun gear at time zero.

Simulation results after signal averaging with a single w20e-5 spall on the planet gear-1 at the 32nd tooth are shown in Figure 9-81.

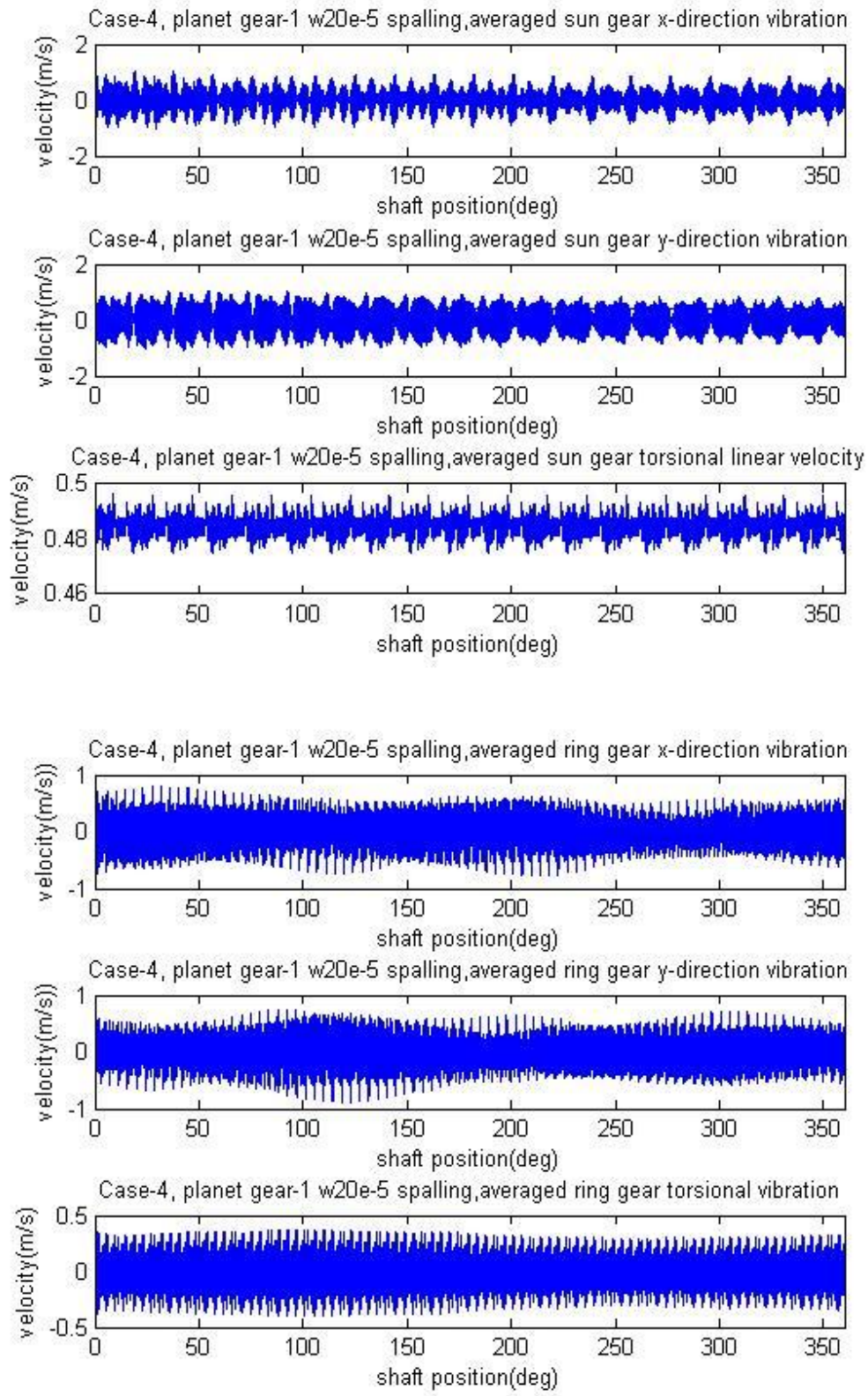


Figure 9-81 Simulation outputs after signal averaging with a single w20e-5 spall on the planet gear-1 at the 32nd tooth

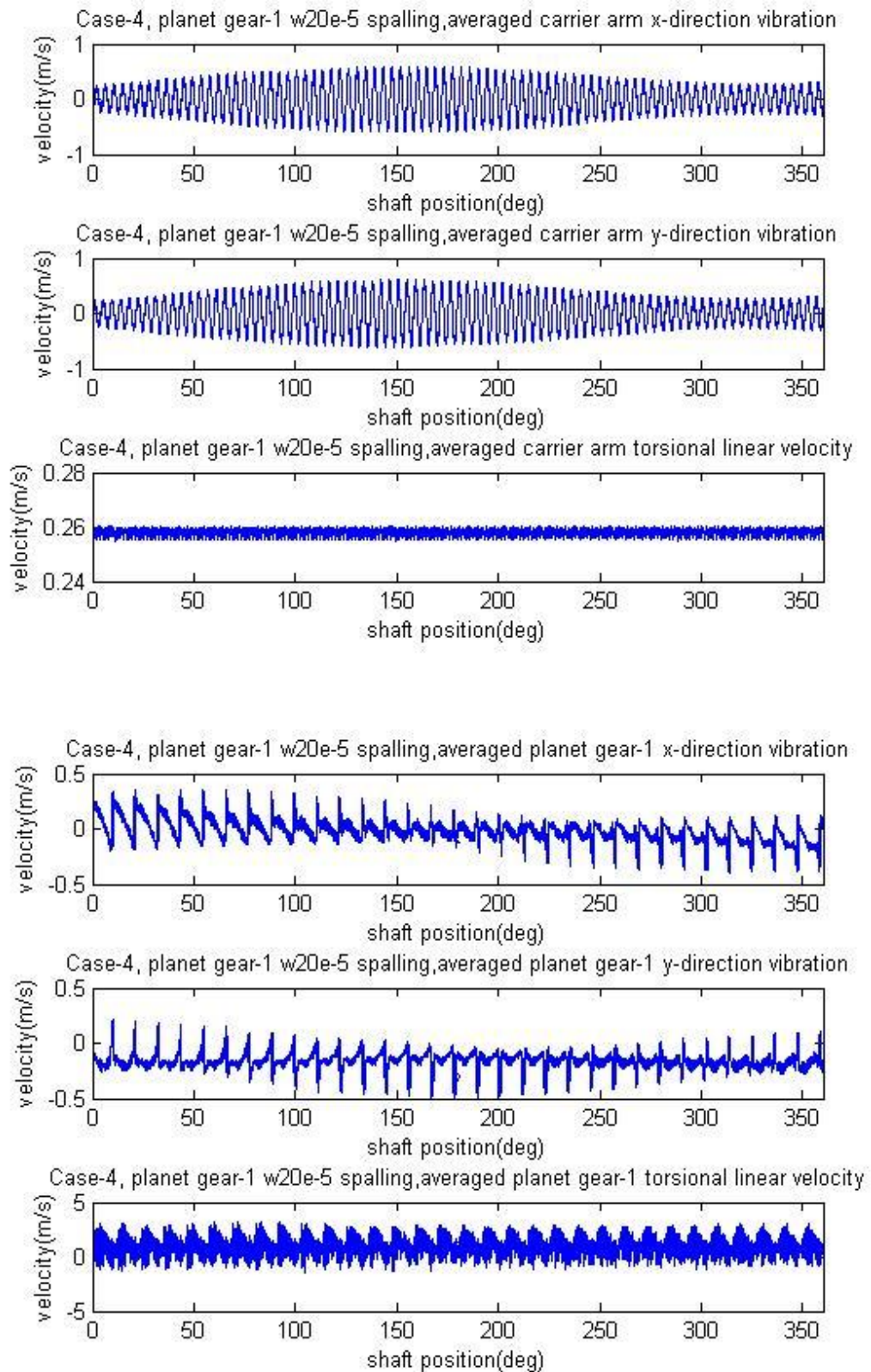


Figure 9-81(continued) Simulation outputs after signal averaging with a single w20e-5 spall on the planet gear at the 32nd tooth

A comparison was made with the planet gear spall using results of a 5e-5 spall on the

planet gear-1 (32nd tooth) as well as a 10e-5 spall shown in Figure 9-82 (left column, 5e-5 spall; middle column, 10e-5 spall; right column, w20e-5 spall). It can be seen that the influence of the planet gear-1 spall was very hard to be seen from the averaged transverse and torsional signals. From the time domain averaged signals, detectability grades can not be obtained due to the poor detectability of all signals.

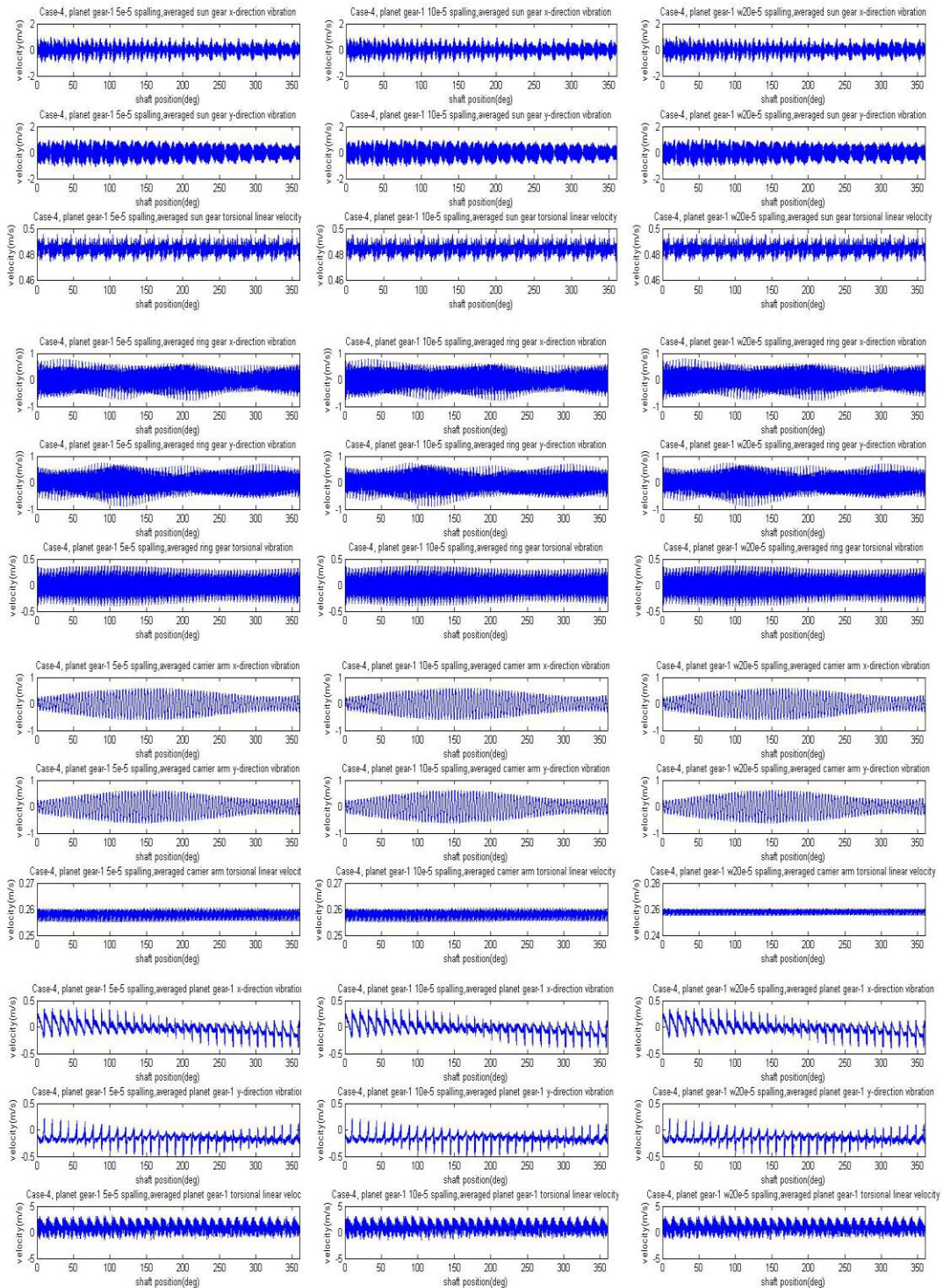


Figure 9-82 Comparison of results, 5e-5 spall, 10e-5 spall and w20e-5 spall on the planet gear-1 at the 32nd tooth

The averaged signal was expected to detect very large spalls as it was shown previously to be capable for detection of planet gear tooth cracks. However, it was unable to detect early stage planet gear tooth spalling as shown in Figure 9-82. Frequency Spectrum Analysis (FSA) was also used here to improve the early stage detectability.

The FSA applied to Case-4 with the planet gear-1 spalling gave the results shown in Figure 9-83 to 9-94. Each figure shows the frequency range covering the first four mesh harmonics.

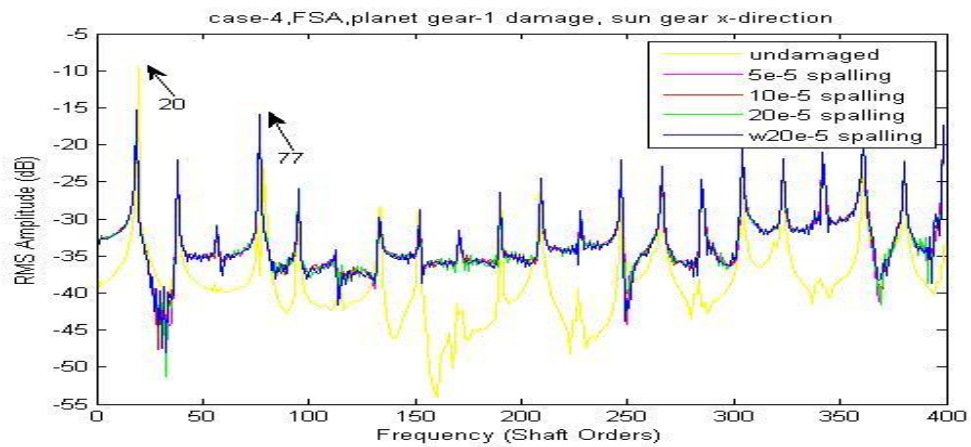


Figure 9-83 Case-4, FSA, planet gear-1 damage, sun gear x-direction

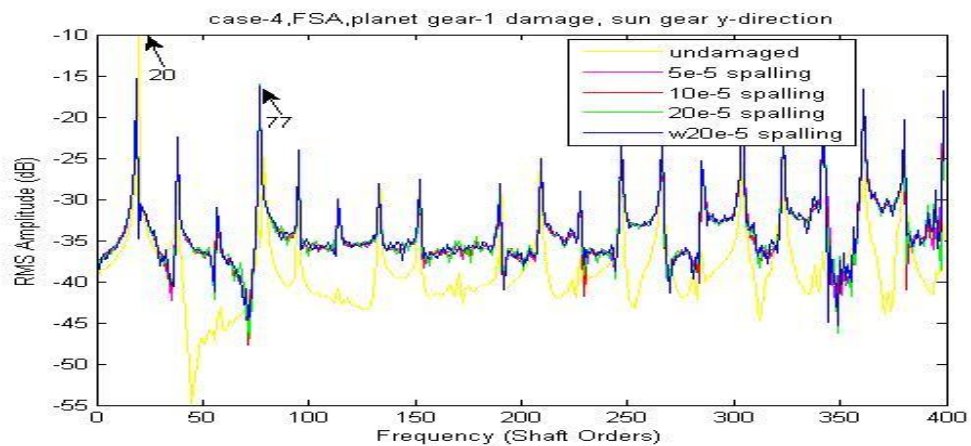


Figure 9-84 Case-4, FSA, planet gear-1 damage, sun gear y-direction

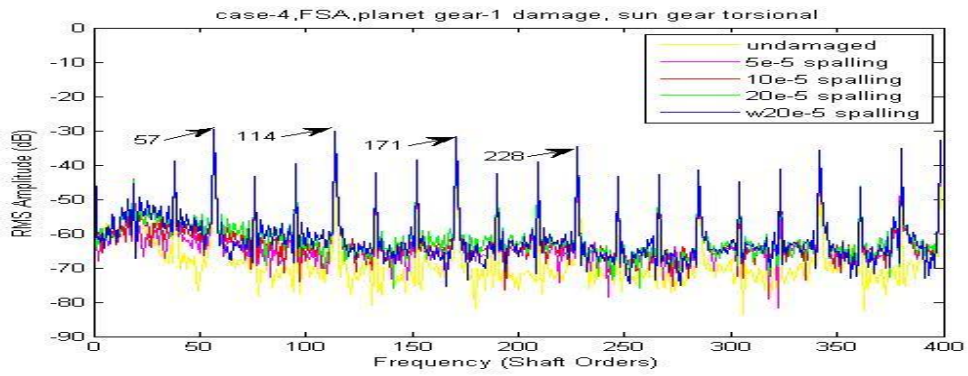


Figure 9-85 Case-4, FSA, planet gear-1 damage, sun gear torsional

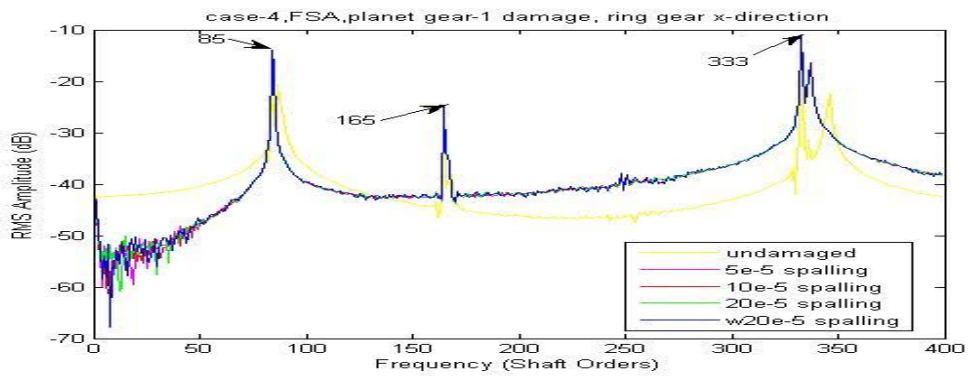


Figure 9-86 Case-4, FSA, planet gear-1 damage, ring gear x-direction

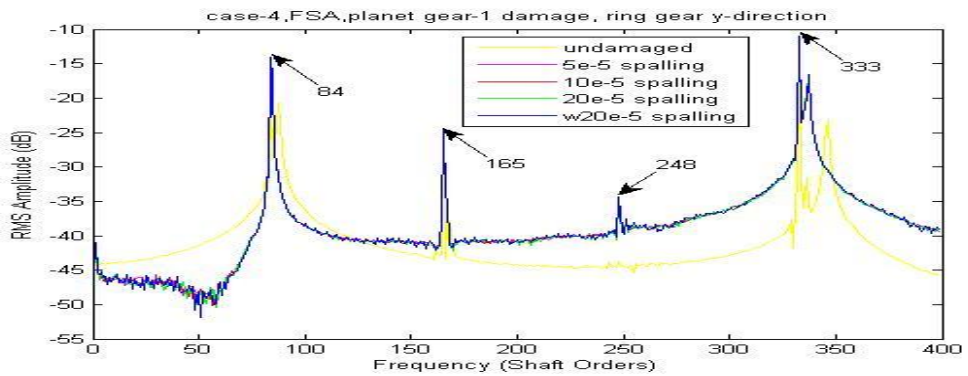


Figure 9-87 Case-4, FSA, planet gear-1 damage, ring gear y-direction

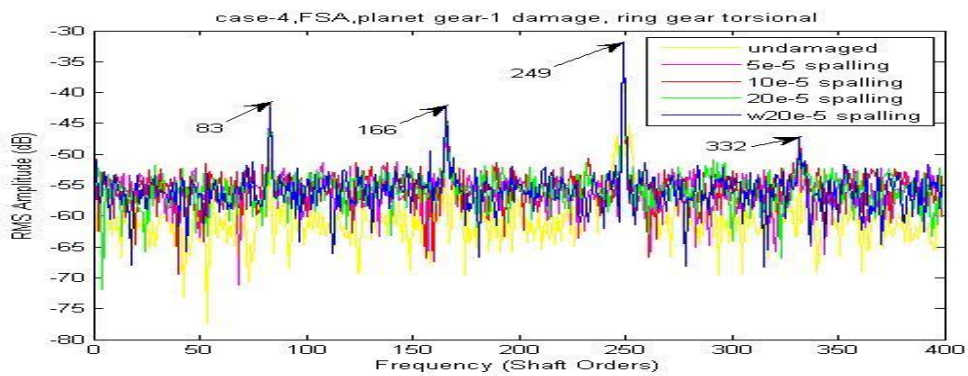


Figure 9-88 Case-4, FSA, planet gear-1 damage, ring gear torsional

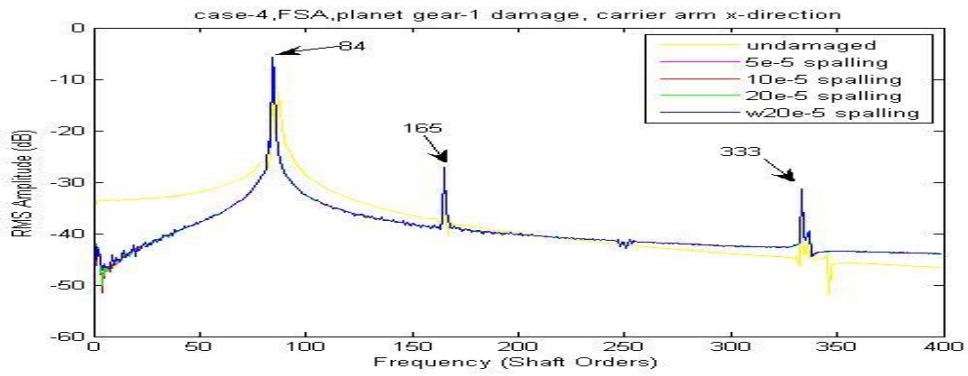


Figure 9-89 Case-4, FSA, planet gear-1 damage, carrier arm x-direction

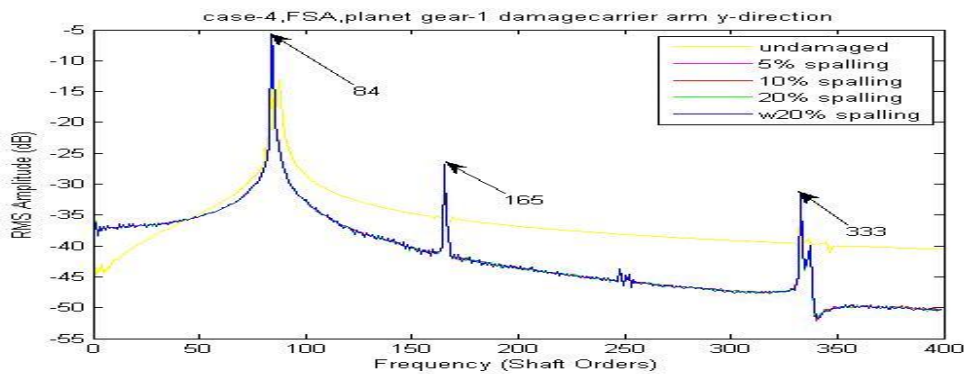


Figure 9-90 Case-4, FSA, planet gear-1 damage, carrier arm y-direction

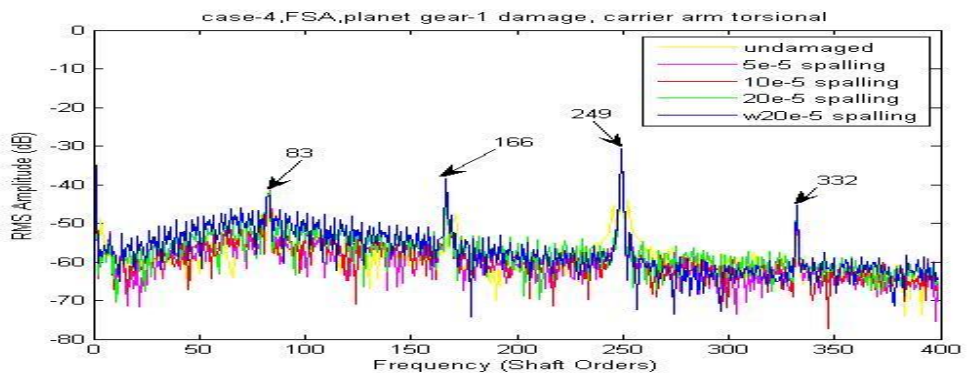


Figure 9-91 Case-4, FSA, planet gear-1 damage, carrier arm torsional

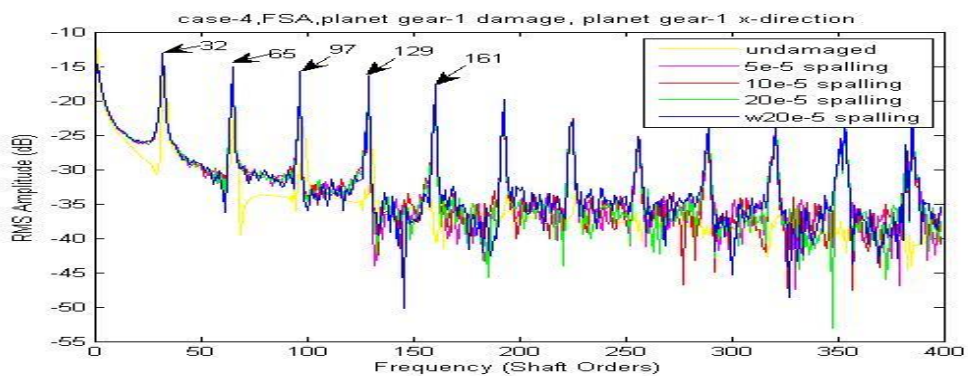


Figure 9-92 Case-4, FSA, planet gear-1 damage, planet gear-1 x-direction

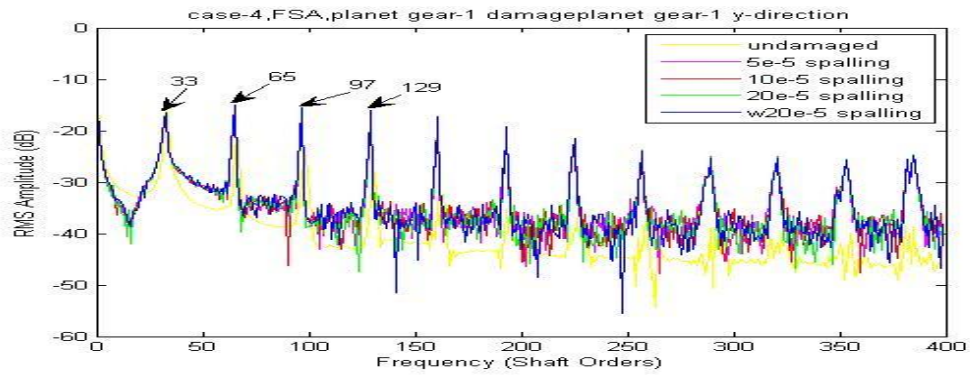


Figure 9-93 Case-4, FSA, planet gear-1 damage, planet gear-1 y-direction

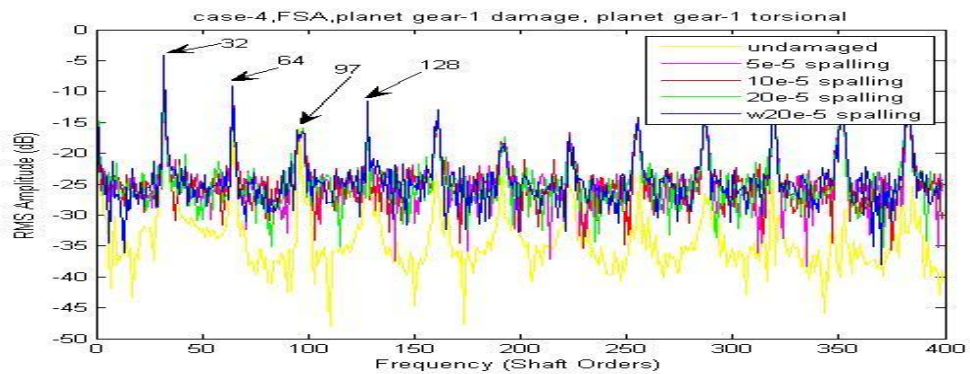


Figure 9-94 Case-4, FSA, s planet gear-1 damage, planet gear-1 torsional

Based on the FSA figures above, the detectability grades are marked as shown in Table 9-14 with discussion.

Detectability of planet gear-1 tooth spalling		Figure	Discussion		
			Low frequency lines	High frequency lines	Lines in details
1 st	up	9-94	In good order with some local disorder		
2 nd	ur, us, uc	9-88, 9-85, 9-91	In order, but distance between lines is small or have unexpected disorder often		
3 rd	xs,ys xp,yp	9-83,9-84 9-92,9-93	Disorder happens very often		
4 th	xr,yr,	9-86,9-87	Mostly in disorder		
5 th	xc,yc	9-89,9-90	In wrong order with local disorder		

Table 9-14 Detectability of planet gear-1 tooth spalling based on FSA

The results show that the FSA method can improve the early stage detectability of the planet gear-1 tooth spalling and refine the grade of detectability, which again shows generally that the torsional signal was superior to the transverse signal for the

planet gear-1 spalling detection. It is expected that the planet gear transverse and torsional signals have high detectability. However, the FSA was not able to locate the tooth fault. In order to do so, the CWTA was utilised. The one dimensional wavelet analysis function using the Morlet wavelet was used with a step by step mode from 1 to 501 with a step size of 10.

Based on the CWTA figures, the detectability grades are marked as shown in Table 9-15.

Detectability of planet gear-1 tooth spalling		Sensitive step range (total data points 2^{16})	Minimum clearly detectable spall	Noise on figure which affects detectability
1 st	uc	300 to 800	20e-5	Very clear in all step range
2 nd	others	--	--	Unable to detect

Table 9-15 Detectability of planet gear-1 tooth spalling based on CWTA

The CWTA results applied to the carrier arm torsional vibration signals are compared with different planet gear spall sizes in Figure 9-95 with both the original step range and a refined step range from 1 to 2001 using step size of 50. As the most fault detectable analysis, the CWTA signal provides very clear information of the faults' location in the very early stage starting from below 20e-5 damage level. It was seen that the step size setting of the CWTA can affect the results as the smaller step size showed improved results.

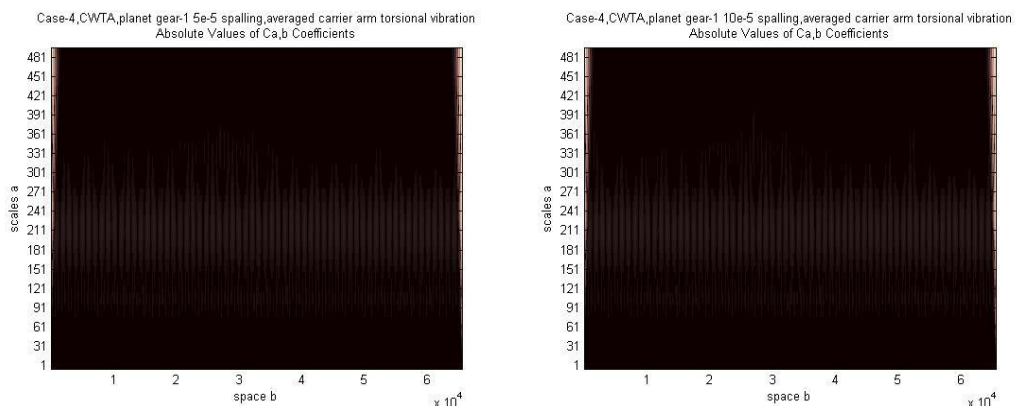


Figure 9-95 Case-2, CWTA, planet gear-1 spall, averaged carrier arm torsional vibration

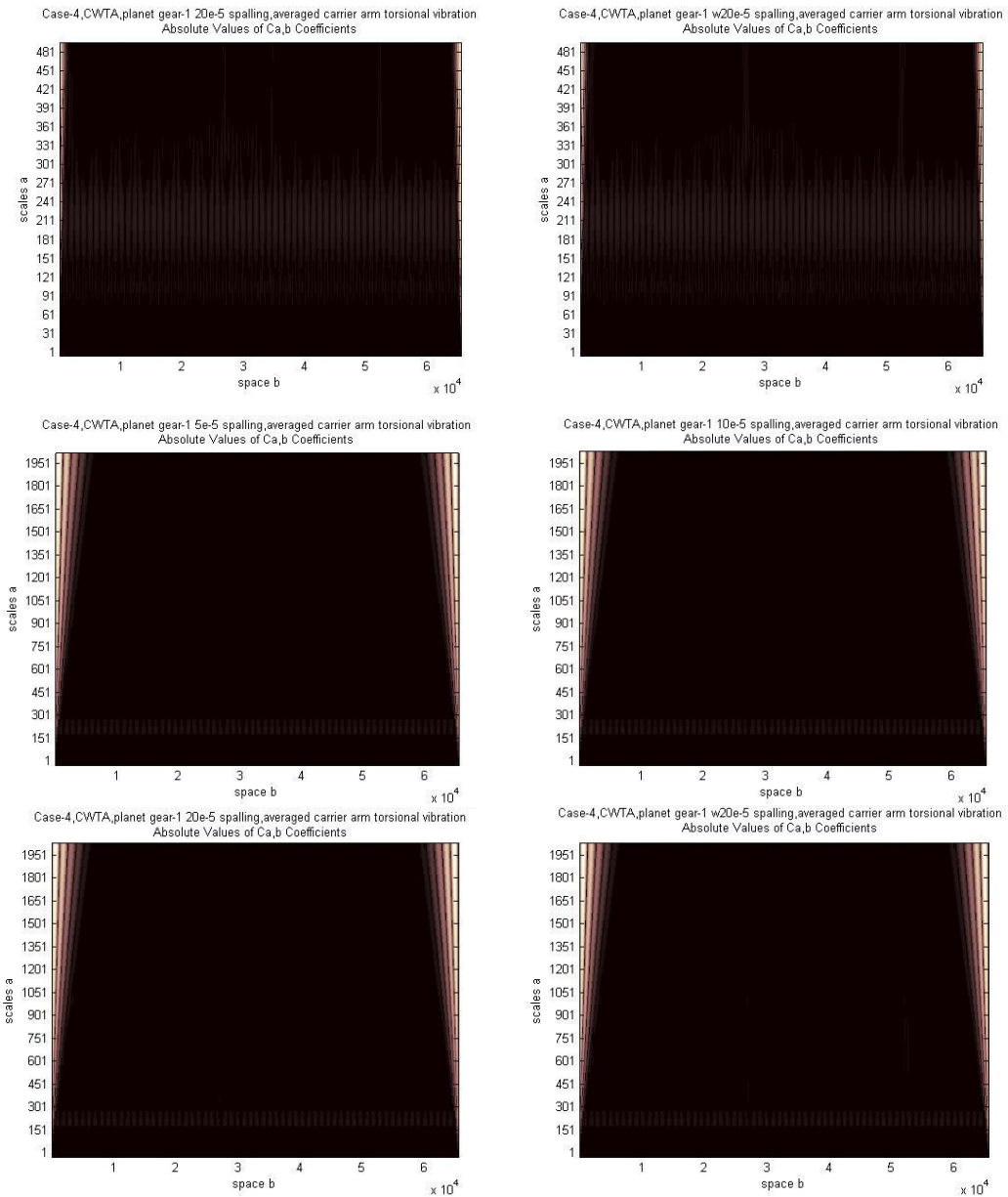


Figure 9-95(continued) Case-2, CWTA, planet gear-1 spall, averaged carrier arm torsional vibration

In conclusion, the CWTA was demonstrated to be an efficient method to show and locate the planet gear-1 tooth spall on the carrier arm torsional signals at an early stage but not for other signals.

9.3. SUMMARY OF CHAPTER

The indication and the detectability of gear tooth faults on both transverse and torsional averaged signals, the FSA results and the CWTA results are summarized and listed in the following tables.

Damages	Components	Signals	Indication of Damage on averaged signals	Detect-ability of averaged signals	Detect-ability of FSA	Detectability of CWTA, starting Level	
Sun gear cracking	Sun gear	xs	A*	3 rd	6 th	6 th	60%
		ys	A*	3 rd	6 th	6 th	60%
		us	A*	1 st	2 nd	2 nd	20%
	Ring gear	xr	B*	2 nd	4 th	5 th	40%
		yr	B*	2 nd	4 th	5 th	40%
		ur	B*	2 nd	3 rd	4 th	20%~40%
	Carrier arm	xc	--	4 th	7 th	3 rd	20%~40%
		yc	--	4 th	7 th	3 rd	20%~40%
		uc	B*	1 st	1 st	1 st	5%
	Planet gear-1	xp	--	4 th	8 th	8 th	--
		yp	--	4 th	8 th	8 th	--
		up	C*	3 rd	5 th	7 th	60%
Ring gear cracking	Sun gear	xs	D*	3 rd	5 th	6 th	60%
		ys	D*	3 rd	5 th	6 th	60%
		us	D*	1 st	1 st	4 th	< 80%
	Ring gear	xr	A*	2 nd	3 rd	3 rd	< 40%
		yr	A*	2 nd	3 rd	3 rd	< 40%
		ur	A*	2 nd	2 nd	2 nd	< 40%
	Carrier arm	xc	--	4 th	6 th	5 th	60%~80%
		yc	--	4 th	6 th	5 th	60%~80%
		uc	A*	1 st	1 st	1 st	< 40%
	Planet gear-1	xp	--	4 th	7 th	7 th	--
		yp	--	4 th	7 th	7 th	--
		up	--	4 th	4 th	7 th	--
Planet gear cracking	Sun gear	xs	E*	3 rd	7 th	6 th	80%
		ys	E*	3 rd	7 th	6 th	80%
		us	E*	1 st	4 th	2 nd	20%
	Ring gear	xr	F*	2 nd	5 th	4 th	40%
		yr	F*	2 nd	5 th	4 th	40%
		ur	F*	1 st	3 rd	3 rd	< 40%
	Carrier arm	xc	--	4 th	8 th	5 th	60%~80%
		yc	--	4 th	8 th	5 th	60%~80%
		uc	F*	1 st	1 st	1 st	< 5%

Table 9-16 Summary of the indication and detectability of gear tooth faults (*indications of damage are listed in Table 9-17 in the case of single tooth damage)

Damages	Components	Signals	Indication of Damage on averaged signals	Detect -ability of averaged signals	Detect -ability of FSA	Detectability of CWTA, starting Level	
Planet gear cracking	Planet gear-1	xp	G*	3 rd	6 th	7 th	--
		yp	G*	3 rd	6 th	7 th	--
		up	G*	1 st	2 nd	7 th	--
Sun gear spalling	Sun gear	xs	H*	2 nd	3 rd	3 rd	--
		ys	H*	2 nd	3 rd	3 rd	--
		us	H*	2 nd	1 st	2 nd	w20e-5
	Ring gear	xr	H*	2 nd	4 th	3 rd	--
		yr	H*	2 nd	4 th	3 rd	--
		ur	H*	2 nd	2 nd	3 rd	--
	Carrier arm	xc	--	3 rd	5 th	3 rd	--
		yc	--	3 rd	5 th	3 rd	--
		uc	B*	1 st	2 nd	1 st	20e-5
	Planet gear-1	xp	--	3 rd	4 th	3 rd	--
		yp	--	3 rd	4 th	3 rd	--
		up	H*	2 nd	2 nd	3 rd	--
Ring gear spalling	Sun gear	xs	H*	2 nd	3 rd	2 nd	--
		ys	H*	2 nd	3 rd	2 nd	--
		us	H*	2 nd	2 nd	2 nd	--
	Ring gear	xr	H*	2 nd	4 th	2 nd	--
		yr	H*	2 nd	4 th	2 nd	--
		ur	H*	2 nd	2 nd	2 nd	--
	Carrier arm	xc	--	3 rd	5 th	2 nd	--
		yc	--	3 rd	5 th	2 nd	--
		uc	E*	1 st	2 nd	1 st	10e-5 ~20e-5
	Planet gear-1	xp	--	3 rd	3 rd	2 nd	--
		yp	--	3 rd	3 rd	2 nd	--
		up	H*	2 nd	1 st	2 nd	--
Planet gear spalling	Sun gear	xs	--	--	3 rd	2 nd	--
		ys	--	--	3 rd	2 nd	--
		us	--	--	2 nd	2 nd	--
	Ring gear	xr	--	--	4 th	2 nd	--
		yr	--	--	4 th	2 nd	--
		ur	--	--	2 nd	2 nd	--
	Carrier arm	xc	--	--	5 th	2 nd	--
		yc	--	--	5 th	2 nd	--
		uc	--	--	2 nd	1 st	20e-5
	Planet gear-1	xp	--	--	3 rd	2 nd	--
		yp	--	--	3 rd	2 nd	--
		up	--	--	1 st	2 nd	--

Table 9-16(continued) Summary of the indication and detectability of gear tooth faults (*indications of damage are listed in Table 9-17 in the case of single tooth damage)

The types of indications of tooth damage (based on the damage levels simulated in

this thesis) used in Table 9-16 are listed in Table 9-17 as shown below.

Indication of damage	Meanings and equations
A*	number of humps equals to the number of planet gears
B*	number of humps equals to the sun gear-carrier arm speed ratio minus one then multiplied by the number of planet gear teeth
C*	number of humps equals to the number of planet gears multiplied by the number of planet gear teeth divided by the number of sun gear teeth
D*	clear humps but unclear links to number of teeth
E*	number of humps equals to the number of sun gear teeth divided by half of the number of planet gear teeth
F*	number of smaller/bigger humps equals to the number of ring gear teeth divided by the number of planet gear teeth
G*	two humps, obvious one corresponds to the ring gear - planet gear mesh and smaller one corresponds to the sun gear - planet gear mesh
H*	not clear

Table 9-17 Types of indications of tooth damage

In Table 9-16, the most sensitive signal for each type of tooth damage is shown in dark grey and the second sensitive signals are shown in light grey colour. In general, it is seen that torsional signals are superior than the transverse signals and most important of all, the carrier arm torsional signal is the most superior one and appears to contain all fault detectability information.

Signal averaging is essential for further analysis such as the FSA and the CWTA, but it may not increase sensitivity to detect tooth faults in the early stage. The FSA certainly improves the early stage detectability of both tooth cracks and spalls, however, it is not capable of locating the tooth faults and is not able to show clear and certain results when applied to some signals. The CWTA has been shown to be the most superior method among these three. It can provide information to detect as well as to locate tooth faults in a much earlier stage.

10. DISCUSSION

This chapter includes two sections, the general discussion and the recommendations for future work.

The small number of rotations of the components of interest has reduced the effectiveness of the signal averaging process in this simulation. This is due to the limitation of computational time where an excess of 2 days was required for the simulation of one carrier arm revolution.

The definition of revolution of each component and the selection of revolution type employed by the signal averaging process have significant effectiveness on both the averaged signals, their understanding and their detectability of tooth fault.

The planet phasing and corresponding tooth mesh phasing have a major effect on the dynamic vibration signals. This was observed especially for the sun gear signals, which appear to have the first harmonic frequency (in shaft order) slightly off that indicated by the number of teeth. Further analysis is needed here based on Parker's work⁶⁸.

In order to measure torsional vibration, an approach of using equidistant pulses (over one shaft revolution or in this case around the gear/carrier circumferences generated by dedicated shaft encoders as well as gear tooth pickup transducers) and the use of dual-beam laser can be practical. However, more accurate and easy-to-apply methods or techniques for measuring and analyzing torsional vibration of gearbox components needs to be developed or invented, as these results show that the system torsional response is much more sensitive than the transverse response.

The selection of step and step range, which can be related to mesh frequency and shaft rotation, in the CWTA method is important to gain satisfied outcome within a certain time frame, especially when the capability of computational hardware is also critical.

A generalized and automatic software model has been developed using MATLAB.

The MATLAB program was developed using symbolic math and was able to generate the differential equations of a general model automatically, adjustable for different amounts of inputs automatically and was formed to be able to include more details or exclude existing details with single modification on the inputs. Every change on the other inputs can also be automatically reflected into the overall equations of motion but may require some find-replace operations (22 in total, all listed in one m-file) to be done manually. Practically all major changes or adding/deleting details on the model can be done within minutes before the program is ready to run.

This thesis studied many aspects on planetary gearbox vibration with tooth cracking and spalling, however, more research is needed to completely understand the influence of gear faults on the signature of gearbox vibration.

Further research works on the dynamic modelling are recommended as follows:

- ◆ Backlash can be included to simulate contact loss under certain operation conditions such as high speed and low torque.
- ◆ Different number of planet gears with different irregularity of planet spacing as well as mounting errors can be simulated to study the influence of those factors.
- ◆ Multistage planetary gear set with or without detailed reduction gearbox can be modeled to improve the understanding of more complicated transmissions such as automotive transmissions, wind turbine transmissions, etc.
- ◆ Friction forces can be included as well as gear mesh run out functions.
- ◆ More complicated loading conditions can be simulated in order to study the detectability of tooth faults under realistic operation conditions.
- ◆ Variable pitch and profile error patterns can be included as well as a model including random manufacturing effects.
- ◆ FEA models can be employed to provide more accurate simulations of tooth mesh stiffness.
- ◆ Multiple tooth damages with different types and parameters can be implanted within multiple gears in order to develop a more advanced fault detection method.
- ◆ More specific development on phase cancellation of mesh components is needed.

Further research works on the development of the simulation program are recommended as follows:

- ◆ The MATLAB program can be developed to be more general and more open to include extra details and sub-systems for future dynamic models. A more user friendly interface can be developed.
- ◆ The MATLAB compiler could be employed to convert the MATLAB programs into self-contained applications and software components in order to reduce the computational time and avoid the limitations of using the MATLAB software.

Further research works on the improvement of fault detection methods are recommended as follows:

- ◆ Different wavelet functions can be explored to improve the detectability of the CWTA.
- ◆ A new technique/program can be developed, based on the findings in Chapter 9 of this thesis, to separate and locate each fault from multiple faults as well as to indicate the damage level. The successful development of such a technique would result in a very significant contribution to the current state of the art of gear tooth fault detection.

11. CONCLUSION

This thesis presents the detailed investigations of dynamic modelling and tooth fault detection for a single-stage planetary gearbox in a bucket wheel reclaimer system. The planetary gear set model has been developed based on Kahraman's work³⁷ with major modifications and including more details. The overall model also includes components such as input motor torque, drive train parts (a fluid coupling and multistage reduction gearbox), and torque output sections (bucket wheel, buckets and load).

This chapter summarizes the significant achievements of this research as follows:

- ◆ A generalized dynamic model for simulation and fault detection of a drive train including detailed planetary gear set has been developed. The model simulates the overall drive train of a bucket wheel reclaimer with a focus on the generalized planetary gearbox. The model contains time variations of the combined gear transmission errors, time variable mesh stiffness and localized tooth cracks and spalling.

The model details the separation and data conversion of the two planet gear rotational motions (one about the sun gear centre; one about the planet gear mount point) very successfully using a new approach. The model has formulated the overall equations in a matrix form in order to introduce further details and is open to further sub-systems.

- ◆ A simulation method for including the combined gear transmission error has been developed for the planetary gearbox. This method includes the time variable features of gear transmission errors of planetary gears due to planet gear phasing. It also includes combined pitch errors, profile errors and random errors to model realistic manufacturing conditions.
- ◆ An approximate approach to calculate the combined torsional stiffness of planetary gear meshes has been conducted and compared to FEA results. This

approach is based on Jia's work⁴⁰ with modifications to obtain satisfactory results for gear meshes with contact ratio greater than 3. This approach requires very short computation time compared to the FEA method and it provides reasonable results with the ability to include tooth mesh stiffness irregularities caused by tooth faults much easier. This gives the advantage of modelling different tooth faults by introducing changes to the tooth mesh stiffness.

- ◆ A detailed and effective simulation approach for change of stiffness caused by localized tooth cracks has been developed. The change of stiffness was defined numerically and linked to the parameters of the tooth for ease of simulation. It also allows for the use of assumed stiffness reduction curves based on previous FEA results.
- ◆ A detailed and effective simulation approach for change of stiffness and change of tooth profile caused by localized tooth spalling was developed. The change of stiffness was also defined numerically and linked to the parameters of tooth spalling for ease of simulation.

The change of tooth profile caused by the localized tooth spalling can be introduced into the combined gear transmission error. The change of profile was also calculated using the parameters of the spall for accuracy as well as time efficient computation.

- ◆ Clarification of the different effects of the localized tooth crack and spalling on the vibration signals has been obtained. The signal averaging analysis, the FSA and the CWTA applied to the dynamic modelling results in this thesis have shown the different influence of tooth faults on different component signals. These will help the diagnosis of the different tooth faults.
- ◆ Detectability of different tooth damage types and levels has been determined. The detectability grades were determined across all three signal analysis methods used in this thesis. The results show that generally torsional signals are superior than transverse signals and the torsional signal of the carrier arm appears to be the most sensitive one. This will help to guide further analytical

and diagnostic research.

In conclusion, the dynamic equations and software model developed in this research work have shown the ability of modelling a detailed complete drive train including a highly detailed planetary gearbox. The analysis methods used in this thesis have also shown the ability to detect tooth crack and spalling in an early stage. The torsional motion has been shown to be superior to transverse motion for the tooth fault detection and diagnosis. The CWTA has been shown to be very sensitive and efficient to detect and locate the tooth faults at an earlier stage than other methods.

12. REFERENCES

1. H. N. Ozguven, and D. R. Houser, 1988, Mathematical models used in gear dynamics – a review, *Journal of Sound and Vibration*, Vol. 121, pp. 383-411.
2. J. J. Zakrajsek, et al., 1990, Gear noise, vibration, and diagnostic studies at NASA Lewis Research Centre, First International Conference, Gearbox Noise and Vibration, *Proceedings of the Institute of Mechanical Engineers*, pp. 27-34.
3. S. Du, 1997, Dynamic modelling and simulation of gear transmission error for gearbox vibration analysis, School of Mechanical and Manufacturing Engineering, The University of New South Wales.
4. D. B. Wallace, and A. Seireg, 1973, Computer simulation of dynamic stress, deformation, and fracture of gear teeth, *Journal of Engineering for Industry, Transactions of the ASME*, pp. 1108-1114.
5. V. Ramamurti, and M. A. Rao, 1988, Dynamic analysis of spur gear teeth, *Computers and Structures*, Vol. 29, No. 5, pp. 831-843.
6. S. L. Harris, 1958, Dynamic load on the teeth of spur gears, *Proceedings of Institute of Mechanical Engineers*, Vol. 172, pp. 87-112.
7. S. M. Vijayakar, H. R. Busby, and D. R. Houser, 1988, Linearization of multibody frictional contact problems, *Computers & Structures*, Vol.29, No. 4, pp. 569-576.
8. H. N. Ozguven, and D. R. Houser, 1988, Dynamic analysis of high speed gears by using loaded static transmission error, *Journal of Sound and Vibration*, Vol. 125, pp. 71-83.
9. A. Kahraman, and R. Singh, Non-linear dynamics of spur gear pair, Department of Mechanical Engineering, The Ohio State University, 206 West 18th Avenue, Columbus, Ohio, USA.
10. S. Sundarajan, and B. G. Young, 1990, Finite element analysis of large spur and helical gear systems, *Journal of Propulsion and Power*, Vol. 6, No. 4, pp. 451-454.
11. S. Sundarajan, and S. Amin, 1990, Finite element analysis of ring gear/casing spline contact, *Journal of Propulsion and Power*, Vol. 7, No. 4, pp. 602-604.
12. S. M. Vijayakar, and D. R. Houser, 1993, Contact analysis of gears using a combined finite element and surface integral method, *Gear Technology*, pp. 26-

33.

13. F. K. Choy, V. Polyshuk, J. J. Zakarajsek, R. F. Handschuh, and D. P. Townsend, 1996, Analysis of the effects of surface pitting and wear on the vibration of gear transmission system, *Trib. Int.*, 29, pp. 77-83.
14. I. Yesilyurt, F. Gu, and D. B. Andrew, 2003, Gear tooth stiffness reduction measurement using modal analysis and its use in wear fault severity assessment of spur gear, *NDT & E Int.*, 36, pp. 357-372.
15. F. Chaari, W. Baccar, and M. Haddar, Effect of spalling or tooth breakage on gear mesh stiffness and dynamic response of a one-stage spur gear transmission, 2007.
16. F. Chaari, T. Fakhfakh, and M. Haddar, Analytical modelling of spur gear tooth crack and influence on gear mesh stiffness, Mechanical Engineering Department, National School of Engineering of Sfax.
17. D. C. Johnson, 1962, Modes and frequencies of shafts coupled by straight spur gears, *Journal of Mechanical Engineering Science*, Vol. 4, No.3, pp. 241-250.
18. D. Seagar, 1969, Dynamic behavior of helical gears, American Society of Mechanical Engineers Paper 69-V76R-16. Seager.
19. S. M. Wang, and I. E. Morse, 1972, Torsional response of a gear train system, *Journal of Engineering for Industry*, Transaction of the America Society of Mechanical Engineers, Vol.94, pp.583-594.
20. H. Rettig, 1975, Vibrations in gear drives; test results and calculation method for dynamic tooth forces, Proceedings of the International Federation of the Theory of Machines and Mechanisms 4th World Congress, Newcastle.
21. H. Iida, et al., 1980, Coupled torsional-flexural vibration of a shaft in a geared system of rotors, *Bulletin of the JSME*, Vol. 23, No. 186, pp.2111-2117.
22. H. Iida, and A. Tamura, 1984, Coupled torsional-flexural vibration of a shaft in a geared system, Third International Conference on: „Vibration in Rotating Machinery“, IME, pp. 67-72.
23. F. Kucukay, 1984, Proceedings of the Third Conference on Vibrations of Rotating Machinery, Institution of an automotive neutral gear rattle.
24. S. V. Neriya, R. B. Bhat, and T. S. Sankar, 1985, Coupled torsional-flexural vibration of a geared shaft system using finite element analysis, *Shock and Vibration Bulletin* 55, pt3, pp. 13-25.
25. H. H. Lin, R. L. Huston, and J. J. Coy, 1987, NASA Technical Memorandum

100180. On dynamic loads in parallel shaft transmissions, I-modelling and analysis.
26. A. Kahraman, et al., 1992, Dynamic analysis of geared rotors by finite elements method, *Journal of Mechanical Design*, Vol. 114, pp. 507-514.
 27. W. Bartelmus, 2000, Mathematical modelling of gearbox vibration for fault diagnosis, *International Journal of COMADEM*, Vol.3, No.4, pp.5-15.
 28. A. D. Lin, and J. H. Kuang, 2001, The effect of tooth wear on the vibration spectrum of spur gear pair, *Journal of Vibration and Acoustics*, Vol.123, pp. 311-317.
 29. T. C. Lim, and R. Singh, 1991, Vibration transmission through rolling element bearings, part III: geared rotor system studies, *Journal of Sound and Vibration*, Vol. 151, No. 1, pp. 31-54.
 30. F. K. Choy, et al., 1991, Effects of gear box vibration and mass imbalance on the dynamics of multistage gear transmission, *Journal of Vibration and Acoustics*, Vol. 113, pp. 333-344.
 31. E. L. Saeidy, and M. A. Fawzi, 1991, Effect of tooth backlash and ball bearing deadband clearance on vibration spectrum in spur gear boxes, *Journal of Acoustical Society of America*, Vol. 89, No. 6, pp. 2766-2773.
 32. F. K. Choy, et al., 1992, Modal analysis of multistage gear systems coupled with gearbox vibrations, *Journal of Mechanical Design*, Transactions of the ASME, Vol. 114, pp. 486-497.
 33. F. K. Choy, et al., 1993, Modal simulation of gear box vibration with experimental correlation, *Journal of Propulsion and Power*, Vol. 9, No. 2, pp. 301-306.
 34. P. Velex, and M. Matar, 1996, A mathematical model for analyzing the influence of shape deviation and mounting errors on gear dynamic behavior, *Journal of Sound and Vibration*, Vol 1991, No.5, pp.629-660.
 35. S. Du, 1997, Dynamic modelling and simulation of gear transmission error for gearbox vibration analysis, School of Mechanical and Manufacturing Engineering, The University of New South Wales.
 36. J. Lin, and R. G. Parker, Planetary gear parametric instability caused by mesh stiffness variation, *Journal of Vibration and Acoustics*, Vol.249, No.1, pp.129-145.
 37. A. Kahraman, Planetary gear train dynamics, 1994, *Journal of Mechanical*

- Design, 1994, Vol. 116, pp. 713-720.
38. A. Kahraman, Load sharing characteristics of planetary transmissions, 1994, *Mech.Mach.Theory*, Vol.29.No.8.pp.1151-1165.
 39. I. Howard, S. Jia, and J. Wang, 2001, The dynamic modelling of a spur gear in mesh including friction and a crack, *Mechanical Systems and Signal Processing*, 2001.15(5), pp. 831-853.
 40. S. Jia, 2004, Dynamic modelling and diagnosis of spur gearbox faults, Curtin University of Technology.
 41. C. Yuksel, and A. Kahraman, 2004, Dynamic tooth loads of planetary gear sets having tooth profile wear, *Mechanism and Machine Theory* 39 (2004), pp.695-715.
 42. D. Vecchiato, 2005, Tooth contact analysis of a misaligned isostatic planetary gear train, *Mechanism and Machine Theory* 41 (2006), pp.617-631.
 43. S. Jia, and I. Howard, 2006, Comparison of localized spalling and crack damage from dynamic modelling of spur gear vibrations, *Mechanical Systems and Signal Processing* 20 (2006), pp.332-349.
 44. V. Abousleiman, and P. Velex, 2006, A hybrid 3D finite element/lumped parameter model for quasi-static and dynamic analyses of planetary/epicyclic gear sets, *Mechanism and Machine Theory* 21 (2006), pp.725-748.
 45. V. K. Ambarisha, and R. G. Parker, 2007, Nonlinear dynamics of planetary gears using analytical and finite element models, *Journal of Sound and Vibration* 302 (2007), pp.577-595.
 46. M. Inalpolat, and A. Kahraman, Dynamic modelling of planetary gears of automatic transmissions, Department of Mechanical Engineering, The Ohio State University, Columbus, Ohio, USA.
 47. S. L. Harris, Dynamic loads on the teeth of spur gears, *Proceedings of the Institution of Mechanical Engineers* 172 (1958)87-112.
 48. R. G. Munro, The DC component of gear transmission error, *Proceedings of the Fifth ASME International Power Transmission and Gearing Conference*, Chicago, 1989, pp.467-470.
 49. M. Amabili, And A. Fregolent, A method to identify model parameters and gear errors by vibrations of a spur gear pair, *Journal of Sound and Vibration* (1998) 214(2), 339-357
 50. H. N. Ozguven, And D. R. Houser, Dynamic analysis of high speed gears by

using loaded static transmission error, Gear Dynamics and Gear Noise Research Laboratory, Department of Mechanical Engineering, The Ohio State University, Columbus, Ohio 43210, U.S.A.

51. R. B. Randall, A new method of modelling gear faults, *Journal of Mechanical Design* 104 (1982) 259-267.
52. W. D. Mark, Analysis of the vibration excitation of gear system, II : tooth error representations, approximations, and application, *Journal of Acoustic Society of American* 66 (1979) 1758-1787.
53. S. Jia, I. Howard, and J. Wang, The dynamic modelling of multiple pairs of spur gear in mesh including friction and geometry errors, *Proceeding of the Sixth International Conference Rotor Dynamics*, Sydney, Australia, September 30-October 4, 2002, pp.698-705.
54. R. Kasuba, And J.W.Evans, An extended model for determining dynamics loads in spur gearing, *Transactions of the American Society of the Mechanical Engineers, Journal of Mechanical Design* 103, 398-409.
55. G. Bonori, And F. Pellicano, Non-smooth dynamics of spur gears with manufacturing errors, Department of Mechanical and Civil Engineering, University of Modena and Reggio Emilia, Modena, Italy.
56. R. G. Parker, And J. Lin, Mesh phasing relationships in planetary and epicyclic gears, *Journal of Mechanical Design*, 2004, 126, pp.365-370
57. J. D. Sirichai, 1999, Torsional properties of spur gears in mesh using non-linear finite element analysis, PHD thesis, Curtin University of Technology, Australia.
58. J. Wang, 2003, Numerical and experimental analysis of spur gears in mesh, PHD thesis, Curtin University of Technology, Australia.
59. Martin, J.W., T.J. Martin, T.P. Bennett, and K.M. Martin, *Surface mining equipment*, 1st edition, Golden, Colorado: Martin Consultants, Inc, 1982.
60. *Bucket wheel excavators*, 2006, *Mining Magazine* 195(4):35-38.
61. ABB, 2009, Low voltage industrial performance motor, Modal: M2CA 400 LKA.
[http://www05.abb.com/global/scot/scot259.nsf/veritydisplay/b96040e2a65670d9c12575600043d817/\\$File/IPM_%20EN%2001_2009_9AKK104559%20lowres.pdf](http://www05.abb.com/global/scot/scot259.nsf/veritydisplay/b96040e2a65670d9c12575600043d817/$File/IPM_%20EN%2001_2009_9AKK104559%20lowres.pdf) (accessed September 17, 2009)
62. Durst, W., and W. Vogt, *Bucket wheel excavator*, Clausthal-Zellerfeld, Germany: Trans Tech Publications, 1988.

63. Juvinall, R.C., and K.M. Marshek, Fundamentals of machine component design, 3rd edition, Hoboken, New Jersey: John Wiley & Sons, Inc, 2000.
64. S. H. Loewenthal, Shafts, couplings, Keys, etc, In Mechanical Design Handbook, H.A. Rothbart, 21.1-21.52, 1996.
65. R. Heptinstall, Dynamic modelling of gears with application to a bucket wheel excavator drive system, 2007, Curtin University of Technology.
66. D. L. Logan, A first course in the finite element method, "Properties of solids", 4th edition, University of Wisconsin-Platteville.
67. MATLAB help, Version R14, The MathWorks, Inc.
68. R. G. Parker, A physical explanation for the effectiveness of planet phasing to suppress planetary gear vibration, Journal of Sound and Vibration (2000) 236(4), pp.561-573.

13. APPENDIX

13.1. MATLAB PROGRAM

13.1.1. ipdata.m

```
function inputdata=ipdata(numberofinput)
%%The program developed to introduce input values
%%It includes all inputs needed in the entire programming
%%except displacement factors of action line of mesh (Sec 7.3)
%%except setting for profile and pitch excitation (Sec 7.4)
%%except settings of tooth faults (Sec 7.5).

in(1)=19; %zs
in(2)=32; %zpz
in(3)=83; %zr
in(4)=20; %as
in(5)=20; %ar
in(6)=16/1000; %module
in(7)=3; %number of planet
in(8)=245/1000; %face width B
in(9)=in(6)/2*(in(1)+in(2)); % centre distance of sun & planet
/rc design radial distance between the centres of planet gear
and carrier arm

%in(11)=in(201); %planet spacing 1
%in(12)=in(202); %planet spacing 2
%in(13)=in(203); %planet spacing 3
in(14)=82/1000; %sun gear shaft radius
in(15)=136/1000; %planet gear shaft radius
in(16)=880/1000; %ring gear host radius

in(21)=210*10^9; % young's modules
in(22)=7850; % density of gear/arm material
in(23)=4700; % density of ore

in(31)=6; % number of poles
in(32)=50; % supply frequency in Hz
in(33)=950; % operation speed of motor
in(34)=450000; % rated power of motor in Watts
in(35)=65*68*38/21/21/13; % reduction gear box ratio
in(36)=in(35)*(1+in(3))/in(2)*in(2)/in(1); % gear box ratio
in(37)=20; % inertia of motor

in(41)=5; %output torque control ratio.
    %case 1, simplified high torque, 1.
    %case 2, simplified mid torque, 1.5.
    %case 3, simplified low torque, 2.25.
    %case 4, detailed torque, 5.
in(42)=12; % number of buckets
in(43)=5;%3+1+1,corresponding to in(92), number of buckets
with ore when in operation
in(44)=in(9)*2*pi/2; %starting up end point/loading up start
point
in(45)=in(44)+in(9)*2*pi*in(43)/in(42);%loading up end
point
in(46)=in(45)+in(9)*2*pi*1.1;%unloading start point
in(47)=in(46)+in(9)*2*pi*in(43)/in(42);%unloading end point
in(48)=in(9)*2*pi/in(42);%single bucket load loading
up/unloading period
in(49)=in(45)+in(9)*2*pi*0.5;%overloading start point

in(50)=in(45)+in(9)*2*pi*0.7;%overloading end point

in(51)=3; % condition controller
in(53)=1; % SPsp controller %%%%%%%%%% can be detailed
as dependent term
in(54)=1; % SPrp controller %%%%%%%%%% can be detailed
as dependent term
in(55)=0.001; % diff step controller
in(56)=0; % shaft-frequency excitation controller

in(61)=10; % Csp
in(62)=10; % Crp
in(63)=10^10; % Cpx
in(64)=10^10; % Cpy
in(65)=10^8; % Kpx
in(66)=10^8; % Kpy
in(67)=(in(6)/2*(in(1)+in(2))+0.0001); % centre distance of
sun & planet / rcp real radial distance between the centres of
planet gear and carrier arm

in(71)=0; % torque from base to ring gear
in(72)=15; % coupling damping coefficient

in(81)=0/1000; % inner radius of carrier arm
in(82)=1000/1000; % outer radius of carrier arm
in(83)=150/1000; % average width of carrier arm
in(84)=1000/1000; % inner radius of wheel
in(85)=2000/1000; % outer radius of wheel
in(86)=100/1000; % average width of wheel
in(87)=in(42); % number of buckets
in(88)=1; % bucket dimension
in(89)=1.2; % bucket dimension
in(90)=0.95; % bucket dimension
in(91)=1.1; % bucket dimension
in(92)=3*0.8+1*0.6+1*0.1; % ore loading condition
in(93)=0.8; %single bucket ore drop
in(94)=in(48)/4; %ore drop period
in(95)=10; %overloading rate

in(101)=300; % csx
in(102)=300; % csy
in(103)=100; % cst
in(104)=450; % crx
in(105)=450; % cry
in(106)=10^6; % crt
in(107)=500; % ccx
in(108)=500; % ccy
in(109)=100; % cct

in(111)=10^7; % ksx
in(112)=10^7; % ksy
in(113)=0; % kst
in(114)=10^8; % krx
in(115)=10^8; % kry
```



```

in(116)=10^10; % krt
in(117)=5*10^7; % kcx
in(118)=5*10^7; % kcy
in(119)=0; % kct

```

```

in(201)=0; %planet spacing 1
in(202)=34/51*pi; %planet spacing 2
in(203)=68/51*pi; %planet spacing 3

```

13.1.2. velocityvector.m

```

function velo=velocityvector(n,cd,eps)
%% determine the velocity vector
%% optionally display each term in the velocity vector
%% with associated physical meaning respectively (after
line.26)
% n, number of planet gears
% cd, condition controller

```

```

%check the number of input
if margin==3
    eps=1.0e-6;
else
    error('incorrect number of input arguments. ');
    return
end

```

```

% determine velocity vector: velo
for j=1:1:(cd*n+3*cd)
    for i=j
        y='y';
        veloo=sym(strcat(y,'(' ,int2str(i+cd*n+3*cd),')'));
    end
    velo(j,1)=veloo;
end

```

```

velo=velo;

if cd==1
    convert(1,1)=sym(strcat('d','x/y/u','s'));
    convert(2,1)=sym(strcat('d','x/y/u','r'));
    convert(3,1)=sym(strcat('d','x/y/u','e'));
    for j=4:1:(cd*n+3*cd)
        convert(j,1)=sym(strcat('d','x/y/u','p',int2str((j-3))));
    end
    for j=1:1:(cd*n+3*cd)
        convert(j,2)=velo(j,1);
    end
end

```

```

if cd==2
    convert(1,1)=sym(strcat('d','x','s'));
    convert(2,1)=sym(strcat('d','y','s'));
    convert(3,1)=sym(strcat('d','x','r'));
    convert(4,1)=sym(strcat('d','y','r'));
    convert(5,1)=sym(strcat('d','x','c'));
    convert(6,1)=sym(strcat('d','y','c'));

```

```

in(301)=0.03; % angular error of planets position on carrier
arm in degrees
in(302)=0.05; % angular error of planets position on carrier
arm in degrees
in(303)=0.08; % angular error of planets position on carrier
arm in degrees

```

```

inputdata=in(numberofinput);

```

```

i=6;
for j=7:2:(cd*n+3*cd)
    convert(j,1)=sym(strcat('d','x','p',int2str((j-i))));
    i=i+1;
end
i=7;
for j=8:2:(cd*n+3*cd)
    convert(j,1)=sym(strcat('d','y','p',int2str((j-i))));
    i=i+1;
end
for j=1:1:(cd*n+3*cd)
    convert(j,2)=velo(j,1);
end
end

```

```

if cd==3
    convert(1,1)=sym(strcat('d','x','s'));
    convert(2,1)=sym(strcat('d','y','s'));
    convert(3,1)=sym(strcat('d','u','s'));
    convert(4,1)=sym(strcat('d','x','r'));
    convert(5,1)=sym(strcat('d','y','r'));
    convert(6,1)=sym(strcat('d','u','r'));
    convert(7,1)=sym(strcat('d','x','c'));
    convert(8,1)=sym(strcat('d','y','c'));
    convert(9,1)=sym(strcat('d','u','c'));
    i=9;
    for j=10:3:(cd*n+3*cd)
        convert(j,1)=sym(strcat('d','x','p',int2str((j-i))));
        i=i+2;
    end
    i=10;
    for j=11:3:(cd*n+3*cd)
        convert(j,1)=sym(strcat('d','y','p',int2str((j-i))));
        i=i+2;
    end
    i=11;
    for j=12:3:(cd*n+3*cd)
        convert(j,1)=sym(strcat('d','u','p',int2str((j-i))));
        i=i+2;
    end
    for j=1:1:(cd*n+3*cd)
        convert(j,2)=velo(j,1);
    end
end

```

```

%velo=convert;%display

```

13.1.3. displacementvector.m

```

function dism=displacementvector(n,cd,eps)
%% determine the displacement vector
%% optionally display each term in the displacement vector
%% with associated physical meaning respectively (after
line.26)
% n, number of planet gears
% cd, condition controller

```

```

%check the number of input
if margin==3
    eps=1.0e-6;
else
    error('incorrect number of input arguments. ');
    return
end
end

```

```

% determine displacement vector: dism
for j=1:1:(cd*n+3*cd)
    for i=j
        y='y';
        diamm=sym(strcat(y,'(int2str(i),''));
    end
    dism(j,1)=diamm;
end

dism=dism;

if cd==1
    convert(1,1)=sym(strcat('x/y/u','s'));
    convert(2,1)=sym(strcat('x/y/u','r'));
    convert(3,1)=sym(strcat('x/y/u','c'));
    for j=4:1:(cd*n+3*cd)
        convert(j,1)=sym(strcat('x/y/u','p',int2str((j-3))));
    end
    for j=1:1:(cd*n+3*cd)
        convert(j,2)=dism(j,1);
    end
end

if cd==2
    convert(1,1)=sym(strcat('x','s'));
    convert(2,1)=sym(strcat('y','s'));
    convert(3,1)=sym(strcat('x','r'));
    convert(4,1)=sym(strcat('y','r'));
    convert(5,1)=sym(strcat('x','c'));
    convert(6,1)=sym(strcat('y','c'));
    i=6;
    for j=7:2:(cd*n+3*cd)
        convert(j,1)=sym(strcat('x','p',int2str((j-i))));
        i=i+1;
    end
    i=7
    for j=8:2:(cd*n+3*cd)
        convert(j,1)=sym(strcat('y','p',int2str((j-i))));
        i=i+1;
    end
end

```

```

end
for j=1:1:(cd*n+3*cd)
    convert(j,2)=dism(j,1);
end
end

if cd==3
    convert(1,1)=sym(strcat('x','s'));
    convert(2,1)=sym(strcat('y','s'));
    convert(3,1)=sym(strcat('u','s'));
    convert(4,1)=sym(strcat('x','r'));
    convert(5,1)=sym(strcat('y','r'));
    convert(6,1)=sym(strcat('u','r'));
    convert(7,1)=sym(strcat('x','c'));
    convert(8,1)=sym(strcat('y','c'));
    convert(9,1)=sym(strcat('u','c'));
    i=9;
    for j=10:3:(cd*n+3*cd)
        convert(j,1)=sym(strcat('x','p',int2str((j-i))));
        i=i+2;
    end
    i=10;
    for j=11:3:(cd*n+3*cd)
        convert(j,1)=sym(strcat('y','p',int2str((j-i))));
        i=i+2;
    end
    i=11;
    for j=12:3:(cd*n+3*cd)
        convert(j,1)=sym(strcat('u','p',int2str((j-i))));
        i=i+2;
    end
    for j=1:1:(cd*n+3*cd)
        convert(j,2)=dism(j,1);
    end
end

%dism=convert;%display

```

13.1.4. cunfangMCKF.m

%% Program cunfangMCKF.m is developed to generate ODE function It requires ipdata.m, displacementvector.m, velocityvector.m
%% and manual inputs (MDsp and MDrp at line.32, 103, 148, 173, 472, 543, 588, 614, 905, 939, 964, 1030, 1096, 1130, 1155, 1221, governing equations at line.277, 285, 293, 301, 309, 317, 710, 718, 726, 734, 742, 750, 1288, 1296, 1304, 1312, 1320, 1332, and submission of Eq3.53-56 at line.1380, 1394, 1410, 1424, 1440, 1500, 1514, 1533, 1547.)

```

n=ipdata(7);
cd=ipdata(51);
syms t
syms tt
syms as % pressure angle of sun gear
syms ar % pressure angle of ring gear
syms rs rc rr rp
%%%%%%%%%%%%%%%%%%%%%%%%%%%%%%%%%%%%%%%%%%%%%%%%%%%%%%%%%%%%%%%%%%%%%%%%
% part one
% form every term of MDspi & DMDspi
%%%%%%%%%%%%%%%%%%%%%%%%%%%%%%%%%%%%%%%%%%%%%%%%%%%%%%%%%%%%%%%%%%%%%%%%
%-----%
% form DMDspi
%-----%
for j=1:1:(cd*n+3*cd)
    y(j)=sym(strcat('y','(int2str(j),''));

```

```

    y(j)=1;
end
for j=1:1:n
    fae(j)=sym(strcat('Dfae','(int2str(j),'')))*t;
end
for j=1:1:n
    fesp(j)=sym(strcat('fesp','(int2str(j),''));
    fEs(j)=sym(strcat('fEs','(int2str(j),''));
    fEsp(j)=sym(strcat('fEsp','(int2str(j),''));
end
for j=1:1:n
    %@@@@@@@@@@@@@@@@@@@@@@@@@@@@@@@@@@@@@@@@@@@@@@@@@@@@@@@@
ENTER MDsp vector
    transMDDsp=[cos(fae(j)-as)*y(2);-cos(fae(j)-
as)*y(8+3*j);sin(fae(j)-as)*y(1);-sin(fae(j)-
as)*y(7+3*j);y(3);-y(3)/(rr+rs)*rs;y(6)/(rr+rs)*rs;-
y(9+3*j);fesp(j);fEs(j);-fEsp(j)];
    sizeofMDDsp=size(transMDDsp);
    for i=1:1:sizeofMDDsp(1)
        MDDsp(i,j)=transMDDsp(i);
    end
end
MDDsp;
sizeMDDsp=size(MDDsp);
for i=1:1:sizeofMDDsp(1)
    for j=1:1:sizeMDDsp(2)

```



```

end
end

Fmatrix(row(1),1)=Fmatrix(row(1),1)+positionsp(1,sizegovern(i));
else
for rowi=1:1:n
roww=row(rowi);
for k=1:1:(sizeofMDsp(1)*2)
for kk=rowi:1:rowi
% solving DMDsp
if DNu1(k,kk)>=(1+cd*n+3*cd+1) &&
DNu1(k,kk)<=(n+cd*n+3*cd+1)
K2matrix(roww,(DNu2(k,kk)-
1))=DMDsp(k,kk)*positionsp(1,2+(kk-
1)*sizegovern(i))+K2matrix(roww,(DNu2(k,kk)-1));
else if DNu1(k,kk)>=2 &&
DNu1(k,kk)<=(cd*n+3*cd+1)
C1matrix(roww,(DNu2(k,kk)-
1))=DMDsp(k,kk)*positionsp(1,2+(kk-
1)*sizegovern(i))+C1matrix(roww,(DNu2(k,kk)-1));
else if DNu1(k,kk)>=(n+cd*n+3*cd+2) &&
DNu1(k,kk)<=(2*n+cd*n+3*cd+1)
Fmatrix(roww,1)=Fmatrix(roww,1)-
DMDsp(k,kk)*positionsp(1,2+(kk-1)*sizegovern(i));
else
end
end
end
end
for k=1:1:sizeofMDsp(1)
for kk=rowi:1:rowi
% solving MDsp
if DNu2(k+sizeofMDsp(1),kk)>=2 &&
DNu2(k+sizeofMDsp(1),kk)<=(cd*n+3*cd+1)
K1matrix(roww,(DNu2(k+sizeofMDsp(1),kk)-
1))=MDsp(k,kk)*positionsp(1,3+(kk-
1)*sizegovern(i))+K1matrix(roww,(DNu2(k+sizeofMDsp(1),
kk)-1));
if
DNu2(k+sizeofMDsp(1),kk)==(cd*3+kk*cd-1)
Fmatrix(roww,1)=Fmatrix(roww,1)-
sym(strcat('sin(fae','int2str(kk),'-as)*(-cos((y','int2str(cd),'-
y','int2str(2*cd),'))/(rs+rr)+pi-
ipdata','int2str(200+kk),'))*rc+cos(pi-
ipdata','int2str(200+kk),'))*rc))*positionsp(1,3+(kk-
1)*sizegovern(i));
else if
DNu2(k+sizeofMDsp(1),kk)==(cd*3+kk*cd)
Fmatrix(roww,1)=Fmatrix(roww,1)-
sym(strcat('cos(fae','int2str(kk),'-as)*(sin((y','int2str(cd),'-
y','int2str(2*cd),'))/(rs+rr)+pi-ipdata','int2str(200+kk),'))*rc-
sin(pi-ipdata','int2str(200+kk),'))*rc))*positionsp(1,3+(kk-
1)*sizegovern(i));
end
Fmatrix(roww,1)=Fmatrix(roww,1);
end
else if
DNu2(k+sizeofMDsp(1),kk)>=(n+cd*n+3*cd+2) &&
DNu2(k+sizeofMDsp(1),kk)<=(2*n+cd*n+3*cd+1)
Fmatrix(roww,1)=Fmatrix(roww,1)-
MDsp(k,kk)*positionsp(1,3+(kk-1)*sizegovern(i));
end
end
end
end

Fmatrix(roww,1)=Fmatrix(roww,1)+positionsp(1,sizegovern(i));

```

```

end
end
row=[0,0,0];
roww=0;
rowi=0;

%%%%%%%%%%%%%%%%%%%%%%%%%%%%%%%%%%%%%%%%%%%%%%%%%%%%%%%%%%%%%%%%%%%%%%%%
% part four
% form every term of MDRpi & DMDrpi
%%%%%%%%%%%%%%%%%%%%%%%%%%%%%%%%%%%%%%%%%%%%%%%%%%%%%%%%%%%%%%%%%%%%%%%%
%-----%
% form DMDrpi
%-----%
for j=1:1:(cd*n+3*cd)
y(j)=sym(strcat('y','int2str(j,'));
y(j)=1;
end
for j=1:1:n
fae(j)=sym(strcat('Dfae','int2str(j,'))*t;
end
for j=1:1:n
ferp(j)=sym(strcat('ferp','int2str(j,'));
fEr(j)=sym(strcat('fEr','int2str(j,'));
fErp(j)=sym(strcat('fErp','int2str(j,'));
end
for j=1:1:n
%@@@@@@@@@@@@@@@@@@@@@@@@@@@@@@@@@@@@@@@@@@@@@@@@@@@@@@@@
ENTER MDRp vector
transMDDrp=[cos(fae(j)+ar)*y(5);-
cos(fae(j)+ar)*y(8+3*j);sin(fae(j)+ar)*y(4);-
sin(fae(j)+ar)*y(7+3*j);-y(6);-
y(3)/(rr+rs)*rr;y(6)/(rr+rs)*rr;y(9+3*j);ferp(j);fEr(j);-fErp(j)];
sizeofMDDrp=size(transMDDrp);
for i=1:1:sizeofMDDrp(1)
MDDrp(i,j)=transMDDrp(i);
end
end
MDDrp;
sizeMDDrp=size(MDDrp);
for i=1:1:sizeofMDDrp(1)
for j=1:1:sizeofMDDrp(2)
DMDrp(i,j)=diff(MDDrp(i,j),'t');
end
end
for i=1:1:sizeofMDDrp(1)
for j=1:1:sizeofMDDrp(2)
if DMDrp(i,j)==0
DMDr1(i,j)=DMDrp(i,j);
else
H=char(DMDrp(i,j));
sizeH=size(H);
HH=sym(strcat('Dfae','int2str(j,'))*t;
HH=char(HH);
HHH=(strcat('fae','int2str(j,'));
sizeHHH=size(HHH);
sizeHH=size(HH);
for ii=1:1:(sizeH(2)-sizeHH(2)+1)
if double(H(ii))==double(HH(1)) &&
double(H(ii+sizeHH(2)-1))==double(HH(sizeHH(2)))
ii;
for jj=1:1:sizeofMDDrp(2)
H(ii+jj-1)=HHH(jj);
end
for jj=sizeHHH(2):1:(sizeH(2)-
sizeHH(2)+sizeHHH(2)-ii)
H(ii+jj)=H(ii+jj+sizeHH(2)-sizeHHH(2));
end
else

```

```

end
end
Hf=";
for k=1:(sizeH(2)-sizeHH(2)+sizeHHH(2))
    Hf(k)=H(k);
end
doubleHf=double(Hf);
sizeHf=size(doubleHf);
HF=char(doubleHf(1,1));
for iii=2:1:sizeHf(2)
    NuHf=doubleHf(1,iii);
    HF=(strcat(char(HF),char(NuHf)));
end
A=sym(HF);
i;
j;
DMDr1(i,j)=A;
end
end
end
for j=1:(cd*n+3*cd)
    y(j)=sym(strcat('y','(',int2str(j+cd*n+3*cd),')'))*tt;
    y(j)=tt;
end
for j=1:1:n
    fae(j)=sym(strcat('fae','(',int2str(j),')'));
end
for j=1:1:n
    ferp(j)=sym(strcat('Dferp','(',int2str(j),')'))*tt;
    fEr(j)=sym(strcat('DEr','(',int2str(j),')'))*tt;
    fErp(j)=sym(strcat('DFErp','(',int2str(j),')'))*tt;
end
for j=1:1:n
    %@@@@@@@@@@@@@@@@@@@@@@@@@@@@@@@@@@@@@@@@
ENTER MDrp vector
    transMDDrp=[cos(fae(j)+ar)*y(5);-
cos(fae(j)+ar)*y(8+3*j);sin(fae(j)+ar)*y(4);-
sin(fae(j)+ar)*y(7+3*j);-y(6);-
y(3)/(rr+rs)*rr;y(6)/(rr+rs)*rr;y(9+3*j);ferp(j);fEr(j);-fErp(j)];
    sizeofMDDrp=size(transMDDrp);
    for i=1:1:sizeofMDDrp(1)
        MDDrp(i,j)=transMDDrp(i);
    end
end
MDDrp;
sizeMDDrp=size(MDDrp);
for i=1:1:sizeofMDDrp(1)
    for j=1:1:sizeofMDDrp(2)
        DMDr2(i,j)=diff(MDDrp(i,j),'t');
    end
end
for i=1:1:sizeofMDDrp(1)
    for j=1:1:sizeofMDDrp(2)
        DMDrp(i,j)=DMDr1(i,j);
    end
end
for i=(sizeofMDDrp(1)+1):1:(2*sizeofMDDrp(1))
    for j=1:1:sizeofMDDrp(2)
        DMDrp(i,j)=DMDr2((i-sizeofMDDrp(1)),j);
    end
end
DMDrp;
%-----%
% form MDrpi
%-----%
for j=1:(cd*n+3*cd)
    y(j)=sym(strcat('y','(',int2str(j),')'));
    y(j)=1;

```

```

%define displacement
end
for j=1:1:n
    fae(j)=sym(strcat('fae','(',int2str(j),')'));
    %define symbol for angular position of each planet gear
end
syms force % selection sign for force terms
for j=1:1:n
    ferp(j)=sym(strcat('ferp','(',int2str(j),')'));
    fEr(j)=sym(strcat('fEr','(',int2str(j),')'));
    fErp(j)=sym(strcat('fErp','(',int2str(j),')'));
end
for j=1:1:n
    %@@@@@@@@@@@@@@@@@@@@@@@@@@@@@@@@@@@@@@@@
ENTER MDrp vector
    transMDrp=[cos(fae(j)+ar)*y(5);-
cos(fae(j)+ar)*y(8+3*j);sin(fae(j)+ar)*y(4);-
sin(fae(j)+ar)*y(7+3*j);-y(6);-
y(3)/(rr+rs)*rr;y(6)/(rr+rs)*rr;y(9+3*j);ferp(j);fEr(j);-fErp(j)];
    sizeofMDrp=size(transMDrp);
    for i=1:1:sizeofMDrp(1)
        MDrp(i,j)=transMDrp(i);
    end
end
MDrp;

%%%%%%%%%%
% part five
% number order every term of MDrpi
%%%%%%%%%%
for j=1:(cd*n+3*cd)
    y(j)=tt^(j+1); %define displacement
end
for j=1:1:n
    fae(j)=tt^(j+cd*n+3*cd+1); %define symbol for angular
position of each planet gear
end
syms force % selection sign for force terms
for j=1:1:n
    ferp(j)=force*tt^(j+n+cd*n+3*cd+1);
    fEr(j)=force*tt^(j+n+cd*n+3*cd+1);
    fErp(j)=force*tt^(j+n+cd*n+3*cd+1);
end
for j=1:1:n
    %@@@@@@@@@@@@@@@@@@@@@@@@@@@@@@@@@@@@@@@@
ENTER MDrp vector
    transMDrp=[cos(fae(j)+ar)*y(5);-
cos(fae(j)+ar)*y(8+3*j);sin(fae(j)+ar)*y(4);-
sin(fae(j)+ar)*y(7+3*j);-y(6);-
y(3)/(rr+rs)*rr;y(6)/(rr+rs)*rr;y(9+3*j);ferp(j);fEr(j);-fErp(j)];
    sizeofMDrp=size(transMDrp);
    for i=1:1:sizeofMDrp(1)
        MDr(i,j)=transMDrp(i);
    end
end
A=diff(MDr,'t');
B=diff(MDr,'tt');
sizeA=size(A);
sizeB=size(B);
sizeD(1)=sizeA(1)+sizeB(1);
sizeD(2)=sizeA(2);
for i=1:1:sizeA(1)
    for j=1:1:sizeA(2)
        D(i,j)=A(i,j);
    end
end
for i=(sizeA(1)+1):1:sizeD(1)
    for j=1:1:sizeA(2)
        D(i,j)=B((i-sizeA(1)),j);
    end
end

```

```

end
for i=1:1:sizeD(1)
for j=1:1:sizeD(2)
DD=D(i,j);
Nu=char(DD);
sizeNu=size(Nu);
ii=0;iii=1;
if double(Nu(1,1))==45
ii=1;iii=2;
for jj=2:1:sizeNu(2)
if double(Nu(1,jj))<=57 && double(Nu(1,jj))>=48
ii=ii+1;
else break
end
end
else
for jj=1:1:sizeNu(2)
if double(Nu(1,jj))<=57 && double(Nu(1,jj))>=48
ii=ii+1;
else break
end
end
end
Nub=0;
for jj=iii:1:ii
Nub=Nub+(double(Nu(jj))-48)*10^(ii-jj);
end
DNur1(i,j)=Nub;
end
end
DNur1;
%------%
% DNur1 number original matrix, to tell terms in to two
different levels of
% matrices
% from DNur1 to DNur2
% DNur2 separates lower level matrix terms into expected
positions
%------%
sizeDNur1=size(DNur1);
for i=1:1:sizeDNur1(1)
for j=1:1:sizeDNur1(2)
if DNur1(i,j)<=(j+cd*n+3*cd+1) &&
DNur1(i,j)>=(1+cd*n+3*cd+1)
DNur2(i,j)=DNur1((i+sizeofMDrp(1)),j);
else
DNur2(i,j)=DNur1(i,j);
end
end
end
DNur2;

%%%%%%%%%%%%%%
% part six
% governing equation
%%%%%%%%%%%%%%

for i=1:1:n
syms xs ys us xr yr ur xc yc xp yp up;
syms kk;
syms Trb rr;
Crp(i)=sym(strcat('Crp','(',int2str(i),')'));
Krp(i)=sym(strcat('Krp','(',int2str(i),')'));
SPrp(i)=sym(strcat('SPrp','(',int2str(i),')'));
fae(i)=sym(strcat('fae','(',int2str(i),')'));
end

%@@@@@@@@@@@@@@@@@@@@@@@@@@@@@@@@@@@@@@@@
ENTER gov vector

%gov1(1,:)= [xr,Crp(j)*sin(fae(j)+ar),SPrp(j)*Krp(j)*sin(fae(j)
)+ar),0];
%gov2(1,:)= [yr,Crp(j)*cos(fae(j)+ar),SPrp(j)*Krp(j)*cos(fae(
j)+ar),0];
%gov3(1,:)= [ur,-Crp(j),-SPrp(j)*Krp(j),Trb/rr];
%gov4(1,:)= [xp,-Crp(j)*sin(fae(j)+ar),-
SPrp(j)*Krp(j)*sin(fae(j)+ar),0];
%gov5(1,:)= [yp,-Crp(j)*cos(fae(j)+ar),-
SPrp(j)*Krp(j)*cos(fae(j)+ar),0];
%gov6(1,:)= [up,Crp(j),SPrp(j)*Krp(j),0];

for j=1:1:n

gov1(1,:)= [xr,Crp(j)*sin(fae(j)+ar),SPrp(j)*Krp(j)*sin(fae(j)+
ar),0];
sizegov=size(gov1);
sizegovern(1)=sizegov(2);
for i=1:1:sizegov(2)
governing(1,i+(j-1)*sizegov(2))=gov1(1,i);
end
end
for j=1:1:n

gov2(1,:)= [yr,Crp(j)*cos(fae(j)+ar),SPrp(j)*Krp(j)*cos(fae(j)
+ar),0];
sizegov=size(gov2);
sizegovern(2)=sizegov(2);
for i=1:1:sizegov(2)
governing(2,i+(j-1)*sizegov(2))=gov2(1,i);
end
end
for j=1:1:n

gov3(1,:)= [ur,-Crp(j),-SPrp(j)*Krp(j),Trb/rr];
sizegov=size(gov3);
sizegovern(3)=sizegov(2);
for i=1:1:sizegov(2)
governing(3,i+(j-1)*sizegov(2))=gov3(1,i);
end
end
for j=1:1:n

gov4(1,:)= [xp,-Crp(j)*sin(fae(j)+ar),-
SPrp(j)*Krp(j)*sin(fae(j)+ar),0];
sizegov=size(gov4);
sizegovern(4)=sizegov(2);
for i=1:1:sizegov(2)
governing(4,i+(j-1)*sizegov(2))=gov4(1,i);
end
end
for j=1:1:n

gov5(1,:)= [yp,-Crp(j)*cos(fae(j)+ar),-
SPrp(j)*Krp(j)*cos(fae(j)+ar),0];
sizegov=size(gov5);
sizegovern(5)=sizegov(2);
for i=1:1:sizegov(2)
governing(5,i+(j-1)*sizegov(2))=gov5(1,i);
end
end
for j=1:1:n

gov6(1,:)= [up,Crp(j),SPrp(j)*Krp(j),0];
sizegov=size(gov6);
sizegovern(6)=sizegov(2);
for i=1:1:sizegov(2)
governing(6,i+(j-1)*sizegov(2))=gov6(1,i);
end
end
governing;
sizegovern;
sizei=size(sizegovern);

for i=1:1:sizei(2)

```



```

1)*sizegovern(i))+K1matrix(roww,(DNur2(k+sizeofMDrp(1),
kk)-1));
    if
DNur2(k+sizeofMDrp(1),kk)==(cd*3+kk*cd-1)
    Fmatrix(roww,1)=Fmatrix(roww,1)-
sym(strcat('sin(fae',int2str(kk),'+ar)*(-cos((y',int2str(cd),'-
y',int2str(2*cd),'))/(rs+rr)+pi-
ipdata(',int2str(200+kk),'))*rc+cos(pi-
ipdata(',int2str(200+kk),'))*rc'))*positionrp(1,3+(kk-
1))*sizegovern(i);
    else if
DNur2(k+sizeofMDrp(1),kk)==(cd*3+kk*cd)
    Fmatrix(roww,1)=Fmatrix(roww,1)-
sym(strcat('cos(fae',int2str(kk),'+ar)*(sin((y',int2str(cd),'-
y',int2str(2*cd),'))/(rs+rr)+pi-ipdata(',int2str(200+kk),'))*rc-
sin(pi-ipdata(',int2str(200+kk),'))*rc'))*positionrp(1,3+(kk-
1))*sizegovern(i));
    end
    Fmatrix(roww,1)=Fmatrix(roww,1);
    end
    else if
DNur2(k+sizeofMDrp(1),kk)>=(n+cd*n+3*cd+2) &&
DNur2(k+sizeofMDrp(1),kk)<=(2*n+cd*n+3*cd+1)
    Fmatrix(roww,1)=Fmatrix(roww,1)-
MDrp(k,kk)*positionrp(1,3+(kk-1))*sizegovern(i);
    end
    end
end
end

Fmatrix(roww,1)=Fmatrix(roww,1)+positionrp(1,sizegovern(i
));
    end
end
row=[0,0,0];
roww=0;
rowi=0;

%%%%%%%%%%
% part seven
% form every term of MDxpci & DMDxpci
%%%%%%%%%%
syms FAEC; % separation factor of fae(i), for sun pair, ring
pair from carrier arm pair
%-----%
% form DMDxpci
%-----%
for j=1:(cd*n+3*cd)
    y(j)=sym(strcat('y',int2str(j+cd*n+3*cd),''))*tt;
    y(j)=tt;
end
for j=1:1:n
    fae(j)=sym(strcat('fae',int2str(j),''));
end
for j=1:1:n
    Dtcp(j)=sym(strcat('Dtcp',int2str(j),''));
    Drcp(j)=sym(strcat('Drcp',int2str(j),''));
end
for j=1:1:n
    %@@@@@@@@@@@@@@@@@@@@@@@@@@@@@@@@@@@@@@@@
ENTER MDxcp vector
    transMDDcp=[y(7+3*j);-y(7);-y(9)*sin(fae(j));-
Dtcp(j)*sin(fae(j));Drcp(j)*cos(fae(j))];
    sizeofMDDcp=size(transMDDcp);
    for i=1:sizeofMDDcp(1)
        MDDcp(i,j)=transMDDcp(i);
    end
end
MDDcp;

```

```

sizeMDDcp=size(MDDcp);
for i=1:sizeofMDDcp(1)
    for j=1:sizeofMDDcp(2)
        DMDxcp(i,j)=diff(MDDcp(i,j),'t');
    end
end
DMDxcp;

%-----%
% form MDxpci
%-----%
for j=1:(cd*n+3*cd)
    y(j)=sym(strcat('y',int2str(j),''));
    y(j)=1;
    %define displacement
end
for j=1:1:n
    fae(j)=sym(strcat('fae',int2str(j),''));
    %define symbol for angular position of each planet gear
end
syms force % selection sign for force terms
for j=1:1:n
    Dtcp(j)=sym(strcat('Dtcp',int2str(j),''));
    Drcp(j)=sym(strcat('Drcp',int2str(j),''));
end
for j=1:1:n
    %@@@@@@@@@@@@@@@@@@@@@@@@@@@@@@@@@@@@@@@@
ENTER MDxcp vector
    transMDcp=[y(7+3*j);-y(7);-y(9)*sin(fae(j));-
Dtcp(j)*sin(fae(j));Drcp(j)*cos(fae(j))];
    sizeofMDcp=size(transMDcp);
    for i=1:sizeofMDcp(1)
        MDxcp(i,j)=transMDcp(i);
    end
end
MDxcp;

%%%%%%%%%%
% part eight
% number order every term of MDxpci
%%%%%%%%%%
for j=1:(cd*n+3*cd)
    y(j)=tt^(j+cd*n+3*cd+1); %define displacement
end
for j=1:1:n
    fae(j)=t^(j+cd*n+3*cd+1); %define symbol for angular
position of each planet gear
end
syms force % selection sign for force terms
for j=1:1:n
    Dtcp(j)=force*tt^(j+n+cd*n+3*cd+1);
    Drcp(j)=force*tt^(j+n+cd*n+3*cd+1);
end
for j=1:1:n
    %@@@@@@@@@@@@@@@@@@@@@@@@@@@@@@@@@@@@@@@@
ENTER MDxcp vector
    transMDcp=[y(7+3*j);-y(7);-y(9)*sin(fae(j));-
Dtcp(j)*sin(fae(j));Drcp(j)*cos(fae(j))];
    sizeofMDcp=size(transMDcp);
    for i=1:sizeofMDcp(1)
        MDc(i,j)=transMDcp(i);
    end
end
Bc=diff(MDc,'t');
sizeBc=size(Bc);
sizeDc(1)=sizeBc(1);
sizeDc(2)=sizeBc(2);
for i=1:sizeofBc(1)
    for j=1:sizeofBc(2)
        Dc(i,j)=Bc(i,j);
    end
end

```

```

end
end
for i=1:1:sizeDc(1)
    for j=1:1:sizeDc(2)
        DDC=DC(i,j);
        Nuc=char(DDC);
        sizeNuc=size(Nuc);
        ii=0;iii=1;
        if double(Nuc(1,1))==45
            ii=1;iii=2;
            for jj=2:1:sizeNuc(2)
                if double(Nuc(1,jj))<=57 &&
double(Nuc(1,jj))>=48
                    ii=ii+1;
                else break
                end
            end
        else
            for jj=1:1:sizeNuc(2)
                if double(Nuc(1,jj))<=57 &&
double(Nuc(1,jj))>=48
                    ii=ii+1;
                else break
                end
            end
        end
        Nuc=0;
        for jj=iii:1:ii
            Nuc=Nuc+(double(Nuc(jj))-48)*10^(ii-jj);
        end
        DNuxc1(i,j)=Nuc;
    end
end
DNuxc1;
%-----%
% DNuxc1 number original matrix, to tell terms in to two
different levels of
% matrices
% from DNuxc1 to DNuxc2
% DNuxc2 separates lower level matrix terms into expected
positions
%-----%
for j=1:1:(cd*n+3*cd)
    y(j)=tt^(j+1); %define displacement
end
for j=1:1:n
    fae(j)=t^(j+cd*n+3*cd+1); %define symbol for angular
position of each planet gear
end
syms force % selection sign for force terms
for j=1:1:n
    Dtcp(j)=force*tt^(j+n+cd*n+3*cd+1);
    Drcp(j)=force*tt^(j+n+cd*n+3*cd+1);
end
for j=1:1:n
    %@@@@@@@@@@@@@@@@@@@@@@@@@@@@@@@@@@@@@@@@
ENTER MDxcp vector
    transMDcp=[y(7+3*j);-y(7);-y(9)*sin(fae(j));-
Dtcp(j)*sin(fae(j));Drcp(j)*cos(fae(j))];
    sizeofMDcp=size(transMDcp);
    for i=1:1:sizeofMDcp(1)
        MDc(i,j)=transMDcp(i);
    end
end
Bc=diff(MDc,'t');
sizeBc=size(Bc);
sizeDc(1)=sizeBc(1);
sizeDc(2)=sizeBc(2);
for i=1:1:sizeBc(1)
    for j=1:1:sizeBc(2)
        Dc(i,j)=Bc(i,j);
    end
end
for i=1:1:sizeDc(1)
    for j=1:1:sizeDc(2)
        DDC=DC(i,j);
        Nuc=char(DDC);
        sizeNuc=size(Nuc);
        ii=0;iii=1;
        if double(Nuc(1,1))==45
            ii=1;iii=2;
            for jj=2:1:sizeNuc(2)
                if double(Nuc(1,jj))<=57 &&
double(Nuc(1,jj))>=48
                    ii=ii+1;
                else break
                end
            end
        else
            for jj=1:1:sizeNuc(2)
                if double(Nuc(1,jj))<=57 &&
double(Nuc(1,jj))>=48
                    ii=ii+1;
                else break
                end
            end
        end
        Nuc=Nuc+(double(Nuc(jj))-48)*10^(ii-jj);
    end
    DNuxc2(i,j)=Nuc;
end
DNuxc2;
%-----%
% part nine
% form every term of MDyypi & DMdyypi
%-----%
% form DMdyypi
%-----%
for j=1:1:(cd*n+3*cd)
    y(j)=sym(strcat('y','(',int2str(j+cd*n+3*cd),')'))*tt;
    y(j)=tt;
end
for j=1:1:n
    fae(j)=sym(strcat('fae','(',int2str(j),')'));
end
for j=1:1:n
    Dtcp(j)=sym(strcat('Dtcp','(',int2str(j),')'));
    Drcp(j)=sym(strcat('Drcp','(',int2str(j),')'));
end
for j=1:1:n
    %@@@@@@@@@@@@@@@@@@@@@@@@@@@@@@@@@@@@@@@@
ENTER MDyyp vector
    transMDDcp=[y(8+3*j);-y(8);-y(9)*sin(fae(j));-
Dtcp(j)*sin(fae(j));Drcp(j)*cos(fae(j))];
    sizeofMDDcp=size(transMDDcp);
    for i=1:1:sizeofMDDcp(1)
        MDDcp(i,j)=transMDDcp(i);
    end
end
MDDcp;
sizeMDDcp=size(MDDcp);
for i=1:1:sizeofMDDcp(1)
    for j=1:1:sizeMDDcp(2)
        DMdyyp(i,j)=diff(MDDcp(i,j),'t');
    end
end

```

```

end
DMDyep;

%-----%
% form MDyepi
%-----%
for j=1:1:(cd*n+3*cd)
    y(j)=sym(strcat('y','(',int2str(j),')'));
    y(j)=1;
    %define displacement
end
for j=1:1:n
    fae(j)=sym(strcat('fae','(',int2str(j),')'));
    %define symbol for angular position of each planet gear
end
syms force % selection sign for force terms
for j=1:1:n
    Dtcp(j)=sym(strcat('Dtcp','(',int2str(j),')'));
    Drcp(j)=sym(strcat('Drcp','(',int2str(j),')'));
end
for j=1:1:n
    %@@@@@@@@@@@@@@@@@@@@@@@@@@@@@@@@@@@@@@@@
    ENTER MDyep vector
    transMDcp=[y(8+3*j);-y(8);-y(9)*sin(fae(j))];
    Dtcp(j)*sin(fae(j));Drcp(j)*cos(fae(j));
    sizeofMDcp=size(transMDcp);
    for i=1:1:sizeofMDcp(1)
        MDyep(i,j)=transMDcp(i);
    end
end
MDyep;

%%%%%%%%%%%%%%
% part ten
% number order every term of MDyepi
%%%%%%%%%%%%%%
for j=1:1:(cd*n+3*cd)
    y(j)=tt^(j+cd*n+3*cd+1); %define displacement
end
for j=1:1:n
    fae(j)=t^(j+cd*n+3*cd+1); %define symbol for angular
    position of each planet gear
end
syms force % selection sign for force terms
for j=1:1:n
    Dtcp(j)=force*tt^(j+n+cd*n+3*cd+1);
    Drcp(j)=force*tt^(j+n+cd*n+3*cd+1);
end
for j=1:1:n
    %@@@@@@@@@@@@@@@@@@@@@@@@@@@@@@@@@@@@@@@@
    ENTER MDyep vector
    transMDcp=[y(8+3*j);-y(8);-y(9)*sin(fae(j))];
    Dtcp(j)*sin(fae(j));Drcp(j)*cos(fae(j));
    sizeofMDcp=size(transMDcp);
    for i=1:1:sizeofMDcp(1)
        MDc(i,j)=transMDcp(i);
    end
end
Bc=diff(MDc,'t');
sizeBc=size(Bc);
sizeDc(1)=sizeBc(1);
sizeDc(2)=sizeBc(2);
for i=1:1:sizeBc(1)
    for j=1:1:sizeBc(2)
        Dc(i,j)=Bc(i,j);
    end
end
for i=1:1:sizeDc(1)
    for j=1:1:sizeDc(2)
        DDc=Dc(i,j);

Nuc=char(DDc);
sizeNuc=size(Nuc);
ii=0;iii=1;
if double(Nuc(1,1))==45
    ii=1;iii=2;
    for jj=2:1:sizeNuc(2)
        if double(Nuc(1,jj))<=57 &&
            double(Nuc(1,jj))>=48
                ii=ii+1;
            else break
            end
        end
    else
        for jj=1:1:sizeNuc(2)
            if double(Nuc(1,jj))<=57 &&
                double(Nuc(1,jj))>=48
                    ii=ii+1;
                else break
                end
            end
        end
    Nubc=0;
    for jj=iii:1:ii
        Nubc=Nubc+(double(Nuc(jj))-48)*10^(ii-jj);
    end
    DNuycl(i,j)=Nubc;
end
DNuycl;
%-----%
% DNuycl number original matrix, to tell terms in to two
different levels of
% matrices
% from DNuycl to DNuyc2
% DNuyc2 separates lower level matrix terms into expected
positions
%-----%
for j=1:1:(cd*n+3*cd)
    y(j)=tt^(j+1); %define displacement
end
for j=1:1:n
    fae(j)=t^(j+cd*n+3*cd+1); %define symbol for angular
    position of each planet gear
end
syms force % selection sign for force terms
for j=1:1:n
    Dtcp(j)=force*tt^(j+n+cd*n+3*cd+1);
    Drcp(j)=force*tt^(j+n+cd*n+3*cd+1);
end
for j=1:1:n
    %@@@@@@@@@@@@@@@@@@@@@@@@@@@@@@@@@@@@@@@@
    ENTER MDyep vector
    transMDcp=[y(8+3*j);-y(8);-y(9)*sin(fae(j))];
    Dtcp(j)*sin(fae(j));Drcp(j)*cos(fae(j));
    sizeofMDcp=size(transMDcp);
    for i=1:1:sizeofMDcp(1)
        MDc(i,j)=transMDcp(i);
    end
end
Bc=diff(MDc,'t');
sizeBc=size(Bc);
sizeDc(1)=sizeBc(1);
sizeDc(2)=sizeBc(2);
for i=1:1:sizeBc(1)
    for j=1:1:sizeBc(2)
        Dc(i,j)=Bc(i,j);
    end
end
for i=1:1:sizeDc(1)
    for j=1:1:sizeDc(2)
        DDc=Dc(i,j);

```



```

end
end
if row(1)==(2*cd+1)
for k=1:1:sizeofMDcp(1)
for kk=1:1:n
% solving DMDxcp
if DNuxc2(k,kk)==3*cd+1
Fmatrix(row(1),1)=Fmatrix(row(1),1)-
sym(streat('Cpx','*',y','(int2str(3*cd+3*cd+n*cd),'','sin'
','y','(int2str(3*cd),'','ipdata','(','9',')',+',','pi','-
','ipdata','(int2str(200+kk),'','y)'));
else if DNuxc2(k,kk)>=2 &&
DNuxc2(k,kk)<=(cd*n+3*cd+1)
C1matrix(row(1),(DNuxc2(k,kk)-
1))=DMDxcp(k,kk)*positioncp(1,2+(kk-
1)*sizegovernc(i))+C1matrix(row(1),(DNuxc2(k,kk)-1));
else if DNuxc2(k,kk)>=(n+cd*n+3*cd+2) &&
DNuxc2(k,kk)<=(2*n+cd*n+3*cd+1)
Fmatrix(row(1),1)=Fmatrix(row(1),1)-
DMDxcp(k,kk)*positioncp(1,2+(kk-1)*sizegovernc(i));
end
end
end
end
for k=1:1:sizeofMDcp(1)
for kk=1:1:n
% solving MDxcp
if DNuxc2(k,kk)==3*cd+1
Fmatrix(row(1),1)=Fmatrix(row(1),1)-
sym(streat('Kpx','*',(',-
','cos','(','y','(int2str(3*cd),'','ipdata','(','9',')',+',','pi','-
','ipdata','(int2str(200+kk),'','y)'),'','ipdata','(','9',')',+',','cos','(','pi'
','-',','ipdata','(int2str(200+kk),'','y)'),'','ipdata','(','9',')',+','));
else if DNuxc2(k,kk)>=2 &&
DNuxc2(k,kk)<=(cd*n+3*cd+1)
K1matrix(row(1),(DNuxc2(k,kk)-
1))=MDxcp(k,kk)*positioncp(1,3+(kk-
1)*sizegovernc(i))+K1matrix(row(1),(DNuxc2(k,kk)-1));
else if DNuxc2(k,kk)>=(n+cd*n+3*cd+2) &&
DNuxc2(k,kk)<=(2*n+cd*n+3*cd+1)
Fmatrix(row(1),1)=Fmatrix(row(1),1)-
MDxcp(k,kk)*positioncp(1,3+(kk-1)*sizegovernc(i));
end
end
end
end
Fmatrix(row(1),1)=Fmatrix(row(1),1)+positioncp(1,sizegovernc(i));
else if row(1)==(2*cd+2)
for k=1:1:sizeofMDcp(1)
for kk=1:1:n
% solving DMDycp
if DNuxc2(k,kk)==3*cd+1
Fmatrix(row(1),1)=Fmatrix(row(1),1)-
sym(streat('Cpy','*',y','(int2str(3*cd+3*cd+n*cd),'','cos'
','y','(int2str(3*cd),'','ipdata','(','9',')',+',','pi','-
','ipdata','(int2str(200+kk),'','y)'));
else if DNuxc2(k,kk)>=2 &&
DNuxc2(k,kk)<=(cd*n+3*cd+1)
C1matrix(row(1),(DNuxc2(k,kk)-
1))=DMDycp(k,kk)*positioncp(1,2+(kk-
1)*sizegovernc(i))+C1matrix(row(1),(DNuxc2(k,kk)-1));
else if DNuxc2(k,kk)>=(n+cd*n+3*cd+2) &&
DNuxc2(k,kk)<=(2*n+cd*n+3*cd+1)
Fmatrix(row(1),1)=Fmatrix(row(1),1)-
DMDycp(k,kk)*positioncp(1,2+(kk-1)*sizegovernc(i));
end
end
end
end
Fmatrix(row(1),1)=Fmatrix(row(1),1)+positioncp(1,sizegovernc(i));

```

```

end
end
end
end
for k=1:1:sizeofMDcp(1)
for kk=1:1:n
% solving MDycp
if DNuxc2(k,kk)==3*cd+1
Fmatrix(row(1),1)=Fmatrix(row(1),1)-
sym(streat('Kpy','*',('sin','(','y','(int2str(3*cd),'','ipdata','(
','9',')',+',','pi','-
','ipdata','(int2str(200+kk),'','y)'),'','ipdata','(','9',')',-
','sin','(','pi','-
','ipdata','(int2str(200+kk),'','y)'),'','ipdata','(','9',')',-
));
else if DNuxc2(k,kk)>=2 &&
DNuxc2(k,kk)<=(cd*n+3*cd+1)
K1matrix(row(1),(DNuxc2(k,kk)-
1))=MDycp(k,kk)*positioncp(1,3+(kk-
1)*sizegovernc(i))+K1matrix(row(1),(DNuxc2(k,kk)-1));
else if DNuxc2(k,kk)>=(n+cd*n+3*cd+2) &&
DNuxc2(k,kk)<=(2*n+cd*n+3*cd+1)
Fmatrix(row(1),1)=Fmatrix(row(1),1)-
MDycp(k,kk)*positioncp(1,3+(kk-1)*sizegovernc(i));
end
end
end
end
Fmatrix(row(1),1)=Fmatrix(row(1),1)+positioncp(1,sizegovernc(i));
else if row(1)==3*cd
for k=1:1:sizeofMDcp(1)
for kk=1:1:n
% solving DMDxcp
if DNuxc2(k,kk)==3*cd+1
Fmatrix(row(1),1)=Fmatrix(row(1),1)+sym(streat('Kpx*((y('i
nt2str(3*cd+cd*kk),'-y('int2str(2*cd),''))/rr*ipdata(9)-
y('int2str(cd*3),'))+Cpx*((y('int2str(3*cd+cd*kk+3*cd+n*c
d),'-y('int2str(2*cd+3*cd+n*cd),''))/rr*ipdata(9)-
y('int2str(3*cd+3*cd+n*cd),''))));
else if DNuxc2(k,kk)>=2 &&
DNuxc2(k,kk)<=(cd*n+3*cd+1)
C1matrix(row(1),(DNuxc2(k,kk)-
1))=C1matrix(row(1),(DNuxc2(k,kk)-1));
else if DNuxc2(k,kk)>=(n+cd*n+3*cd+2) &&
DNuxc2(k,kk)<=(2*n+cd*n+3*cd+1)
Fmatrix(row(1),1)=Fmatrix(row(1),1)-
DMDxcp(k,kk)*positioncp(1,2+(kk-1)*sizegovernc(i));
end
end
end
end
for k=1:1:sizeofMDcp(1)
for kk=1:1:n
% solving MDxcp
if DNuxc2(k,kk)==3*cd+1
Fmatrix(row(1),1)=Fmatrix(row(1),1)-0;
else if DNuxc2(k,kk)>=2 &&
DNuxc2(k,kk)<=(cd*n+3*cd+1)
K1matrix(row(1),(DNuxc2(k,kk)-
1))=K1matrix(row(1),(DNuxc2(k,kk)-1));
else if DNuxc2(k,kk)>=(n+cd*n+3*cd+2) &&
DNuxc2(k,kk)<=(2*n+cd*n+3*cd+1)
Fmatrix(row(1),1)=Fmatrix(row(1),1)-
MDxcp(k,kk)*positioncp(1,4+(kk-1)*sizegovernc(i));
end
end
end
end

```

```

end
end
end
for k=1:1:sizeofMDcp(1)
for kk=1:1:n
% solving DMDyep
if DNuxc2(k,kk)==3*cd+1
Fmatrix(row(1),1)=Fmatrix(row(1),1)-0;
else if DNuy2(k,kk)>=2 &&
DNuy2(k,kk)<=(cd*n+3*cd+1)
C1matrix(row(1),(DNuy2(k,kk)-
1))=C1matrix(row(1),(DNuy2(k,kk)-1));
else if DNuy2(k,kk)>=(n+cd*n+3*cd+2) &&
DNuy2(k,kk)<=(2*n+cd*n+3*cd+1)
Fmatrix(row(1),1)=Fmatrix(row(1),1)-
DMDyep(k,kk)*positioncp(1,3+(kk-1)*sizegovernc(i));
end
end
end
end
end
for k=1:1:sizeofMDcp(1)
for kk=1:1:n
% solving MDyep
if DNuxc2(k,kk)==3*cd+1
Fmatrix(row(1),1)=Fmatrix(row(1),1)-0;
else if DNuy2(k,kk)>=2 &&
DNuy2(k,kk)<=(cd*n+3*cd+1)
K1matrix(row(1),(DNuy2(k,kk)-
1))=K1matrix(row(1),(DNuy2(k,kk)-1));
else if DNuy2(k,kk)>=(n+cd*n+3*cd+2) &&
DNuy2(k,kk)<=(2*n+cd*n+3*cd+1)
Fmatrix(row(1),1)=Fmatrix(row(1),1)-
MDyep(k,kk)*positioncp(1,5+(kk-1)*sizegovernc(i));
end
end
end
end
end
Fmatrix(row(1),1)=Fmatrix(row(1),1)+positioncp(1,sizegovernc(i));
else if row(1)==(3*cd+1)
for rowi=1:1:n
roww=row(rowi);
for k=1:1:sizeofMDcp(1)
for kk=rowi:1:rowi
% solving DMDxcp
if DNuxc2(k,kk)==3*cd+1
Fmatrix(roww,1)=Fmatrix(roww,1)+sym(strcat('Cpx','*',y','(,
int2str(3*cd+3*cd+n*cd),')','*',('sin','(','y','(,int2str(3*cd),')','/
','ipdata','(','9',')','+','pi','-',','ipdata','(,int2str(200+kk),')',')'));
else if DNuxc2(k,kk)>=2 &&
DNuxc2(k,kk)<=(cd*n+3*cd+1)
C1matrix(roww,(DNuxc2(k,kk)-
1))=DMDxcp(k,kk)*positioncp(1,2+(kk-
1)*sizegovernc(i))+C1matrix(roww,(DNuxc2(k,kk)-1));
else if DNuxc2(k,kk)>=(n+cd*n+3*cd+2) &&
DNuxc2(k,kk)<=(2*n+cd*n+3*cd+1)
Fmatrix(roww,1)=Fmatrix(roww,1)-
DMDxcp(k,kk)*positioncp(1,2+(kk-1)*sizegovernc(i));
end
end
end
end
end
for k=1:1:sizeofMDcp(1)
for kk=rowi:1:rowi
% solving MDxcp

```

```

if DNuxc2(k,kk)==3*cd+1
Fmatrix(roww,1)=Fmatrix(roww,1)+sym(strcat('Kpx','*',(',-
','cos','(','y','(,int2str(3*cd),')','/','ipdata','(','9',')','+','pi','-',
','ipdata','(,int2str(200+kk),')',')','*',('9',')','+','cos','(','pi
','-',','ipdata','(,int2str(200+kk),')',')','*',('9',')',')'));
else if DNuxc2(k,kk)>=2 &&
DNuxc2(k,kk)<=(cd*n+3*cd+1)
K1matrix(roww,(DNuxc2(k,kk)-
1))=MDxcp(k,kk)*positioncp(1,3+(kk-
1)*sizegovernc(i))+K1matrix(roww,(DNuxc2(k,kk)-1));
else if DNuxc2(k,kk)>=(n+cd*n+3*cd+2) &&
DNuxc2(k,kk)<=(2*n+cd*n+3*cd+1)
Fmatrix(roww,1)=Fmatrix(roww,1)-
MDxcp(k,kk)*positioncp(1,3+(kk-1)*sizegovernc(i));
end
end
end
end
end
Fmatrix(roww,1)=Fmatrix(roww,1)+positioncp(1,sizegovernc(i));
else if row(1)==(3*cd+2)
for rowi=1:1:n
roww=row(rowi);
for k=1:1:sizeofMDcp(1)
for kk=rowi:1:rowi
% solving DMDyep
if DNuxc2(k,kk)==3*cd+1
Fmatrix(roww,1)=Fmatrix(roww,1)+sym(strcat('Cpy','*',y','(,
int2str(3*cd+3*cd+n*cd),')','*',('cos','(','y','(,int2str(3*cd),')','/
','ipdata','(','9',')','+','pi','-',','ipdata','(,int2str(200+kk),')',')'));
else if DNuy2(k,kk)>=2 &&
DNuy2(k,kk)<=(cd*n+3*cd+1)
C1matrix(roww,(DNuy2(k,kk)-
1))=DMDyep(k,kk)*positioncp(1,2+(kk-
1)*sizegovernc(i))+C1matrix(roww,(DNuy2(k,kk)-1));
else if
DNuy2(k,kk)>=(n+cd*n+3*cd+2) &&
DNuy2(k,kk)<=(2*n+cd*n+3*cd+1)
Fmatrix(roww,1)=Fmatrix(roww,1)-
DMDyep(k,kk)*positioncp(1,2+(kk-1)*sizegovernc(i));
end
end
end
end
end
for k=1:1:sizeofMDcp(1)
for kk=rowi:1:rowi
% solving MDyep
if DNuxc2(k,kk)==3*cd+1
Fmatrix(roww,1)=Fmatrix(roww,1)+sym(strcat('Kpy','*',('si
n','(','y','(,int2str(3*cd),')','/','ipdata','(','9',')','+','pi','-',
','ipdata','(,int2str(200+kk),')',')','*',('9',')','+','pi','-',
','sin','(','pi','-',
','ipdata','(,int2str(200+kk),')',')','*',('9',')',')'));
else if DNuy2(k,kk)>=2 &&
DNuy2(k,kk)<=(cd*n+3*cd+1)
K1matrix(roww,(DNuy2(k,kk)-
1))=MDyep(k,kk)*positioncp(1,3+(kk-
1)*sizegovernc(i))+K1matrix(roww,(DNuy2(k,kk)-1));
else if
DNuy2(k,kk)>=(n+cd*n+3*cd+2) &&
DNuy2(k,kk)<=(2*n+cd*n+3*cd+1)

```

```

Fmatrix(roww,1)=Fmatrix(roww,1)-
MDyep(k,kk)*positioncp(1,3+(kk-1)*sizegovernc(i));
    end
    end
    end
    end
    end

Fmatrix(roww,1)=Fmatrix(roww,1)+positioncp(1,sizegovernc
(i));
    end
    end
    end
    end
    end
end
row=[0,0,0];
roww=0;
rowi=0;

%%%%%%%%%%%%%%%%%%%%%%%%%%%%%%%%%%%%%%%%%%%%%%%%%%%%%%%%%%%%%%%%%%%%%%%%
% Mass matrix
%%%%%%%%%%%%%%%%%%%%%%%%%%%%%%%%%%%%%%%%%%%%%%%%%%%%%%%%%%%%%%%%%%%%%%%%

mass(1)=sym(strcat('mass','1','1',''));
mass(2)=sym(strcat('mass','1','2',''));
mass(3)=sym(strcat('mass','1','3',''));
mass(4)=sym(strcat('mass','1','4',''));
mass(5)=sym(strcat('mass','1','5',''));
mass(6)=sym(strcat('mass','1','6',''));
mass(7)=sym(strcat('mass','1','7',''));
mass(8)=sym(strcat('mass','1','8',''));
mass(9)=sym(strcat('mass','1','9',''));
for i=1:1:ipdata(7)
    mass(9+1+(i-1)*3)=sym(strcat('mass','1','10',''));
    mass(9+2+(i-1)*3)=sym(strcat('mass','1','11',''));
    mass(9+3+(i-1)*3)=sym(strcat('mass','1','12',''));
end

if ipdata(51)==1
    for i=1:1:(3*ipdata(51)+ipdata(7)*ipdata(51))
        M(i,i)=mass(i*(4-ipdata(51)));
    end
else if ipdata(51)==3
    for i=1:1:(3*ipdata(51)+ipdata(7)*ipdata(51))
        M(i,i)=mass(i*(4-ipdata(51)));
    end
else if ipdata(51)==2
    for i=1:1:(3*ipdata(51)+ipdata(7)*ipdata(51))
        M(i,i)=mass(i-1+int8(i/2));
    end
end
end
end

%%%%%%%%%%%%%%%%%%%%%%%%%%%%%%%%%%%%%%%%%%%%%%%%%%%%%%%%%%%%%%%%%%%%%%%%
% OUT put
%%%%%%%%%%%%%%%%%%%%%%%%%%%%%%%%%%%%%%%%%%%%%%%%%%%%%%%%%%%%%%%%%%%%%%%%
%M
%C1matrix
%C2matrix
%K1matrix
%K2matrix
%Fmatrix
%size(C1matrix)
%size(C2matrix)
%size(K1matrix)

```

```

%size(K2matrix)
%size(Fmatrix)
%%%%%%%%%%%%%%%%%%%%%%%%%%%%%%%%%%%%%%%%%%%%%%%%%%%%%%%%%%%%%%%%%%%%%%%%
% dydt
%%%%%%%%%%%%%%%%%%%%%%%%%%%%%%%%%%%%%%%%%%%%%%%%%%%%%%%%%%%%%%%%%%%%%%%%
if ipdata(51)==1
    for i=1:1:(3*ipdata(51))
        cs(i,i)=sym(strcat('ipdata','1',int2str(100+i*(4-
ipdata(51))),','));
    end
else if ipdata(51)==3
    for i=1:1:(3*ipdata(51))
        cs(i,i)=sym(strcat('ipdata','1',int2str(100+i*(4-
ipdata(51))),','));
    end
else if ipdata(51)==2
    for i=1:1:(3*ipdata(51))
        cs(i,i)=sym(strcat('ipdata','1',int2str(100+i-
1+int8(i/2)),','));
    end
end
end
end
for i=(3*ipdata(51)+1):1:(3*ipdata(51)+ipdata(7)*ipdata(51))
    for j=1:1:(3*ipdata(51))
        cs(i,j)=0;
        cs(j,i)=0;
    end
end
end
for i=(3*ipdata(51)+1):1:(3*ipdata(51)+ipdata(7)*ipdata(51))
    for
j=(3*ipdata(51)+1):1:(3*ipdata(51)+ipdata(7)*ipdata(51))
        cs(i,j)=0;
    end
end
end
C=C1matrix+cs;

if ipdata(51)==1
    for i=1:1:(3*ipdata(51))
        ks(i,i)=sym(strcat('ipdata','1',int2str(110+i*(4-
ipdata(51))),','));
    end
else if ipdata(51)==3
    for i=1:1:(3*ipdata(51))
        ks(i,i)=sym(strcat('ipdata','1',int2str(110+i*(4-
ipdata(51))),','));
    end
else if ipdata(51)==2
    for i=1:1:(3*ipdata(51))
        ks(i,i)=sym(strcat('ipdata','1',int2str(110+i-
1+int8(i/2)),','));
    end
end
end
end
end
for i=(3*ipdata(51)+1):1:(3*ipdata(51)+ipdata(7)*ipdata(51))
    for j=1:1:(3*ipdata(51))
        ks(i,j)=0;
        ks(j,i)=0;
    end
end
end

for i=(3*ipdata(51)+1):1:(3*ipdata(51)+ipdata(7)*ipdata(51))
    for
j=(3*ipdata(51)+1):1:(3*ipdata(51)+ipdata(7)*ipdata(51))
        ks(i,j)=0;
    end
end
end

```



```

K=KImatrix+ks;
velo=velocityvector(n,cd,eps);
disp=displacementvector(n,cd,eps);

DYDT=inv(M)*(Fmatrix-C*velo-K*disp);
for i=1:(3*ipdata(51)+ipdata(51)*ipdata(7))
    dydt(i,1)=velo(i,1);
end
for i=1:(3*ipdata(51)+ipdata(51)*ipdata(7))
    dydt(i+(3*ipdata(51)+ipdata(51)*ipdata(7)),1)=DYDT(i,1);
end

for j=(cd*n+3*cd)*2+1:(cd*n+3*cd)*2+1
    y(j)=sym(strcat('y','(',int2str(j),')'));
    dydt(j,1)=(1/sym(strcat('l','m')))*(sym(strcat('TorqueM','(',y','(',int2str(j),')')-
    sym(strcat('q','e','e'))*sym(strcat('y','(',int2str(j),')'))*(y(j)-
    sym(strcat('y','(',int2str(cd*n+3*cd+cd),')'))*sym(strcat('ipdata','(',35,')'))/sym(strcat('r','s'))));
end

dydt
end

```

13.1.5. erppp.m & esppp.m

```

function erppp=erppp(ttt)
%% Program erppp.m is developed to generate planet gear pitch error for ring-planet pairs. Same pitch error pattern is applied to all
planet gears with a start at the defined first tooth respectively.
erppp=-0.0015*sin(ttt*360/180*pi)+0.001*sin(2*ttt*360/180*pi)+0.002*sin(3*ttt*360/180*pi);

```

13.1.6. erppr.m

```

function erppr=erppr(ttt)
%% Program erppr.m is developed to generate ring gear pitch error for ring-planet pairs.
erppr=-0.0015*sin(ttt*360/180*pi)+0.002*sin(2*ttt*360/180*pi)-0.0015*sin(3*ttt*360/180*pi);

```

13.1.7. espps.m

```

function espps=espps(ttt)
%% Program espps.m is developed to generate sun gear pitch error for sun-planet pairs.
espps=-0.002*sin(ttt*360/180*pi)+0.0015*sin(2*ttt*360/180*pi)-0.001*sin(3*ttt*360/180*pi);

```

13.1.8. espp.m

```

function espp=espp(tt,PBEs)
%% Program espp.m is developed to generate assumed sun-planet profile error over the time of mesh for one pair of teeth.
if tt>=0 && tt<=PBEs
    espp=0.001*sin(tt/PBEs*360/180*pi)+0.0015*sin(2*tt/PBEs*360/180*pi)+0.002*sin(3*tt/PBEs*360/180*pi);
else
    if tt-1>=0 && tt-1<=PBEs
        tt=tt-1;
        espp=0.001*sin(tt/PBEs*360/180*pi)+0.0015*sin(2*tt/PBEs*360/180*pi)+0.002*sin(3*tt/PBEs*360/180*pi);
    else
        if tt-2>=0 && tt-2<=PBEs
            tt=tt-2;
            espp=0.001*sin(tt/PBEs*360/180*pi)+0.0015*sin(2*tt/PBEs*360/180*pi)+0.002*sin(3*tt/PBEs*360/180*pi);
        else
            if tt-3>=0 && tt-3<=PBEs
                tt=tt-3;
                espp=0.001*sin(tt/PBEs*360/180*pi)+0.0015*sin(2*tt/PBEs*360/180*pi)+0.002*sin(3*tt/PBEs*360/180*pi);
            else
                if tt-4>=0 && tt-4<=PBEs
                    tt=tt-4;
                    espp=0.001*sin(tt/PBEs*360/180*pi)+0.0015*sin(2*tt/PBEs*360/180*pi)+0.002*sin(3*tt/PBEs*360/180*pi);
                else
                    end
                end
            end
        end
    end
end
end
end
end

```

13.1.9. erpp.m

```

function erpp=erpp(tt,PBEr)
%% Program erpp.m is developed to generate assumed ring-planet profile error over the time of mesh for one pair of teeth.
if tt>=0 && tt<=PBEr
    erpp=-0.001*sin(tt/PBEr*360/180*pi)+0.0015*sin(2*tt/PBEr*360/180*pi)-0.002*sin(3*tt/PBEr*360/180*pi);
else
end
end
end
end

```

```

if tt-1>=0 && tt-1<=PBEr
    tt=tt-1;
    erpp=-
0.001*sin(tt/PBEr*360/180*pi)+0.0015*sin(2*tt/PBEr*360/1
80*pi)-0.002*sin(3*tt/PBEr*360/180*pi);
else
    if tt-2>=0 && tt-2<=PBEr
        tt=tt-2;
        erpp=-
0.001*sin(tt/PBEr*360/180*pi)+0.0015*sin(2*tt/PBEr*360/1
80*pi)-0.002*sin(3*tt/PBEr*360/180*pi);

    else
        if tt-3>=0 && tt-3<=PBEr
            tt=tt-3;

```

```

        erpp=-
0.001*sin(tt/PBEr*360/180*pi)+0.0015*sin(2*tt/PBEr*360/1
80*pi)-0.002*sin(3*tt/PBEr*360/180*pi);
    else
        if tt-4>=0 && tt-4<=PBEr
            tt=tt-4;
            erpp=-
0.001*sin(tt/PBEr*360/180*pi)+0.0015*sin(2*tt/PBEr*360/1
80*pi)-0.002*sin(3*tt/PBEr*360/180*pi);
        else
            end
        end
    end
end
end
end

```

13.1.10. esprran.m

```

function esprran=esprran(xx)
%% Program esprran.m is developed to generate random
excitation due to tooth profile error for sun-planet pairs.
esprran=randint(1,1,[-400 100])/100000;
if esprran>=0

```

```

    esprran=esprran;
else
    esprran=0;
end
esprran;

```

13.1.11. erppran.m

```

function erppran=erppran(xx)
%% Program erppran.m is developed to generate random
excitation due to tooth profile error for ring-planet pairs.
erppran=randint(1,1,[-400 100])/100000;
if erppran>=0

```

```

    erppran=erppran;
else
    erppran=0;
end
erppran;

```

13.1.12. Ymr1.m / Ymr2.m / Ymr3.m

```

function Ymr1=Ymr1(Xmr)
%% Program package (including ymr1.m, ymr2.m, ymr3.m,
ymrr.m, yms1.m,
%% yms2.m, yms3.m, and ymss.m) is developed to determine
number of teeth in mesh based on time of meshing for all
ring-planet and sun-planet pairs.
%% change line 123 the 'i'
of rrm(i)

%% calculation for rrs
%% input data

zs=ipdata(1);

zp=ipdata(2);
zr=ipdata(3);
as=ipdata(4);
ar=ipdata(5);

module=ipdata(6);
nofp=ipdata(7);

for i=1:1:ipdata(7)
    apofps(i)=pi-ipdata(200+i); %angular position of planet
spacing i
end

%%
ds=zs*module;
dp=zp*module;
dr=zr*module;

```

```

ha=module;
hf=1.25*module;
h=ha+hf;
dsa=ds+2*ha;
dpa=dp+2*ha;
dra=dr+2*ha;
dsf=ds-2*hf;
dpf=dp-2*hf;
drf=dr-2*hf;
dsb=ds*cos(as/180*pi);
dpb=dp*cos(as/180*pi);
drb=dr*cos(ar/180*pi);
Rsa=dsa/2;
Rpa=dpa/2;
Rra=drf/2;
Rsb=dsb/2;
Rpb=dpb/2;
Rrb=drb/2;

%%for sun-planet mesh
MsEs=sqrt(Rsa^2-Rsb^2);
BsNs=sqrt(Rpa^2-Rpb^2);
MsNs=(Rsb+Rpb)*tan(as/180*pi);
BsEs=MsEs+BsNs-MsNs;
MsPs=Rsb*tan(as/180*pi);
MsBs=MsEs-BsEs;
BsPs=MsPs-MsBs;
%pb=2*pi*Rsb/zs;
pb=pi*module*cos(as/180*pi);
BsCs=BsEs-pb;
BsDs=pb;

%%for ring-planet mesh

```

```

MrNr=module/2*(zs+zp)*sin(ar/180*pi);
NrEr=sqrt(Rpa^2-Rpb^2);
MrBr=sqrt(Rra^2-Rrb^2);
BrEr=MrNr+NrEr-MrBr;
MrPr=Rrb*tan(ar/180*pi);
BrPr=MrPr-MrBr;
BrCr=BrEr-pb;
BrDr=pb;

% rrs
PsPr=Rpb*tan(as/180*pi)+Rpb*(pi-as/180*pi-
ar/180*pi)+Rpb*tan(ar/180*pi);
tb=module*(pi/2+2*inv(as));
Q2Br=PsPr-BrPr-tb;
dec1=Q2Br/pb;
dec2=int32(Q2Br/pb);
dec3=dec1-dec2;
if dec3>=0
    dec=dec2;
else dec=dec2-1;
end
BrQ3=pb-pb*(double(dec1)-double(dec));
PrQ3=BrQ3-BrPr;
if PrQ3>=0
    PrQ3=PrQ3;
else PrQ3=-PrQ3;
end
rrs=PrQ3/pb;
if rrs>=0
    rrs=rrs;
else rrs=-rrs;
end
if BrQ3-BrPr<=0
    rrs=rrs;
else rrs=-rrs;
end

PBEs=BsEs/pb;
PBPs=BsPs/pb;
PBCs=BsCs/pb;
PBDs=BsDs/pb;

BrEr;
BrPr;
BrCr;
BrDr;

PBEr=BrEr/pb;
PBPr=BrPr/pb;
PBCr=BrCr/pb;
PBDr=BrDr/pb;

rrs;

%% calculation of spacing difference between ring-planet
meshes
for i=1:1:nofp
    rrn(i)=zr*ipdata(200+i)/pi;
    rrmn=double(int64(rrn(i)));
    if rrmn>rrn(i)
        rrmn=rrmn-1;
    else
        rrmn=rrmn;
    end
    rrn(i)=rrn(i)-rrmn;
end

Xmr=Xmr+(PBPr-PBDr)-rrn(1)-rrs;
xx=double(int64(Xmr));
if xx<=Xmr;
    xx=xx;
else xx=xx-1;
end
tt=Xmr-xx;
Ymr1=0;
for i=1:(double(int8(PBEr))+2)
    ymrrr(i)=ymrr(tt+i-1,PBEr);
    Ymr1=Ymr1+ymrrr(i);
end
Ymr1=Ymr1;

```

13.1.13. Yms1.m / Yms2.m / Yms3.m

```

function Yms1=Yms1(Xms)

%% Program package (including ymr1.m, ymr2.m, ymr3.m,
ymrr.m, yms1.m,
%% yms2.m, yms3.m, and ymss.m) is developed to determine
number of teeth in mesh based on time of meshing for all
ring-planet and sun-planet pairs.
%% change line 123 the 'i'
of rsn(i)

%% calculation for rrs

%% input data
zs=ipdata(1);
zp=ipdata(2);
zr=ipdata(3);
as=ipdata(4);
ar=ipdata(5);
module=ipdata(6);
nofp=ipdata(7);

for i=1:1:ipdata(7)
    apofps(i)=pi-ipdata(200+i); %angular position of planet
spacing i
end

ds=zs*module;
dp=zp*module;
dr=zr*module;
ha=module;
hf=1.25*module;
h=ha+hf;
dsa=ds+2*ha;
dpa=dp+2*ha;
dra=dr+2*ha;
dsf=ds-2*hf;
dpf=dp-2*hf;
drf=dr-2*hf;
dsb=ds*cos(as/180*pi);
dpb=dp*cos(as/180*pi);
drb=dr*cos(ar/180*pi);
Rsa=dsa/2;
Rpa=dpa/2;
Rra=drf/2;
Rsb=dsb/2;
Rpb=dpb/2;
Rrb=drb/2;

```

```

%%for sun-planet mesh
MsEs=sqrt(Rsa^2-Rsb^2);
BsNs=sqrt(Rpa^2-Rpb^2);
MsNs=(Rsb+Rpb)*tan(as/180*pi);
BsEs=MsEs+BsNs-MsNs;
MsPs=Rsb*tan(as/180*pi);
MsBs=MsEs-BsEs;
BsPs=MsPs-MsBs;
%pb=2*pi*Rsb/zs;
pb=pi*module*cos(as/180*pi);
BsCs=BsEs-pb;
BsDs=pb;

%%for ring-planet mesh
MrNr=module/2*(zs+zp)*sin(ar/180*pi);
NrEr=sqrt(Rpa^2-Rpb^2);
MrBr=sqrt(Rra^2-Rrb^2);
BrEr=MrNr+NrEr-MrBr;
MrPr=Rrb*tan(ar/180*pi);
BrPr=MrPr-MrBr;
BrCr=BrEr-pb;
BrDr=pb;

% rrs
PsPr=Rpb*tan(as/180*pi)+Rpb*(pi-as/180*pi-
ar/180*pi)+Rpb*tan(ar/180*pi);
tb=module*(pi/2+2*inv(as));
Q2Br=PsPr-BrPr-tb;
dec1=Q2Br/pb;
dec2=int32(Q2Br/pb);
dec3=dec1-dec2;
if dec3>=0
    dec=dec2;
else dec=dec2-1;
end
BrQ3=pb-pb*(double(dec1)-double(dec));
PrQ3=BrQ3-BrPr;
if PrQ3>=0
    PrQ3=PrQ3;
else PrQ3=-PrQ3;
end
rrs=PrQ3/pb;
if rrs>=0
    rrs=rrs;
else rrs=-rrs;
end
if BrQ3-BrPr<=0
    rrs=rrs;
else rrs=-rrs;

end

PBEs=BsEs/pb;
PBPs=BsPs/pb;
PBCs=BsCs/pb;
PBDs=BsDs/pb;

BrEr;
BrPr;
BrCr;
BrDr;

PBEr=BrEr/pb;
PBPr=BrPr/pb;
PBCr=BrCr/pb;
PBDr=BrDr/pb;

rrs;

%%calculation of spacing difference between sun-planet
meshes
for i=1:1:nofp
    rsn(i)=zs*ipdata(200+i)/2/pi;
    rsnn=double(int64(rsn(i)));
    if rsnn>rsn(i)
        rsnn=rsnn-1;
    else
        rsnn=rsnn;
    end
    rsn(i)=rsn(i)-rsnn;
end
rsn=-rsn;

Xms=Xms+(PBPs-PBDs);
xx=double(int64(Xms));
if xx<=Xms;
    xx=xx;
else xx=xx-1;
end
tt=Xms-xx;
Yms1=0;
for i=1:(double(int8(PBEs))+2)
    ymsss(i)=ymss(tt+i-1,PBEs);
    Yms1=Yms1+ymsss(i);
end
Yms1=Yms1;

function ymr=ymrr(tt,PBEr)
%% Program package (including ymr1.m, ymr2.m, ymr3.m,
ymrr.m, yms1.m,

%% yms2.m, yms3.m, and ymss.m) is developed to determine
number of teeth in mesh based on time of meshing for all
ring-planet and sun-planet pairs.

if tt>=0 && tt<=PBEr
    ymr=1;
else
    ymr=0;
end

function yms=ymss(tt,PBEs)
%% Program package (including ymr1.m, ymr2.m, ymr3.m,
ymrr.m, yms1.m,

%% yms2.m, yms3.m, and ymss.m) is developed to determine
number of teeth in mesh based on time of meshing for all
ring-planet and sun-planet pairs.

```

13.1.14. ymrr.m

```

function ymr=ymrr(tt,PBEr)
%% Program package (including ymr1.m, ymr2.m, ymr3.m,
ymrr.m, yms1.m,

%% yms2.m, yms3.m, and ymss.m) is developed to determine
number of teeth in mesh based on time of meshing for all
ring-planet and sun-planet pairs.

if tt>=0 && tt<=PBEr
    ymr=1;
else
    ymr=0;
end

```

13.1.15. ymss.m

```

function yms=ymss(tt,PBEs)
%% Program package (including ymr1.m, ymr2.m, ymr3.m,
ymrr.m, yms1.m,

%% yms2.m, yms3.m, and ymss.m) is developed to determine
number of teeth in mesh based on time of meshing for all
ring-planet and sun-planet pairs.

```

```

if tt>=0 && tt<=PBEs
    yms=1;
else

```

```

    yms=0;
end

```

13.1.16. erp1.m / erp2.m / erp3.m

```

function erp1=erp1(Xmr)
%% Program package (including erp1.m, erp2.m, erp3.m,
esp1.m, esp2.m, and
%% esp3.m) is developed to generate the combined excitation
due to pitch error, profile error and random features.
%%%%%%%%%%%%%%%%%%%%%%%%%%%%%%%%%%%%%%%%%%%%%%%%%%%%%%%%%%%%%%%%%%%%%%%% change line 123 the 'i'
of rrm(i)

```

```

%% calculation for rrs

```

```

%% input data

```

```

zs=ipdata(1);
zp=ipdata(2);
zr=ipdata(3);
as=ipdata(4);
ar=ipdata(5);
module=ipdata(6);
nofp=ipdata(7);

```

```

for i=1:1:ipdata(7)

```

```

    apofps(i)=ipdata(200+i); %angular position of planet
spacing i
end

```

```

%%%%%%%%%%%%%%%%%%%%%%%%%%%%%%%%%%%%%%%%%%%%%%%%%%%%%%%%%%%%%%%%%%%%%%%%

```

```

ds=zs*module;
dp=zp*module;
dr=zr*module;
ha=module;
hf=1.25*module;
h=ha+hf;
dsa=ds+2*ha;
dpa=dp+2*ha;
dra=dr+2*ha;
dsf=ds-2*hf;
dpf=dp-2*hf;
drf=dr-2*hf;
dsb=ds*cos(as/180*pi);
dpb=dp*cos(as/180*pi);
drb=dr*cos(ar/180*pi);
Rsa=dsa/2;
Rpa=dpa/2;
Rra=drf/2;
Rsb=dsb/2;

```

```

Rpb=dpb/2;
Rrb=drb/2;

```

```

%%for sun-planet mesh

```

```

MsEs=sqrt(Rsa^2-Rsb^2);
BsNs=sqrt(Rpa^2-Rpb^2);

```

```

MsNs=(Rsb+Rpb)*tan(as/180*pi);
BsEs=MsEs+BsNs-MsNs;
MsPs=Rsb*tan(as/180*pi);
MsBs=MsEs-BsEs;
BsPs=MsPs-MsBs;
%pb=2*pi*Rsb/zs;
pb=pi*module*cos(as/180*pi);
BsCs=BsEs-pb;
BsDs=pb;

```

```

%%for ring-planet mesh

```

```

MrNr=module/2*(zs+zp)*sin(ar/180*pi);
NrEr=sqrt(Rpa^2-Rpb^2);
MrBr=sqrt(Rra^2-Rrb^2);
BrEr=MrNr+NrEr-MrBr;
MrPr=Rrb*tan(ar/180*pi);
BrPr=MrPr-MrBr;
BrCr=BrEr-pb;
BrDr=pb;

```

```

% rrs

```

```

PsPr=Rpb*tan(as/180*pi)+Rpb*(pi-as/180*pi-
ar/180*pi)+Rpb*tan(ar/180*pi);
tb=module*(pi/2+2*inv(as));
Q2Br=PsPr-BrPr-tb;
dec1=Q2Br/pb;
dec2=int32(Q2Br/pb);
dec3=dec1-dec2;
if dec3>=0
    dec=dec2;
else dec=dec2-1;
end

```

```

BrQ3=pb-pb*(double(dec1)-double(dec));

```

```

PrQ3=BrQ3-BrPr;

```

```

if PrQ3>=0

```

```

    PrQ3=PrQ3;

```

```

else PrQ3=-PrQ3;

```

```

end

```

```

rrs=PrQ3/pb;

```

```

if rrs>=0

```

```

    rrs=rrs;

```

```

else rrs=-rrs;

```

```

end

```

```

if BrQ3-BrPr<=0

```

```

    rrs=rrs;

```

```

else rrs=-rrs;

```

```

end

```

```

PBEs=BsEs/pb;

```

```

PBPs=BsPs/pb;

```

```

PBCs=BsCs/pb;

```

```

PBDs=BsDs/pb;

```

```

BrEr;

```

```

BrPr;

```

```

BrCr;

```

```

BrDr;

```

```

PBEr=BrEr/pb;

```

```

PBPr=BrPr/pb;

```

```

PBCr=BrCr/pb;

```

```

PBDr=BrDr/pb;

```

```

rrs;

```

```

%%calculation of spacing difference between ring-planet
meshes

```

```

for i=1:1:nofp

```

```

    rrm(i)=zr*apofps(i)/2/pi;

```

```

    rrnn=double(int64(rrm(i)));

```

```

    if rrnn>rrm(i)

```

```

        rrnn=rrnn-1;

```

```

    else

```

```

        rrnn=rrnn;

```

```

    end

```



```

tb=module*(pi/2+2*inv(as));
Q2Br=PsPr-BrPr-tb;
dec1=Q2Br/pb;
dec2=int32(Q2Br/pb);
dec3=dec1-dec2;
if dec3>=0
    dec=dec2;
else dec=dec2-1;
end
BrQ3=pb-pb*(double(dec1)-double(dec));
PrQ3=BrQ3-BrPr;
if PrQ3>=0
    PrQ3=PrQ3;
else PrQ3=-PrQ3;
end
rrs=PrQ3/pb;
if rrs>=0
    rrs=rrs;
else rrs=-rrs;
end
if BrQ3-BrPr<=0
    rrs=rrs;
else rrs=-rrs;
end

PBEs=BsEs/pb;
PBPBs=BsPs/pb;
PBCs=BsCs/pb;
PBDs=BsDs/pb;

BrEr;
BrPr;
BrCr;
BrDr;

PBEr=BrEr/pb;
PBPr=BrPr/pb;
PBCr=BrCr/pb;
PBDr=BrDr/pb;

rrs;
%%calculation of spacing difference between sun-planet
meshes
for i=1:nofp
    rsn(i)=zs*apofps(i)/pi;
    rsnn=double(int64(rsn(i)));
    if rsnn>rsn(i)
        rsnn=rsnn-1;
    else
        rsnn=rsnn;
    end
    rsn(i)=rsn(i)-rsnn;
end

ems=ems1(Xms);Xms=Xms+(PBPBs-PBDs)-rsn(1);
xx=double(int64(Xms));
if xx<=Xms;
    xx=xx;
else xx=xx-1;
end
tt=Xms-xx;

%%profile error
Yms1=0;
for i=1:(double(int8(PBEs))+2)
    ymsss(i)=espp(tt+i-1,PBEs);
    %Yms1=Yms1+ymsss(i);
end
Yms1=Yms1;
YMSSS=-1000;
for i=1:(double(int8(PBEs))+2)
    if YMSSS>=ymsss(i)
        YMSSS=YMSSS;
    else YMSSS=ymsss(i);
    end
end

%%random profile error
ymssr=esppran(tt);

%%pitch error of sun
Xmssun=Xms/zs;
xxx=double(int64(Xmssun));
if xxx<=Xmssun;
    xxx=xxx;
else xxx=xxx-1;
end
ttx=Xmssun-xxx;
ymssun=espps(ttx);

%%pitch error of planet
Xmspla=Xms/zp;
xxxx=double(int64(Xmspla));
if xxxx<=Xmspla;
    xxxx=xxxx;
else xxxx=xxxx-1;
end
tttt=Xmspla-xxxx;
ymspla=esppp(tttt);

%esp1=YMSSS+ymssr+ymssun+ymspla;
esp1=YMSSS-ems*1000+ymsun+ymspla;
esp1=esp1/1000;

```

13.1.18. Kmr1.m / Kmr2.m / Kmr3.m

```

function Kmr1=Kmr1(Xmr)

ar=ipdata(5); %% pressure angle of ring-planet
module=ipdata(6); %% module
nofp=ipdata(7); %% number of planet gears

%%change the value for
the number of planet
Nofplanet=1;

%% calculation for rrs
%% input data
zs=ipdata(1); %% tooth number of sun gear
zp=ipdata(2); %% tooth number of planet gear
zr=ipdata(3); %% tooth number of ring gear
as=ipdata(4); %% pressure angle of sun-planet

for i=1:ipdata(7)
    apofps(i)=pi-ipdata(200+i); %angular position of planet
    spacing i
end

%%input data
ds=zs*module;
dp=zp*module;

```

```

dr=zr*module;
ha=module;
hf=1.25*module;
h=ha+hf;
dsa=ds+2*ha;
dpa=dp+2*ha;
dra=dr+2*ha;
dsf=ds-2*hf;
dpf=dp-2*hf;
drf=dr-2*hf;
dsb=ds*cos(as/180*pi);
dpb=dp*cos(as/180*pi);
drb=dr*cos(ar/180*pi);
Rsa=dsa/2;
Rpa=dpa/2;
Rra=drf/2;
Rsb=dsb/2;
Rpb=dpb/2;
Rrb=drb/2;

%%for sun-planet mesh
MsEs=sqrt(Rsa^2-Rsb^2);
BsNs=sqrt(Rpa^2-Rpb^2);
MsNs=(Rsb+Rpb)*tan(as/180*pi);
BsEs=MsEs+BsNs-MsNs;
MsPs=Rsb*tan(as/180*pi);
MsBs=MsEs-BsEs;
BsPs=MsPs-MsBs;
%opb=2*pi*Rsb/zs;
pb=pi*module*cos(as/180*pi);
BsCs=BsEs-pb;
BsDs=pb;

%%for ring-planet mesh
MrNr=module/2*(zs+zp)*sin(ar/180*pi);
NrEr=sqrt(Rpa^2-Rpb^2);
MrBr=sqrt(Rra^2-Rrb^2);
BrEr=MrNr+NrEr-MrBr;
MrPr=Rrb*tan(ar/180*pi);
BrPr=MrPr-MrBr;
BrCr=BrEr-pb;

BrDr=pb;

% rrs
PsPr=Rpb*tan(as/180*pi)+Rpb*(pi-as/180*pi-
ar/180*pi)+Rpb*tan(ar/180*pi);
tb=module*(pi/2+2*inv(as));
Q2Br=PsPr-BrPr-tb;
dec1=Q2Br/pb;
dec2=int32(Q2Br/pb);
dec3=dec1-dec2;
if dec3>=0
    dec=dec2;
else dec=dec2-1;
end
BrQ3=pb-pb*(double(dec1)-double(dec));
PrQ3=BrQ3-BrPr;
if PrQ3>=0
    PrQ3=PrQ3;
else PrQ3=-PrQ3;
end
rrs=PrQ3/pb;
if rrs>=0
    rrs=rrs;
else rrs=-rrs;
end
if BrQ3-BrPr<=0
    rrs=rrs;
else rrs=-rrs;
end

end

PBEs=BsEs/pb;
PBPs=BsPs/pb;
PBCs=BsCs/pb;
PBDs=BsDs/pb;

BrEr;
BrPr;
BrCr;
BrDr;

PBEr=BrEr/pb;
PBPr=BrPr/pb;
PBCr=BrCr/pb;
PBDr=BrDr/pb;

rrs;

%%calculation of spacing difference between ring-planet
meshes
for i=1:1:nofp
    rrn(i)=zr*ipdata(200+i)/2/pi;
    rrmn=double(int64(rrn(i)));
    if rrmn>rrn(i)
        rrmn=rrmn-1;
    else
        rrmn=rrmn;
    end
    rrn(i)=rrn(i)-rrmn;
end

Xmr=Xmr+(PBPr-PBDr)-rrn(Nofplanet)-rrs;
xx=double(int64(Xmr));
if xx<=Xmr;
    xx=xx;
else xx=xx-1;
end
tt=Xmr-xx;
Ymr=0;
for i=1:(double(int8(PBEr))+2)
    ymrrr(i)=ymrrr(tt+i-1,PBEr);
    Ymr=Ymr+ymrrr(i);
end
Ymr=Ymr;

for i=1:1:Ymr
    xxx=xx+i-Ymr+ipdata(2);
    xxP=xxx/ipdata(2);
    xxPP=double(int64(xxxP));
    if xxPP<=xxP
        xxPP=xxPP;
    else xxPP=xxPP-1;
    end
    NumofP(i)=Nofplanet*100+xxx-xxPP*ipdata(2)+1;
end
for i=1:1:Ymr
    xxxx=xx+rrn(Nofplanet)+i-
Ymr+ipdata(3)+(2*pi+apofps(Nofplanet)+apofps(1))/2/pi*ipd
ata(3)+1;
    xxx=double(int64(xxxx));
    if xxxx<=xxxx
        xxx=xxxx;
    else xxx=xxxx-1;
    end
    xxR=xxx/ipdata(3);

    xxRR=double(int64(xxR));
    if xxRR<=xxR
        xxRR=xxRR;

```



```

else xxRR=xxRR-1;
end

NumofR(i)=xxx-xxRR*ipdata(3)+1;
end

fract=Xmr+10;
fractt=double(int64(fract));
if fractt<=fract
    fract=fractt;
else fractt=fractt-1;
end

```

```

frac=fract-fractt;
if frac<(PBCr-PBDr)
    fra=frac/(PBCr-PBDr);
else fra=(frac-(PBCr-PBDr))/(2*PBDr-PBCr);
end
for i=1:1:Ymr
    posit(i)=(fract-fractt+(Ymr-i))/PBEr;
end
Ymr=Ymr+fra;

Kmr1=mstiffR(Ymr,NumofP,NumofR,posit);

```

13.1.19. Kms1.m / Kms2.m / Kms3.m

```

function Kms1=Kms1(Xms)
%% change the value for
the number of planet
Nofplanet=1;

%% calculation for rrs
%% input data
zs=ipdata(1);
zp=ipdata(2);
zr=ipdata(3);
as=ipdata(4);
ar=ipdata(5);
module=ipdata(6);
nofp=ipdata(7);

for i=1:1:ipdata(7)
    apofps(i)=pi-ipdata(200+i); %angular position of planet
spacing i
end

%%
ds=zs*module;
dp=zp*module;
dr=zr*module;
ha=module;
hf=1.25*module;
h=ha+hf;
dsa=ds+2*ha;
dpa=dp+2*ha;
dra=dr+2*ha;
dsf=ds-2*hf;
dpf=dp-2*hf;
drf=dr-2*hf;
dsb=ds*cos(as/180*pi);
dpb=dp*cos(as/180*pi);
drb=dr*cos(ar/180*pi);
Rsa=dsa/2;
Rpa=dpa/2;

Rra=drf/2;
Rsb=dsb/2;
Rpb=dpb/2;

Rrb=drb/2;

%%for sun-planet mesh
MsEs=sqrt(Rsa^2-Rsb^2);
BsNs=sqrt(Rpa^2-Rpb^2);
MsNs=(Rsb+Rpb)*tan(as/180*pi);
BsEs=MsEs+BsNs-MsNs;
MsPs=Rsb*tan(as/180*pi);
MsBs=MsEs-BsEs;
BsPs=MsPs-MsBs;

```

```

%pb=2*pi*Rsb/zs;
pb=pi*module*cos(as/180*pi);
BsCs=BsEs-pb;
BsDs=pb;

%for ring-planet mesh
MrNr=module/2*(zs+zp)*sin(ar/180*pi);
NrEr=sqrt(Rpa^2-Rpb^2);
MrBr=sqrt(Rra^2-Rrb^2);
BrEr=MrNr+NrEr-MrBr;
MrPr=Rrb*tan(ar/180*pi);
BrPr=MrPr-MrBr;
BrCr=BrEr-pb;
BrDr=pb;

% rrs
PsPr=Rpb*tan(as/180*pi)+Rpb*(pi-as/180*pi-
ar/180*pi)+Rpb*tan(ar/180*pi);
tb=module*(pi/2+2*inv(as));
Q2Br=PsPr-BrPr-tb;
dec1=Q2Br/pb;
dec2=int32(Q2Br/pb);
dec3=dec1-dec2;
if dec3>=0
    dec=dec2;
else dec=dec2-1;
end
BrQ3=pb-pb*(double(dec1)-double(dec));
PrQ3=BrQ3-BrPr;
if PrQ3>=0
    PrQ3=PrQ3;
else PrQ3=-PrQ3;
end
rrs=PrQ3/pb;
if rrs>=0
    rrs=rrs;
else rrs=-rrs;
end
if BrQ3-BrPr<=0
    rrs=rrs;
else rrs=-rrs;
end

PBEs=BsEs/pb;
PBPs=BsPs/pb;
PBCs=BsCs/pb;
PBDs=BsDs/pb;

BrEr;
BrPr;
BrCr;
BrDr;

PBEr=BrEr/pb;

```

```

PBPr=BrPr/pb;
PBCr=BrCr/pb;
PBDr=BrDr/pb;

rrs;

%%calculation of spacing difference between sun-planet
meshes
for i=1:1:nofp
    rsn(i)=zs*ipdata(200+i)/2/pi;
    rsnn=double(int64(rsn(i)));
    if rsnn>rsn(i)
        rsnn=rsnn-1;
    else
        rsnn=rsnn;
    end
    rsn(i)=rsn(i)-rsnn;
end
rsn=-rsn;

Xms=Xms+(PBPs-PBDs)-rsn(Nofplanet);
xx=double(int64(Xms));
if xx<=Xms;
    xx=xx;
else xx=xx-1;

end
tt=Xms-xx;
Yms=0;

for i=1:1:(double(int8(PBEs))+2)
    ymsss(i)=ymss(tt+i-1,PBEs);
    Yms=Yms+ymsss(i);

end
Yms=Yms;

for i=1:1:Yms
    xxx=xx+i-Yms+ipdata(2)+double(int64(ipdata(2)/2))-1;
    xxP=xxx/ipdata(2);
    xxPP=double(int64(xxP));

    if xxPP<=xxP
        xxPP=xxPP;
    else xxPP=xxPP-1;
    end
    NumofP(i)=Nofplanet*100+xxx-xxPP*ipdata(2)+1;
end
for i=1:1:Yms
    xxxx=xx+rsn(Nofplanet)+i-Yms+ipdata(1)+(2*pi-
apofps(Nofplanet)+apofps(1))/2/pi*ipdata(1);
    xxx=double(int64(xxxx));
    if xxx<=xxxx
        xxx=xxx;
    else xxx=xxx-1;
    end
    xxS=xxx/ipdata(1);
    xxSS=double(int64(xxS));
    if xxSS<=xxS
        xxSS=xxSS;
    else xxSS=xxSS-1;
    end
    NumofS(i)=xxx-xxSS*ipdata(1)+1;
end

fract=Xms+10;
fractt=double(int64(fract));
if fractt<=fract
    fractt=fractt;
else fractt=fractt-1;
end
frac=fract-fractt;
if frac<PBCs
    fra=frac/PBCs;
else fra=(frac-PBCs)/(PBDs-PBCs);
end
for i=1:1:Yms
    posit(i)=(fract-fractt+(Yms-i))/PBEs;
end
Yms=Yms+fra;

Kms1=mstiffs(Yms,NumofP,NumofS,posit);

```

13.1.20. mstiffr.m

```

function mstiffr=mstiffr(noft,NumofP,NumofR,posit)

%% input data
zs=ipdata(1);
zp=ipdata(2);
zr=ipdata(3);
as=ipdata(4);
ar=ipdata(5);
module=ipdata(6);
nofp=ipdata(7);
B=ipdata(8);

for i=1:1:ipdata(7)

apofps(i)=pi-ipdata(200+i); %angular position of planet
spacing i
end

Rss=ipdata(14);

Rps=ipdata(15);
Rrs=ipdata(16);

E=ipdata(21); % young's modules

%%%%%%%%%%%%%%%%%%%%%%%%%%%%%%%%%%%%%%%%%%%%%%%%%%%%%%%%%%%%%%%%%%%%%%%%%%
ds=zs*module;
dp=zp*module;
dr=zr*module;
ha=module;
hf=1.25*module;
h=ha+hf;
h=h;
dsa=ds+2*ha;
dpa=dp+2*ha;
dra=dr+2*ha;
dsf=ds-2*hf;
dpf=dp-2*hf;
drf=dr-2*hf;
dsb=ds*cos(as/180*pi);
dpb=dp*cos(as/180*pi);
drb=dr*cos(ar/180*pi);
Rsa=dsa/2;
Rpa=dpa/2;
Rra=drf/2;
Rsb=dsb/2;
Rpb=dpb/2;
Rrb=drb/2;
Rsf=dsf/2;
Rpf=dpf/2;

```



```
end
mstiffi=mstiff;
```

13.1.21. mstiffs.m

```
function mstiffss=mstiffs(noft,NumofP,NumofS,posit)
```

```
%% input data
zs=ipdata(1);
zp=ipdata(2);
zr=ipdata(3);
as=ipdata(4);
ar=ipdata(5);
module=ipdata(6);
nofp=ipdata(7);
B=ipdata(8);

for i=1:1:ipdata(7)
    apofps(i)=pi-ipdata(200+i); %angular position of planet
    spacing i
end

Rss=ipdata(14);
Rps=ipdata(15);
Rrs=ipdata(16);

E=ipdata(21); % young's modules
%%%%%%%%%%%%%%%%%%%%%%%%%%%%%%%%%%%%%%%%%%%%%%%%%%%%%%%%%%%%%%%%%%%%%%%%
ds=zs*module;
dp=zp*module;
dr=zr*module;
ha=module;
hf=1.25*module;
h=ha+hf;
h=h;
dsa=ds+2*ha;
dpa=dp+2*ha;
dra=dr+2*ha;
dsf=ds-2*hf;
dpf=dp-2*hf;
drf=dr-2*hf;
dsb=ds*cos(as/180*pi);
dpb=dp*cos(as/180*pi);
drb=dr*cos(ar/180*pi);
Rsa=dsa/2;
Rpa=dpa/2;
Rra=dra/2;
Rsb=dsb/2;
Rpb=dpb/2;
Rrb=drb/2;
Rsf=dsf/2;
Rpf=dpf/2;

Rrf=dra/2;

Rs=ds/2;
Rp=dp/2;
Rr=dr/2;

a=[2.7462 1.9479/2];
b=[2.2932 2.2853];

Numoft=int8(noft);
NumofS=double(NumofS);
if NumofP-nofp<=0
    NumofP=NumofP;
else NumofP=NumofP-1;
end
```

```
stiffAo=0;
for i=1:1:Numoft
    %if NumofP(i)==132
    %VNumofP(i)=0.05;
    %else
        VNumofP(i)=0;
    %end
    %if NumofS(i)==19
    %VNumofS(i)=0.05;
    %else
        VNumofS(i)=0;
    %end
    sS(i)=pi*module/2*(1-VNumofS(i));
    Is(i)=B*sS(i)^3/12;
    sP(i)=pi*module/2*(1-VNumofP(i));
    Ip(i)=B*sP(i)^3/12;
    stiffA(i)=a(Numoft)/Numoft*((h/2)^3/(3*E*Is(i))+(h/2)^3/(3*E*Ip(i)))/Rs;
    stiffAo=stiffAo+stiffA(i);
end

startstiff=Rsb/(stiffAo+b(Numoft)*((Rsf-Rss)/(E*B*Rss)+(Rpf-Rps)/(E*B*Rps))/Rsf);

s=pi*module/2;
IIs=B*s^3/12;
IIp=B*s^3/12;

endstiff=Rsb/(a(Numoft)*((h/2)^3/(3*E*IIs)+(h/2)^3/(3*E*IIp)))/Rs+b(Numoft)*((Rsf-Rss)/(E*B*Rss)+(Rpf-Rps)/(E*B*Rps))/Rsf);

%%%%%%%%%%%%%%%%%%%%%%%%%%%%%%%%%%%%%%%%%%%%%%%%%%%%%%%%%%%%%%%%%%%%%%%%
% simulation of curve shape of undamaged mesh
%%%%%%%%%%%%%%%%%%%%%%%%%%%%%%%%%%%%%%%%%%%%%%%%%%%%%%%%%%%%%%%%%%%%%%%%
mstiffss=endstiff;
dedu=endstiff-startstiff;
%%%%%%%%%%%%%%%%%%%%%%%%%%%%%%%%%%%%%%%%%%%%%%%%%%%%%%%%%%%%%%%%%%%%%%%%
% simulation of curve shape of stiffness function
%%%%%%%%%%%%%%%%%%%%%%%%%%%%%%%%%%%%%%%%%%%%%%%%%%%%%%%%%%%%%%%%%%%%%%%%

if Numoft==1
    mstiff=mstiffss-dedu;
else if Numoft==2
    if startstiff-endstiff==0
        mstiff=mstiffss-dedu;
        else if VNumofP(1)+VNumofS(1)>0 &&
VNumofP(2)+VNumofS(2)>0
            mstiff=mstiffss-dedu;
        else if VNumofP(1)+VNumofS(1)>0
            mstiff=mstiffss-dedu;
        else if VNumofP(2)+VNumofS(2)>0
            mstiff=mstiffss-(endstiff-startstiff)*(noft-
Numoft)^3/2;
        else
            mstiff=mstiffss-dedu;
        end
    end
end
end
end
end
```

```

%% simulation of spalling
stiffAos=0;
for i=1:1:Numoft
if NumofP(i)==132
PNumofP(i)=0;
WNumofP(i)=0;
DNumofP(i)=0;
else
PNumofP(i)=0;
WNumofP(i)=0;
DNumofP(i)=0;
end
if NumofS(i)==19
PNumofS(i)=0.6;
WNumofS(i)=0.05;
DNumofS(i)=20e-5/sqrt(PNumofS(i));
else
PNumofS(i)=0;
WNumofS(i)=0;
DNumofS(i)=0;
end
sS(i)=pi*module/2*(1-DNumofS(i));
Is(i)=B*sS(i)^3/12;
sP(i)=pi*module/2*(1-DNumofP(i));
Ip(i)=B*sP(i)^3/12;
stiffAs(i)=a(Numoft)/Numoft*((h/2)^3/(3*E*Is(i)))+(h/2)^3/(3
*E*Ip(i))/Rs;

```

13.1.22. TorM.m

```

function TorqueM=TorqueM(speedM)
p=ipdata(31);
f=ipdata(32);
opspeedM=ipdata(33);
power=ipdata(34);

topspeedM=120*f/p;
Tfl=power*60/opspeedM/2/pi*0.96; % full load torque
Tsu=2.3*Tfl; % start-up torque
Tm=2.6*Tfl; % maximum torque

```

13.1.23. inertiaC.m

```

function inertiaC=inertiaC(speedC,dispC)

inertiaore=ipdata(92)*(1/4*1/2*ipdata(23)*pi*ipdata(90)^4*ipdata(91)+1/4*ipdata(85)^2*ipdata(23)*pi*ipdata(90)^2*ipdata(91));
inertiawithoutore=1/2*pi*ipdata(22)*(ipdata(82)^4-ipdata(81)^4)*ipdata(83)+1/2*pi*ipdata(22)*(ipdata(85)^4-ipdata(84)^4)*ipdata(86)+ipdata(85)^2*ipdata(87)*1/4*pi*ipdata(22)*(ipdata(88)^2*ipdata(89)-ipdata(90)^2*ipdata(91))+ipdata(87)*1/4*1/2*pi*ipdata(22)*(ipdata(88)^4*ipdata(89)-ipdata(90)^4*ipdata(91));

if dispC<=ipdata(44)
inertia=inertiawithoutore;
else if dispC<=ipdata(45)
inertia=inertiawithoutore+inertiaore*(dispC-ipdata(44))/(ipdata(45)-ipdata(44));

```

```

stiffAos=stiffAos+stiffAs(i);
end

startstiff=Rs/(stiffAos+b(Numoft))*((Rs/Rss)/(E*B*Rss)+(Rpf-Rps)/(E*B*Rps))/Rsf);
endstiff=endstiff;
dedus=endstiff-startstiff;

for i=1:1:Numoft
if posit(i)-PNumofP(i)<WNumofP(i) && posit(i)-PNumofP(i)>=0
mstiff=mstiff-dedus*cos((posit(i)-PNumofP(i))/WNumofP(i)*pi/2)^(1/5);
else if posit(i)-PNumofP(i)<0
mstiff=mstiff-dedus*posit(i)/PNumofP(i);
else
mstiff=mstiff;
end
end
if posit(i)-PNumofS(i)<WNumofS(i) && posit(i)-PNumofS(i)>=0
mstiff=mstiff-dedus*cos((posit(i)-PNumofS(i))/WNumofS(i)*pi/2)^(1/5);
else if posit(i)-PNumofS(i)<0
mstiff=mstiff-dedus*posit(i)/PNumofS(i);
else
mstiff=mstiff;
end
end
end
mstiff=mstiff;

```

```

toploadspeedM=topspeedM-Tm*(topspeedM-opspeedM)/Tfl;

if speedM>=0 && speedM<=toploadspeedM
TorqueM=(Tm-Tsu)/(toploadspeedM-0)*speedM+Tsu;
else if speedM>=toploadspeedM && speedM<=topspeedM
TorqueM=(Tfl-0)/(topspeedM-opspeedM)*(-speedM+topspeedM);
else TorqueM=0;
end
end

```

```

else if dispC<=ipdata(46)
Lstep=(dispC-ipdata(45))/ipdata(48);
Lstepint=double(int64(Lstep));
if Lstepint<=Lstep
Lstepint=Lstepint;
else Lstepint=Lstepint-1;
end
LstepL=ipdata(48)*(Lstep-Lstepint);
if LstepL<=ipdata(94)
inertia=inertiawithoutore+inertiaore*(ipdata(92)-ipdata(93)*LstepL/ipdata(94))/ipdata(92);
else
inertia=inertiawithoutore+inertiaore*(ipdata(92)-ipdata(93)+ipdata(93)*(LstepL-ipdata(94))/(ipdata(48)-ipdata(94)))/ipdata(92);
end
else if dispC<=ipdata(47)
Lstep=(ipdata(46)-ipdata(45))/ipdata(48);

```

```

Lstepint=double(int64(Lstep));
if Lstepint<=Lstep
    Lstepint=Lstepint;
else Lstepint=Lstepint-1;
end
LstepL=ipdata(48)*(Lstep-Lstepint);

if LstepL<=ipdata(94)
    inertia=inertiawithoutore+inertiaore*(ipdata(92)-
ipdata(93)*LstepL/ipdata(94))/ipdata(92);
else
    inertia=inertiawithoutore+inertiaore*(ipdata(92)-
ipdata(93)+ipdata(93)*(LstepL-ipdata(94))/(ipdata(48)-
ipdata(94)))/ipdata(92);

```

13.1.24. massC.m

```

function massC=massC(speedC,dispC)
massore=ipdata(92)*(ipdata(23)*pi*ipdata(90)^2*ipdata(91)/
4);
masswithoutore=pi*ipdata(22)*(ipdata(82)^2-
ipdata(81)^2)*ipdata(83)+pi*ipdata(22)*(ipdata(85)^2-
ipdata(84)^2)*ipdata(86)+ipdata(87)*1/4*pi*ipdata(22)*(ipda
ta(88)^2*ipdata(89)-ipdata(90)^2*ipdata(91));

if dispC<=ipdata(44)
    mass=masswithoutore;
else if dispC<=ipdata(45)
    mass=masswithoutore+massore*(dispC-
ipdata(44))/(ipdata(45)-ipdata(44));
else if dispC<=ipdata(46)
    Lstep=(dispC-ipdata(45))/ipdata(48);
    Lstepint=double(int64(Lstep));
    if Lstepint<=Lstep
        Lstepint=Lstepint;
    else Lstepint=Lstepint-1;
    end
    LstepL=ipdata(48)*(Lstep-Lstepint);
    if LstepL<=ipdata(94)
        mass=masswithoutore+massore*(ipdata(92)-
ipdata(93)*LstepL/ipdata(94))/ipdata(92);
    else
        mass=masswithoutore+massore*(ipdata(92)-
ipdata(93)+ipdata(93)*(LstepL-ipdata(94))/(ipdata(48)-
ipdata(94)))/ipdata(92);

```

13.1.25. TorqueS.m

```

function TorqueS=TorqueS(speedS)
speedM=speedS*ipdata(35);

p=ipdata(31);
f=ipdata(32);

opspeedM=ipdata(33);
power=ipdata(34);

topspeedM=120*f/p;
Tfl=power*60/opspeedM/2/pi; % full load torque
Tsu=2.3*Tfl; % start-up torque
Tm=2.6*Tfl; % maximum torque

```

13.1.26. torqueOUT.m

```

function torqueOUT4=torqueOUT4(speedC,dispC)
p=ipdata(31);

```

```

end
inertia=(inertia-inertiawithoutore)*(ipdata(47)-
dispC)/(ipdata(47)-ipdata(46))+inertiawithoutore;
else inertia=inertiawithoutore;
end
end
end

inertiaC=inertia;

```

```

end
else if dispC<=ipdata(47)
    Lstep=(ipdata(46)-ipdata(45))/ipdata(48);
    Lstepint=double(int64(Lstep));
    if Lstepint<=Lstep
        Lstepint=Lstepint;
    else Lstepint=Lstepint-1;
    end
    LstepL=ipdata(48)*(Lstep-Lstepint);
    if LstepL<=ipdata(94)
        mass=masswithoutore+massore*(ipdata(92)-
ipdata(93)*LstepL/ipdata(94))/ipdata(92);
    else
        mass=masswithoutore+massore*(ipdata(92)-
ipdata(93)+ipdata(93)*(LstepL-ipdata(94))/(ipdata(48)-
ipdata(94)))/ipdata(92);
    end
    mass=(mass-masswithoutore)*(ipdata(47)-
dispC)/(ipdata(47)-ipdata(46))+masswithoutore;
else mass=masswithoutore;
end
end
end
end

massC=mass;

```

```

toploadspeedM=topspeedM-Tm*(topspeedM-op-speedM)/Tfl;

if speedM<=toploadspeedM && speedM>=0
    TorqueM=(Tm-Tsu)/(toploadspeedM-0)*speedM+Tsu;
else if speedM>=toploadspeedM && speedM<=topspeedM
    TorqueM=(Tfl-0)/(topspeedM-op-speedM)*(-
speedM+topspeedM);
else TorqueM=0;
end
end

TorqueS=TorqueM*ipdata(35);

```

```

f=ipdata(32);
op-speedM=ipdata(33);

```

```

power=ipdata(34);
topspeedM=120*f/p;
Tfl=power*60/opspeedM/2/pi; % full load torque
Tsu=2.3*Tfl; % start-up torque
Tm=2.6*Tfl; % maximum torque

%torqueOUT4=Tfl*ipdata(36)/(ipdata(41)*opspeedM/ipdata(
36))^2*speedC^2+(ipdata(41)^2-
1)*Tfl*ipdata(36)/(ipdata(41)*opspeedM/ipdata(36))^2*speed
C^2;

if dispC<=ipdata(44)

torqueOUT=Tfl*ipdata(36)/(ipdata(41)*opspeedM/ipdata(36)
)^2*speedC^2;
else if dispC<=ipdata(45)

torqueOUT=Tfl*ipdata(36)/(ipdata(41)*opspeedM/ipdata(36)
)^2*speedC^2+(ipdata(41)^2-
1)*Tfl*ipdata(36)/(ipdata(41)*opspeedM/ipdata(36))^2*speed
C^2*(dispC-ipdata(44))/(ipdata(45)-ipdata(44));
    else if dispC<=ipdata(46)
        Lstep=(dispC-ipdata(45))/ipdata(48);
        Lstepint=double(int64(Lstep));
        if Lstepint<=Lstep
            Lstepint=Lstepint;
        else Lstepint=Lstepint-1;
        end
        LstepL=ipdata(48)*(Lstep-Lstepint);
        if LstepL<=ipdata(94)

torqueOUT=Tfl*ipdata(36)/(ipdata(41)*opspeedM/ipdata(36)
)^2*speedC^2+(ipdata(41)^2-
1)*Tfl*ipdata(36)/(ipdata(41)*opspeedM/ipdata(36))^2*speed
C^2*(ipdata(92)-ipdata(93)*LstepL/ipdata(94))/ipdata(92);
        else

torqueOUT=(torqueOUT-
Tfl*ipdata(36)/(ipdata(41)*opspeedM/ipdata(36))^2*speedC^
2)*(ipdata(47)-dispC)/(ipdata(47)-
ipdata(46))+Tfl*ipdata(36)/(ipdata(41)*opspeedM/ipdata(36)
)^2*speedC^2;
        else
torqueOUT=Tfl*ipdata(36)/(ipdata(41)*opspeedM/ipdata(36)
)^2*speedC^2;
        end
    end
end
if dispC<=ipdata(50) && dispC>=ipdata(49)
    torqueOUT=torqueOUT*ipdata(95);
end
if speedC<=0
    torqueOUT=0;
end
torqueOUT4=torqueOUT;

```

```

end
else if dispC<=ipdata(47)
    Lstep=(ipdata(46)-ipdata(45))/ipdata(48);
    Lstepint=double(int64(Lstep));
    if Lstepint<=Lstep
        Lstepint=Lstepint;
    else Lstepint=Lstepint-1;
    end
    LstepL=ipdata(48)*(Lstep-Lstepint);
    if LstepL<=ipdata(94)

torqueOUT=Tfl*ipdata(36)/(ipdata(41)*opspeedM/ipdata(36)
)^2*speedC^2+(ipdata(41)^2-
1)*Tfl*ipdata(36)/(ipdata(41)*opspeedM/ipdata(36))^2*speed
C^2*(ipdata(92)-ipdata(93)*LstepL/ipdata(94))/ipdata(92);
    else

torqueOUT=(torqueOUT-
Tfl*ipdata(36)/(ipdata(41)*opspeedM/ipdata(36))^2*speedC^
2)*(ipdata(47)-dispC)/(ipdata(47)-
ipdata(46))+Tfl*ipdata(36)/(ipdata(41)*opspeedM/ipdata(36)
)^2*speedC^2;
    else
torqueOUT=Tfl*ipdata(36)/(ipdata(41)*opspeedM/ipdata(36)
)^2*speedC^2;
    end
end
end
if dispC<=ipdata(50) && dispC>=ipdata(49)
    torqueOUT=torqueOUT*ipdata(95);
end
if speedC<=0
    torqueOUT=0;
end
torqueOUT4=torqueOUT;

```

13.1.27. Vdp1.m

```

%% dynamic modelling of planetary gear
system %%% input
%% Notice: replace fae(i) with ((y(3)-y(6))/(rr+rs)+pi-
ipdata(20i))

%% Notice: replace Ksp(i) with

%% (SKmsi((ipdata(36)/ipdata(35)-1)*zs*(y(3)-
y(6))/(rr+rs)/2/pi))
%% Notice: replace Krp(i) with
%% (SKmri(zr*(y(3)-y(6))/(rr+rs)/2/pi))
%% Notice: replace Dfesp(i) with 0
%% ((espi(ipdata(36)/ipdata(35)-1)*zs*(y(3)-
y(6))/(rr+rs)/2/pi+ipdata(55))-espi(ipdata(36)/ipdata(35)-
1)*zs*(y(3)-y(6))/(rr+rs)/2/pi-ipdata(55))/ipdata(55)/2)
%% Notice: replace Dferp(i) with 0
%% ((erpi(zr*(y(3)-y(6))/(rr+rs)/2/pi+ipdata(55))-
erpi(zr*(y(3)-y(6))/(rr+rs)/2/pi-ipdata(55))/ipdata(55)/2))
%% Notice: replace fesp(i) with

```

```

%% (espi(ipdata(36)/ipdata(35)-1)*zs*(y(3)-
y(6))/(rr+rs)/2/pi))

%% Notice: replace ferp(i) with
%% (erpi(zr*(y(3)-y(6))/(rr+rs)/2/pi))
%% Notice: replace Dtcp(i) with 0
%% (ipdata(67)*ipdata(30i)/180*pi)
%% Notice: replace Ts s with
%% (qcc*y(38)*(y(38)-y(21))*ipdata(35)/rs)*ipdata(35))
%% (TorqueS(y(21)/rs/2/pi*60))
%% Notice: replace T c with
%% (torqueOUT(y(27)/rc/2/pi*60,y(9)))

%% Notice: replace options
%% mass (1)=
(pi*ipdata(8)*ipdata(22)*((ipdata(6)*ipdata(1)/2)^2-
ipdata(14)^2))
%% mass (2)=
(pi*ipdata(8)*ipdata(22)*((ipdata(6)*ipdata(1)/2)^2-
ipdata(14)^2))
%% mass (3)=
(pi*ipdata(8)*ipdata(22)*((ipdata(6)*ipdata(1)/2)^4-
ipdata(14)^4)/2/rs/rs)

```



```

MrNr=module/2*(zs+zp)*sin(ar/180*pi);
NrEr=sqrt(Rpa^2-Rpb^2);
MrBr=sqrt(Rra^2-Rrb^2);
BrEr=MrNr+NrEr-MrBr;
MrPr=Rrb*tan(ar/180*pi);
BrPr=MrPr-MrBr;
BrCr=BrEr-pb;
BrDr=pb;

% rrs
PsPr=Rpb*tan(as/180*pi)+Rpb*(pi-as/180*pi-
ar/180*pi)+Rpb*tan(ar/180*pi);
tb=module*(pi/2+2*inv(as));
Q2Br=PsPr-BrPr-tb;
dec1=Q2Br/pb;
dec2=int32(Q2Br/pb);
dec3=dec1-dec2;
if dec3>=0
    dec=dec2;
else dec=dec2-1;
end
BrQ3=pb-pb*(double(dec1)-double(dec));
PrQ3=BrQ3-BrPr;
if PrQ3>=0
    PrQ3=PrQ3;
else PrQ3=-PrQ3;
end
rrs=PrQ3/pb;
if rrs>=0
    rrs=rrs;
else rrs=-rrs;
end
if BrQ3-BrPr<=0
    rrs=rrs;
else rrs=-rrs;
end

PBEs=BsEs/pb;
PBPs=BsPs/pb;
PBCs=BsCs/pb;
PBDs=BsDs/pb;

BrEr;
BrPr;
BrCr;
BrDr;

PBEr=BrEr/pb;
PBPr=BrPr/pb;
PBCr=BrCr/pb;
PBDr=BrDr/pb;

rrs;

%%calculation of spacing difference between ring-planet
meshes
for i=1:1:nofp
    rm(i)=zr*apofps(i)/2/pi;
    rmn=double(int64(rm(i)));
    if rmn>rmn(i)
        rmn=rmn-1;
    else
        rmn=rmn;
    end
end

rmn(i)=rmn(i)-rmn;
end
rmn=rmn-1;

Xmr=Xmr+(PBPr-PBDr)-rmn(Nofplanet)-rrs;
xx=double(int64(Xmr));
if xx<=Xmr;
    xx=xx;
else xx=xx-1;
end
tt=Xmr-xx;
Ymr=0;
for i=1:(double(int8(PBEr))+2)
    ymrr(i)=ymrr(tt+i-1,PBEr);
    Ymr=Ymr+ymrr(i);
end
Ymr=Ymr;

for i=1:1:Ymr
    xxx=xx+i-Ymr+ipdata(2);
    xxP=xxx/ipdata(2);
    xxPP=double(int64(xxP));
    if xxPP<=xxP
        xxPP=xxPP;
    else xxPP=xxPP-1;
    end
    NumofP(i)=Nofplanet*100+xxx-xxPP*ipdata(2)+1;
end
for i=1:1:Ymr
    xxxx=xx+rm(Nofplanet)+i-Ymr+ipdata(3)+(2*pi-
apofps(Nofplanet)+apofps(1))/2/pi*ipdata(3)+1;
    xxx=double(int64(xxxx));
    if xxx<=xxxx
        xxx=xxx;
    else xxx=xxx-1;
    end
    xxR=xxx/ipdata(3);
    xxRR=double(int64(xxR));
    if xxRR<=xxR
        xxRR=xxRR;
    else xxRR=xxRR-1;
    end
    NumofR(i)=xxx-xxRR*ipdata(3)+1;
end

fract=Xmr+10;
fractt=double(int64(fract));
if fractt<=fract
    fractt=fractt;
else fractt=fractt-1;
end
frac=fract-fractt;
if frac<(PBCr-PBDr)
    fra=frac/(PBCr-PBDr);
else fra=(frac-(PBCr-PBDr))/(2*PBDr-PBCr);
end
for i=1:1:Ymr
    posit(i)=(fract-fractt+(Ymr-i))/PBEr;
end
Ymr=Ymr+fra;

emr1=emrrr(Ymr,NumofP,NumofR,posit);

```

13.1.29. emrrr.m

```
function emrrr=emrrr(noft,NumofP,NumofR,posit)
```

```
%% input data
```

```

zs=ipdata(1);
zp=ipdata(2);
zr=ipdata(3);
as=ipdata(4);
ar=ipdata(5);
module=ipdata(6);
nofp=ipdata(7);
B=ipdata(8);

for i=1:1:ipdata(7)
    apofps(i)=pi-ipdata(200+i); %angular position of planet
spacing i
end

Rss=ipdata(14);
Rps=ipdata(15);
Rrs=ipdata(16);

E=ipdata(21); % young's modules
%%%%%%%%%%
ds=zs*module;
dp=zp*module;
dr=zr*module;
ha=module;
hf=1.25*module;
h=ha+hf;
h=h;
dsa=ds+2*ha;
dpa=dp+2*ha;
dra=dr+2*ha;
dsf=ds-2*hf;
dpf=dp-2*hf;
drf=dr-2*hf;
dsb=ds*cos(as/180*pi);
dpb=dp*cos(as/180*pi);
drb=dr*cos(ar/180*pi);
Rsa=dsa/2;
Rpa=dpa/2;
Rra=drf/2;
Rsb=dsb/2;
Rpb=dpb/2;
Rrb=drb/2;
Rsf=dsf/2;
Rpf=dpf/2;
Rrf=dra/2;
Rs=ds/2;
Rp=dp/2;
Rr=dr/2;

a=[2.7462 1.9479/2 1.7754/3];
b=[2.2932 2.2853 2.2771];

```

```

Numoft=int8(noft);
Numoft=double(Numoft);

```

13.1.30. **ems1.m / ems2.m / ems3.m**

```

function ems1=ems1(Xms)
%%%%%%%%%% change the value for
the number of planet
Nofplanet=1;

%% calculation for rrs
%% input data
zs=ipdata(1);
zp=ipdata(2);
zr=ipdata(3);

```

```

if Numoft-noft<=0

    Numoft=Numoft;
else Numoft=Numoft-1;
end

```

```

rrAos=0;
for i=1:1:Numoft
if NumofP(i)==132
PNumofP(i)=0;
WNumofP(i)=0;
DNumofP(i)=0;
else
PNumofP(i)=0;
WNumofP(i)=0;
DNumofP(i)=0;
end

```

```

if NumofR(i)==83
PNumofR(i)=0.6;
WNumofR(i)=0.2;
DNumofR(i)=0;
else
PNumofR(i)=0;
WNumofR(i)=0;
DNumofR(i)=0;
end
end

```

```

startrrs=0;

```

```

for i=1:1:Numoft
    mrr(i)=0;
if posit(i)-PNumofP(i)<WNumofP(i) && PNumofP(i)-
posit(i)<WNumofP(i)
    mrr(i)=mrr(i)+DNumofP(i)*cos((posit(i)-
PNumofP(i))/WNumofP(i)*pi/2)^(1/5);
else
    mrr(i)=mrr(i)+0;
end
if posit(i)-PNumofR(i)<WNumofR(i) && PNumofR(i)-
posit(i)<WNumofR(i)
    mrr(i)=mrr(i)+DNumofR(i)*cos((posit(i)-
PNumofR(i))/WNumofR(i)*pi/2)^(1/5);
else
    mrr(i)=mrr(i)+0;
end
if startrrs<=mrr(i)
    startrrs=mrr(i);
else startrrs=startrrs;
end
end

```

```

emrrr=startrrs;

```

```

as=ipdata(4);
ar=ipdata(5);
module=ipdata(6);

nofp=ipdata(7);

```

```

for i=1:1:ipdata(7)
    apofps(i)=pi-ipdata(200+i); %angular position of planet
spacing i
end

```

```

%%
ds=zs*module;
dp=zp*module;
dr=zr*module;
ha=module;
hf=1.25*module;
h=ha+hf;
dsa=ds+2*ha;
dpa=dp+2*ha;
dra=dr+2*ha;
dsf=ds-2*hf;
dpf=dp-2*hf;
drf=dr-2*hf;
dsb=ds*cos(as/180*pi);
dpb=dp*cos(as/180*pi);
drb=dr*cos(ar/180*pi);
Rsa=dsa/2;
Rpa=dpa/2;
Rra=drf/2;
Rsb=dsb/2;
Rpb=dpb/2;
Rrb=drb/2;

%%for sun-planet mesh
MsEs=sqrt(Rsa^2-Rsb^2);
BsNs=sqrt(Rpa^2-Rpb^2);
MsNs=(Rsb+Rpb)*tan(as/180*pi);
BsEs=MsEs+BsNs-MsNs;
MsPs=Rsb*tan(as/180*pi);
MsBs=MsEs-BsEs;
BsPs=MsPs-MsBs;
%pb=2*pi*Rsb/zs;
pb=pi*module*cos(as/180*pi);
BsCs=BsEs-pb;
BsDs=pb;

%%for ring-planet mesh
MrNr=module/2*(zs+zp)*sin(ar/180*pi);
NrEr=sqrt(Rpa^2-Rpb^2);
MrBr=sqrt(Rra^2-Rrb^2);
BrEr=MrNr+NrEr-MrBr;
MrPr=Rrb*tan(ar/180*pi);
BrPr=MrPr-MrBr;
BrCr=BrEr-pb;
BrDr=pb;

% rrs
PsPr=Rpb*tan(as/180*pi)+Rpb*(pi-as/180*pi-
ar/180*pi)+Rpb*tan(ar/180*pi);
tb=module*(pi/2+2*inv(as));
Q2Br=PsPr-BrPr-tb;
dec1=Q2Br/pb;
dec2=int32(Q2Br/pb);
dec3=dec1-dec2;
if dec3>=0
    dec=dec2;
else dec=dec2-1;
end
BrQ3=pb-pb*(double(dec1)-double(dec));
PrQ3=BrQ3-BrPr;
if PrQ3>=0
    PrQ3=PrQ3;
else PrQ3=-PrQ3;
end
rrs=PrQ3/pb;
if rrs>=0
    rrs=rrs;
else rrs=-rrs;
end
if BrQ3-BrPr<=0

```

```

rrs=rrs;
else rrs=-rrs;
end

PBEs=BsEs/pb;
PBPs=BsPs/pb;
PBCs=BsCs/pb;
PBDs=BsDs/pb;

BrEr;
BrPr;
BrCr;
BrDr;

PBEr=BrEr/pb;
PBPr=BrPr/pb;
PBCr=BrCr/pb;
PBDr=BrDr/pb;

rrs;

%%calculation of spacing difference between sun-planet
meshes
for i=1:nofp
    rsn(i)=zs*apofps(i)/2/pi;
    rsnn=double(int64(rsn(i)));
    if rsnn>rsn(i)
        rsnn=rsnn-1;
    else
        rsnn=rsnn;
    end
    rsn(i)=rsn(i)-rsnn;
end

Xms=Xms+(PBPs-PBDs)-rsn(Nofplanet);
xx=double(int64(Xms));
if xx<=Xms;
    xx=xx;
else xx=xx-1;
end
tt=Xms-xx;
Yms=0;
for i=1:(double(int8(PBEs))+2)
    ymsss(i)=ymss(tt+i-1,PBEs);
    Yms=Yms+ymsss(i);
end
Yms=Yms;

for i=1:Yms
    xxx=xx+i-Yms+ipdata(2)+double(int64(ipdata(2)/2))-1;
    xxP=xxx/ipdata(2);
    xxPP=double(int64(xxP));
    if xxPP<=xxP
        xxPP=xxPP;
    else xxPP=xxPP-1;
    end
    NumofP(i)=Nofplanet*100+xxx-xxPP*ipdata(2)+1;
end
for i=1:Yms
    xxxx=xx+rsn(Nofplanet)+i-Yms+ipdata(1)+(2*pi-
apofps(Nofplanet)+apofps(1))/2/pi*ipdata(1);
    xxx=double(int64(xxxx));
    if xxx<=xxxx
        xxx=xxx;
    else xxx=xxx-1;
    end
    xxS=xxx/ipdata(1);
    xxSS=double(int64(xxS));
    if xxSS<=xxS

```

```

        xxSS=xxSS;
    else xxSS=xxSS-1;
    end
    NumofS(i)=xxx-xxSS*ipdata(1)+1;
end

fract=Xms+10;
fractt=double(int64(fract));
if fractt<=fract
    fractt=fractt;
else fractt=fractt-1;
end

```

```

frac=frac-fractt;
if frac<PBCs
    fra=frac/PBCs;
else fra=(frac-PBCs)/(PBDs-PBCs);
end
for i=1:1:Yms
    posit(i)=(frac-fractt+(Yms-i))/PBEs;
end
Yms=Yms+fra;

emssl=emsss(Yms,NumofP,NumofS,posit);

```

13.1.31. emsss.m

```
function emsss=emsss(noft,NumofP,NumofS,posit)
```

```

%% input data
zs=ipdata(1);
zp=ipdata(2);
zr=ipdata(3);
as=ipdata(4);
ar=ipdata(5);
module=ipdata(6);
nofp=ipdata(7);
B=ipdata(8);

for i=1:1:ipdata(7)
    apofps(i)=pi-ipdata(200+i); %angular position of planet
spacing i
end

Rss=ipdata(14);
Rps=ipdata(15);
Rrs=ipdata(16);

E=ipdata(21); % young's modules
%%%%%%%%%%%%%%%%%%%%%%%%%%%%%%%%%%%%%%%%%%%%%%%%%%%%%%%%%%%%%%%%%%%%%%%%
ds=zs*module;
dp=zp*module;
dr=zr*module;
ha=module;
hf=1.25*module;
h=ha+hf;
h=h;
dsa=ds+2*ha;
dpa=dp+2*ha;
dra=dr+2*ha;
dsf=ds-2*hf;
dpf=dp-2*hf;
drf=dr-2*hf;
dsb=ds*cos(as/180*pi);
dpb=dp*cos(as/180*pi);
drb=dr*cos(ar/180*pi);
Rsa=dsa/2;
Rpa=dpa/2;
Rra=dra/2;
Rsb=dsb/2;
Rpb=dpb/2;
Rrb=drb/2;
Rsf=dsf/2;
Rpf=dpf/2;
Rrf=dra/2;
Rs=ds/2;
Rp=dp/2;
Rr=dr/2;
a=[2.7462 1.9479/2];
b=[2.2932 2.2853];
Numoft=int8(noft);

```

```

Numoft=double(Numoft);
if Numoft-noft<=0
    Numoft=Numoft;
else Numoft=Numoft-1;
end

ssAos=0;
for i=1:1:Numoft
    if NumofP(i)==132
        PNumofP(i)=0;
        WNumofP(i)=0;
        DNumofP(i)=0;
    else
        PNumofP(i)=0;
        WNumofP(i)=0;
        DNumofP(i)=0;
    end
end
if NumofS(i)==19
    PNumofS(i)=0.6;
    WNumofS(i)=0.05;
    DNumofS(i)=20e-5;
else
    PNumofS(i)=0;
    WNumofS(i)=0;
    DNumofS(i)=0;
end
end

startsss=0;

for i=1:1:Numoft
    mss(i)=0;
    if posit(i)-PNumofP(i)<WNumofP(i) && PNumofP(i)-
        posit(i)<WNumofP(i)
        mss(i)=mss(i)+DNumofP(i)*cos((posit(i)-
        PNumofP(i))/WNumofP(i)*pi/2)^(1/5);
    else
        mss(i)=mss(i)+0;
    end
    if posit(i)-PNumofS(i)<WNumofS(i) && PNumofS(i)-
        posit(i)<WNumofS(i)
        mss(i)=mss(i)+DNumofS(i)*cos((posit(i)-
        PNumofS(i))/WNumofS(i)*pi/2)^(1/5);
    else
        mss(i)=mss(i)+0;
    end
end
if startsss<=mss(i)
    startsss=mss(i);
else startsss=startsss;
end
end

emsss=startsss;

```

13.2. RESULTS OF UNDAMAGED GEARBOX, CASE-2

